

University of Science and Technology of China  
A dissertation for doctor's degree



**$H \rightarrow \gamma\gamma$  search and direct photon  
pair production differential cross  
section measurement at DØ**

Author's Name :                      Xuebing Bu  
Speciality :                              High Energy Physics  
Supervisors :      Prof. Liang Han and Yanwen Liu  
Finished Time :                          June 2010



## Acknowledgements

At first, I would like to thank my past and current DØ colleagues, without their tremendous, fundamental and essential work, the studies presented in this thesis could never be done. I appreciate the help from lots of people during these 5 years, some of discussions remain fresh in my memory, taking this opportunity, I would like to mention some of them.

I would like to thank my supervisors Liang Han and Yanwen Liu for bringing me to the world of high energy physics, and giving me invaluable guidance in the past 5 years. Especially, giving me the opportunity to continuously study at Fermilab for 3 years, where I could work with the world-class scientists and am proud to be a member of the "dream team" - DØ collaboration.

A large part of the studies presented in this thesis is related to the photon identification, which belongs to the DØ Electron and Photon Identification (EMID) group. I am glad to be a member of this group, and would like to thank the experienced EMID experts Dmitry Bandurin and Junjie Zhu, for teaching me and helping out at the beginning and along the way. I am proud to be the first graduate student to be the co-convener of the EMID group since last September. I would like to thank my co-convener Maiko Takahashi for lots of useful and important suggestions and discussions. Also big thanks to my EMID colleagues: Betty Calpas, Guo Chen, Mark Cooke, Pengfei Ding, Tim Head, Ketino

Kaadze, Andrew Kobach, Sehwook Lee, Jorge Martinez, Alexander Verkheev, Mika Vesterinen, Yunhe Xie, Siqi Yang, Hang Yin and Ning Zhou for their continuously hard and excellent work.

I would like to thank my "local" supervisor, Aurelio Juste, the smart and energetic man, who supervised me locally at DØ . He is knowledgeable, to be the physics coordinator of the DØ experiment would approve this. He is also "critical" due to his inexhaustible energy and determination to always improve. I can not thank him too much with the world-best words, and I could not remember how many times he stopped by my office, as well as how long our discussions went, but I know lots of them seemed to just happen at yesterday.

A lot of thanks to the ex-convener of DØ Higgs group, Gavin Davies. I really appreciate his always positive support, encouragement and useful suggestions. Also, I would like to thank the DØ Editorial Board 13, chaired by Elemer Nagy, to review our results and help a lot to improve the quality.

I would like to thank Gavin Davies, Yuanning Gao, Shan Jin, Aurelio Juste, Xueqian Li, Zuotang Liang, Jianping Ma, Wengan Ma, Xiaoyan Shen, Stefan Soldner-Rembold, Ziping Zhang and Shouhua Zhu for reviewing my thesis. And lots of thanks to my thesis committee members: Yuanning Gao, Xueqian Li, Jianping Ma, Wengan Ma, Yadong Yang and Zhaoxi Zhang.

Finally, I would like to thank my wife, Shan, for her love, support and encouragement, as well as understanding of her "naive" husband.

## Abstract

At a hadron collider, diphoton ( $\gamma\gamma$ ) production allows detailed studies of the Standard Model (SM), as well as searches for new phenomena, such as new heavy resonances, extra spatial dimensions or cascade decays of heavy new particles. Within the SM, continuum  $\gamma\gamma+X$  production is characterized by a steeply-falling  $\gamma\gamma$  mass spectrum, on top of which a heavy resonance decaying into  $\gamma\gamma$  can potentially be observed. In particular, this is considered one of the most promising discovery channels for a SM Higgs boson at the LHC, despite the small branching ratio of  $\text{BR}(H \rightarrow \gamma\gamma) \sim 0.2\%$  for  $110 < M_{\text{Higgs}} < 140$  GeV. At the Tevatron, the dominant SM Higgs boson production mechanism is gluon fusion, followed by associated production with a W or Z boson, and vector boson fusion. While the SM Higgs production rate at the Tevatron is not sufficient to observe it in the  $\gamma\gamma$  mode, the  $Hgg$  and  $H\gamma\gamma$  couplings, being loop-mediated, are particularly sensitive to new physics effects. Furthermore, in some models beyond the SM, for instance, fermiophobic Higgs, with no couplings to fermions, the  $\text{BR}(H \rightarrow \gamma\gamma)$  can be enhanced significantly relative to the SM prediction, while has the SM-like production cross sections except the gluon fusion is absent.

In this thesis, we present a search for a light Higgs boson in the diphoton final state using  $4.2 \pm 0.3 \text{ fb}^{-1}$  of the DØ Run II data, collected at the Fermilab Tevatron collider from April 2002

to December 2008. Good agreement between the data and the SM background prediction is observed. Since there is no evidence for new physics, we set 95% C.L. limits on the production cross section times the branching ratio ( $\sigma \times BR(H \rightarrow \gamma\gamma)$ ) relative to the SM-like Higgs prediction for different assumed Higgs masses. The observed limits ( $\frac{\sigma(limit)}{\sigma(SM)}$ ) range from 11.9 to 35.2 for Higgs masses from 100 to 150 GeV, while the expected limits range from 17.5 to 32.0. This search is also interpreted in the context of the particular fermiophobic Higgs model. The corresponding results have reached the same sensitivity as a single LEP experiment, setting a lower limit on the fermiophobic Higgs of  $M_{h_f} > 102.5$  GeV ( $M_{h_f} > 107.5$  GeV expected). We are slightly below the combined LEP limit ( $M_{h_f} > 109.7$  GeV). We also provide access to the  $M_{h_f} > 125$  GeV region which was inaccessible at LEP.

During the study, we found the major and irreducible background direct  $\gamma\gamma$  (DPP) production is not well modelled by the current theoretical predictions: RESBOS, DIPHOX or PYTHIA. There is  $\sim 20\%$  theoretical uncertainty for the predicted values. Thus, for our Higgs search, we use the side-band fitting method to estimate DPP contribution directly from the data events. Furthermore, DPP production is also a significant background in searches for new phenomena, such as new heavy resonances, extra spatial dimensions, or cascade decays of heavy new particles. Thus, precise measurements of the DPP cross sections for various kinematic variables and their theoretical understanding are extremely

important for future Higgs and new phenomena searches.

In this thesis, we also present a precise measurement of the DPP single differential cross sections as a function of the diphoton mass, the transverse momentum of the diphoton system, the azimuthal angle between the photons, and the polar scattering angle of the photons, as well as the double differential cross sections considering the last three kinematic variables in three diphoton mass bins, using  $4.2 \text{ fb}^{-1}$  data. These results are the first of their kind at DØ Run II, and in fact the double differential measurements are the first of their kind at Tevatron. The results are compared with different perturbative QCD predictions and event generators.





## Selected publications by the author

Primary analyzer of the following DØ publications:

- V. Abazov, *et al.*, “Search for Sneutrino resonance in the  $e+\mu$  final states in RPV SUSY at DZero with  $5.0\text{ fb}^{-1}$  data”, DØ Note 5894-CONF, under publication review (2010)
- V. Abazov, *et. al.*, “ Measurement of Direct Photon Pair Production Cross Sections in  $p\bar{p}$  Collisions at  $\sqrt{s} = 1.96\text{ TeV}$ ”, arXiv.org:1002.4917, accepted by Phys. Lett. B (2010)
- V. Abazov, *et. al.*, “Search for Resonant Diphoton Production with the DØ Detector”, Phys. Rev. Lett. 102, 231801 (2009)
- V. Abazov, *et. al.*, “Search for Scalar Neutrino Superpartners in  $e+\mu$  Final States in  $p\bar{p}$  Collisions at  $\sqrt{s} = 1.96\text{ TeV}$ ”, Phys. Rev. Lett. 100, 241803 (2008)

## Conference Presentations

- July 2009:** Invited talk at DPF2009, Detroit, USA, July 2009  
“Search for a light Higgs boson via diphoton final state at Tevatron”
- June 2009:** Invited talk at SUSY2009, Boston, USA, June 2009  
“Search for Sneutrino Production and Decay in the  $e+\mu$  Final State at DØ ”
- June 2009:** Invited talk at New Perspective 2009, Fermilab, USA, June 2009

“ Search for a light Higgs boson via diphoton final state at DØ ”

#### Internal DØ Notes

1. X. Bu *et al.*, “Search for Sneutrino resonance in the  $e+\mu$  final states in RPV SUSY at DØ ”, DØ Note 5299 (December 2006)
2. X. Bu *et al.*, “Artificial neural network for Run IIb electron and photon identification”, DØ Note 5545 (December 2007)
3. X. Bu *et al.*, “Search for a light Higgs boson in diphoton final states at DØ with  $2.3 \text{ fb}^{-1}$  data”, DØ Note 5592, 5601-CONF (February 2008)
4. X. Bu *et al.*, “Artificial neural network using central preshower detector information for electron and photon selection”, DØ Note 5650 (April 2008)
5. X. Bu *et al.*, “Search for the standard model Higgs boson in diphoton final states at DØ with  $2.7 \text{ fb}^{-1}$  data”, DØ Note 5734, 5737-CONF (July 2008)
6. X. Bu *et al.*, “Electron and Photon Identification with p20 data”, DØ Note 5761 (August 2008)
7. X. Bu, “Utilizing CFT and SMT hits count for forward region photon and electron selection”, DØ note 5764 (August 2008)

8. X. Bu *et al.*, “Search for a light Higgs boson in diphoton final states at DØ with  $4.2\text{ fb}^{-1}$  data”, DØ Note 5846, 5858-CONF (January 2009)
9. X. Bu *et al.*, “Search for Sneutrino resonance in the  $e+\mu$  final states in RPV SUSY at DZero with  $4.2\text{ fb}^{-1}$  data”, DØ Note 5848, 5894-CONF (February 2009)
10. X. Bu *et al.*, “Search for the Fermiophobic Higgs Boson in diphoton final states at DZero with  $4.2\text{ fb}^{-1}$  data”, DØ Note 5859, 5880-CONF (February 2009)
11. X. Bu *et al.*, “Artificial neural network for forward photon selection”, DØ Note 5895 (March 2009)
12. X. Bu *et al.*, “Direct Diphoton Production cross section measurement at DØ with  $4.2\text{ fb}^{-1}$  data”, DØ Note 5959 (July 2009)
13. X. Bu *et al.*, “Photon Identification for Run II data”, DØ Note 6004 (October 2009)
14. X. Bu *et al.*, “Electron Preselection Efficiency study for Run II data”, DØ Note 6009 (November 2009)

The author has been a member of DØ since August 2006, and an author for DØ publications since May 2008. He has been staying continuously at Fermilab as a graduate student from USTC China from April 2007 to March 2010. He is the co-convener of the DØ Electron and Photon Identification (EMID) Group since September 2009. He coordinates and leads this group with about

20 members which has the central responsibility for the identification of electromagnetic objects (electrons and photons) in the Calorimeter, and is the first graduate student to hold such position in the DØ Experiment. As a leader of the EMID group he is responsible for developing improved electron and photon identification, and measuring the identification efficiencies and purities as well as providing centralized tools for the whole DØ collaboration. These are used in many high profile results, such as Higgs searches and Top quark measurements.

The author has been working on electron and photon identification since April 2007, he included information from the Central Preshower Detector for the first time in standard photon and electron identification. This development significantly improved the performance of electron and photon identification and has been extensively used since then. He developed several new identification variables using a Artificial Neural Network, and completely redesigned the electron and photon identification to cope with the challenges of high instantaneous luminosity. He also expanded the photon identification into the forward region of the detector, and have developed a new method, based on “hits on a road”, to identify photons and electrons. This is essential for many physics analyzes, for example, the measurement of the  $W\gamma$  process. The author was also the Monte Carlo production coordinator for the DØ Electroweak Physics Group from 2008 to 2009, who has central responsibility for the production of all Monte Carlo requests of this physics group.

The author co-supervised the undergraduate student Pengfei Ding on his Bachelor thesis “Search for Sneutrino particle via  $e+\mu$  final state at  $D\bar{D}$  with  $4.2 \text{ fb}^{-1}$  data” from 2008 to 2009. He was a primary author of the conference note for this result, and was a primary analyzer of the first  $D\bar{D}$  publication on this channel using  $1 \text{ fb}^{-1}$  data in Physics Review Letters. In this publication, we set the world’s best limits on the parameters of an RPV-SUSY model and probe the Standard Model by searching for lepton flavor violation. From 2007 to 2009, the author performed the first search of the Standard Model  $H \rightarrow \gamma\gamma$  decay signature at the Tevatron as a primary analyzer. This search is a forerunner to similar planned searches at LHC and has been published in Physics Review Letters. The author developed a data-driven method for estimating the backgrounds, and this search contributes 5% to the  $D\bar{D}$  SM Higgs combination in the intermediate mass region from 115 to 130 GeV, and has the world’s best per-experiment sensitivity on a particular Fermiophobic Higgs model. Since January 2009, he has been performing the first  $D\bar{D}$  measurement of direct photon pair production cross sections as a primary analyzer. The results has been accepted by the Physics Letters B.



## Contents

Acknowledgements .....	I
Abstract .....	III
Selected publications by the author .....	VII
Contents .....	XIII
List of Figures .....	XVI
List of Tables .....	XXX
Chapter 1 Introduction .....	1
1.1 Standard Model .....	1
1.2 Higgs production and decay at the Tevatron .....	5
1.2.1 SM Higgs production .....	5
1.2.2 Decays of the Higgs Boson .....	5
1.3 Direct photon pair production .....	10
Chapter 2 Fermilab and DØ detector .....	15
2.1 The Fermilab Accelerator System .....	15
2.1.1 Pre-accelerator, Linear Accelerator and Booster .....	15
2.1.2 Main Injector .....	16
2.1.3 Tevatron .....	17
2.1.4 Antiproton Source .....	17
2.2 DØ Detector .....	18
2.2.1 Central Tracking System .....	19
2.2.2 Solenoid and Preshower .....	22
2.2.3 Calorimeter .....	24
2.2.4 Muon System .....	30
Chapter 3 Photon identification .....	31
3.1 Vertex reconstruction .....	31
3.2 Reconstruct the EM object .....	34
3.3 Separation of jets and photons using Artificial Neural Network .....	37
3.4 Separation of electrons and photons .....	38

3.5	Photon ID efficiency	43
3.5.1	General ID efficiency	43
3.5.2	No-track matching efficiency	44
3.5.3	$O_{NN}$ efficiency	46
3.6	Photon energy scale and resolution	55
3.6.1	Energy loss correction	56
3.6.2	Energy scale and offset	59
3.6.3	Energy resolution	62
3.6.4	Photon energy scale correction	64
Chapter 4	$H \rightarrow \gamma\gamma$ search	67
4.1	Data and Monte Carlo samples	68
4.2	Event selection	72
4.3	Backgrounds	73
4.3.1	Drell-Yan $Z/\gamma^* \rightarrow ee$ contributions	73
4.3.2	$\gamma$ +jet and di-jet background	74
4.3.3	Direct photon pair production	77
4.4	Systematic uncertainties	82
4.5	Final event distributions and Limits	84
4.5.1	Final event distributions	84
4.5.2	Limit setting	89
4.6	Fermiphobic $H \rightarrow \gamma\gamma$ search	93
4.6.1	Data, MC samples and Event selection	93
4.6.2	Backgrounds	94
4.6.3	Final event distributions and limits	100
Chapter 5	Direct photon pair production differential cross section measurement	109
5.1	Review of previous Tevatron Run II measurements	110
5.2	Data samples	114
5.3	Event selection and binning	115
5.3.1	Event selection and selection efficiencies	115
5.3.2	Binning	118
5.4	Acceptance	120
5.5	Backgrounds	128
5.5.1	Drell-Yan $Z/\gamma^* \rightarrow ee$ contributions	128



5.5.2	$\gamma$ +jet and di-jet background	128
5.5.3	Di-photon purity	128
5.6	Photon energy scale correction	130
5.7	Systematics	132
5.8	Correction of theory for MPI and hadronization effects	135
5.9	Comparison with Theory	141
5.10	Closure tests	149
5.11	Measurement of double differential cross sections	156
5.11.1	Acceptances	156
5.11.2	Selection efficiencies	158
5.11.3	Diphoton purity	158
5.11.4	Double differential cross sections and comparison with theory	161
Chapter 6	Conclusion	169
Chapter 7	Bibliography	173
Chapter 8	Appendices	181
8.1	$Z/\gamma^* \rightarrow ee$ background	181
8.2	Photon energy scale	183
8.3	H $p_T$ reweighting	187
8.4	Fitting function from $O_{NN}$ -reversed sample	189
8.5	$4 \times 4$ matrix background subtraction	192
8.6	Interpolated signal mass points	197
8.7	Bin-by-bin purity	206
8.8	Unfolded results using different re-weightings to data	208
8.9	Cross-check of diphoton purity using 2D template fitting.	216
8.10	Systematic uncertainty for purity estimation	218
8.11	Systematic uncertainties for the 2D acceptance	220
8.12	Cross-check of background-subtracted data vs. fast MC simulation	223



## List of Figures

1.1	The fundamental particles in the Standard Model. . . . .	4
1.2	SM Higgs production mechanism. . . . .	6
1.3	The major SM Higgs boson production cross sections (fb) as a function of the Higgs boson mass at the Tevatron. . . . .	7
1.4	Branching ratios for the SM Higgs boson as a function of assumed Higgs boson mass. . . . .	8
1.5	Branching fraction into two photons for four different types of Higgs boson. .	9
1.6	Fraction of $gg \rightarrow \gamma\gamma$ contribution to the total “direct” contribution caused by $q\bar{q} \rightarrow \gamma\gamma$ and $gg \rightarrow \gamma\gamma$ . . . . .	11
1.7	Main direct diphoton production processes. . . . .	12
1.8	DIPHOX predictions for the $d\sigma/dM_{\gamma\gamma}$ cross section for “direct”, one and two fragmentation contributions. . . . .	12
2.1	Accelerator Overview. . . . .	16
2.2	DØ Detector. . . . .	19
2.3	DØ Tracking System. . . . .	20
2.4	DØ Silicon Detector. . . . .	21
2.5	DØ Central Fiber Tracker. . . . .	22
2.6	Cross section and layout geometry of the CPS and FPS scintillator stirps. . .	24
2.7	Complete $\phi$ -segment of a FPS module. . . . .	25
2.8	DØ Uranium/Liquid-argon Calorimeter. . . . .	26
2.9	DØ Uranium/Liquid-argon Calorimeter showing segmentation in $\eta$ and depth.	27
2.10	Calorimeter channel layout in directions of depth and $\eta$ . . . . .	28
2.11	Liquid argon gap and signal board unit cell for the calorimeter. . . . .	28

2.12	Simplified diagram of the calorimeter data flow path. . . . .	29
3.1	Photon's signature in the detector. . . . .	32
3.2	Diphoton invariant mass distribution comparison between using reco vertex and new vertex for $M_H = 130$ GeV Higgs. . . . .	34
3.3	Isolation definition. . . . .	36
3.4	General photon identification variables distributions. . . . .	37
3.5	Normalized $O_{NN}$ input variables for photons and jets. . . . .	39
3.6	The three-body (di-lepton+ $\gamma$ ) mass versus the two-body (di-lepton) mass from $Z \rightarrow \ell^+ \ell^- \gamma$ ( $\ell = e, \mu$ ) data events. . . . .	40
3.7	Normalized $O_{NN}$ spectrum for photons and jets. . . . .	41
3.8	Hits along the road. . . . .	42
3.9	Tag-and-probe method used to measure the general ID efficiency. . . . .	44
3.10	The general ID efficiency. . . . .	45
3.11	Tag-and-probe method used to measure the electron track match inefficiency. . . . .	46
3.12	Electron track match inefficiency. . . . .	47
3.13	$O_{NN} > 0.3$ selection efficiency as a function of $E_T$ for photons. . . . .	47
3.14	Electron selection efficiencies (top plots) and data/MC scale factors (bottom plots) w.r.t. $O_{NN} > 0.3$ as a function of $\eta_{det}$ and $p_T$ . . . . .	48
3.15	$O_{NN} > 0.6$ selection efficiency from DPP and dijet MC samples. . . . .	51
3.16	Top-left plot shows the normalized distributions of number of tracks in $\Delta R < 0.05$ ( $N_{trks}^{\Delta R < 0.05}$ ) for the photon candidates. Top-right and bottom plots show the $O_{NN} > 0.6$ selection efficiency as a function of $E_T$ and $\eta_{det}$ after requiring $N_{trks}^{\Delta R < 0.05} \geq 1$ . . . . .	51
3.17	The $O_{NN} > 0.6$ selection efficiency as a function of $f_{iso}$ (isolation) from jets in data and MC. . . . .	52

3.18	Normalized $O_{NN}$ distributions from jet data and MC in the regions of $N_{trks}^{\Delta R < 0.05} \geq 1$ (left) and $0.07 < f_{iso} < 0.10$ (right). . . . .	52
3.19	Electron selection efficiencies (left) and data/MC scale factors (right plots) w.r.t. $O_{NN} > 0.6$ as a function of $\eta_{det}$ and $p_T$ . . . . .	53
3.20	The electron and photon based SFs for $O_{NN} > 0.6$ obtained from $Z \rightarrow ee$ and $Z \rightarrow ll + \gamma (l = e, \mu)$ events in data and MC vs. $\eta_{det}$ . . . . .	54
3.21	$O_{NN} > 0.6$ selection efficiency as a function of $\eta_{det}$ for photons from DPP (left) and fakes from jet (right) MC samples. . . . .	54
3.22	Overview of the material in front of the Central Calorimeter. . . . .	57
3.23	Average longitudinal profile of showers from $E = 45$ GeV single electrons full MC events. . . . .	58
3.24	EM energy fractions for electrons from $Z \rightarrow ee$ data and MC simulation events.	59
3.25	Fit for $nX_0$ , the amount of additional copper (in radiation lengths) missing from the nominal material map in the full MC simulation of the DØ detector. . .	60
3.26	Results of the fit for $nX_0$ . . . . .	61
3.27	EM energy fractions for electrons from $Z \rightarrow ee$ events data and MC simu- lation events after adding $nX_0 = 0.1633$ copper before the CC calorimeter. . .	62
3.28	The central value for $\alpha$ and $\beta$ as determined from the 2D $M_{obs.}(Z)$ vs $f_Z^{obs.}$ fit to the $Z$ mass distribution and the error ellipse defined by $\Delta\chi^2 = 1$ . . . .	63
3.29	Invariant mass distribution between data and fast MC simulation for $Z \rightarrow$ $ee$ events. . . . .	65
3.30	Energy resolution for electrons and photons in the three $\eta$ intervals. . . . .	65
3.31	Photon energy scale correction for the MC with tuned GEANT. . . . .	66
4.1	Dominant SM Higgs production used in this analysis. . . . .	68
4.2	DØ Run II integrated luminosity vs. time. . . . .	68
4.3	Calorimeter-only di-em trigger efficiency as a function of di-em invariant mass.	70

4.4	Main Feynman digram for the $Z/\gamma^* \rightarrow ee$ production. . . . .	73
4.5	Main Feynman digram for $\gamma$ +jet and di-jet production. . . . .	74
4.6	Non- $\gamma\gamma$ component invariant mass distribution. . . . .	77
4.7	Main Feynman digram for the direct photon pair production. . . . .	78
4.8	Top-left plot show the diphoton invariant mass distribution of $\gamma\gamma$ compo- nent of data and DPP MC. Top-right plot is the log scale of the left plot. Bottom plot shows the results of using the exponential function described below on the DPP MC after normalization. . . . .	79
4.9	Differential cross sections ( $\frac{d\sigma}{dM_{\gamma\gamma}}$ ) (left) and the ratio (right) between DIPHOX and PYTHIA. . . . .	79
4.10	Side-band fitting results from background subtracted data events for $100$ $\leq M_H \leq 120$ GeV mass regions. . . . .	80
4.11	Side-band fitting results from background subtracted data events for $125$ $\leq M_H \leq 150$ GeV mass regions. . . . .	81
4.12	Left plot shows the invariant mass distribution of two photon candidates in mass region $70 \text{ GeV} \leq M_{\gamma\gamma} \leq 200 \text{ GeV}$ , right plot is the corresponding log scale distribution. . . . .	84
4.13	Invariant mass distribution of the two photon candidates in mass interval of ( $M_H-15 \text{ GeV}$ , $M_H+15 \text{ GeV}$ ) for 100 to 120 GeV Higgs mass. . . . .	85
4.14	Invariant mass distribution of the two photon candidates in mass interval of ( $M_H-15 \text{ GeV}$ , $M_H+15 \text{ GeV}$ ) for 125 to 150 GeV Higgs mass with 2.5 GeV step for each mass bin. . . . .	86
4.15	Invariant mass distribution of the two photon candidates in mass interval of ( $M_H-15 \text{ GeV}$ , $M_H+15 \text{ GeV}$ ) for 100 to 120 GeV Higgs mass with 2.5 GeV step for each mass bin after adding the statisical and systematic uncertain- ties on the total background. . . . .	87

4.16	Invariant mass distribution of the two photon candidates in mass interval of $(M_H-15 \text{ GeV}, M_H+15 \text{ GeV})$ for 125 to 150 GeV Higgs mass with 2.5 GeV step for each mass bin after adding the statistical and systematic uncertainties on the total background. . . . .	88
4.17	The predicted (interpolated) diphoton invariant distribution for $M_H = 110$ GeV based on the existing $M_H = 100$ and 120 GeV templates versus the actual one (direct). . . . .	91
4.18	95% C.L. limits on the $\sigma \times BR$ (top) and on the $\sigma \times BR$ relative to the SM prediction (bottom) as a function of Higgs mass. . . . .	91
4.19	$p_T$ of di-photon system ( $p_T^{\gamma\gamma}$ ) distribution from data and 110 GeV associated production and vector boson fusion signal. . . . .	94
4.20	Normalized invariant mass distribution from $Z/\gamma^* \rightarrow ee$ contribution (top) and the invariant mass template fitting after removing the $D_{hor} < 0.9$ requirement. . . . .	96
4.21	Top-left plot shows the non- $\gamma\gamma$ component invariant mass from the $4 \times 4$ matrix background subtraction and reversing the $O_{NN}$ cut. Top-right plot shows the corresponding ratio for the two distributions shown in the left plot. Bottom plot shows the fitting results on the samples by reversing the $O_{NN}$ cut. . . . .	97
4.22	Side-band fitting results for 80 GeV (top left) to 120 GeV (bottom right) mass regions. . . . .	98
4.23	Side-band fitting results for 125 GeV (top left) to 150 GeV (bottom right) mass regions. . . . .	99
4.24	Left plot shows the invariant mass distribution of the photon candidates in mass region $60 \text{ GeV} \leq M_{\gamma\gamma} \leq 180 \text{ GeV}$ , right plot is the corresponding log scale distribution. . . . .	100

4.25	Invariant mass distribution of the two photon candidates in mass interval of $(M_{h_f}-10 \text{ GeV}, M_{h_f}+10 \text{ GeV})$ for 80 (top left) to 120 GeV (bottom) Higgs mass in 5 GeV step for each mass bin after adding the systematic uncertainties on the total background. . . . .	102
4.26	Invariant mass distribution of the two photon candidates in mass interval of $(M_{h_f}-10 \text{ GeV}, M_{h_f}+10 \text{ GeV})$ for 125 (top left) to 150 GeV (bottom) Higgs mass in 5 GeV step for each mass bin after adding the systematic uncertainties on the total background. . . . .	103
4.27	Invariant mass distribution of the two photon candidates in mass interval of $(M_{h_f}-10 \text{ GeV}, M_{h_f}+10 \text{ GeV})$ for the interpolated 102.5 (top left) to 122.5 GeV (bottom) Higgs mass in 5 GeV step for each mass bin after adding the systematic uncertainties on the total background. . . . .	104
4.28	Invariant mass distribution of the two photon candidates in mass interval of $(M_{h_f}-10 \text{ GeV}, M_{h_f}+10 \text{ GeV})$ for the interpolated 127.5 (top left) to 147.5 GeV (bottom) Higgs mass in 5 GeV step for each mass bin after adding the systematic uncertainties on the total background. . . . .	105
4.29	95% C.L. limits on $\sigma \times BR$ (top) and $BR$ (bottom) as a function of fermio-phobic Higgs mass. . . . .	107
5.1	The $\gamma\gamma$ mass distribution from the CDF Run II data. . . . .	112
5.2	The $\gamma\gamma \ q_T$ distribution from the CDF Run II data. . . . .	112
5.3	The azimuthal angle between the two photons ( $\Delta\phi_{\gamma\gamma}$ ) from the CDF Run II data. . . . .	113
5.4	v15 and v16 calorimeter-only di-em trigger efficiency as a function of leading and sub-leading EM cluster $E_T$ . . . . .	114
5.5	Primary vertex selection efficiency with requiring $z_{vtx} < 60 \text{ cm}$ versus the di-photon mass with using the maxtrk (new) and reco vertex. . . . .	117



5.6	Overall diphoton selection efficiency (with only statistical uncertainty) versus $M_{\gamma\gamma}$ , $p_T^{\gamma\gamma}$ , $\Delta\phi_{\gamma\gamma}$ and $\cos\theta^*$ . . . . .	119
5.7	Acceptance as a function of $M_{\gamma\gamma}$ , $p_T^{\gamma\gamma}$ , $\Delta\phi_{\gamma\gamma}$ and $\cos\theta^*$ . . . . .	123
5.8	Acceptance due to $\phi$ -fiducial requirement as a function of $M_{\gamma\gamma}$ , $p_T^{\gamma\gamma}$ , $\Delta\phi$ and $\cos\theta^*$ . . . . .	125
5.9	Contributions from signal and different types of background events in data in the bins of $M_{\gamma\gamma}$ , $p_T^{\gamma\gamma}$ , azimuthal angle $\Delta\phi_{\gamma\gamma}$ and polar angle $\cos\theta^*$ . . . .	129
5.10	$\gamma\gamma$ purity as a function of $M_{\gamma\gamma}$ , $\Delta\phi_{\gamma\gamma}$ , $p_T^{\gamma\gamma}$ and $\cos\theta^*$ . The shown uncertainties are statistical only. . . . .	130
5.11	Total $p_T$ sum in the photon isolation cone ( $\Delta R < 0.4$ ) for the diphoton events ( $pT_{iso}$ ) simulated with PYTHIA in the four cases. . . . .	137
5.12	Left: Efficiency to pass the isolation cut $pT_{iso} < 2.5$ GeV due to ISR/FSR (red circles) and due to 'ISR/FSR + MPI + hadronization effects in $p_T^{\gamma}$ bins. Right: Corrections to the NLO QCD predictions due to MPI and hadronization effects in bins of $p_T^{\gamma}$ . . . . .	138
5.13	Corrections to the NLO QCD predictions due to MPI and hadronization effects in bins of $M_{\gamma\gamma}$ , $p_T^{\gamma\gamma}$ , $\Delta\phi_{\gamma\gamma}$ and $\cos\theta^*$ with tunes A and S0. . . . .	139
5.14	Corrections to the NLO QCD predictions due to MPI and hadronization effects in bins of $p_T^{\gamma\gamma}$ , $\Delta\phi_{\gamma\gamma}$ and $\cos\theta^*$ with tunes A for the three mass intervals. . . . .	140
5.15	The main sources of systematic uncertainties for the four single differential cross sections. . . . .	144
5.16	The differential cross sections as a function of $M_{\gamma\gamma}$ , $p_T^{\gamma\gamma}$ , $\Delta\phi_{\gamma\gamma}$ and $\cos\theta^*$ . . . . .	145
5.17	Theoretical uncertainties caused by variation of the three scales. . . . .	146
5.18	Ratio of theoretical NLO predictions with HERA2001 (dashed line) and MSTW2008 PDFs (full line) to those with CTEQ6.6M PDF (default). . . . .	147

5.19	The ratio of PYTHIA predictions done with Tune A and using CTEQ6L1 as well as with Tune Perugia0 to those with Tune A and CTEQ5L (default). . . .	148
5.20	The ratio between unfolded smeared $Resbos_0$ and $Resbos_0$ "truth" cross sections. Here " $\sigma(0th-iteration)$ " simply means (non-reweighted/default) $Resbos_0$ "truth" cross section, while " $\sigma(1st - iteration)$ " means the unfolded smeared $Resbos_0$ events with $Acc_1$ . . . . .	150
5.21	The ratio between unfolded smeared $Resbos_1$ and $Resbos_1$ "truth" cross sections. Here " $\sigma(1th-iteration)$ " simply means (non-reweighted/default) $Resbos_1$ "truth" cross section, while " $\sigma(2nd - iteration)$ " means the unfolded smeared $Resbos_1$ events with $Acc_2$ . . . . .	151
5.22	The ratio between unfolded smeared PYTHIA cross section with using default RESBOS for the acceptance calculation and truth PYTHIA cross sections. . . . .	152
5.23	The ratio between unfolded smeared PYTHIA cross section with using default RESBOS for the acceptance calculation and truth PYTHIA cross sections, where the input RESBOS distributions have been reweighted to the input PYTHIA distributions. . . . .	153
5.24	The comparison of the default RESBOS and PYTHIA distributions. . . . .	154
5.25	The comparison of the default RESBOS and PYTHIA distributions. . . . .	154
5.26	Acceptances for $p_T^{\gamma\gamma}$ , $\cos\theta^*$ and $\Delta\phi_{\gamma\gamma}$ variables in the three mass bins. Statistical uncertainties only are shown on the plots. . . . .	157
5.27	Diphoton selection efficiency. Statistical uncertainties only are shown on the plots. . . . .	159
5.28	Diphoton fraction (purity) in data. Statistical uncertainties only are shown on the plots. . . . .	160

5.29	The measured double differential diphoton production cross sections as functions of (a) $p_T^{\gamma\gamma}$ , (b) $\Delta\phi_{\gamma\gamma}$ and (c) $\cos\theta^*$ for the diphoton mass bin $30 < M_{\gamma\gamma} < 50$ GeV. . . . .	165
5.30	The measured double differential diphoton production cross sections as functions of (a) $p_T^{\gamma\gamma}$ , (b) $\Delta\phi_{\gamma\gamma}$ and (c) $\cos\theta^*$ for the diphoton mass bin $50 < M_{\gamma\gamma} < 80$ GeV. . . . .	166
5.31	The measured double differential diphoton production cross sections as functions of (a) $p_T^{\gamma\gamma}$ , (b) $\Delta\phi_{\gamma\gamma}$ and (c) $\cos\theta^*$ for the diphoton mass bin $80 < M_{\gamma\gamma} < 350$ GeV. . . . .	167
6.1	Energy resolution improvement as a function of electron rapidity from $E = 45$ GeV single electron MC events. . . . .	172
8.1	Normalized invariant mass distribution from $Z/\gamma^* \rightarrow ee$ contribution. . . .	182
8.2	Left plot is the invariant mass distribution of the two electrons candidates for the Zee data and MC, middle and right plots show the corresponding fitting results for the data and MC respectively, where the fitting function is $p_3 * TMath :: Voigt(M_{ee} - p_0, p_1, p_2, 4) + exp(e_1 * M_{ee} + e_2)$ . . . .	184
8.3	Invariant mass distribution of the two photon candidates for the Higgs MC samples in mass interval of $(M_H - 15 \text{ GeV}, M_H + 15 \text{ GeV})$ for 100 (top-left), 110 (top-right), 120 (middle-left), 130 (middle-right), 140 (bottom-left), and 150 (bottom-right) GeV Higgs mass with 2.5 GeV step for each mass bin. The dotted lines show the positive (red) and negative (blue) shape systematic uncertainties from photon energy scale. . . . .	185

8.4	Invariant mass distribution of the two photon candidates for the Higgs MC samples in mass interval of $(M_H-15 \text{ GeV}, M_H+15 \text{ GeV})$ for 105 (top-left), 115 (top-right), 125 (middle-left), 135 (middle-right), 145 (bottom) GeV Higgs mass with 2.5 GeV step for each mass bin. The dotted lines show the positive (red) and negative (blue) shape systematic uncertainties from photon energy scale. . . . .	186
8.5	The ratio for the invariant mass distribution of the two photon candidates for the Higgs MC samples between with and without $H \ p_T$ weight in mass interval of $(M_H-15 \text{ GeV}, M_H+15 \text{ GeV})$ for 100 (top-left), 110 (top-right), 120 (middle-left), 130 (middle-right), 140 (bottom-left), and 150 (bottom-right) GeV, where the uncertainty maybe overestimated since the statistical uncertainties are treated as uncorrelated for the original two mass distributions.	188
8.6	Invariant mass distribution of the two photon candidates for the non- $\gamma\gamma$ component in mass interval of $(M_H-15 \text{ GeV}, M_H+15 \text{ GeV})$ for 100 (top-left), 110 (top-right), 120 (middle-left), 130 (middle-right), 140 (bottom-left), and 150 (bottom-right) GeV Higgs mass with 2.5 GeV step for each mass bin. The dotted lines show the positive (red) and negative (blue) shape systematic uncertainties from the fitting function of $O_{NN}$ -reversed sample. .	190
8.7	Invariant mass distribution of the two photon candidates for the direct $\gamma\gamma$ contribution in mass interval of $(M_H-15 \text{ GeV}, M_H+15 \text{ GeV})$ for 100 (top-left), 110 (top-right), 120 (middle-left), 130 (middle-right), 140 (bottom-left), and 150 (bottom-right) GeV Higgs mass with 2.5 GeV step for each mass bin. The dotted lines show the positive (red) and negative (blue) shape systematic uncertainties from the fitting function of $O_{NN}$ -reversed sample. .	191

8.8	Invariant mass distribution of the two photon candidates for the non- $\gamma\gamma$ component in mass interval of ( $M_H-15$ GeV, $M_H+15$ GeV) for 100 (top-left), 110 (top-right), 120 (middle-left), 130 (middle-right), 140 (bottom-left), and 150 (bottom-right) GeV Higgs mass with 2.5 GeV step for each mass bin. The dotted lines show the positive (red) and negative (blue) shape systematic uncertainties from $4\times 4$ matrix background subtraction. . . . .	193
8.9	Invariant mass distribution of the two photon candidates for the non- $\gamma\gamma$ component in mass interval of ( $M_H-15$ GeV, $M_H+15$ GeV) for 105 (top-left), 115 (top-right), 125 (middle-left), 135 (middle-right), 145 (bottom) GeV Higgs mass with 2.5 GeV step for each mass bin. The dotted lines show the positive (red) and negative (blue) shape systematic uncertainties from $4\times 4$ matrix background subtraction. . . . .	194
8.10	Invariant mass distribution of the two photon candidates for the direct $\gamma\gamma$ component in mass interval of ( $M_H-15$ GeV, $M_H+15$ GeV) for 100 (top-left), 110 (top-right), 120 (middle-left), 130 (middle-right), 140 (bottom-left), and 150 (bottom-right) GeV Higgs mass with 2.5 GeV step for each mass bin. The dotted lines show the positive (red) and negative (blue) shape systematic uncertainties from $4\times 4$ matrix background subtraction. . . . .	195
8.11	Invariant mass distribution of the two photon candidates for the direct $\gamma\gamma$ component in mass interval of ( $M_H-15$ GeV, $M_H+15$ GeV) for 105 (top-left), 115 (top-right), 125 (middle-left), 135 (middle-right), 145 (bottom) GeV Higgs mass with 2.5 GeV step for each mass bin. The dotted lines show the positive (red) and negative (blue) shape systematic uncertainties from $4\times 4$ matrix background subtraction. . . . .	196
8.12	Shifting comparison for GF from 102.5 GeV to 122.5 GeV. . . . .	198
8.13	Shifting comparison for GF from 127.5 GeV to 147.5 GeV. . . . .	199

8.14	Shifting comparison for VH from 102.5 GeV to 122.5 GeV. . . . .	200
8.15	Shifting comparison for VH from 127.5 GeV to 147.5 GeV. . . . .	201
8.16	Shifting comparison for VBF. . . . .	202
8.17	Shifting comparison for VBF. . . . .	203
8.18	Invariant mass distribution of the two photon candidates in mass interval of ( $M_H-15$ GeV, $M_H+15$ GeV) for 102.5 to 122.5 GeV Higgs mass with 2.5 GeV step for each mass bin. . . . .	204
8.19	Invariant mass distribution of the two photon candidates in mass interval of ( $M_H-15$ GeV, $M_H+15$ GeV) for 127.5 to 147.5 GeV Higgs mass with 2.5 GeV step for each mass bin. . . . .	205
8.20	Bin-to-bin migration purity and efficiency as a function of $M_{\gamma\gamma}$ , $p_T^{\gamma\gamma}$ , $\Delta\phi_{\gamma\gamma}$ and $\cos\theta^*$ . . . . .	207
8.21	The ratio between the RESBOS predictions and the data cross sections for which the acceptance is calculated using fast MC (section 5.4) and non- reweighted RESBOS. . . . .	208
8.22	Comparisons between the background-subtracted data distributions and the smeared distributions from the generator-level-reweighted resbos fast MC simulation. . . . .	210
8.23	Comparisons between the background-subtracted data distributions and the smeared distributions from the generator-level-reweighted resbos fast MC simulation for leading and sub-leading photon $p_T$ . . . . .	211
8.24	Acceptance calculation with different re-weightings of RESBOS to data. . .	211
8.25	Ratio of the acceptance calculated with the reweightings to $M_{\gamma\gamma}$ or $p_T^{\gamma\gamma}$ or $\Delta\phi_{\gamma\gamma}$ or $\cos\theta^*$ spectra to the acceptance with default RESBOS for $M_{\gamma\gamma}$ . . .	212
8.26	Ratio of the acceptance calculated with the reweightings to $M_{\gamma\gamma}$ or $p_T^{\gamma\gamma}$ or $\Delta\phi_{\gamma\gamma}$ or $\cos\theta^*$ spectra to the acceptance with default RESBOS for $p_T^{\gamma\gamma}$ . . .	212

8.27	Ratio of the acceptance calculated with the reweightings to $M_{\gamma\gamma}$ or $p_T^{\gamma\gamma}$ or $\Delta\phi_{\gamma\gamma}$ or $\cos\theta^*$ spectra to the acceptance with default RESBOS for $\Delta\phi_{\gamma\gamma}$ . . . . .	213
8.28	Ratio of the acceptance calculated with the reweightings to $M_{\gamma\gamma}$ or $p_T^{\gamma\gamma}$ or $\Delta\phi_{\gamma\gamma}$ or $\cos\theta^*$ spectra to the acceptance with default RESBOS for $\cos\theta^*$ . . . . .	213
8.29	The mass acceptance calculated either with smooth reweighting function for all the bins shown in the upper left plot of Fig. 8.21 or with the smooth reweighting for all the bin excepting the 1st one, where we used the RESBOS/data ratio directly. . . . .	214
8.30	Acceptance as a function of $M_{\gamma\gamma}$ , $p_T^{\gamma\gamma}$ , $\Delta\phi_{\gamma\gamma}$ and $\cos\theta^*$ from full PYTHIA (black) and fast RESBOS (red) MC simulation. . . . .	215
8.31	Diphoton purities in bins of $M_{\gamma\gamma}$ , $\Delta\phi_{\gamma\gamma}$ , $p_T^{\gamma\gamma}$ and $\cos\theta^*$ calculated using template 2D fitting of diphoton, photon+jet and dijet ANN outputs to data. . . . .	217
8.32	$\gamma\gamma$ purity as a function of $M_{\gamma\gamma}$ , $p_T^{\gamma\gamma}$ , $\Delta\phi_{\gamma\gamma}$ and $\cos\theta^*$ . . . . .	219
8.33	Comparisons between the background-subtracted data distributions (red points) and the smeared distributions (blue points) from the generator-level-reweighted RESBOS fast MC simulation for $p_T^{\gamma\gamma}$ in the three mass bins. Just statistical uncertainties are shown. . . . .	223
8.34	Comparisons between the background-subtracted data distributions (red points) and the smeared distributions (blue points) from the generator-level-reweighted RESBOS fast MC simulation for $\Delta\phi_{\gamma\gamma}$ (upper right) in the three mass bins. Just statistical uncertainties are shown. . . . .	224
8.35	Comparisons between the background-subtracted data distributions (red points) and the smeared distributions (blue points) from the generator-level-reweighted RESBOS fast MC simulation for $\cos\theta^*$ in the three mass bins. Just statistical uncertainties are shown. . . . .	225





## List of Tables

3.1	The fraction of events with using the reco and new vertex matched to the true one for $M_H = 130$ GeV Higgs. . . . .	33
3.2	The average $O_{NN} > 0.3$ selection efficiencies for photons in different samples. . . . .	47
3.3	The average $O_{NN} > 0.6$ selection efficiencies for photons in different samples.	50
3.4	The average $O_{NN} > 0.6$ selection efficiencies for jet data and MC. . . . .	50
4.1	Cross section(pb) and branching ratio(BR) for the signal samples. . . . .	71
4.2	Event selection efficiencies with its statistical error. . . . .	72
4.3	The number of $\gamma\gamma$ , $\gamma$ +jet and di-jet events in the data samples from the $4 \times 4$ matrix method. . . . .	76
4.4	Uncertainties of SM $H \rightarrow \gamma\gamma$ are listed. . . . .	83
4.5	The number of events in data, signal and the background estimation in the mass interval of $(M_H - 15 \text{ GeV}, M_H + 15 \text{ GeV})$ from 100 GeV to 150 GeV with 10 GeV step. . . . .	85
4.6	Number of events in data, signal and the background estimation in the mass interval of $(M_H - 15 \text{ GeV}, M_H + 15 \text{ GeV})$ from 105 GeV to 145 GeV with 10 GeV step. . . . .	86
4.7	95% C.L. limits on $\sigma \times BR$ for the different Higgs masses from 100 GeV to 125 GeV. . . . .	90
4.8	95% C.L. limits on $\sigma \times BR$ for the different Higgs masses from 127.5 GeV to 150 GeV. . . . .	90
4.9	95% C.L. limits on $\sigma \times BR$ relative to the SM prediction for different Higgs masses from 100 GeV to 125 GeV. . . . .	90

4.10	95% C.L. limits on $\sigma \times BR$ relative to the SM prediction for different Higgs masses from 127.5 GeV to 150 GeV. . . . .	92
4.11	Cross section (pb) and branching ratio (BR) for a Fermiophobic Higgs boson. . . . .	95
4.12	Event selection efficiencies( $\epsilon_{sel}$ ) with their statistical errors for signal. . . . .	95
4.13	The number of $\gamma\gamma$ and non- $\gamma\gamma$ events in the data samples from the $4 \times 4$ matrix method. . . . .	97
4.14	Number of events in data, signal and the background estimation in the mass interval of $(M_{h_f} - 15 \text{ GeV}, M_{h_f} + 15 \text{ GeV})$ , where the systematic uncertainties have been included for the background, the correlation between the different backgrounds has been considered when calculating the error for the total background. . . . .	101
4.15	95% C.L. limits on $\sigma \times BR$ for different fermiophobic Higgs masses from 80 GeV to 120 GeV. . . . .	106
4.16	95% C.L. limits on $\sigma \times BR$ for different fermiophobic Higgs masses from 122.5 GeV to 150 GeV. . . . .	106
5.1	Fraction of events by requiring the distance in $z$ ( $dz$ ) between true vertex and default vertex or the vertex with maximum multiplicity ( $maxtrk$ ) within $ dz  < 1 \text{ cm}$ . . . . .	116
5.2	The systematic uncertainty for per-photon selection efficiencies. . . . .	118
5.3	Acceptance with statistical and systematic uncertainties (in %) in $M_{\gamma\gamma}$ bins. . . . .	125
5.4	Acceptance with statistical and systematic uncertainties (in %) in $p_T^{\gamma\gamma}$ bins. . . . .	126
5.5	Acceptance with statistical and systematic uncertainties (in %) in $\Delta\phi_{\gamma\gamma}$ bins. . . . .	126
5.6	Acceptance with statistical and systematic uncertainties (in %) in $\cos\theta^*$ bins. . . . .	127
5.7	The total numbers of $\gamma\gamma$ , $\gamma j + j\gamma$ and $jj$ events in the data samples from the $4 \times 4$ matrix method. . . . .	129

5.8	Systematic uncertainties (%) due to purity, photon acceptance ( $Acpt$ ), trigger $\epsilon_t$ , photon $\epsilon_s^\gamma$ selection efficiencies and luminosity ( $Lum$ ) in $M_{\gamma\gamma}$ bins.	133
5.9	Systematic uncertainties (%) in $p_T^{\gamma\gamma}$ bins.	133
5.10	Systematic uncertainties (%) in $\Delta\phi_{\gamma\gamma}$ bins.	134
5.11	Systematic uncertainties (%) in $ \cos\theta^* $ bins.	134
5.12	$d\sigma/dM_{\gamma\gamma}$ (pb/GeV) cross section with uncertainties.	143
5.13	$d\sigma/dp_T^{\gamma\gamma}$ (pb/GeV) cross section with uncertainties.	143
5.14	$d\sigma/d\Delta\phi_{\gamma\gamma}$ (pb/rad.) cross section with uncertainties.	143
5.15	$d\sigma/d\cos\theta^*$ (pb) cross section with uncertainties.	143
5.16	$d^2\sigma/dM_{\gamma\gamma}dp_T^{\gamma\gamma}$ cross section with uncertainties in $30 \text{ GeV} < M_{\gamma\gamma} < 50$ GeV region.	162
5.17	$d^2\sigma/dM_{\gamma\gamma}dp_T^{\gamma\gamma}$ cross section with uncertainties in $50 \text{ GeV} < M_{\gamma\gamma} < 80$ GeV region.	162
5.18	$d^2\sigma/dM_{\gamma\gamma}dp_T^{\gamma\gamma}$ cross section with uncertainties in $80 \text{ GeV} < M_{\gamma\gamma} < 350$ GeV region.	163
5.19	$d^2\sigma/dM_{\gamma\gamma}d\Delta\phi_{\gamma\gamma}$ cross section with uncertainties in $30 \text{ GeV} < M_{\gamma\gamma} < 50$ GeV region.	163
5.20	$d^2\sigma/dM_{\gamma\gamma}d\Delta\phi_{\gamma\gamma}$ cross section with uncertainties in $50 \text{ GeV} < M_{\gamma\gamma} < 80$ GeV region.	163
5.21	$d^2\sigma/dM_{\gamma\gamma}d\Delta\phi_{\gamma\gamma}$ cross section with uncertainties in $80 \text{ GeV} < M_{\gamma\gamma} < 350$ GeV region.	163
5.22	$d^2\sigma/dM_{\gamma\gamma}d \cos\theta^* $ cross section with uncertainties in $30 \text{ GeV} < M_{\gamma\gamma} < 50$ GeV region.	163
5.23	$d^2\sigma/dM_{\gamma\gamma}d \cos\theta^* $ cross section with uncertainties in $50 \text{ GeV} < M_{\gamma\gamma} < 80$ GeV region.	164

5.24	$d^2\sigma/dM_{\gamma\gamma}d\cos\theta^*$ cross section with uncertainties in $80 \text{ GeV} < M_{\gamma\gamma} < 350 \text{ GeV}$ region. . . . .	164
8.1	Relative acceptance change for each mass points. . . . .	187
8.2	Systematic uncertainties for the non- $\gamma\gamma$ component. . . . .	192
8.3	Cross section(pb) and Branching ratio(BR) for the signal samples. . . . .	197
8.4	Number of events in data, signal and the background estimation in the mass interval of $(M_H - 15 \text{ GeV}, M_H + 15 \text{ GeV})$ . . . . .	199
8.5	Acceptance with statistical and systematic uncertainties (in %) in $p_T^{\gamma\gamma}$ bins for $30 < M_{\gamma\gamma} < 50 \text{ GeV}$ . The two numbers in each box correspond to $+1\sigma$ and $-1\sigma$ variations. . . . .	220
8.6	Acceptance with statistical and systematic uncertainties (in %) in $p_T^{\gamma\gamma}$ bins for $50 < M_{\gamma\gamma} < 80 \text{ GeV}$ . The two numbers in each box correspond to $+1\sigma$ and $-1\sigma$ variations. . . . .	220
8.7	Acceptance with statistical and systematic uncertainties (in %) in $p_T^{\gamma\gamma}$ bins for $80 < M_{\gamma\gamma} < 350 \text{ GeV}$ . The two numbers in each box correspond to $+1\sigma$ and $-1\sigma$ variations. . . . .	221
8.8	Acceptance with statistical and systematic uncertainties (in %) in $\Delta\phi_{\gamma\gamma}$ bins for $30 < M_{\gamma\gamma} < 50 \text{ GeV}$ . The two numbers in each box correspond to $+1\sigma$ and $-1\sigma$ variations. . . . .	221
8.9	Acceptance with statistical and systematic uncertainties (in %) in $\Delta\phi_{\gamma\gamma}$ bins for $50 < M_{\gamma\gamma} < 80 \text{ GeV}$ . The two numbers in each box correspond to $+1\sigma$ and $-1\sigma$ variations. . . . .	221
8.10	Acceptance with statistical and systematic uncertainties (in %) in $\Delta\phi_{\gamma\gamma}$ bins for $80 < M_{\gamma\gamma} < 350 \text{ GeV}$ . The two numbers in each box correspond to $+1\sigma$ and $-1\sigma$ variations. . . . .	221

8.11	Acceptance with statistical and systematic uncertainties (in %) in $\cos\theta^*$ bins for $30 < M_{\gamma\gamma} < 50$ GeV. The two numbers in each box correspond to $+1\sigma$ and $-1\sigma$ variations. . . . .	222
8.12	Acceptance with statistical and systematic uncertainties (in %) in $\cos\theta^*$ bins for $50 < M_{\gamma\gamma} < 80$ GeV. The two numbers in each box correspond to $+1\sigma$ and $-1\sigma$ variations. . . . .	222
8.13	Acceptance with statistical and systematic uncertainties (in %) in $\cos\theta^*$ bins for $80 < M_{\gamma\gamma} < 350$ GeV. The two numbers in each box correspond to $+1\sigma$ and $-1\sigma$ variations. . . . .	222



## Chapter 1 Introduction

Particle physics is the branch of science concerned with the ultimate constituents of matter and the fundamental interactions that occur among them. It is also known as high energy physics, to study the smallest elements of the universe, the subatomic particles via the high energetic collisions of other particles. The Standard Model of particle physics is a theory of three of the four known fundamental interactions and the elementary particles that describe these interactions. Experiments over the past half of a century have eventually yielded findings consistent with this Model. The following chapter will briefly discuss the Standard Model, especially the Higgs mechanism, which is believed to be the key to resolve the mass puzzle of the fundamental particles. The Higgs boson is the only unobserved Standard Model particle.

### 1.1 Standard Model

At the present, there are four fundamental interactions, believed to sufficiently explain all phenomena in physics:

- Strong interactions
- Electromagnetic interactions
- Weak interactions
- Gravitational interactions

The strong interaction is the interaction among quarks, modelled by Quantum Chromodynamics (QCD), while the electromagnetic and weak interactions are unified by the electroweak sector. The Standard Model (SM) is a gauge theory of the strong and electroweak interactions.

SM is a simple and comprehensive theory that explains all the hundreds of particles and complex interactions with only:

- 6 quarks( $u, d, s, c, b, t$ )
- 6 leptons( $e, \mu, \tau, \nu_e, \nu_\mu, \nu_\tau$ )
- Force carrier particles (gluon, photon,  $W^\pm, Z^0$ )

In the SM, fundamental particles (see Fig. 1.1 ) are of two types: particles with half-integral spin ( $\frac{\hbar}{2}, \frac{3\hbar}{2}, \dots$ ) are called fermions because they obey Fermi-Dirac statistics, while those with integral spin ( $0, \hbar, 2\hbar, \dots$ ) obey Bose-Einstein statistics and are called bosons. Among the fermions, there are 6 quarks and 6 leptons. The leptons are particles that don't participate the strong interaction, and carry integral electric charge. The neutral leptons are called neutrinos. The quarks are the fundamental constituents of matter, they carry one-third or two-thirds of the electron's charge, and free quarks have never been observed in scattering experiments. In the QCD model a quark attempting to leave the interior of a hadron would cause new partons to be created. The quarks and antiquarks would then recombine in such a way as to form new hadrons. Very energetic quarks would form a narrow spray of hadrons known as a jet. There are two types of hadrons: mesons



and baryons, composed of a quark-antiquark pair or three quarks respectively. Also, for every particle there is an antiparticle with the same mass and spin, but with opposite values for the charge and some of the internal quantum numbers.

Besides the leptons and the quarks, there is a third group of particles known as the gauge bosons. These integral spin particles responsible for transmitting the basic interactions are:

- massless gluons, mediating the strong interactions between color charged quarks, described by the QCD model.
- massless photons, mediating the electromagnetic force between electrically charged particles, well-described by the theory of quantum electrodynamics.
- massive  $W^\pm$  and  $Z$  vector bosons, mediating the weak interactions between particles of different flavors (all quarks and leptons).

However, the SM predicts massless fermions and gauge bosons, which obviously deviates from the experimental observations, where except for the photons and gluons, all gauge bosons have a substantial mass. To resolve this mass puzzle, the Higgs mechanism is brought in, which explains how the masses of the  $W$  and  $Z$  bosons arise through spontaneous electroweak symmetry breaking. The Higgs mechanism which breaks the SM gauge group to Electromagnetism is also responsible for giving all the leptons and quarks their masses. This Higgs mechanism also gives rise to a new single neutral scalar boson with an unpredicted mass, the

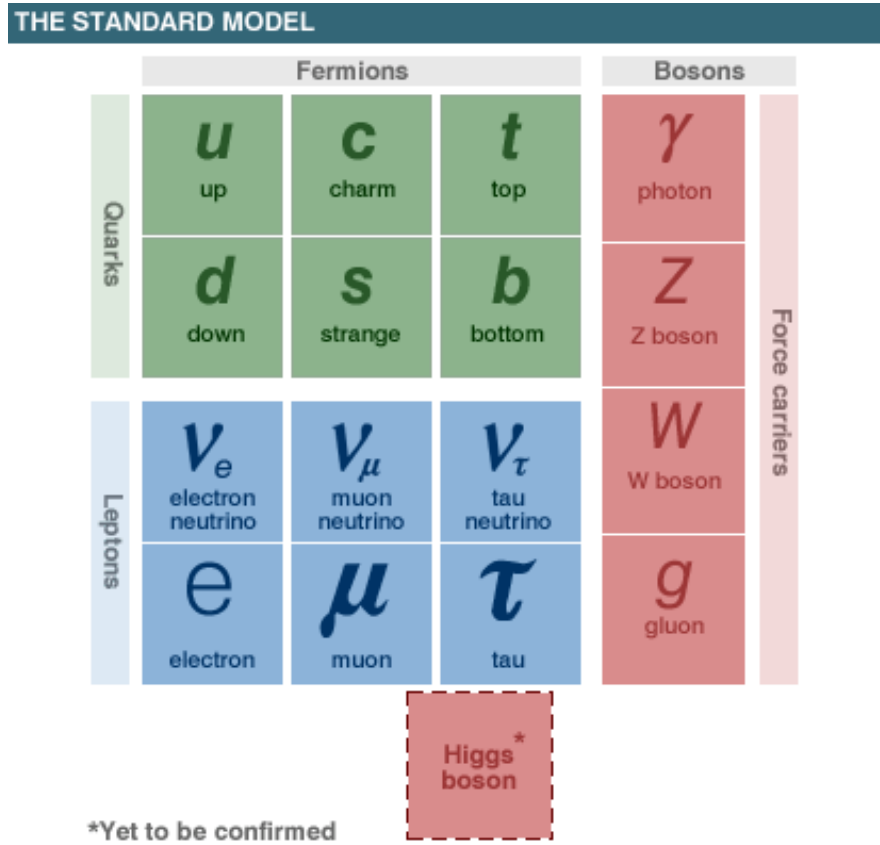


**Figure 1.1** The fundamental particles in the Standard Model.

Higgs boson, which is the only unobserved SM particle.

In the past three decades, particle physicists around the world try to search for the Higgs boson, unfortunately, it still escapes direct observation. However, the direct searches at the CERN LEP collider have set a limit on the Higgs boson mass of  $M_H > 114.4$  GeV at the 95% C.L.<sup>[1]</sup>. Combining this limit with precision electroweak measurements constrains the mass of the SM Higgs boson to be less than 186 GeV at the 95% C.L.<sup>[2]</sup>. The Fermilab Tevatron collider is sensitive to this interesting mass region. The first combined Tevatron search for the SM Higgs boson using the  $H \rightarrow WW$  decay mode has excluded the SM Higgs boson mass from 162 to 166 GeV at the 95% C.L.<sup>[3]</sup>, which is the first direct

constraint on the mass of the Higgs boson beyond that obtained at LEP.

## 1.2 Higgs production and decay at the Tevatron

### 1.2.1 SM Higgs production

At the Tevatron, the dominant SM Higgs production mechanism is gluon fusion ( $gg \rightarrow h + X$ , or GF), followed by associated production with a  $W$  or  $Z$  boson ( $q\bar{q} \rightarrow Vh + X$ , or VH) and vector boson fusion ( $VV \rightarrow H$ , or VBF)<sup>[4–6]</sup>. The Feynman digrams of these processes are shown in Fig. 1.2. The relevant fully inclusive cross sections as a function of the Higgs mass are presented in Fig. 1.3.

### 1.2.2 Decays of the Higgs Boson

The SM Higgs boson decay branching ratio predictions can be calculated using HDECAY<sup>[7]</sup>. The relevant decay branching ratio as a function of Higgs mass is shown in Fig. 1.4. For the low mass region with  $M_H < 140$  GeV, the Higgs boson mainly decays to  $b\bar{b}$ . The  $WW$  channel dominates in the high mass region with  $M_H > 140$  GeV, while the contribution from  $\gamma\gamma$  channel is just at the order of 0.2% around  $M_H = 130$  GeV. However, for the  $b\bar{b}$  decay, due to the overwhelming background contribution in the low mass region, one has to use the  $WH$  and  $ZH$  production channels. Also, the branching ratios for both the  $b\bar{b}$  and  $WW$  channels decrease visibly in the difficult intermediate mass region  $110 \text{ GeV} < M_H < 140 \text{ GeV}$ . Thus  $\gamma\gamma$  is an important channel to fill the gap of the intermediate mass region due to its clean

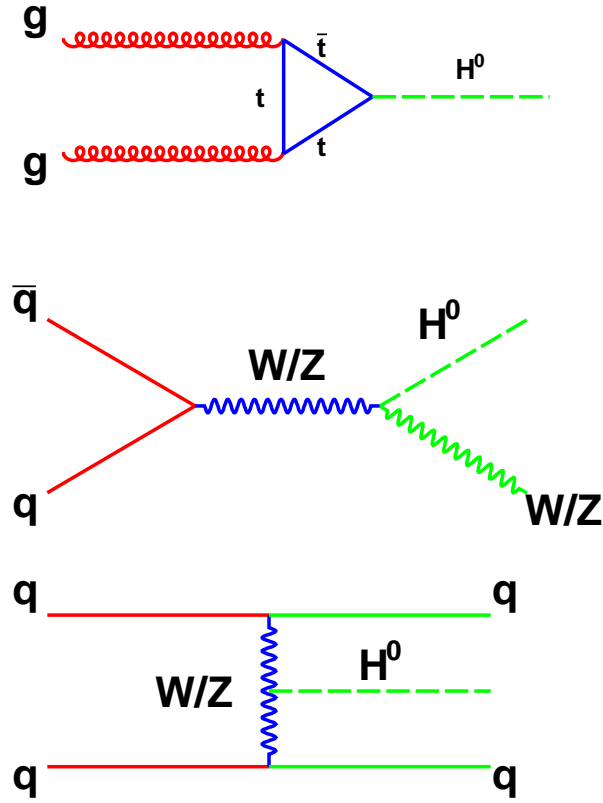


**Figure 1.2** SM Higgs production mechanism: gluon fusion ( $gg \rightarrow h + X$ ), associated production with a  $W$  or  $Z$  boson ( $q\bar{q} \rightarrow Vh + X$ ,  $V = W/Z$ ) and vector boson fusion ( $VV \rightarrow H$ ,  $V = W/Z$ ).

signature. In particular, it is considered to be one of the most promising discovery channels for a light SM Higgs boson at the LHC<sup>[8]</sup>.

While the SM Higgs production rate at the Tevatron is not sufficient to observe it in the  $\gamma\gamma$  mode, the  $Hgg$  and  $H\gamma\gamma$  couplings, being loop-mediated, are particularly sensitive to new physics effects. Furthermore, in some models beyond the SM<sup>[10]</sup>,  $\text{BR}(H \rightarrow \gamma\gamma)$  (see Fig. 1.5) can be enhanced significantly relative to the SM prediction, as a consequence of suppressed Higgs couplings to either (i) all fermions (known as bosonic or fermiophobic Higgs

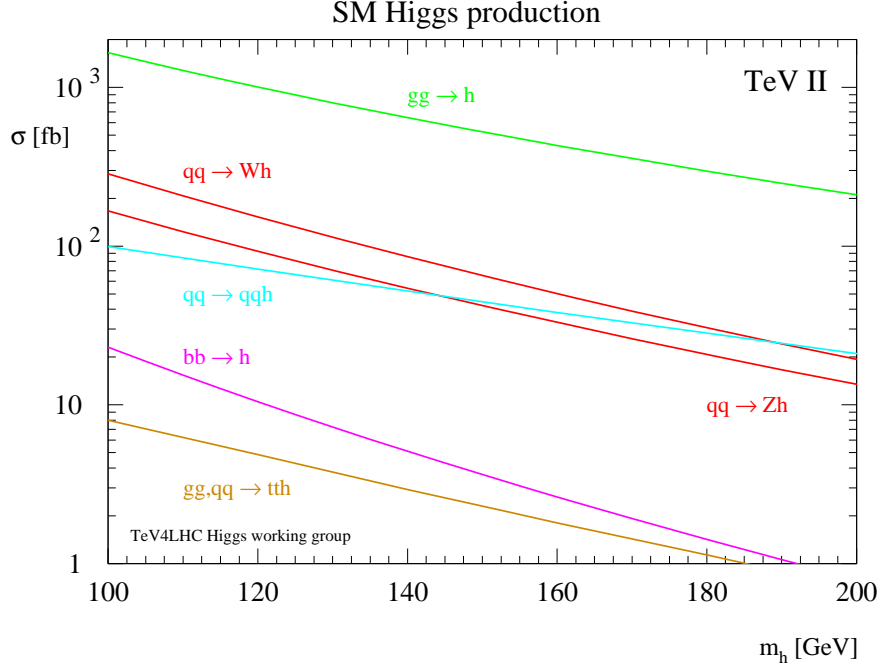


**Figure 1.3** The major SM Higgs boson production cross sections (fb) as a function of the Higgs boson mass at the Tevatron. The three dominant production mechanism, gluon fusion, associated production with a  $W$  or  $Z$  boson, and the vector boson fusion, shown in green, red and cyan respectively, are used in this analysis. Results for  $gg \rightarrow h$  and  $q\bar{q} \rightarrow Vh$  are at NNLO in the QCD expansion. Results for vector boson fusion ( $qq \rightarrow qqh$ ) is at NLO accuracy.

boson,  $H_f$ ); (ii) only down-type fermions ( $H_u$ , as it gives mass to up-type fermions); or (iii) only top and bottom quarks (known as electroweak Higgs boson,  $H_{ew}$ ). All models considered have SM-like production cross sections, with the exception of the  $H_f$  and  $H_{ew}$  models, where GF is absent or has a negligibly small cross section.

In this thesis, we present the first SM Higgs boson search using the  $\gamma\gamma$  final state at the Tevatron. The three dominant production mechanisms, gluon fusion, associated production with a  $W$  or  $Z$  boson, and the vector boson fusion have been used as the possible signal. As a result, it contributes to the overall sensitivity of the SM Higgs boson search at the Tevatron from the com-

bination of multiple channels<sup>[11]</sup>. Assuming the same integrated luminosity in all channels and a single Tevatron experiment, this result is expected to improve the combined upper limit on the SM Higgs production cross section by  $\sim 5\%$  for  $115 < M_H < 130$  GeV. Later, we extend this search to a particular Fermiophobic Higgs model, where the GF production is absent. The corresponding results have achieved the same sensitivity as a single LEP experiment, additionally providing access to the  $M_{H_f} > 125$  GeV region, which was inaccessible at LEP.

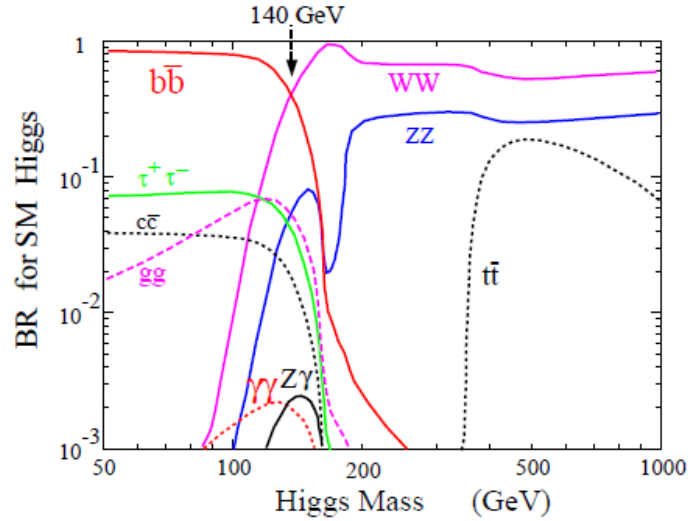


**Figure 1.4** Branching ratios for the SM Higgs boson as a function of assumed Higgs boson mass. As we can see, the major decay channel for the low mass region ( $M_H < 140$  GeV) is  $b\bar{b}$ , and  $WW$  channel dominates in the high mass region, while the  $\gamma\gamma$  channel is just at the order of 0.2%.

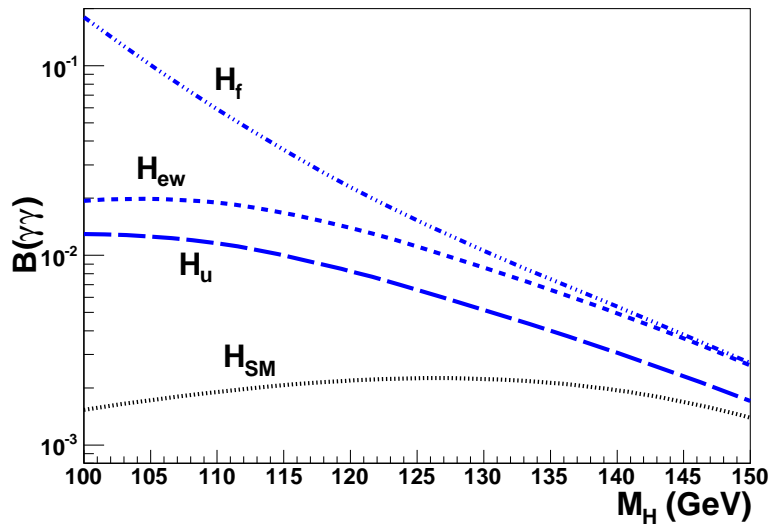


**Figure 1.5** Branching fraction into two photons for four different types of Higgs boson: 1.  $H_{SM}$  is the standard model Higgs boson, 2.  $H_u$  is the Higgs boson with Yukawa couplings only with up-type fermions, which can be a mass eigenstate in large  $\tan \beta$  supersymmetric theories, 3.  $H_{ew}$  is the Higgs boson that may help complete top quark condensation models, and 4.  $H_f$  is a Higgs boson with tree level couplings only to W and Z bosons.

### 1.3 Direct photon pair production

At a hadron collider, the direct photon pair (DPP) production with large invariant masses  $M_{\gamma\gamma}$  is a huge and irreducible background to the Higgs boson production with a decay into the photon pair at intermediate masses ( $110 \text{ GeV} < M_H < 140 \text{ GeV}$ ) for both, the Tevatron<sup>[9]</sup> and the forthcoming LHC experiments<sup>[8]</sup>. The DPP production is also significant background in searches for other new phenomena (NP), such as new heavy resonances<sup>[10]</sup>, extra spatial dimensions or cascade decays of heavy new particles<sup>[12]</sup>. Thus, a precise measurement of the diphoton differential production cross sections for various kinematic variables and their following theoretical understanding is extremely important for the future NP and Higgs searches.

In addition, studying the DPP production is important to check validity of predictions of perturbative QCD (pQCD), parton-to-photon fragmentation effects and soft-gluon resummation methods implemented in theoretical calculations.

The DPP events produced in  $p\bar{p} \rightarrow \gamma\gamma + X$  at Tevatron are expected to be dominantly produced via  $q\bar{q}$  scattering ( $q\bar{q} \rightarrow \gamma\gamma$ ) and gluon-gluon fusion ( $gg \rightarrow \gamma\gamma$ ) through a quark-loop diagram. In spite of the suppression factor of  $\alpha_s^2$  for  $gg \rightarrow \gamma\gamma$  as compared to  $q\bar{q} \rightarrow \gamma\gamma$ , the former still gives a significant contribution in kinematic regions where the  $gg$  parton luminosity is high, especially at low  $M_{\gamma\gamma}$ . Fig. 1.6 shows the expected contribution to the total DPP rate from  $gg \rightarrow \gamma\gamma$ , as predicted by the PYTHIA<sup>[13]</sup> Monte Carlo (MC) event generator with the



CTEQ6.1L parton distribution function (PDF) set<sup>[14]</sup>. In addition, direct photons may result from single photon one or two fragmentation processes of the partons produced in the hard scattering<sup>[15,16]</sup>. However, a strict photon isolation requirement significantly reduces the rate for these processes. The corresponding Feynman digrams for the above DPP processes are shown in Fig. 1.7 (Please see<sup>[15,16]</sup> for a thorough depiction of Feynman diagrams involved).

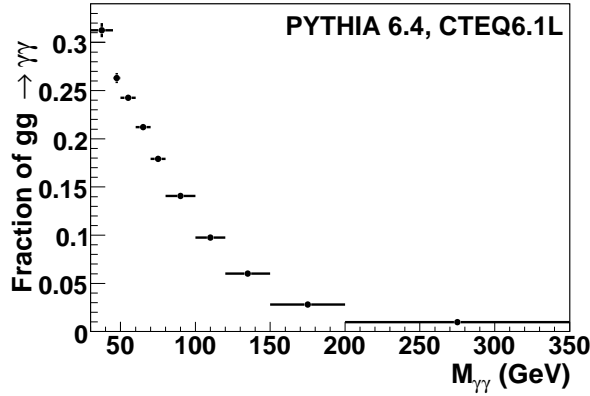


**Figure 1.6** Fraction of  $gg \rightarrow \gamma\gamma$  contribution to the total “direct” contribution caused by  $q\bar{q} \rightarrow \gamma\gamma$  and  $gg \rightarrow \gamma\gamma$ .

Both RESBOS<sup>[15]</sup> and DIPHOX<sup>[16]</sup> provide next-to-leading order (NLO) predictions in pQCD, however the  $gg \rightarrow \gamma\gamma$  contribution is considered only at leading order (LO) in DIPHOX. PYTHIA<sup>[13]</sup> is a parton shower MC event generator that includes the above processes at LO. In DIPHOX, the explicit parton-to-photon fragmentation functions are included up to NLO, while in RESBOS a function approximating rate from the NLO fragmentation diagrams is introduced. Also, only in RESBOS, the effects of soft and collinear initial state gluon emissions are resummed to all orders. This is particularly important for the description of

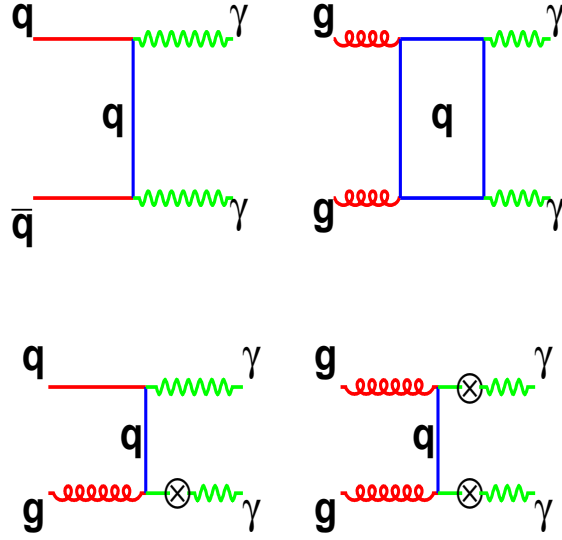


**Figure 1.7** Main direct diphoton production processes: “direct” contributions are presented by the first two diagrams while contributions from single photon one and two fragmentations are presented by the last two diagrams.

the  $p_T^{\gamma\gamma}$  ( $\Delta\phi_{\gamma\gamma}$ ) distribution, which is a delta-function at LO and diverges at NLO as  $p_T^{\gamma\gamma} \rightarrow 0$  ( $\Delta\phi_{\gamma\gamma} \rightarrow \pi$ ).

We have limited our phase space by the region with  $M_{\gamma\gamma} > p_T^{\gamma\gamma}$  where most part (92 – 93%) of the DPP signal events is located. With this cut contribution from (and thus sensitivity to) the fragmentation diagrams is significantly reduced and it con-

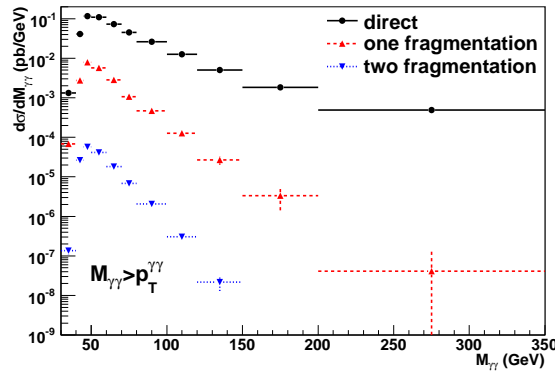


**Figure 1.8** DIPHOX predictions for the  $d\sigma/dM_{\gamma\gamma}$  cross section for “direct”, one and two fragmentation contributions.

strains the data-to-theory comparison to the region where the theory should be better understood and have smaller uncertainties<sup>[15,16]</sup>. From point of view of the measurement, it is also motivated by insufficient statistics of MC events and a low reliability of the MC distributions needed to estimate acceptance corrections in the region with  $M_{\gamma\gamma} < p_T^{\gamma\gamma}$ . Fig. 1.8 shows DIPHOX predictions for the  $d\sigma/dM_{\gamma\gamma}$  cross section for “direct”, one and two fragmentation contributions with the cut  $M_{\gamma\gamma} > p_T^{\gamma\gamma}$ .

The DPP cross sections are measured differentially as a function of  $M_{\gamma\gamma}$ , the diphoton transverse momentum ( $p_T^{\gamma\gamma}$ ), the azimuthal angle between the photons ( $\Delta\phi_{\gamma\gamma}$ ) and the cosine of the polar scattering angle of the photon in the frame with no net transverse momentum of the diphoton system (defined as  $\cos\theta^* = \tanh[(\eta_1 - \eta_2)/2]$ , where  $\eta_{1(2)}$  is the pseudorapidity of the highest (next-to-highest)  $p_T$  photon). These kinematic variables probe different aspects of the DPP production mechanism. For instance, the shapes of the  $p_T^{\gamma\gamma}$  and  $\Delta\phi_{\gamma\gamma}$  distributions are mostly affected by initial state gluon radiation and fragmentation effects. In addition, the  $M_{\gamma\gamma}$  spectrum is particularly sensitive to potential contributions from new phenomena. The  $\cos\theta^*$  distribution probes PDF effects and the angular momentum of the final state, which should be different for QCD-mediated production as compared, for example, to the decay of a spin-0 Higgs boson<sup>[15]</sup>. The measured cross sections are compared to theoretical predictions from RESBOS<sup>[15]</sup>, DIPHOX<sup>[16]</sup>, and PYTHIA<sup>[13]</sup>, which represents the first of public results at DØ also we for the first time at Tevatron

measure the double differential cross sections in bins of  $M_{\gamma\gamma}$ .

Besides the  $M_{\gamma\gamma} > p_T^{\gamma\gamma}$  requirement, the following kinematic cuts are imposed to the theoretical calculations and data analysis:

- transverse momentum  $p_T > 21$  (20) GeV for the highest (next-to-highest)  $p_T$  photon candidate;
- $|\eta_{1(2)}| < 0.9$ ;
- $\Delta R_{\gamma\gamma} \equiv \sqrt{(\Delta\eta_{\gamma\gamma})^2 + (\Delta\phi_{\gamma\gamma})^2} > 0.4$ , where  $\Delta\eta_{\gamma\gamma} = \eta_1 - \eta_2$ ;
- the scalar sum of all stable particles produced around the photon within  $\Delta R < 0.4$  ( $\sum_{particles}^{\Delta R < 0.4} p_T$ )  $< 2.5$  GeV,

where the asymmetry transverse momentum requirement on the two photons are introduced to void producing critical kinematic regions where the cancellations between virtual and real soft/collinear gluon divergences become imperfect in fixed-order calculations.

## Chapter 2 Fermilab and DØ detector

### 2.1 The Fermilab Accelerator System

The proton-antiproton collision beams are provided by the Tevatron, which is a circular particle accelerator at the Fermi National Accelerator Laboratory (FNAL) in Batavia, Illinois, USA. It is the highest energy proton-antiproton collider operating in the world<sup>[17,18]</sup>.

The accelerator (see Fig. 2.1) is composed of a number of different accelerator systems: the Pre-accelerator, Linear Accelerator, and Booster (collectively known as the Proton Source), Main Injector, Tevatron, Debuncher and Accumulator (These last two machines are referred to as the Antiproton Source).

#### 2.1.1 Pre-accelerator, Linear Accelerator and Booster

The Pre-accelerator, is a Cockcroft-Walton accelerator. It provides the source of the negatively charged  $H^-$  ions accelerated by the linear accelerator. The  $H^-$  gas is accelerated through a column from the charged dome(-750 kV) to the grounded wall to acquire an energy of 750 keV.

The Linear Accelerator(Linac) accelerates the  $H^-$  ions with an energy of 750 KeV to an energy of 400 MeV. It has two main sections, the low energy drift tube Linac(DTL) and the high energy side coupled cavity Linac(SCL). DTL focuses the beam by means of quadrupole magnets located inside the drift tubes. The beam traveling through the SCL is focused by quadrupoles placed

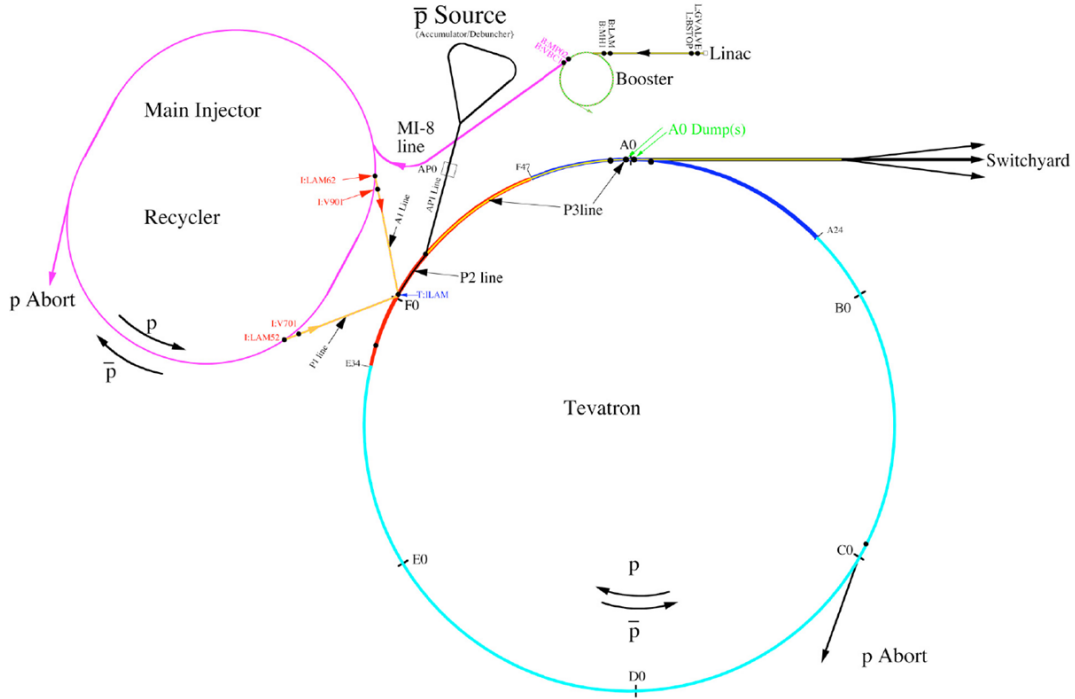


**Figure 2.1** Accelerator Overview.

between the accelerating modules.

The Booster is the first circular accelerator, or synchrotron, in the chain of accelerators. It takes the 400 MeV negative hydrogen ions from the Linac and strips the electrons off, which leaves only the proton, and accelerates the protons to 8 GeV. The Booster can accelerate beam once every 66 milliseconds (15 Hz).

### 2.1.2 Main Injector

The Main Injector (MI) is a circular synchrotron seven times the circumference of the Booster and slightly more than half the circumference of the Tevatron. It consists of 6 sections, labeled MI-10 through MI-60. The MI can accelerate 8 GeV protons from the Booster to either 120 GeV or 150 GeV, depending on their destination. The Main Injector can provide beam to a number of

different places at a number of different energies. It can operate in different modes:

- $\bar{P}$  Production: It produces  $\bar{p}$ , to put in a stack in the accumulator.
- Shot Setup: This mode relates to the act of extracting a bunch of antiprotons from the Antiproton Source and inserting them into the Tevatron.
- The NuMI experiment: The MI sends protons to the NuMI target to produce neutrinos.
- Other modes

### 2.1.3 Tevatron

The Tevatron is the largest of the Fermilab accelerators, with a circumference of approximately 4 miles. The Tevatron accepts both protons and antiprotons from Main Injector and accelerates them from 150 GeV to 980 GeV. In Collider mode, the Tevatron can store beam for hours at a time. Because the Tevatron is a primarily storage ring, the length of time between acceleration cycles is widely variable. The magnets used in the Tevatron use wire made from superconducting niobium/titanium alloy that needs to be kept extremely cold ( $\sim 4$  K) by liquid helium to remain as a superconductor.

### 2.1.4 Antiproton Source

The Antiproton Source is composed of the following parts:

- Target: During stacking, 120 GeV protons coming from the MI are directed to strike a nickel target. 8 GeV antiprotons are collected by using magnets out of all sorts of secondary particles produced by the collision. These antiprotons are directed down into the Debuncher.
- Debuncher: It can accept 8 GeV protons from Main Injector for beam studies, and 8 GeV antiprotons from the target station. Its primary purpose is to efficiently capture the high momentum spread antiprotons coming off of the target.
- Accumulator: It is the second synchrotron of the antiproton source and used to store the antiprotons.

## 2.2 DØ Detector

The DØ detector is a multi-purpose particle detector. It has been constructed to study proton-antiproton collisions at a center of mass energy  $\sqrt{s} = 1.96$  TeV. Fig. 2.2 is the overview of the DØ detector. A Cartesian coordinate system is used with the z axis defined by the direction of the proton beam, the x axis pointing radially out of the Tevatron ring, and the y axis pointing up<sup>[20]</sup>. In proton-antiproton collisions the center of mass frame of the colliding partons is approximately at rest in the plane transverse to the beam direction, but the motion along the beam direction of some secondaries can not be determined because of the beam pipe. Therefore the plane transverse to the beam direction is of special importance, and sometimes we work with two-dimensional vectors defined in the x-y plane. We use rapidity



$y = +\frac{1}{2}\ln\left(\frac{E+p_z}{E-p_z}\right)$  to define the direction of a particle relative to the beam direction. The rapidity is additive under Lorentz boosts in the beam direction. For a particle with energy much greater than its mass, the pseudorapidity  $\eta = -\ln \tan(\theta/2)$  is used as a good approximation of rapidity. The DØ detector covers a range of  $|\eta| < 4.2$  and consists of the three major sub-systems:

- Tracking system;
- Calorimeter system;
- Muon system.

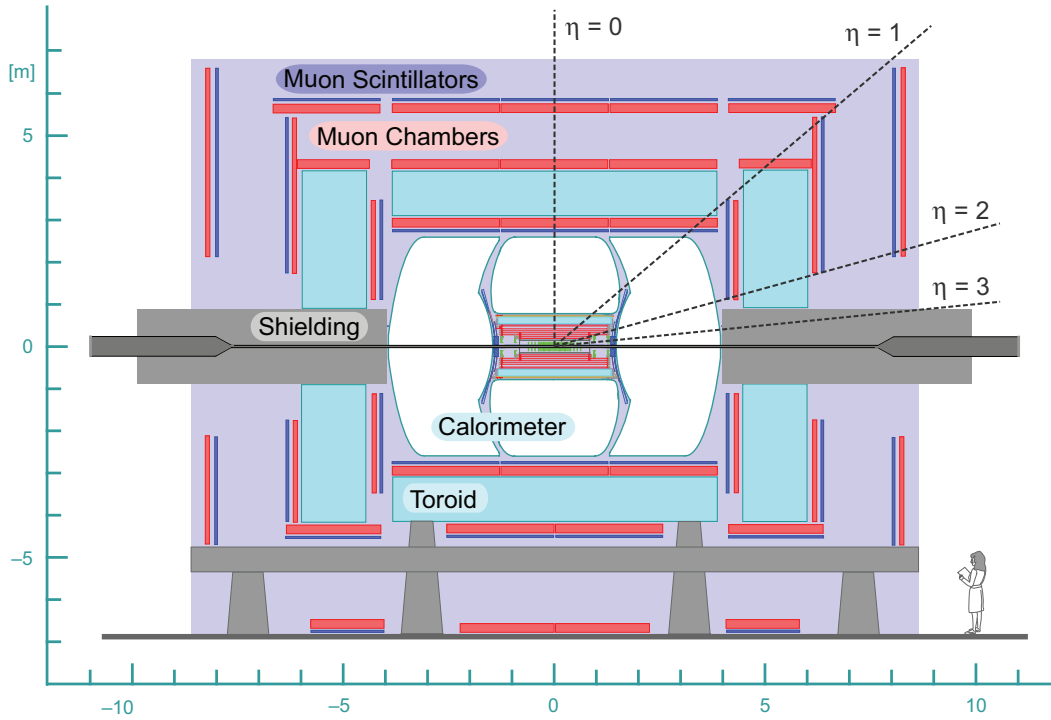


**Figure 2.2** DØ Detector.

### 2.2.1 Central Tracking System

The central tracking system consists of the silicon microstrip tracker (SMT) and the central fiber tracker (CFT) surrounded by

a solenoidal magnet as shown in Fig. 2.3. Both the SMT and CFT provide tracking information to the trigger. And they were designed for the excellent tracking measurement in the central region for studies of top quark, electroweak, and b physics and to search for new phenomena, including the Higgs boson.

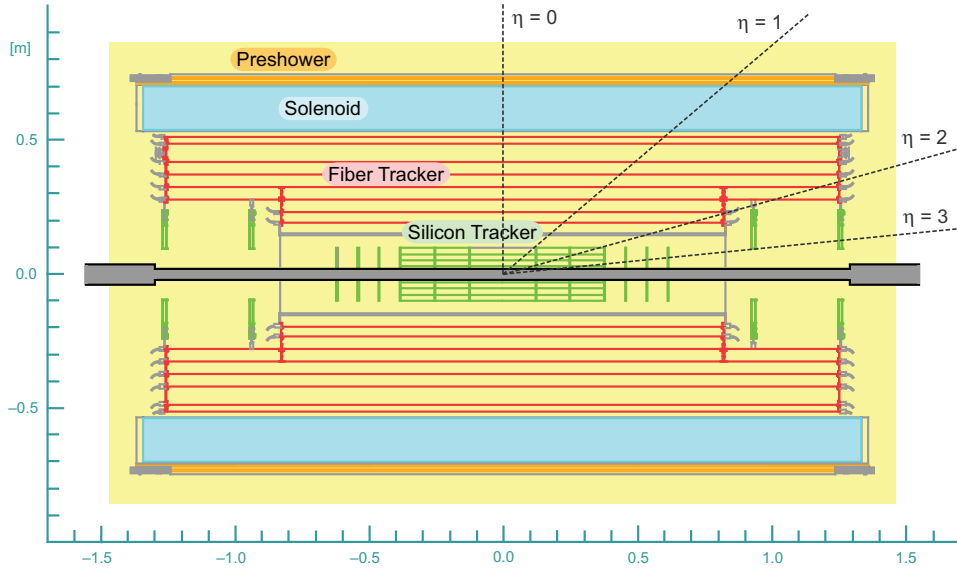


**Figure 2.3** DØ Tracking System.

### Silicon Microstrip Tracker (SMT)

The SMT<sup>[22]</sup> provides both tracking and vertexing over nearly the full coverage of the calorimeter and muon systems. An isometric overview of the SMT is shown in Fig. 2.4. It has six barrels in the central region, with four silicon readout layers for each barrel. The silicon modules installed in the barrels are called "ladders". Layers 1 and 2 have twelve ladders each; layers 3 and 4 have twenty-four ladders each, for a total of 432 ladders. Each barrel is capped at high  $|z|$  with a disk of twelve double-sided wedge detectors, called an "F-disk". In the far forward re-

gions, two large-diameter disks, “H-disk” , provide tracking at high  $\eta$ . The barrel detectors primarily measure the position in the  $r$ - $\phi$  plane and the disk detectors measure the position in both  $r$ - $z$  and  $r$ - $\phi$  planes. Thus vertices for particles at high  $\eta$  are reconstructed in three dimensions by the disks, and vertices of particles at small values of  $\eta$  are measured in the barrels and central fiber tracker.

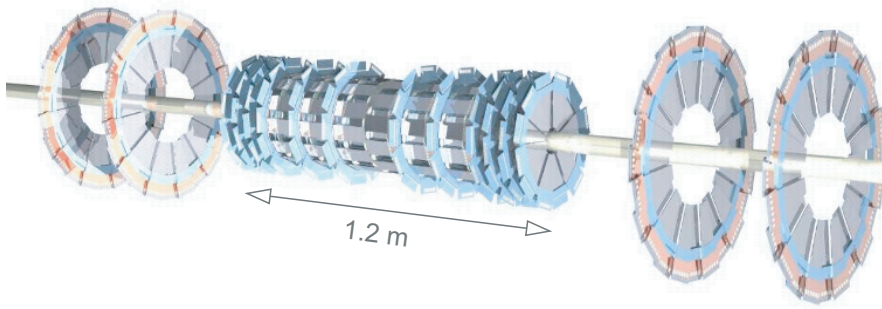


**Figure 2.4** DØ Silicon Detector.

### Central Fiber Tracker (CFT)

Outside the SMT is the Central fiber tracker (CFT)<sup>[23]</sup> as shown in Fig. 2.5. The CFT consists of scintillating fibers mounted on eight concentric support cylinders, at radii from 20 to 52 cm from the center of beampipe. The two innermost cylinders are 1.66 m long; the outer six cylinders are 2.52 m long. It covers a range of  $\eta \leq 1.7$ . Each cylinder supports one doublet layer of fibers oriented along the beam direction ( $z$ ) and a second doublet layer at a stereo angle in  $\phi$  of  $+3^\circ$  ( $u$ ) or  $-3^\circ$  ( $v$ ). Doublet layers with fibers oriented along the beam axis are referred to as axial layers, while the doublet layers oriented at small angles are referred to as stereo layers. Photons produced by an ionizing particle are

detected by a Visible Light Photon Counter (VLPC) that converts the photons into an electrical pulse. The CFT has 76,800 scintillating fibers grouped into doublet layers and can measure the position with a resolution on the order of  $100 \mu\text{m}$ , corresponding to a  $\phi$  resolution of  $2 \times 10^{-4}$  radians.

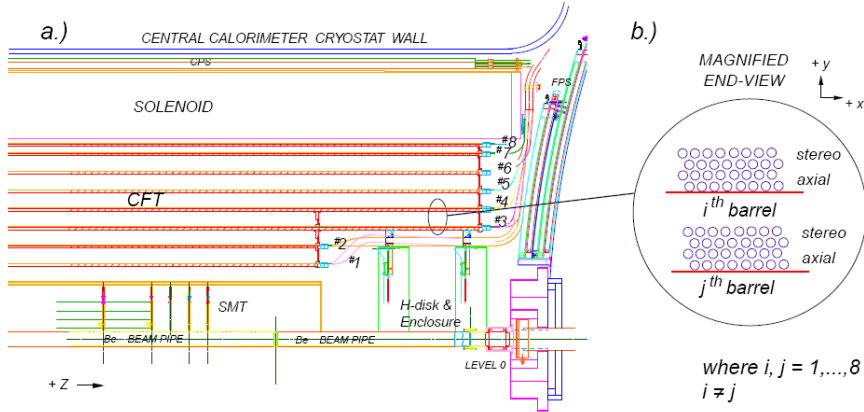


**Figure 2.5** DØ Central Fiber Tracker.

### 2.2.2 Solenoid and Preshower

The 2T magnetic field in the central tracking system is provided by the superconducting solenoidal magnet. The magnet was designed to optimize the momentum resolution and tracking pattern recognition within the constraints imposed by the DØ calorimeter.

The preshower<sup>[24,25]</sup> detectors are added to help identify electrons and photons and reject background during both triggering and offline reconstruction by enhancing the spatial matching between tracks and calorimeter showers. The detectors also can be used offline to correct the electromagnetic energy measurement for losses in the solenoid and upstream material, such as

cables and supports. The central preshower detector (CPS) covers the region  $|\eta| < 1.3$  and the two forward preshower detectors (FPS) cover  $1.5 < |\eta| < 2.5$ . Both CPS and FPS are made from triangular strips of scintillator, as shown in Fig. 2.6. Since the triangles are interleaved, there is no dead space between strips and most tracks tranverse more than one strip, allowing for strip-to-strip interpolations and improved position measurement, which would be very useful to help to identify the vertex for the photons.

### **Central Preshower (CPS)**

The CPS consists of three concentric cylindrical layers of triangular scintillator strips and is located in the nominal 5 cm gap between the solenoid and the central calorimeter. Between the solenoid and the CPS is a  $1 X_0$  thick lead radiator. The three layers of scintillator are arranged in an axial- $u$ - $v$  geometry, with a  $u$  stereo angle of  $23.774^\circ$  and a  $v$  stereo angle of  $24.016^\circ$ . Each layer contains 1280 strips and made from eight octant modules. The modules consist of two  $1/32''$  stainless steel skins with the scintillator strips sandwiched in between. The WLS fibers are split at  $z = 0$  and read out from each end resulting in 2560 read-out channels/layer.

### **Forward Preshower (FPS)**

The two FPS detectors (north and south) are mounted on the spherical heads of the end calorimeter cryostats. Each detector is made from two layers, at different  $z$ , of two planes of scintillator strips. A  $2X_0$ -thick lead-stainless-steel absorber separates

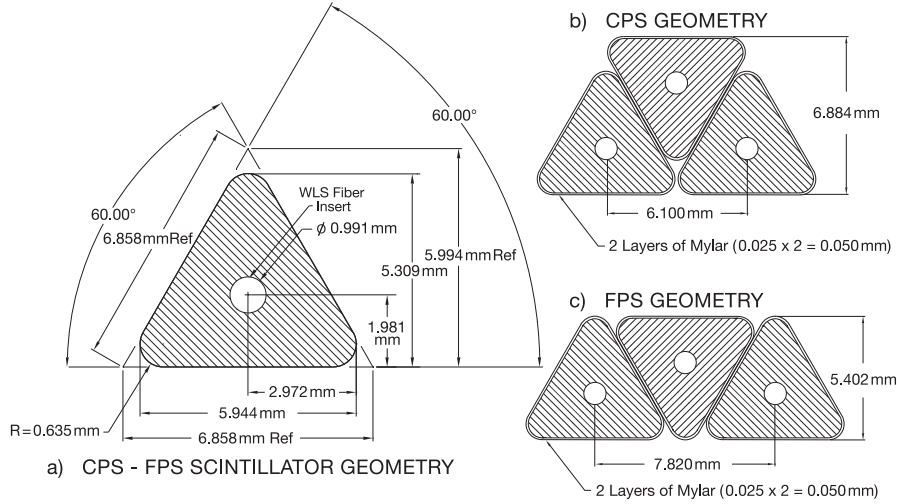


**Figure 2.6** Cross section and layout geometry of the CPS and FPS scintillator strips.

the two layers, as shown in Fig. 2.7. The upstream layers (those nearest the interaction region) are known as the minimum ionizing particle, or MIP, layers while the downstream layers behind the absorber are called the shower layers. Charged particles passing through the detector will register minimum ionizing signals in the MIP layer, allowing measurement of the location (in  $\eta$ ,  $\phi$  and  $z$ ) of the track. Photons will not generally interact in the MIP layer, but will produce a shower signal in the shower layer.

### 2.2.3 Calorimeter

Photons are the electromagnetic object, so the most important subdetector is the uranium/liquid-argon sampling calorimeter (Fig. 2.8). It is well suited to identify electrons, photons and jets and also measure their energies. A significant improvement to the detector's performance resulted from the removal of the old Main Ring beam pipe from the calorimeters (compared to Run I). Removal of the Main Ring increased the livetime of the detec-

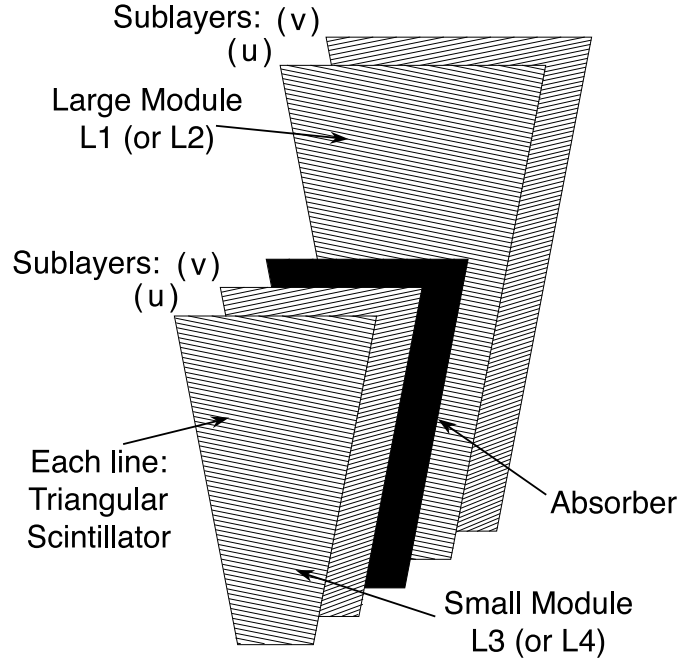
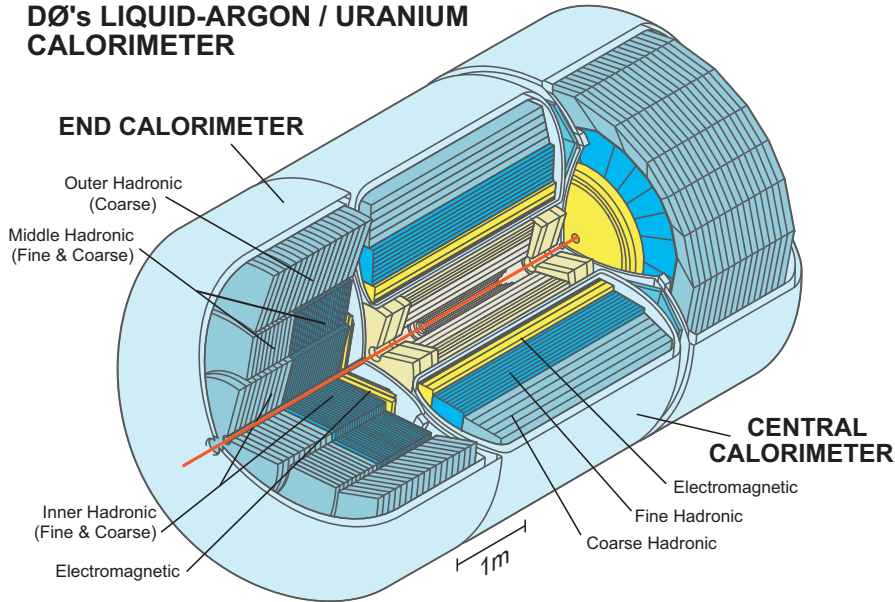


**Figure 2.7** Complete  $\phi$ -segment of a FPS module.

tor by approximately 10%, depending on the trigger<sup>[20,21]</sup>.

The calorimeter has one central calorimeter (CC) covering  $|\eta| < 1.1$ . The two forward calorimeter (EC) cover  $1.5 < |\eta| < 4.2$ , as shown in Fig. 2.9. Each of them is contained in its own cryostat and can be further categorized into an electromagnetic section closest to the interaction region and hadronic sections. The hadronic section is composed of fine and coarse calorimeters. Liquid argon is chosen as the active medium because it does not trap charges and allows the ionization produced in electromagnetic or hadronic showers to be collected by the signal boards without amplification. Liquid argon is chosen also because of the relative simplicity of calibration, the flexibility provided in segmenting the calorimeter into transverse and longitudinal cells, the good radiation hardness, and the relatively low cost per channel for readout electronics<sup>[19]</sup>. The three calorime-

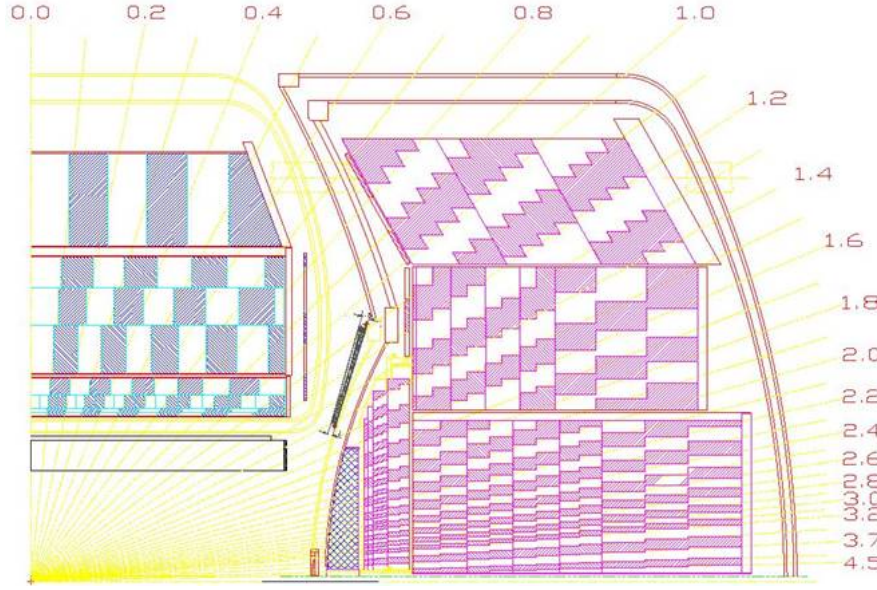
ters, Central Calorimeter, North End-Cap (ECN) and South End-Cap (ECS), are located within their own cryostats with a temperature maintained at approximately 90 K. In the electromagnetic sections (EM), the absorber plates are made of nearly pure depleted uranium. 6-mm-thick uranium-niobium (2%) alloy is used for the fine hadronic calorimeter and relatively thick (46.5 mm) plates of copper (in the CC) or stainless steel (in the EC) are used for the coarse hadronic modules .



**Figure 2.8** DØ Uranium/Liquid-argon Calorimeter.

The CC-EM section is composed of 32 azimuthal modules. The entire calorimeter is divided into about 5000 pseudoprojective towers, each covering  $0.1 \times 0.1$  in  $\eta \times \phi$ . The EM section is segmented into four layers, 2, 2, 7, and 10 radiation lengths thick respectively. The third layer, in which electromagnetic showers typically reach their maximum, is transversely segmented into cells covering  $0.05 \times 0.05$  in  $\eta \times \phi$  (Fig. 2.10). We call region

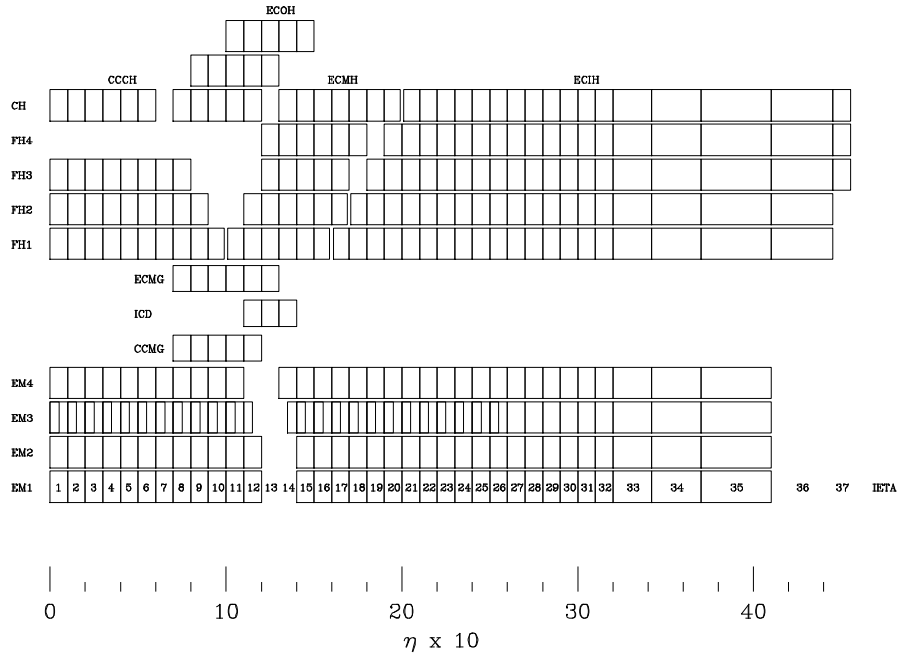




**Figure 2.9** DØ Uranium/Liquid-argon Calorimeter showing segmentation in  $\eta$  and depth.

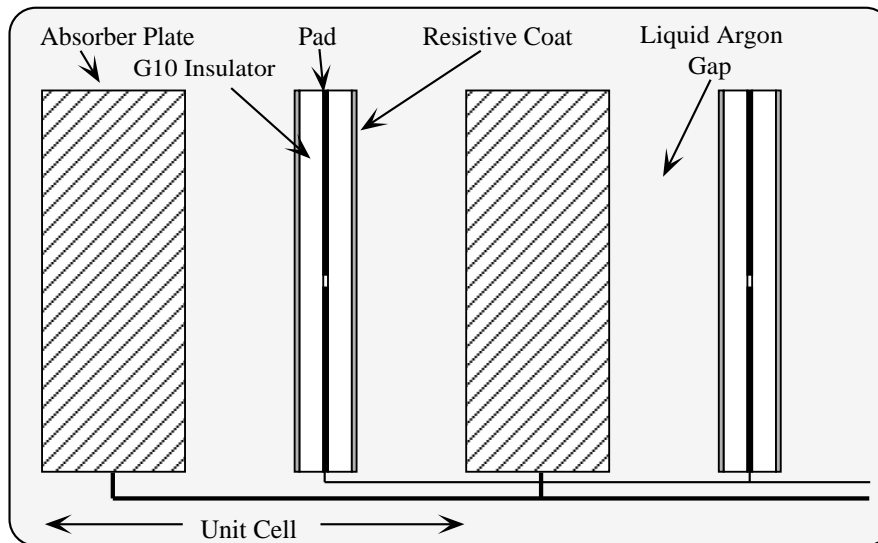
”fiducial in  $\phi$ ” in CC, if the EM cluster position (at EM3) in  $\phi$  is located by  $> 0.02$  from the crack. The hadronic section is segmented into four layers (CC) or five layers (EC). The entire calorimeter is 7 to 9 nuclear interaction lengths thick. The signals from arrays of  $2 \times 2$  calorimeter towers, covering  $0.2 \times 0.2$  in  $\eta \times \phi$ , are added together electronically for the EM section only and for all sections, and shaped with a fast rise time for use in the level 1 trigger. We refer to these arrays of  $2 \times 2$  calorimeter towers as ‘‘trigger towers’’ [26].

Fig. 2.11 is the schematic view of a typical calorimeter cell. The metal absorber plates are grounded and the signal boards(G10 boards) with resistive surfaces are placed at a high voltage of 2.0 kV. The electron drift time across the 2.3 mm liquid argon gap is approximately 450 ns. The gap thickness was chosen to be large enough to observe minimum ionizing particle signals and to



**Figure 2.10** Calorimeter channel layout in directions of depth and  $\eta$ .

avoid fabrication difficulties. Particles traversing the gap generate an ionized trail of electrons and ions. The current, produced by the electrons drift in the electric field, induces an image charge on a copper pad etched on the G10 board under the resistive coat. The charge is then transferred to calorimeter readout system.



**Figure 2.11** Liquid argon gap and signal board unit cell for the calorimeter.

Fig. 2.12 shows a schematic of this data path. The signal from each readout cell is brought to a feed-through port on a  $30\ \Omega$  coaxial cable. The signals are carried from the feed-through ports to the preamplifier inputs on  $115\ \Omega$  twist & flat cables. The image charge induced on the readout pads by the charge collected on the resistive coat is integrated by the charge-sensitive preamplifiers. The voltage pulses are transferred to the shaper and baseline subtractor (BLS), where the preamplifier outputs are shaped, sampled before and after the bunch crossing, and the difference is stored on a sample & hold circuit. The sample & hold outputs are then read out and digitized by the analog to digital converters(ADCs) when a trigger is received.

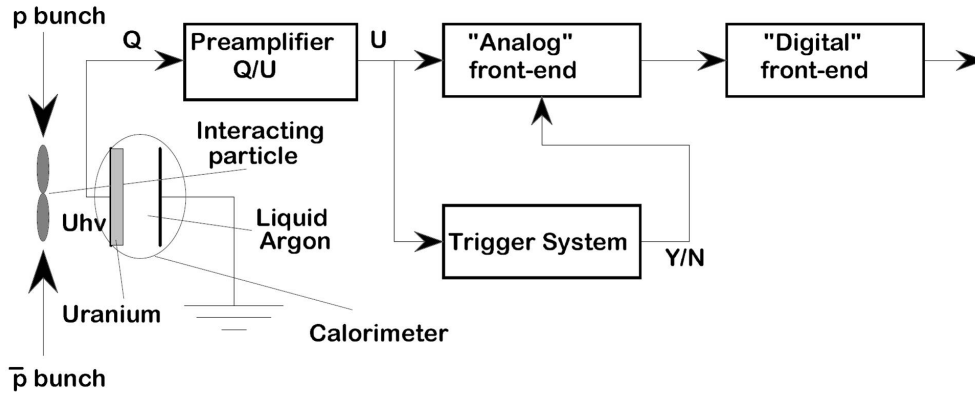


**Figure 2.12** Simplified diagram of the calorimeter data flow path.

It is very important to understand the calorimeter performance. The energy resolution of the calorimeter can be written as equation 2.1.

$$\frac{\sigma_E}{E} = \sqrt{\left(\frac{N}{E}\right)^2 + \left(\frac{S}{\sqrt{E}}\right)^2 + C^2} \quad (2.1)$$

where  $N$ ,  $S$  and  $C$  are used in the noise, sampling, and constant terms, respectively. The noise term is from electronic noise summed over readout channels. The sampling term reflects statistical fluctuations such as intrinsic shower fluctuations, including dead material in front of the calorimeter and sampling fluctuations. The constant term accounts for contributions from detector non-uniformity and calibration uncertainty.

#### 2.2.4 Muon System

The upgraded detector uses the original central muon system proportional drift tubes (PDTs) and toroidal magnets, central scintillation counters (some new and some installed during Run I), and a completely new forward muon system. The new forward muon system extends muon detection from  $|\eta| \leq 1.0$  to  $|\eta| \approx 2.0$ , using mini drift tubes (MDTs) instead of PDTs and including trigger scintillation counters and beam pipe shielding. A 1.8 T magnetic field is generated by a toroidal iron magnet in a second tracking system outside the calorimeter to detect muons. Positions are measured by drift chambers.

## Chapter 3 Photon identification

Fig. 3.1 shows signatures for the detectable particles in the multi-system detector. For photons, there are 2 significant features:

- shower in the EM calorimeter, and the corresponding shape should be consistent with the EM object;
- no associated tracks in the tracking system with matching to its shower.

Based on these features, we know to identify the photon, we need

- reconstruct the primary vertex, where all general photon identification variables are calculated with respect to it, especially the photon 4-momentum;
- reconstruct the photon candidates with using the EM shower;
- separate the photon and jet further with using the additional information from the energy deposit in the tracker and PS;
- separate the photon and electron with using the tracking information.

### 3.1 Vertex reconstruction

The reconstruction of the primary interaction vertex is important for the photon reconstruction, since later, almost all photon identification variables are computed with respect to this hard

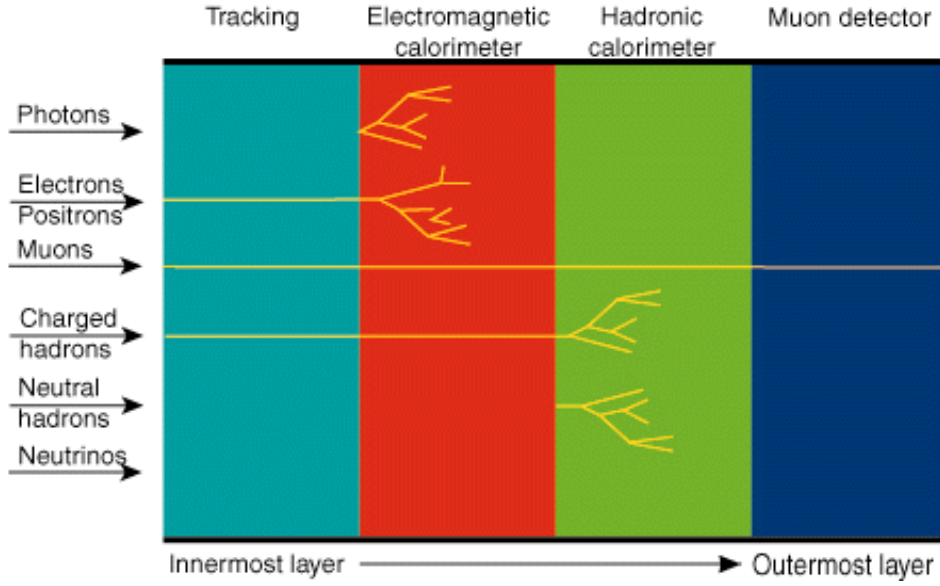


**Figure 3.1** Photon's signature in the detector.

interaction point. Currently, DØ uses the Adaptive fitter algorithm<sup>[27]</sup> to reconstruct the vertex. And later the hard-scatter vertex is selected using the minimum bias probability selection algorithm<sup>[28]</sup>. The probability is calculated for each vertex with using the  $\log_{10} p_T^{track}$  distribution of the  $p_T^{track} > 0.5$  GeV tracks from the minimum bias processes, and the product is then weighted to make it independent of the total number of tracks. The primary vertex (PV) is the one with the lowest minimum bias probability.

As we can see, such method used for choosing the PV mainly rely on the tracks, especially the high  $p_T$  tracks. So it would work well for charged particles involved physical processes, but may not for the photon involved ones, especially the diphoton ones. In this thesis, we select the new primary vertex with the maximum associated tracks for each event, but it is not always consistent with the primary vertex used at the reconstruction level ( selected with using the minimum bias probability). We use the  $M_H = 130$

GeV Higgs MC samples to check which vertex is better by comparison with the true vertex at generator level, further we compare the diphoton invariant mass distribution between using the new and the default reconstruction (reco) vertex. Table 3.1 shows the fraction of events where the reconstructed vertex (new and reco) matched to the true one within 1 cm. Fig. 3.2 shows the corresponding invariant mass distribution comparison. We find the new vertex we select performs better than the default vertex used by the reco, especially for the gluon fusion process. Finally we recalculate the 4-momentum and invariant mass, as well as the corresponding photon identification variables for our photon candidates with respect to the new PV.

signal sample	reco vertex	new vertex
GF	$0.762 \pm 0.001$	$0.937 \pm 0.001$
VH	$0.931 \pm 0.001$	$0.954 \pm 0.001$
VBF	$0.959 \pm 0.001$	$0.960 \pm 0.001$

**Table 3.1** The fraction of events with using the reco and new vertex matched to the true one for  $M_H = 130$  GeV Higgs from gluon fusion (GF), associated production (VH) and vector boson fusion (VBF) processes.

And the new PV is required to be within 60 cm of the geometrical center of the detector along the beam axis. The average PV reconstruction efficiency in  $\gamma\gamma + X$  events is  $\sim 98\%$ , with  $\sim 95\%$  probability to match the true vertex. Here the 98% is the primary vertex selection efficiency, which is almost fully efficient, and will be the same for the  $H \rightarrow \gamma\gamma$  search and DPP processes. The 5% mix-vertex rate is not important for the  $H \rightarrow \gamma\gamma$  search. While for the DPP cross section measurement, such mis-vertex rate will go high in some kinematic region, for instance in the

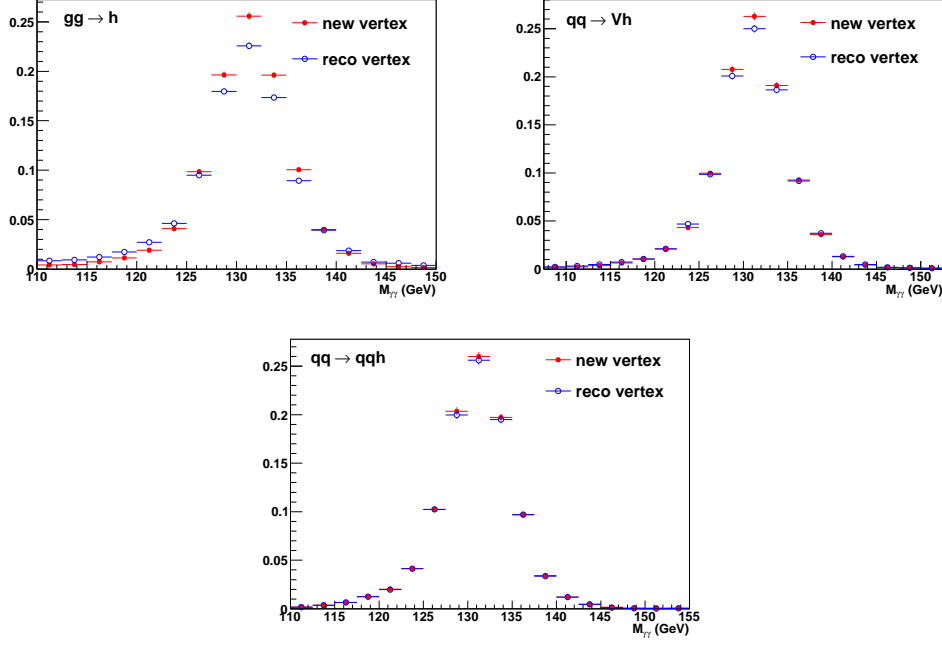


**Figure 3.2** Diphoton invariant mass distribution comparison between using reco vertex and new vertex for  $M_H = 130$  GeV Higgs from gluon fusion (GF) (top-left), associated production (VH) (top-right) and vector boson fusion (VBF) (bottom) processes.

$M_{\gamma\gamma} < 50$  GeV region, especially during the high luminosity environment. So in Chapter 5, there will be more specifically detailed discussion, as well as some precise quantification on the mis-vertex effect for the DPP cross section measurement.

### 3.2 Reconstruct the EM object

A photon is identified as a cluster of adjacent calorimeter cells. Its energy is calculated as the sum of the energies in all the EM and FH1 cells in a cone of size  $\Delta R = \sqrt{(\Delta\eta)^2 + (\Delta\phi)^2} = 0.2$ , centered on the tower with the highest fraction of the photon energy. The photon direction is calculated using the calorimeter shower centroid position and the primary vertex position.

The electromagnetic clusters found by the reconstruction (EM-



Reco) are required to satisfy  $E_T > 1.5 \text{ GeV}$ ,  $f_{EM} > 0.9$  and  $f_{iso} < 0.15$ .  $E_T$  is the transverse energy of the EM cluster deposited in the calorimeter.  $f_{EM}$  is the EM cluster energy fraction in the EM part of the calorimeter

$$f_{EM} = \frac{E_{EM}}{E_{EM} + E_{Had}}, \quad (3.1)$$

where  $E_{EM}$  and  $E_{Had}$  are the energy measured in the EM and Hadronic part of the calorimeter in a cone of radius  $\Delta R = 0.2$ , respectively.  $f_{iso}$  is the isolation with the definition

$$f_{iso} = \frac{E_{Tot}(\Delta R < 0.4) - E_{EM}(\Delta R < 0.2)}{E_{EM}(\Delta R < 0.2)}, \quad (3.2)$$

where  $E_{Tot}(\Delta R < 0.4)$  is the total energy in a cone of radius  $\Delta R = 0.4$  around the direction of the cluster, summed over the entire depth of the calorimeter and  $E_{EM}(\Delta R < 0.2)$  is the energy in a cone of  $\Delta R = 0.2$ , summed over the EM layers only. Fig. 3.3 gives a straightforward view of the isolation definition.

The variables  $f_{EM}$  and  $f_{iso}$  provide powerful rejection to the hadronic jets that tend to deposit most of their energies in the hadronic calorimeter and are composed of nonisolated particles.

The shower shape of a photon is defined using the width of the transverse shape in the  $r - \phi$  space, which is calculated with using energy weighted distance ( $dr$ ) between all fired EM3 cells and the centroid position. This variable is named *sigphi*, with the definition:

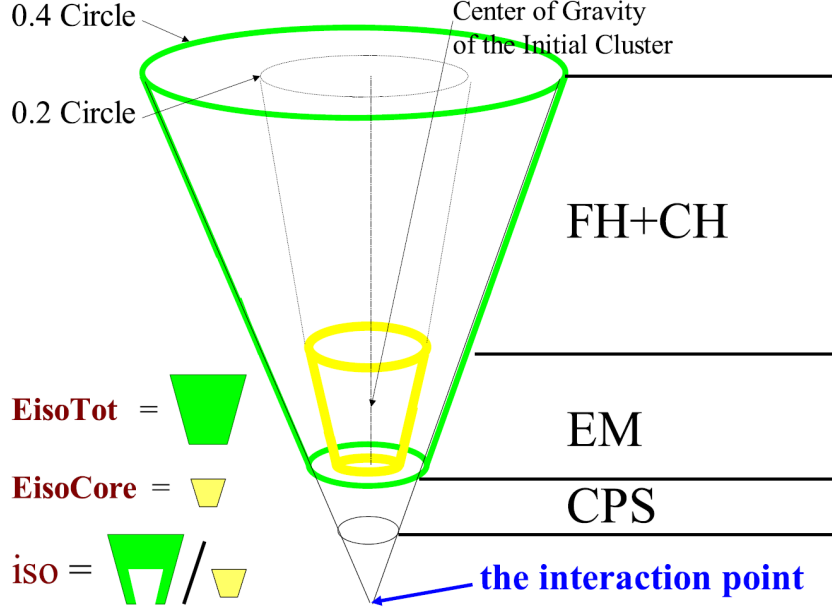
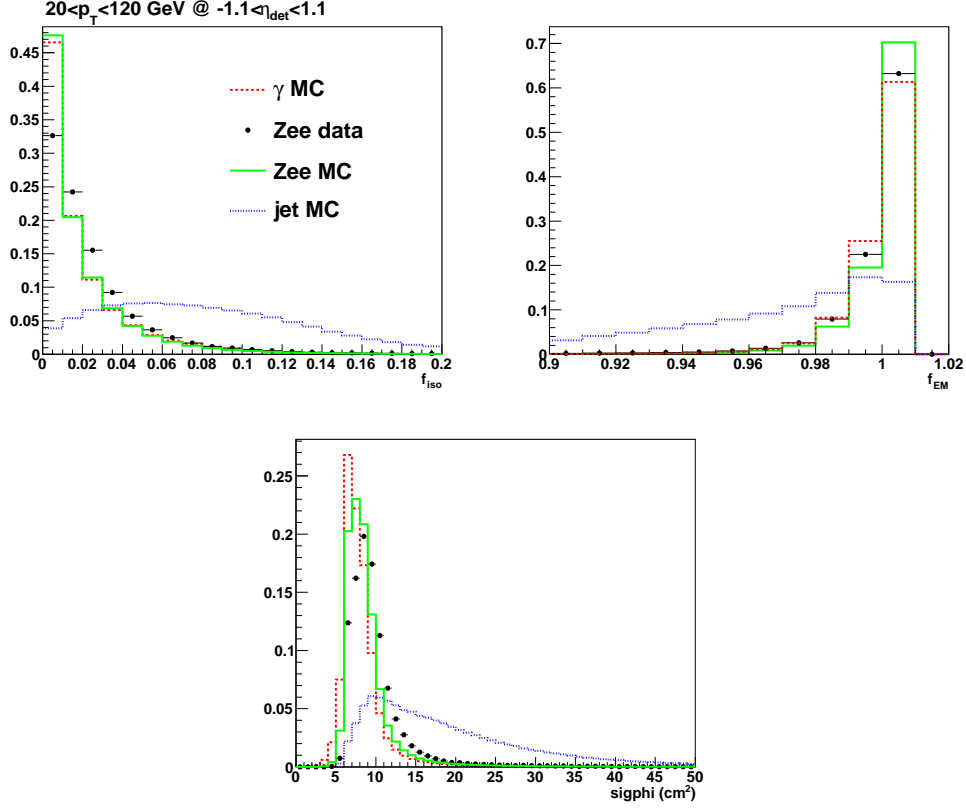


Figure 3.3 Isolation definition.

$$\begin{aligned}
 sigphi &= \sum \log\left(\frac{E_{cell}^i}{E_{EM3}}\right) \times dr^2 \\
 &= \sum \log\left(\frac{E_{cell}^i}{E_{EM3}}\right) \times (-\sin\phi_{EM} \cdot x_{cell}^i + \cos\phi_{EM} \cdot y_{cell}^i)^2,
 \end{aligned}
 \tag{3.3}$$

where  $E_{cell}^i$  is the energy of the cell  $i$ ,  $E_{EM3}$  is the energy of the EM3 layer, and  $dr$  is the distance between the cell  $i$  and the centroid position, which could be simply resolved with rotating the cell  $i$  position at  $x - y$  space by the centroid azimuthal angle  $\phi_{EM}$ .

Fig. 3.4 shows the distributions for these general photon identification variables from  $Z \rightarrow ee$  data and MC,  $\gamma$  MC and jet MC.



**Figure 3.4** General photon identification variables distributions.

### 3.3 Separation of jets and photons using Artificial Neural Network

To suppress jets misidentified as photons further, we trained a neural network (NN)<sup>[29]</sup> with using a set of variables sensitive to differences between photons and jets in the tracker activity and in the energy distributions in the calorimeter and CPS (see Fig. 3.5):

- the scalar sum of the  $p_T$  of all  $p_T > 0.5$  GeV tracks ( $p_{T\text{trk}}^{\text{sum}}$ ) originating from the primary vertex in an annulus of  $0.05 < \Delta R < 0.4$  around the EM cluster,
- the numbers of cells above the transverse energy ( $E_T$ ) dependent threshold ( $0.004 \times E_T + 0.25$  GeV) in the first EM calorimeter layer within  $\Delta R < 0.2$  and  $0.2 < \Delta R < 0.4$  of

the EM cluster,

- the number of CPS clusters within  $\Delta R < 0.1$  of the EM cluster,
- the squared-energy-weighted width of the energy deposit in the CPS:  $\frac{\sum_i E_i^2 \times (\phi_{EM} - \phi_i)^2}{\sum_i E_i^2}$ , where  $E_i$  and  $\phi_i$  are the energy and azimuthal angle of the  $i^{th}$  strip, and  $\phi_{EM}$  is the azimuthal angle of the EM cluster at EM3 layer.

The NN is trained using diphoton and dijet Monte Carlo (MC) samples and its performance is verified using a data sample of  $Z \rightarrow \ell^+ \ell^- \gamma$  ( $\ell = e, \mu$ ) events (see Fig. 3.6). Fig. 3.7 compares the NN output ( $O_{NN}$ ) spectrum for photons and jets. If photon candidates are required to have  $O_{NN} > 0.1$ , which is  $\sim 98\%$  efficient for real photons and rejects  $\sim 50\%$  of misidentified jets.

### 3.4 Separation of electrons and photons

A photon can be rejected if there is a track pointing to its calorimeter cluster. There are two possibilities for this to happen: 1) the photon has converted in the inner tracker causing a reconstructed track, the probability is about  $5.9\% \pm 0.2\%$ ; 2) the photon is overlaid with a random track from underlying events, the average probability is about  $0.05\%$ .

To reject the electron background, a spatial track match  $\chi_{trk}^2$  probability ( $p_{trk}$ ) is defined using both the track and calorimeter information.

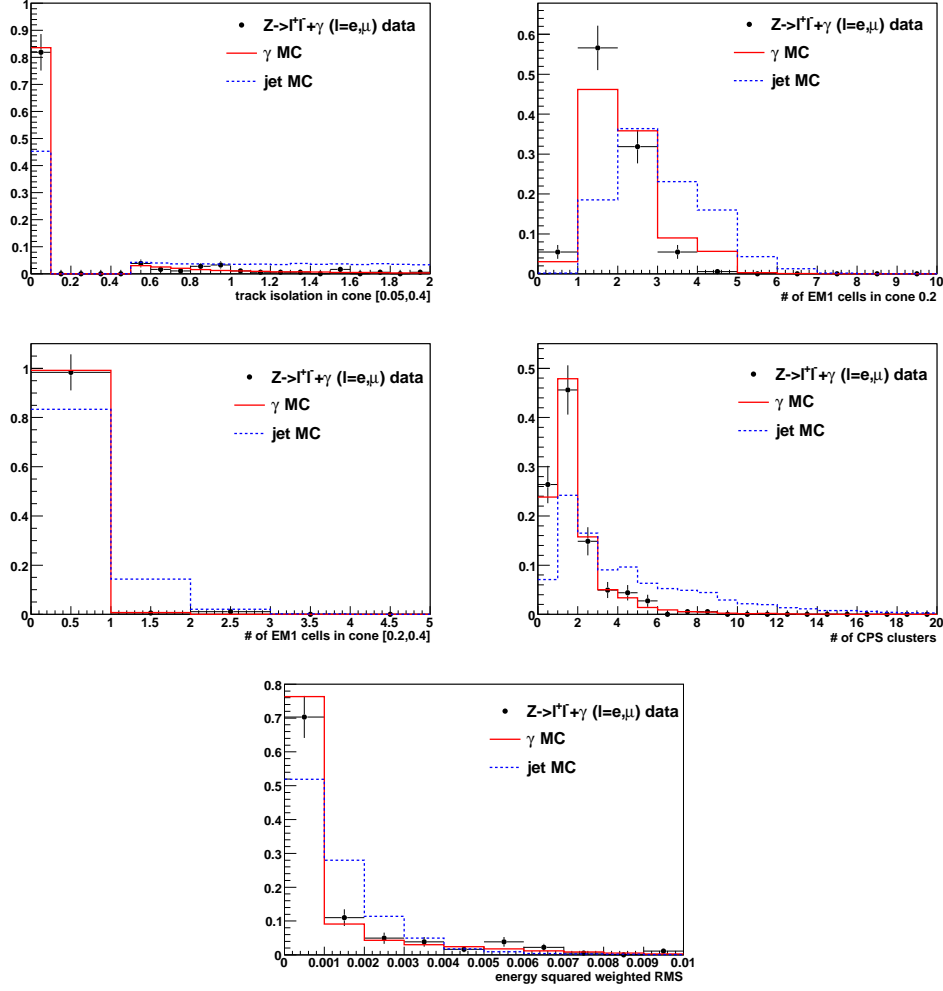


**Figure 3.5** Normalized  $O_{NN}$  input variables for photons and jets.

$$\chi_{trk}^2 = \left(\frac{\Delta\eta}{\sigma_\eta}\right)^2 + \left(\frac{\Delta\phi}{\sigma_\phi}\right)^2, \quad (3.4)$$

where  $\Delta\eta$  and  $\Delta\phi$  are the differences between the track position and the EM cluster position in the calorimeter. The  $\sigma_\eta$  and  $\sigma_\phi$  are the tracking resolution in  $\eta$  and  $\phi$ , respectively. The default value for  $p_{trk}$  is  $-1$ , which means there is no track found for matching. And we usually require  $p_{trk} < 0$  for photons.

However,  $p_{trk}$  is not perfect, due to the track inefficiency, especially during the high luminosity environment. There is still

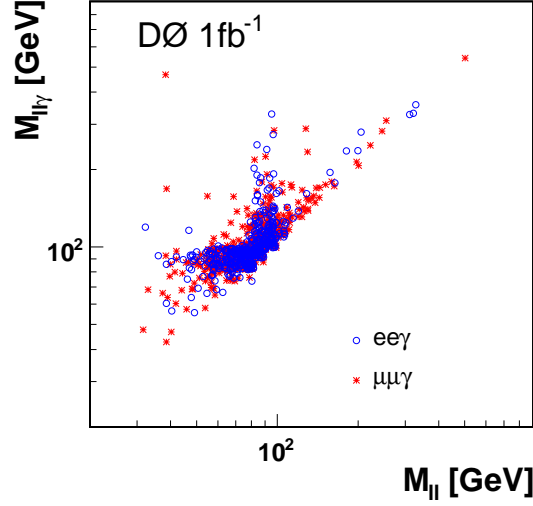


**Figure 3.6** The three-body (di-lepton+ $\gamma$ ) mass versus the two-body (di-lepton) mass from  $Z \rightarrow \ell^+ \ell^- \gamma$  ( $\ell = e, \mu$ ) data events<sup>[30]</sup>. To pick up the pure FSR  $\gamma$  candidates, the two-body mass is required to be less than 82 GeV while simultaneously the three-body mass is required to be within 82 - 102 GeV.

8  $\sim$  10 % electron does not have a track, to reduce such fake electron further, a "hits along the road" discriminant ( $D_{hor}$ ) is defined. As shown in Fig. 3.8, for each EM object, a road is defined by using primary vertex of the event and either the CPS cluster's coordinates if matched with a CPS cluster or EM cluster's coordinates of the EM3 calorimeter. Considering the charge of the electrons, two roads (left and right roads) are defined, the number of fired CFT fibers and SMT pixels are counted within  $4\sigma$  from the road.  $D_{hor}$  is calculated with considering such recorded hits ( $N_{hits}$ ) information along the road:

$$D_{hor} = \frac{P_e(N_{hits})}{P_e(N_{hits}) + P_\gamma(N_{hits})}, \quad (3.5)$$

where  $P_e$  and  $P_\gamma$  are the probabilities for an EM object to be a electron or photon:

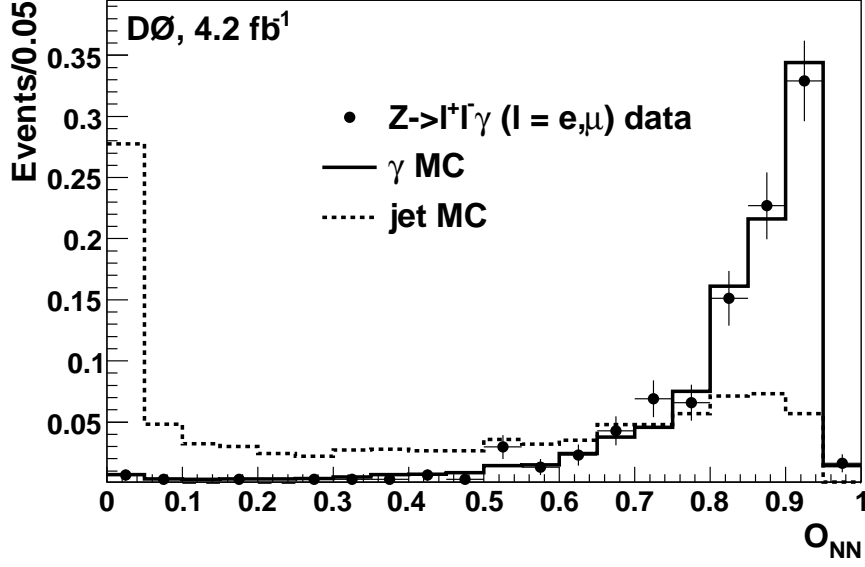


**Figure 3.7** Normalized  $O_{NN}$  spectrum for photons and jets.

$$P_e(N_{hits}) = \frac{\sum_{i=0}^{N_{hits}} (N_{hits}^e(i))}{\sum_{i=0}^{24} (N_{hits}^e(i))}; \quad (3.6)$$

$$P_\gamma(N_{hits}) = \frac{\sum_{i=N_{hits}}^{24} (N_{hits}^\gamma(i))}{\sum_{i=0}^{24} (N_{hits}^\gamma(i))}, \quad (3.7)$$

where  $N_{hits}^e$  and  $N_{hits}^\gamma$  are the distributions for the total number of fired CFT fibers and SMT pixels. The maximum fired hits are 24 since 16 CFT fibers and 8 SMT pixels are used for the study.

This variable is well modelled by the MC simulation, and help to reduce the electron faking per photon rate by a factor of 4.

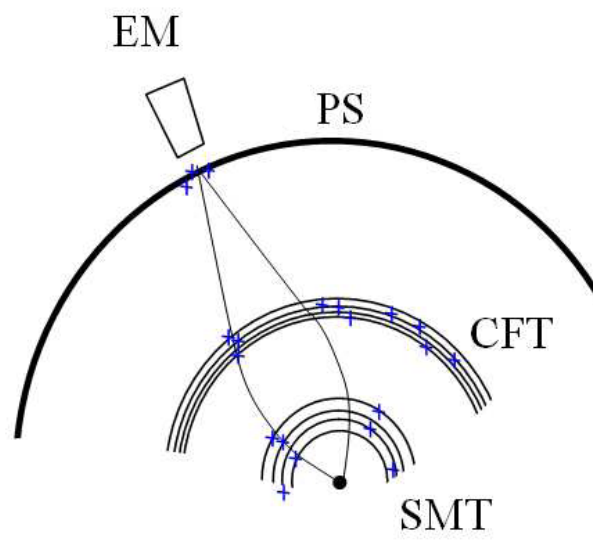


**Figure 3.8** Hits along the road.



### 3.5 Photon ID efficiency

As discussed in the above sections, the photon ID could be split to three major parts:

- general calorimeter based cuts, which are defined with mainly using the EM shower activity, where we expect the photon and electron would have the similar performance. Thus the difference between the data and MC simulation is calibrated with using  $Z \rightarrow ee$  events.
- no-track matching cut, which is mainly used to separate the electron and photon, the difference between the data and MC simulation is calibrated with using  $Z \rightarrow l^+l^- + \gamma (l = e, \mu)$  ( $Z\gamma$ ) events.
- photon  $O_{NN}$  cut, which is mainly used to further reduce the jet misidentification, the corresponding difference between the data and MC is calibrated with using both  $Z \rightarrow ee$  and  $Z\gamma$  events.

#### 3.5.1 General ID efficiency

Since electrons and photons have similar shower development in the calorimeter and we don't have enough statistics of  $Z\gamma$  events, we use  $Z \rightarrow ee$  events in data and the MC simulation to measure the relative data/MC scale factor (SF) of electron selection efficiencies, and use that to correct photon efficiencies in MC simulation.

The well-known tag-and-probe method (see Fig. 3.9) has been used on both  $Z \rightarrow ee$  data and MC to measure the general

ID efficiency, where the tag electron is selected with using very tight electron ID cuts with a good associated track, in the opposite azimuthal direction a probe track is selected within the 80 – 100 GeV Z mass window as the electron candidates. The general ID efficiency for these electron candidates to pass the  $f_{EM} > 0.97$ ,  $f_{iso} < 0.07$ ,  $sigphi < 18$  and  $p_{T\text{trk}}^{\text{sum}} < 1.5$  GeV are shown in Fig. 3.10.

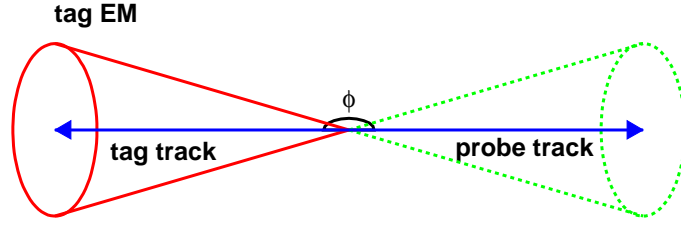


**Figure 3.9** Tag-and-probe method used to measure the general ID efficiency.

The efficiencies for these selections are in very good agreement between data and MC simulation with SF close to unity and without a visible dependence on  $E_T$  or  $\eta_{det}$ . A 1.0% systematic uncertainty is assigned to cover most points of SF around unity within  $1\sigma$  statistical deviation.

### 3.5.2 No-track matching efficiency

#### (1) Photon "no-track matching" efficiency

A photon can be rejected if there is a track pointing to its calorimeter cluster. There are two possibilities for this to happen: 1) the photon has converted in the inner tracker causing a reconstructed track, the probability is about  $5.9\% \pm 0.2\%$ <sup>[9]</sup>; 2) the photon is overlaid with a random track from underlying

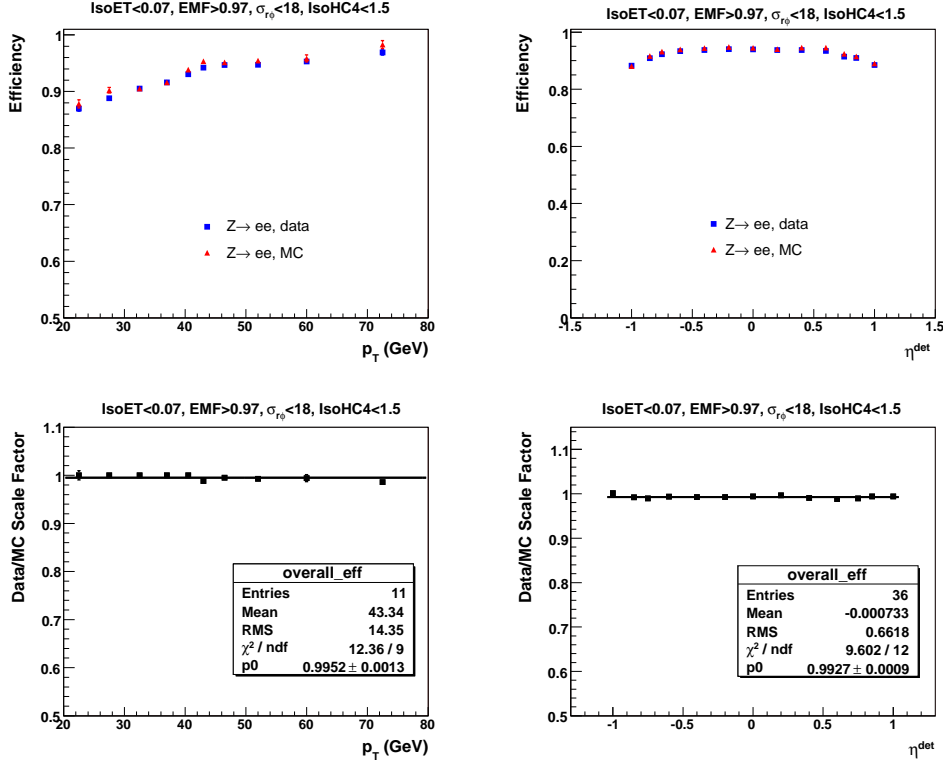


**Figure 3.10** The general ID efficiency by cuts  $f_{EM} > 0.97$ ,  $f_{iso} < 0.07$ ,  $sigphi < 18$  and  $p_{Trk}^{sum} < 1.5$  GeV as a function of electron  $E_T$  and  $\eta_{det}$ . The bottom plots show the ratio of the efficiencies in data and MC simulation ( $\epsilon_{data}/\epsilon_{MC}$ ), a.k.a the scale factor.

events, the probability is about 0.05%<sup>[9]</sup>. We select  $Z \rightarrow \mu\mu\gamma$  data events to measure the “no-track matching” ( $P_{trkm} < 0$  and  $D_{hor} < 0.9$ ) efficiencies. The “no-track matching” efficiency measured from the  $Z \rightarrow \mu\mu\gamma$  data is  $0.895 \pm 0.020$ . The corresponding efficiency measured from MC ( $e$  and  $\mu$  channels) is  $\epsilon^{MC} = 0.903 \pm 0.001(stat)$ . The data/MC scale factor (SF) is thus defined as

$$SF = \frac{0.895}{0.903} = 0.991 \pm 0.020 \quad (3.8)$$

A 2.0% systematic uncertainties is used to take into account the statistical uncertainty on the efficiency measured in data. More details on the efficiency studies using  $Z \rightarrow \mu\mu\gamma$  data and MC can

be found in Ref. [30].

## (2) Electron track match inefficiency

The contribution of Drell-Yan events is estimated from the full MC simulation. We need to measure the electron track match inefficiency in both data and MC simulation so that we can correct the full MC predictions using  $Z \rightarrow ee$  events. The electron track match inefficiency is determined using the tag-and-probe method (see Fig. 3.11) and is defined as the fraction of probe electron candidates that have  $P_{trk} < 0$  and  $D_{hor} < 0.9$ . Fig. 3.12 shows the corresponding results for the inefficiency and data/MC SF vs.  $\phi_{det}$ , on which it has the largest dependence. A 15.0% systematic uncertainty is used to cover most points of SF within  $1\sigma$  statistical deviation.

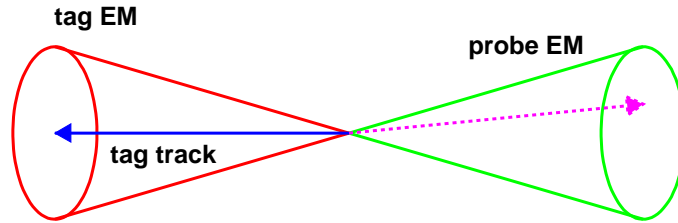


**Figure 3.11** Tag-and-probe method used to measure the electron track match inefficiency. This is different with the one used to measure the general ID efficiency (Fig. 3.9), here the EM cluster in the opposite azimuthal side to the tag electron (instead of a track) is selected as the electron candidates.

### 3.5.3 $O_{NN}$ efficiency

#### (1) $O_{NN} > 0.3$ efficiency

The photon ANN output value  $O_{NN}$  is an essential variable in this thesis. We use  $O_{NN} > 0.3$  in the event selection as a

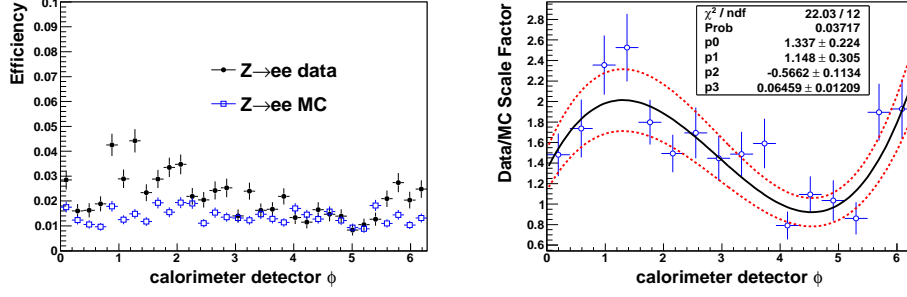


**Figure 3.12** Electron track match inefficiency ( $P_{trkm} < 0$  and  $D_{hor} < 0.9$ ) as a function of  $\phi_{det}$  (left plot) for the electron candidates. Right plot shows the scale factor between data and MC.

final  $\gamma$  ID cut to reduce large fraction of the background events while keeping about 98% signal efficiency for the DPP cross section measurement. Fig. 3.13 shows the  $O_{NN} > 0.3$  selection efficiency as a function of  $E_T$  in the three samples:  $Z\gamma$  MC and data, and DPP MC. The corresponding average efficiencies are shown in Table 3.2.

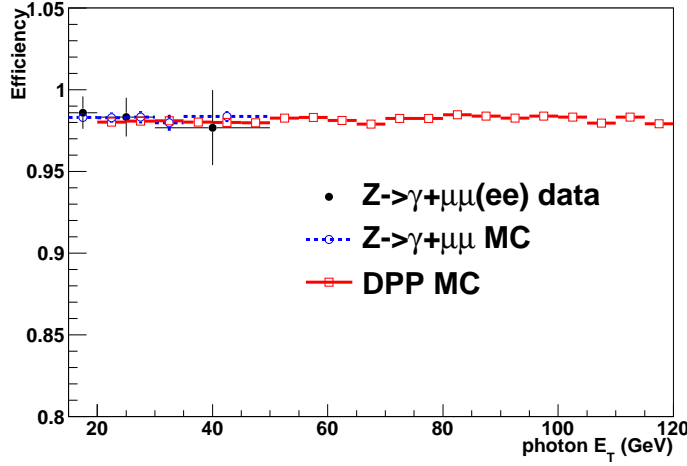


**Figure 3.13**  $O_{NN} > 0.3$  selection efficiency as a function of  $E_T$  for photons.

Samples	mean efficiency
DPP pythia MC	$0.981 \pm 0.001$
$Z \rightarrow \mu\mu(ee)\gamma$ data	$0.984 \pm 0.007$
$Z \rightarrow \mu\mu\gamma$ MC	$0.983 \pm 0.002$

**Table 3.2** The average  $O_{NN} > 0.3$  selection efficiencies for photons in different samples.

We also measure the  $O_{NN} > 0.3$  efficiency from  $Z \rightarrow ee$  data and MC events, and then use the corresponding scale factors ( $0.994 \pm 0.015$ ) on the diphoton MC events. Fig. 3.14 shows the corresponding results.

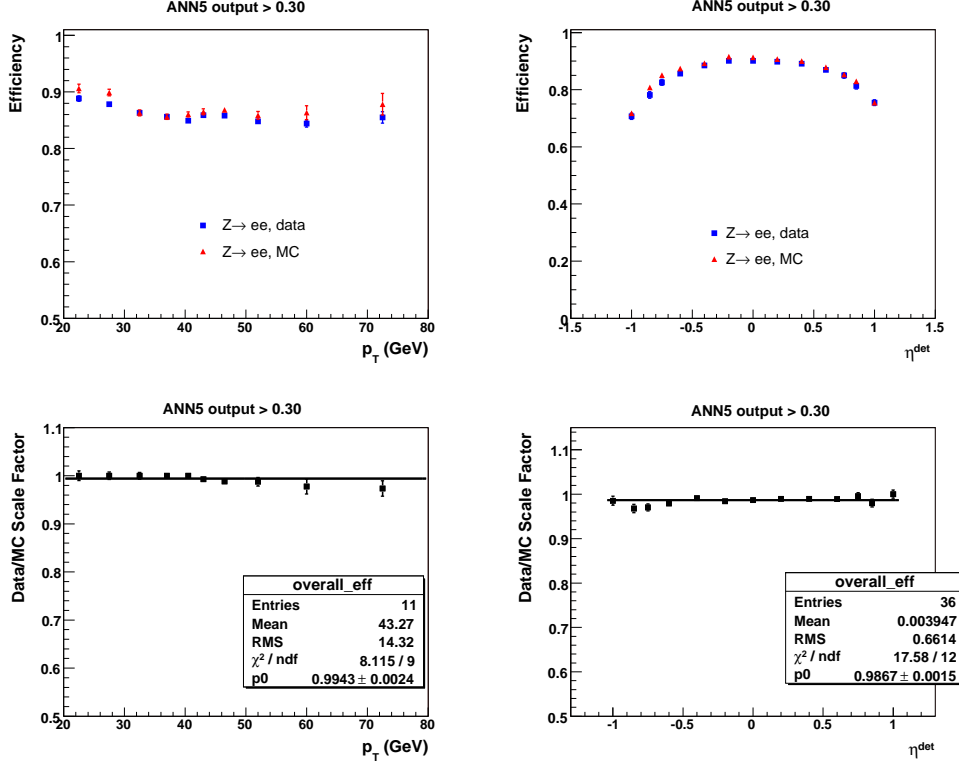


**Figure 3.14** Electron selection efficiencies (top plots) and data/MC scale factors (bottom plots) w.r.t.  $O_{NN} > 0.3$  as a function of  $\eta_{det}$  and  $p_T$ .

## (2) $O_{NN} > 0.6$ efficiency

After application of all the photon ID cuts (including  $O_{NN} > 0.3$ ), we use the criterion  $O_{NN} > 0.6$  as a boundary to estimate and then subtract the background contribution using the  $4 \times 4$  matrix method (described in Section 4.3.2).

Fig. 3.15 shows the efficiencies for the photons that have passed all the photon ID selections (including  $O_{NN} > 0.3$  criterion) to also pass the  $O_{NN} > 0.6$  cut as a function of  $E_T$ , detector  $\eta$ , detector  $\phi$  and instantaneous luminosity. Table 3.3 shows the corresponding average values.

Analogous results for the rate of real jets to fake photons in data and MC are shown in Table 3.4. The jet data is selected from the jet-enriched data using the tag-and-probe method: At first, we select a tag jet, reconstructed with using "DØ RunII cone algorithm"<sup>[31]</sup>, with  $p_T > 20$  GeV and  $|\eta| < 2.5$  in the events. Then the EM candidate at the opposite side in the azimuthal plane ( $\Delta\phi(EM, j) > 2.5$  rad) that pass the event selection described in Section 5.3.1 or 4.2 are used as the probe to study the  $O_{NN} > 0.60(0.75)$  efficiency. To reduce the possible contamination from the  $Z(ee) + jet$  events, we reject events that have two EM clusters with  $E_T > 15$  GeV or the invariant mass between the EM cluster and one good track ( $p_T > 15$  GeV and at least 5 CFT hits) within  $60 < M_{EMtrk} < 120$  GeV. To reduce the contamination from  $W(e\nu) + jet$  events, we reject events that have missing transverse energy  $> 10$  GeV. Thus, the selected jet+EM events are either jet+jet or jet+ $\gamma$  events.

To reduce photon admixture, at least one track around the EM candidate inside  $\Delta R < 0.05$  ( $N_{trks}^{\Delta R < 0.05} \geq 1$ ) is required (see Fig. 3.16) or the tail of the isolation region ( $0.07 < f_{iso} < 0.10$ ) (see Fig. 3.17) is chosen. The data samples in the regions of  $N_{trks}^{\Delta R < 0.05} \geq 1$  and  $0.07 < f_{iso} < 0.10$  are used to estimate the rate for a real jet to pass the  $O_{NN} > 0.6$  cut. Fig. 3.18 shows the  $O_{NN}$  distributions for the jet data and MC in these two regions.

The efficiencies in Table 3.4 (for both jet data and MC) are shown for the particular regions of  $N_{trks}^{\Delta R < 0.05} \geq 1$  and  $0.07 < f_{iso} < 0.10$ , where the real  $\gamma$  contamination for the jet data should be minimal due to inverted  $N_{trks}^{\Delta R < 0.05}$  and  $f_{iso}$  cuts.

Samples	mean efficiency
DPP pythia MC	$0.938 \pm 0.001$
$Z \rightarrow \mu\mu(ee)\gamma$ data	$0.940 \pm 0.014$
$Z \rightarrow \mu\mu\gamma$ MC	$0.957 \pm 0.002$

**Table 3.3** The average  $O_{NN} > 0.6$  selection efficiencies for photons in different samples.

jet MC ( $N_{trks}^{\Delta R < 0.05} \geq 1$ )	$0.621 \pm 0.020$
jet data ( $N_{trks}^{\Delta R < 0.05} \geq 1$ )	$0.684 \pm 0.035$
jet MC ( $0.07 < f_{iso} < 0.10$ )	$0.642 \pm 0.022$
jet data ( $0.07 < f_{iso} < 0.10$ )	$0.695 \pm 0.017$

**Table 3.4** The average  $O_{NN} > 0.6$  selection efficiencies for jet data and MC.

Due to a fair agreement between jets in data and MC we use the jet MC samples to estimate the  $O_{NN} > 0.6$  selection efficiency. We also use photons from the PYTHIA DPP whose efficiencies are corrected by the SF determined from  $Z \rightarrow ee$  data and MC events. Those SFs are shown at the bottom plots of Fig. 3.19. While SF vs.  $E_T$  is flat, one can see some slight parabolic



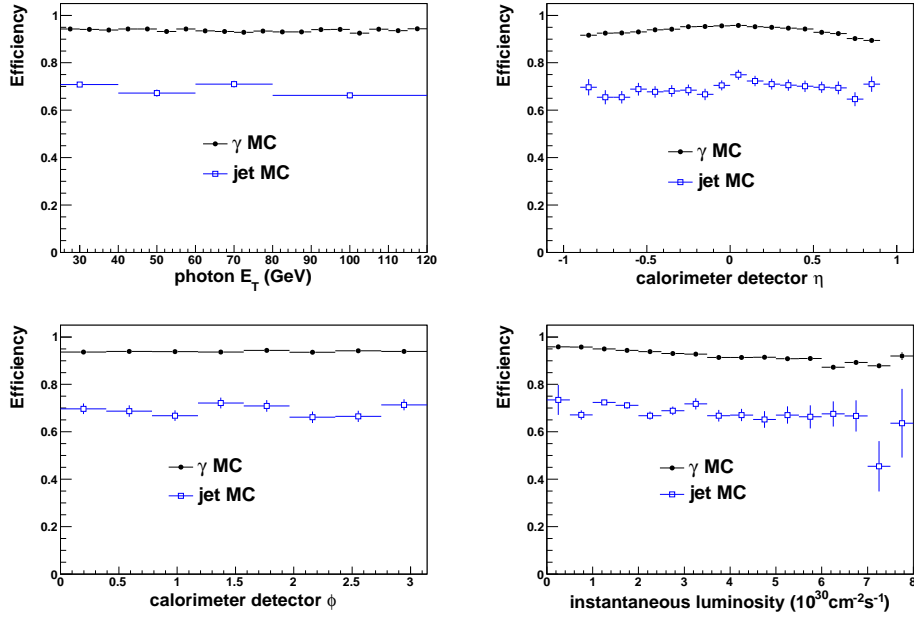


**Figure 3.15**  $O_{NN} > 0.6$  selection efficiency as a function of  $E_T$ (top-left), detector  $\eta$ (top-right), detector  $\phi$ (bottom-left) and instantaneous luminosity(bottom-right) for photon candidates from DPP and di-jet MC samples.

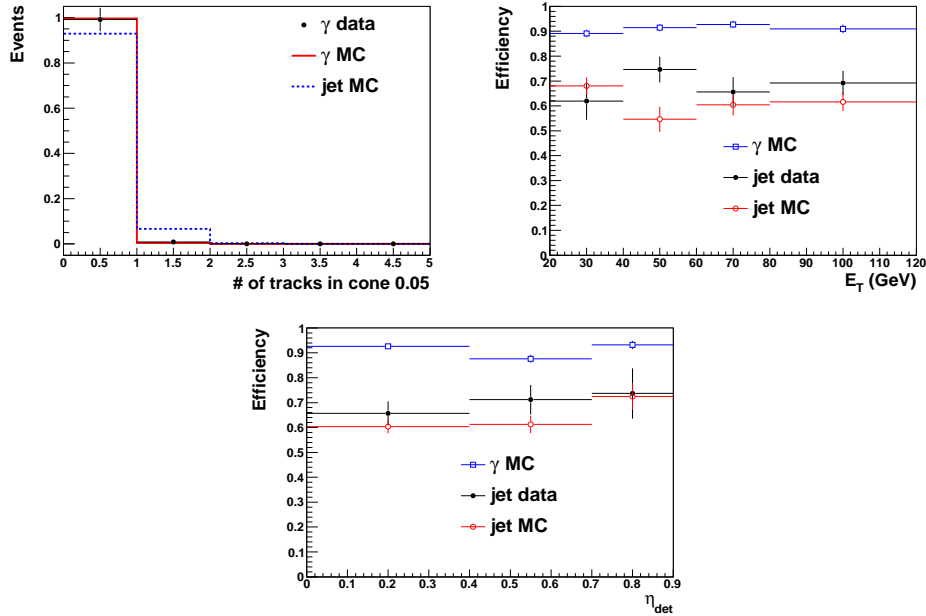


**Figure 3.16** Top-left plot shows the normalized distributions of number of tracks in  $\Delta R < 0.05$  ( $N_{trks}^{\Delta R < 0.05}$ ) for the photon candidates. Top-right and bottom plots show the  $O_{NN} > 0.6$  selection efficiency as a function of  $E_T$  and  $\eta_{det}$  after requiring  $N_{trks}^{\Delta R < 0.05} \geq 1$ .

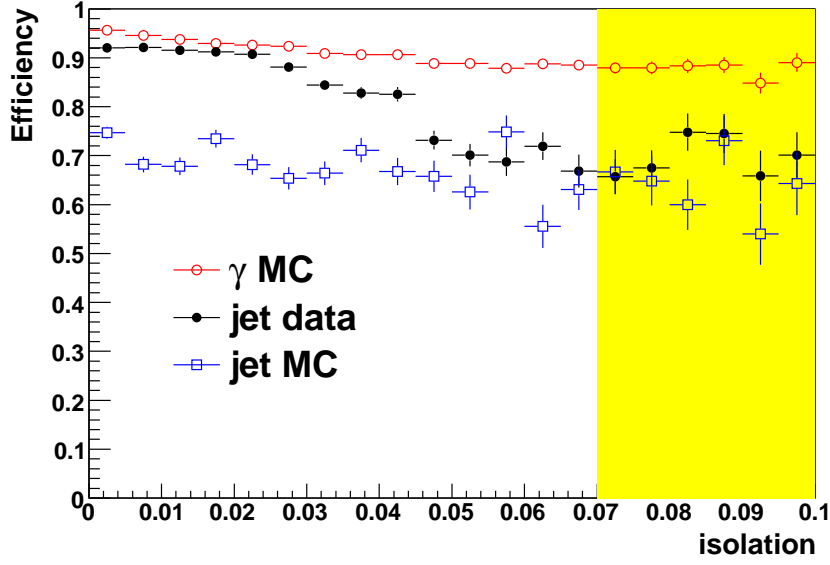


**Figure 3.17** The  $O_{NN} > 0.6$  selection efficiency as a function of  $f_{iso}$  (isolation) from jets in data and MC.

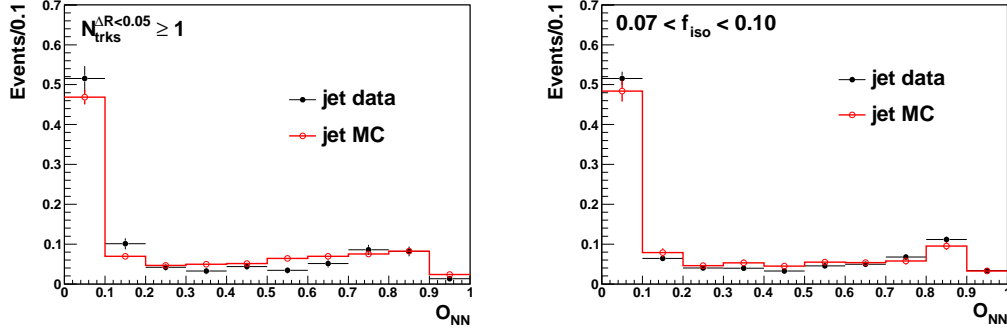


**Figure 3.18** Normalized  $O_{NN}$  distributions from jet data and MC in the regions of  $N^{\Delta R < 0.05}_{trks} \geq 1$  (left) and  $0.07 < f_{iso} < 0.10$  (right).

shape vs.  $\eta_{det}$ . In Fig. 3.20 we also compare SFs obtained from  $Z \rightarrow ee$  and  $Z \rightarrow l^+l^-\gamma$ , ( $l = e, \mu$ ) events in data and MC vs.  $\eta_{det}$ . We see that additional 1.5% correction is required to tune the electron to photon SFs.

We parameterize the photon and jet  $O_{NN} > 0.6$  efficiencies as a function of  $\eta_{det}$  to take into account a noticeable  $\eta$  ( $\eta_{det}$ ) dependence of those efficiencies. Fig. 3.21 shows the corresponding

results. The efficiencies are estimated as

$$\begin{aligned}\varepsilon_{\gamma}^{O_{NN}>0.6}(\eta_{det}) &= p_0 * |\eta|^2 + p_1 \times (1.0 \pm 0.015) \\ \varepsilon_{jet}^{O_{NN}>0.6}(\eta_{det}) &= p_0 * |\eta|^2 + p_1 \times (1.0 \pm 0.10)\end{aligned}\quad (3.9)$$

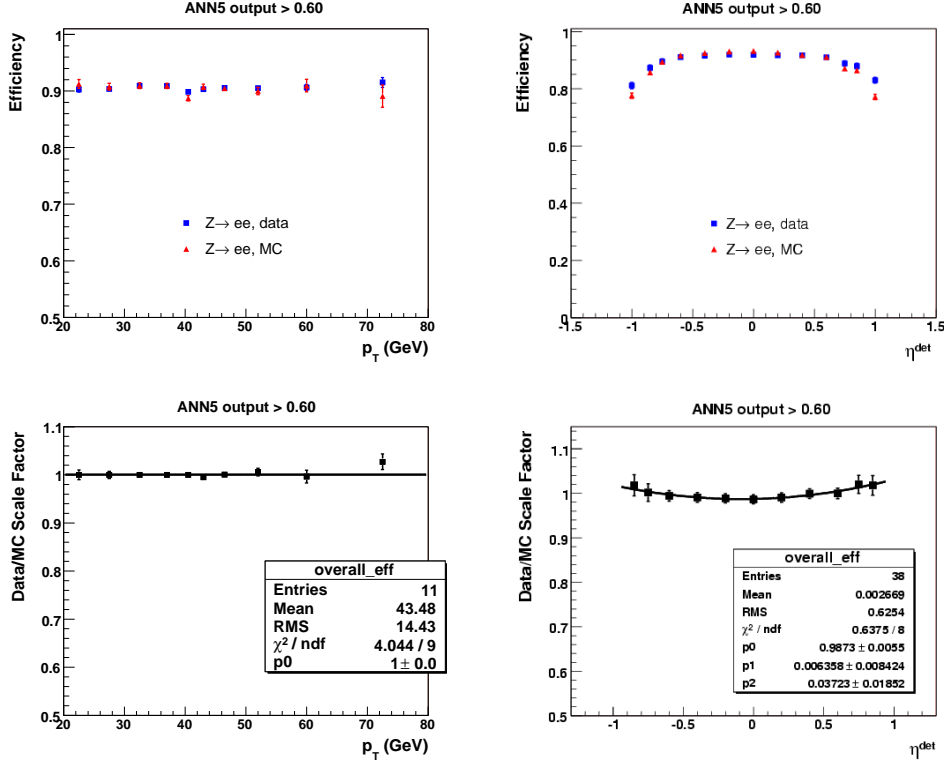


**Figure 3.19** Electron selection efficiencies (left) and data/MC scale factors (right plots) w.r.t.  $O_{NN} > 0.6$  as a function of  $\eta_{det}$  and  $p_T$ .

A 1.5% and 10% relative uncertainties have been assigned for the photon and jet  $O_{NN} > 0.6$  efficiencies respectively (see Tables 3.3 and 3.4). It is also worth mentioning that, as measured by the Ref.<sup>[9]</sup>, a difference of the  $O_{NN} > 0.6$  selection efficiencies between quark and gluon jets is within 2%, which is far less than the assigned 10% systematic uncertainty.

For the  $H \rightarrow \gamma\gamma$  search, we mainly do the search in the  $100 \leq M_H \leq 150$  GeV region, which are respect to the high  $p_T$  photons, so a looser  $O_{NN} > 0.1$  cut is chosen for the final

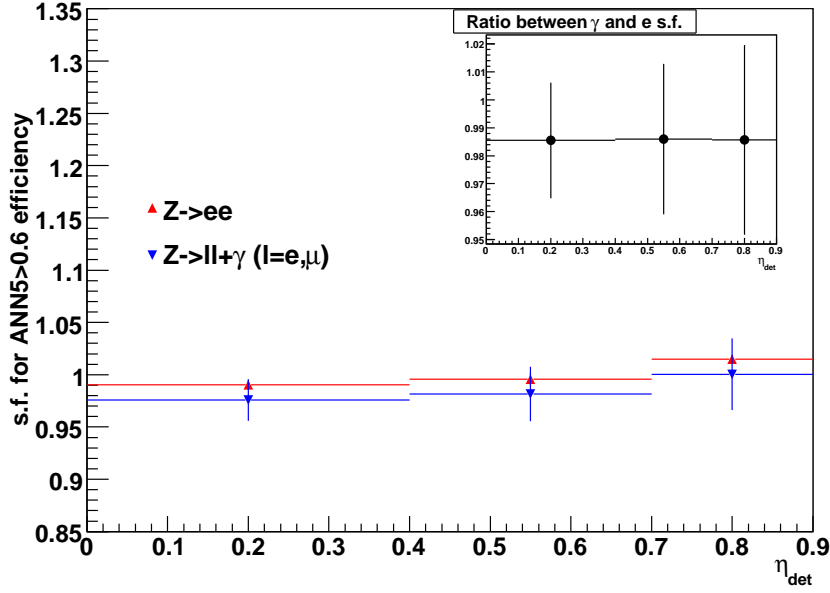


**Figure 3.20** The electron and photon based SFs for  $O_{NN} > 0.6$  obtained from  $Z \rightarrow ee$  and  $Z \rightarrow ll + \gamma (l = e, \mu)$  events in data and MC vs.  $\eta_{det}$ .

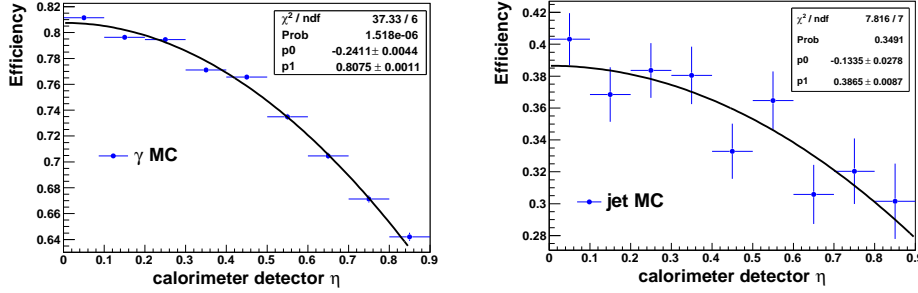


**Figure 3.21**  $O_{NN} > 0.6$  selection efficiency as a function of  $\eta_{det}$  for photons from DPP (left) and fakes from jet (right) MC samples.

$\gamma$  ID cut to maintain higher acceptance. Corresponding, further  $O_{NN} > 0.75$  is chosen as the operating point for the background subtraction, with achieving the smallest statistical uncertainties for the  $4 \times 4$  background subtraction. All relative efficiencies and scale factors are measured with using the same technical and samples discussed in the above, there is no visible  $p_T$  dependence, and final  $O_{NN} > 0.6$  efficiency is parameterized as a function of  $\eta_{det}$  for both signal and background. More details could be found in Ref.<sup>[9]</sup>.

### 3.6 Photon energy scale and resolution

At hadron collider, we do not have enough pure  $\gamma$  data events to do the precise energy calibration. However, both electrons and photons are the electromagnetic shower, and have very similar performance in the DØ uranium/liquid-argon sampling calorimeter. Thus, we could tune the energy scale/smearing parameters with using  $Z \rightarrow ee$  events to extensively calibrate the detector response to the energy of electrons. Then using the same parameters for the photons. However, the EM clusters have to travel through some dead material such as the inner detector, solenoidal magnet *et al.*, before reaching the calorimeter (see Fig. 3.22). The electrons would lose more energy in these dead material than photons, so the electron energy scale corrections effectively "overcorrect" the photon energies, thus further photon-to-electron energy scale uncertainty need be taken into account. For instance, a comparison of the reconstructed and particle-level electron/photon energies as a function of the reconstructed energy for different scenarios are studied to remove the overcorrection with using the MC samples<sup>[34]</sup>.

Generally, most MC samples used in this thesis are generated using pythia with CTEQ6L parton distribution functions (PDFs), and processed through a GEANT based<sup>[32]</sup> simulation of the DØ detector and the same reconstruction software as the data (full simulation). However, such full simulation need take a while to detailedly model the interaction between particles and detector material. Thus, modifications from precise tuning are limited,

and consequently the full MC simulation is not feasible to simulate the real detector to the precision needed by general precise measurement, especially the  $W$  mass measurement. So, instead of the full simulation, the parameterized fast MC simulation, also used for the  $DØ$   $W$  mass measurement<sup>[26]</sup>, is used for our DPP cross section measurement.

By comparison with the full MC simulation, there are several characteristic features for such fast MC simulation:

- better modeling of phi-mod (described in Section 2.2.3) efficiency and phi-mod shift around CC module boundary;
- better modeling of energy resolution dependence on electron/photon energy and incident angle;
- easier interface with other generators for systematic studies.

In the following of this section, the related electron/photon energy scale and resolution calibration with using full and fast MC simulation as well as data events will be discussed.

### 3.6.1 Energy loss correction

As shown in Fig. 3.22, there is about 3.7 radiation lengths ( $X_0$ ) from the beam line to the calorimeter. The electrons would lose energy in these material. Fig. 3.23 shows the average longitudinal energy profile of showers with two different incident angles for the  $E = 45$  GeV single electron full MC events. As we can see, the energy deposit in different longitudinal layers will be "shifted" visibly with increasing the amount of dead material. Thus more detailed study on the  $Z \rightarrow ee$  events is essential to

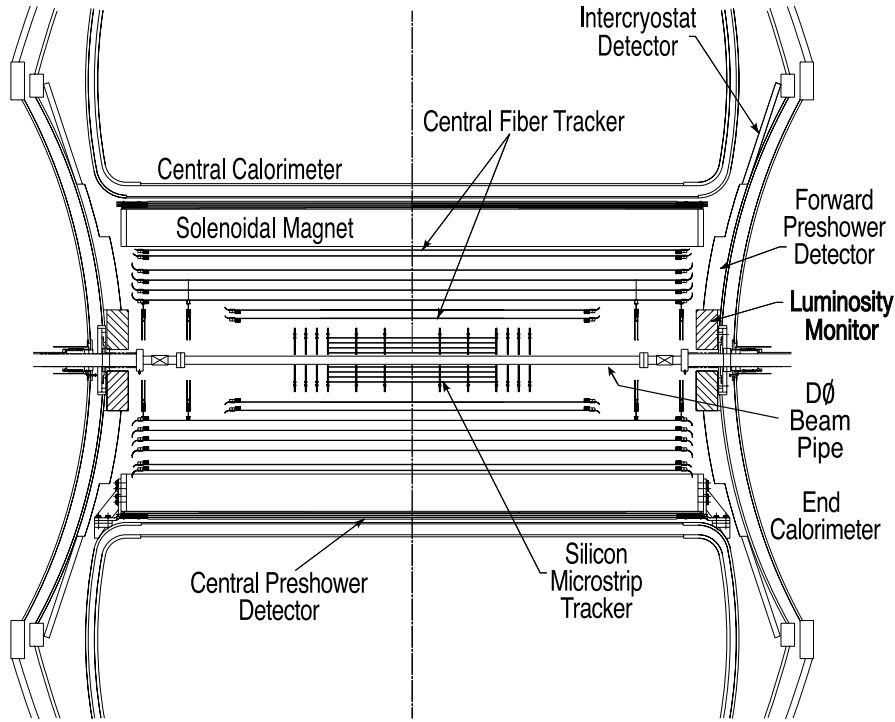


**Figure 3.22** Overview of the material in front of the Central Calorimeter. This drawing has been reproduced from Ref.<sup>[20]</sup> and shows a cross-sectional view of the central tracking system and in the  $x-z$  plane. Also shown are the locations of the solenoid, the preshower detectors, luminosity monitor and the calorimeters.

demonstrate if the full MC events could model the same amount of dead material as the data events have. Fig. 3.24 shows the EM energy fractions from  $Z \rightarrow ee$  data and MC events with splitting the  $Z$  samples to 10 different  $\eta$  regions, which demonstrates the amount of dead material is underestimated in the default detector simulation.

Some additional material need be added to the MC simulation to better model the data events. The relatively low- $Z$  material, copper, is added cylindrically inside the solenoid, which also has the same axis of rotational symmetry as the solenoid. The radiation lengths ( $nX_0$ ) of the additional copper is added to the MC

simulation, and the minimization of the  $\chi^2$  for the fit of the first 3 EM layers are performed (see Fig. 3.25). Also the fit is repeated separately for each of the three layers, the corresponding results (see Fig. 3.26) shows good agreement between the combined and separated fit. After adding the additional  $nX_0 = 0.1633$  copper before the CC calorimeter, the EM energy fractions from  $Z \rightarrow ee$  data and MC events are re-plotted in Fig. 3.27, which shows better agreement between the data and MC.

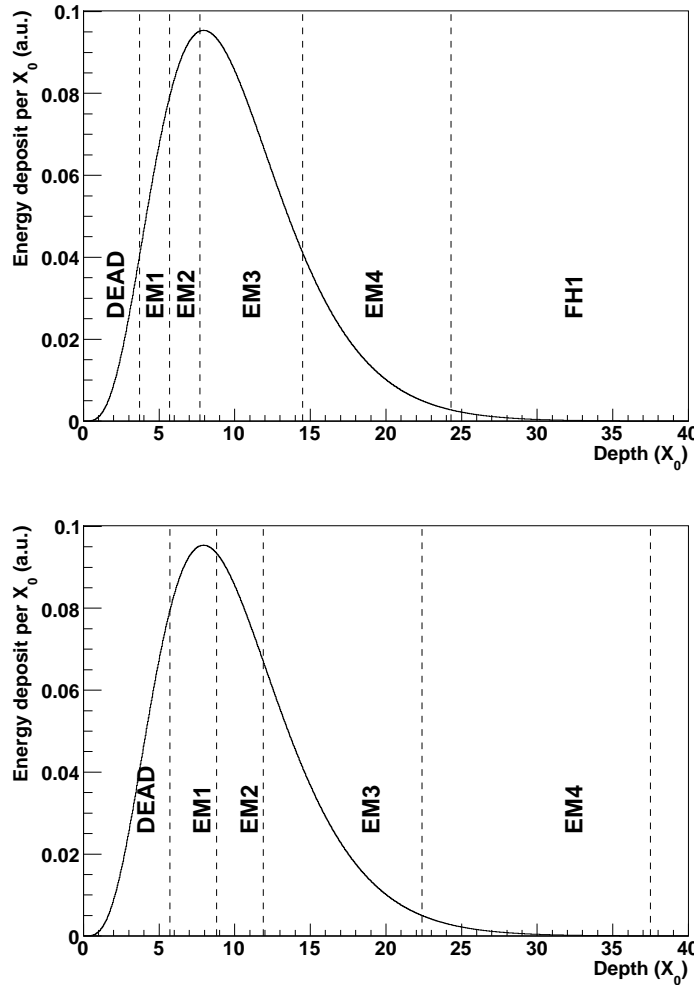


**Figure 3.23** Top: Average longitudinal profile of showers from  $E = 45$  GeV single electrons full MC events. Top: Assuming normal incidence, the position of the active parts of the CC are also indicated. Bottom: The same average shower profile, but this time the active parts of the CC are indicated for highly non-normal incidence (specifically  $\eta_{\text{phys}} = 1$ ).



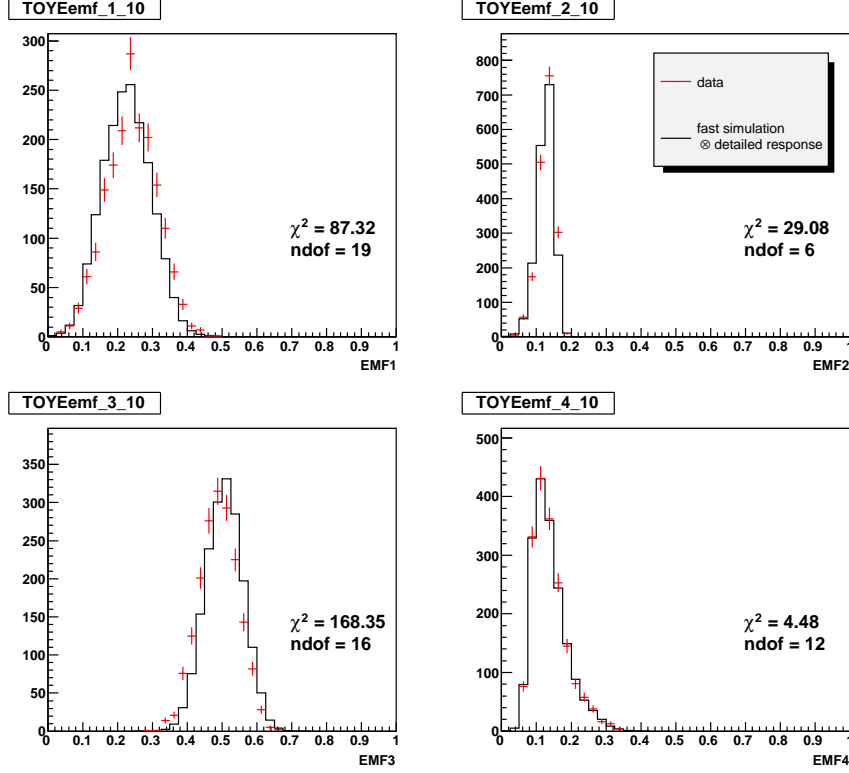


**Figure 3.24** EM energy fractions for electrons from  $Z \rightarrow ee$  events with using 10  $\eta$  regions for data and MC simulation. The four individual plots are respect to the four longitudinal EM layers. The detailed response simulation uses the same default amount of dead material as the full MC simulation.

### 3.6.2 Energy scale and offset

The energy response of the calorimeter to electrons is calibrated using  $Z \rightarrow ee$  events from data, and parameterized to the fast MC. In the fast MC, the observed electron energy ( $E_{obs.}$ ) is related to the true energy ( $E_{true}$ ) in the calorimeter by

$$E_{obs.} = \alpha \times E_{true} + \beta, \quad (3.10)$$

where  $\alpha$  is the scale and  $\beta$  is the offset<sup>[35]</sup>. A general non-linear term is not considered here, since it is mainly caused by the dead material which has already been dealt with by the energy loss correction. In case of small offsets when  $\beta \ll E_{obs.}(e_1) + E_{obs.}(e_2)$ ,

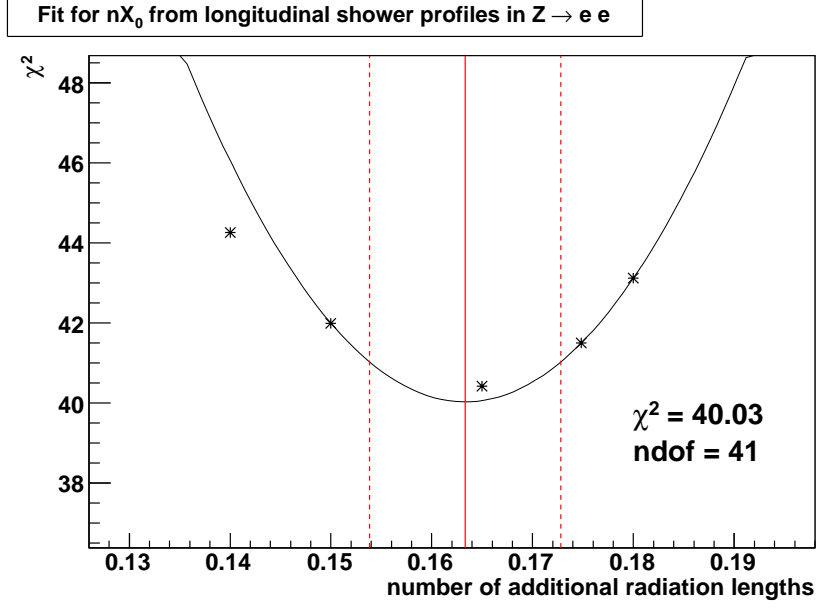


**Figure 3.25** Fit for  $nX_0$ , the amount of additional copper (in radiation lengths) missing from the nominal material map in the full MC simulation of the DØ detector. The five stars indicate the value of the combined  $\chi^2$  for EM1-EM3, evaluated for five values of  $nX_0$ . A parabola is fit through these points in order to determine the minimum of the combined  $\chi^2$ . Also shown in the figure are the value of the combined  $\chi^2$  at its minimum as well as the one-sigma variations of  $nX_0$ .

the observed  $Z$  mass ( $M_{obs.}(Z)$ ) can be related to the true values  $M_{true}(Z)$  as

$$M_{obs.}(Z) = \alpha M_{true}(Z) + \beta f_Z^{obs.} + \mathcal{O}(\beta^2), \quad (3.11)$$

where  $f_Z^{obs.}$  is a kinematic variable defined as:

$$f_Z^{obs.} = \frac{E_{obs.}(e_1) + E_{obs.}(e_2)}{M_{obs.}(Z)}(1 - \cos \theta), \quad (3.12)$$

where  $E_{obs.}(e_1)$  and  $E_{obs.}(e_2)$  are the observed energies of the two electrons, and  $\theta$  is the opening angle between the electrons. Thus it is possible to extract the scale and offset from the  $M_{obs.}(Z)$  vs.  $f_Z^{obs.}$  distributions. The scale and offset cannot be distinguished to the precision required using only the  $Z$  boson mass

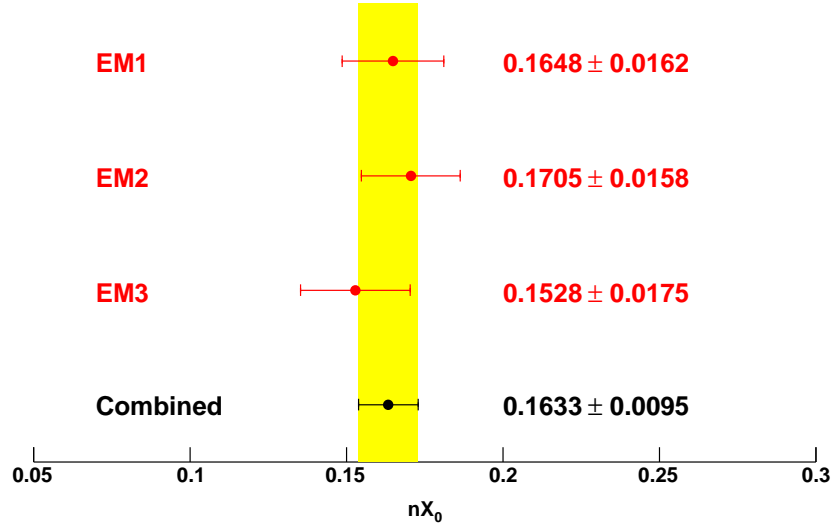


**Figure 3.26** Results of the fit for  $nX_0$ , performed separately for each of the three layers (EM1, EM2 and EM3), versus the combined fit on these 3 layers together.

distribution. So the fact that the two electrons from  $Z$  decays are not monochromatic is used as an additional constraint.

The  $Z \rightarrow ee$  data events is used to simultaneously fit for the scale and offset with the distribution of the  $Z$  boson mass as a function of energy. The fast MC templates are compared to the data for the  $M_{obs.}(Z)$  vs  $f_Z^{obs.}$  distributions via a binned likelihood fit to extract the best  $\alpha$  and  $\beta$  values. Fig. 3.28 shows the measured result of  $\alpha$  and  $\beta$ , which is highly anti-correlated. The fitted values are

$$\alpha = 1.0111 \pm 0.0043$$

$$\beta = -0.4036 \pm 0.2093 \text{ GeV},$$

with the correlation -0.997.

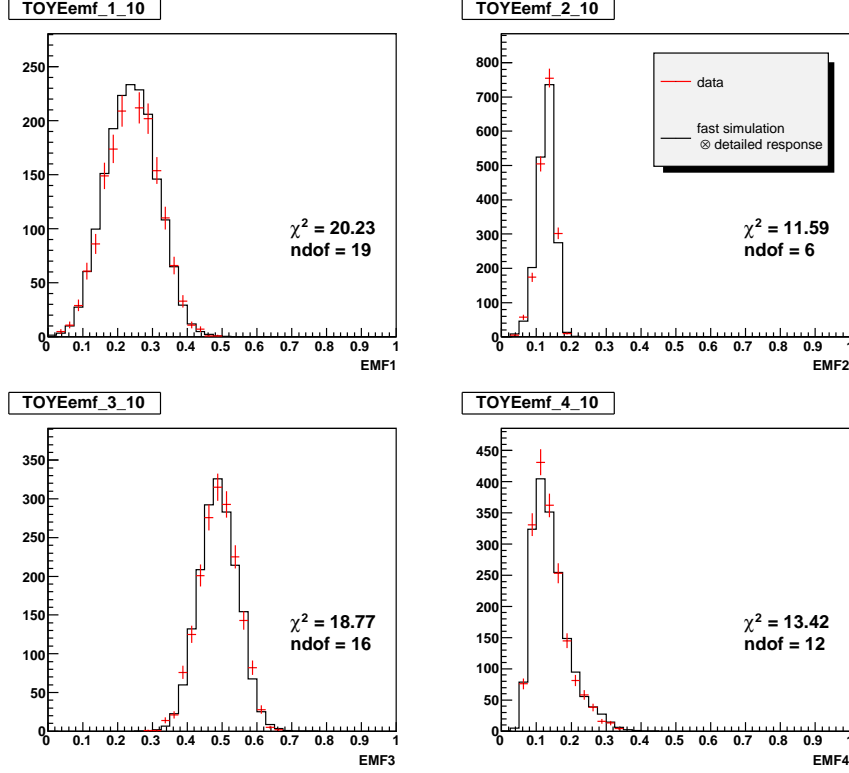


**Figure 3.27** EM energy fractions for electrons from  $Z \rightarrow ee$  events with using 10  $\eta$  regions for data and MC simulation after adding  $nX_0 = 0.1633$  copper before the CC calorimeter. The four individual plots are respect to the four longitudinal EM layers. The detailed response simulation uses the same default amount of dead material as the full MC simulation.

### 3.6.3 Energy resolution

The energy resolution of the calorimeter can be written as

$$\frac{\sigma_{EM}(E)}{E} = \sqrt{C_{EM}^2 + \frac{S_{EM}^2}{E} + \frac{N_{EM}^2}{E^2}} \quad (3.13)$$

with  $C$ ,  $S$  and  $N$  as the constant, sampling and noise terms respectively<sup>[36]</sup>. The constant term accounts for the non-uniformity of the calorimeter response. It has a constant effect on the fractional resolution, independent of the energy, and therefore is the dominant effect at high energies. The sampling term is due to the fluctuations related to the physical development of the shower,

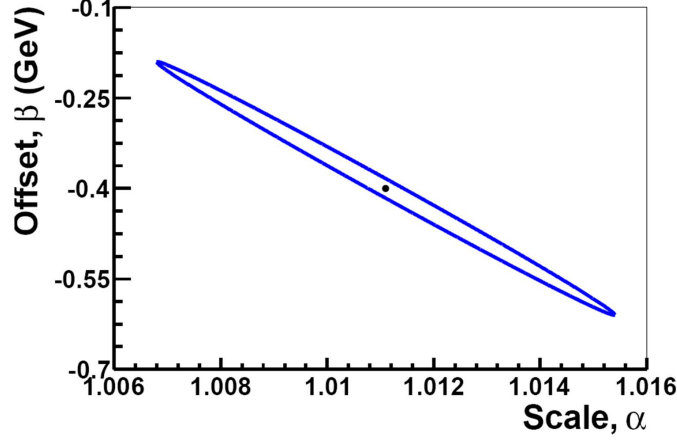


**Figure 3.28** The central value for  $\alpha$  and  $\beta$  as determined from the 2D  $M_{obs.}(Z)$  vs  $f_Z^{obs.}$  fit to the  $Z$  mass distribution and the error ellipse defined by  $\Delta\chi^2 = 1$ .

especially in sampling calorimeters where the energy deposited in the active medium fluctuates event by event because the active layers are interleaved with absorber layers. The noise term comes from the electronic noise of the readout system, radioactivity from the Uranium, and underlying events. Since the noise contribution is proportional to  $1/E$  and is basically negligible for the high energy electrons/photons.

Due to the large amount of material in front of the calorimeter,  $S_{EM}$  is no longer a constant and need to be parameterized as

$$S_{EM} = \left( S_1 + \frac{S_2}{\sqrt{E}} \right) \times \frac{e^{S_{exp}/\sin\theta}}{e^{S_{exp}}}$$

where

$$S_{exp} = S_3 - S_4/E - S_5^2/E^2$$

This formula and the constants  $S_i$ ,  $i = 1, \dots, 5$  were derived using the full MC with adding the additional dead material (Sec-

tion 3.6.1). The noise term was found to be 0.29 GeV, whose contribution, for the reason mentioned above, is negligible. The constant term is derived by a fit to the measured width of the  $Z \rightarrow ee$  peak. The fast MC templates are compared to the data with the  $Z$  mass distribution to extract the best value of the constant term<sup>[37]</sup>. The measured constant term is found to be

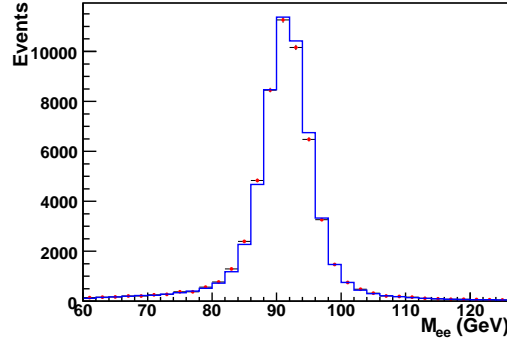
$$C_{EM} = (2.04 \pm 0.13)\%$$

#### 3.6.4 Photon energy scale correction

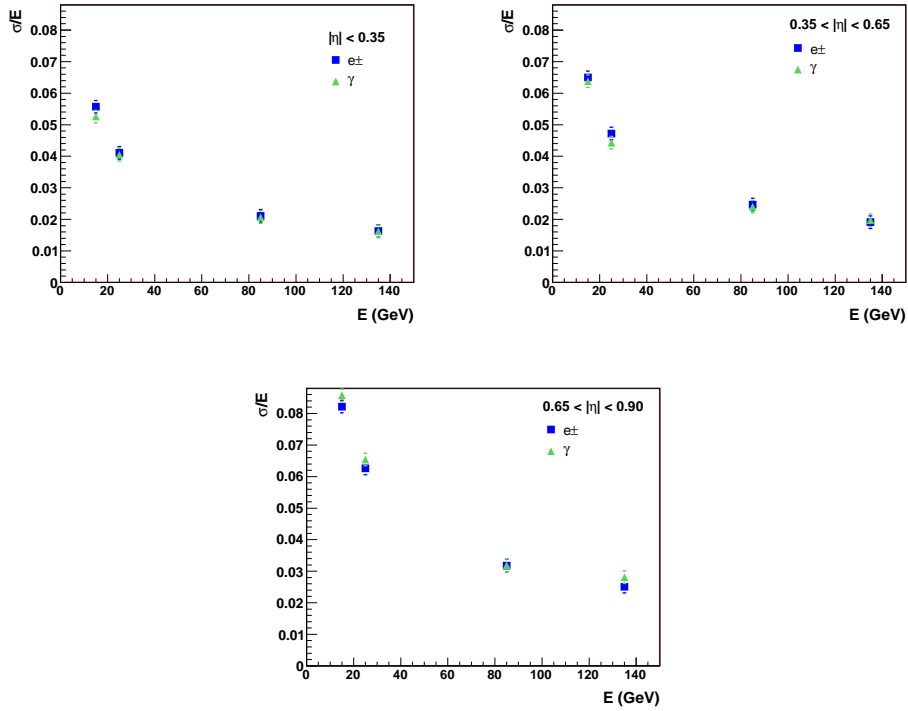
For the DPP cross section measurement, we have used the fast MC to measure the acceptance and the related systematics. As discussed at before, the energy scale and resolution are measured from electrons, and later directly applied on the photons. So at first we have to confirm that electron and photon energy resolutions are close to each other. For this aim, we used single electron and photon full MC events simulated with modified GEANT (slow MC) with added 0.17X0 of  $Cu$ , tuned by W mass measurement to reproduce the energy losses in data (Section 3.6.1). Those events are simulated with fixed energies  $E = 15, 25, 85$  and 135 GeV in the CC region with flat  $\eta$  distribution. We have calculated energy resolution in those four energy points in the three (physics)  $\eta$  intervals. Results are shown in Fig. 3.30. We can see that the  $e$  and  $\gamma$  resolutions are in a very good agreement with each other for all the cases and justifies the use of fast MC, tuned to the electron data, for photons.

Fig. 3.29 shows peak in  $Z \rightarrow ee$  events in data and fast

MC. One can see a good agreement between data and fast MC in description of the peak position and  $Z$ -peak width.



**Figure 3.29** Invariant mass distribution between data and fast MC simulation for  $Z \rightarrow ee$  events. Red points for data and blue histogram for fast MC simulation.



**Figure 3.30** Energy resolution for electrons and photons in the three  $\eta$  intervals.

However, as we know, due to a different nature of the interactions, the photons lose noticeably less energy in the dead material before the calorimeter than electrons. This fact leads to a systematic over-correction in the photon energy scale and would

yield a shift in the cross section<sup>[38]</sup>. The detailed comparison of the reconstructed and particle-level photon energies as a function of the reconstructed energy for three (physics)  $\eta$  intervals are studied to remove such over-correction with using the single photon slow MC events (see Fig. 3.31). As one can see, we should expect, on the average, about 2-2.5% over-estimation of the reconstructed photon energy in data at  $E^{reco} = 20$  GeV and  $< 1\%$  at  $E^{reco} > 40$  GeV. We took conservative systematic uncertainty for those corrections, equal to a half of those corrections.

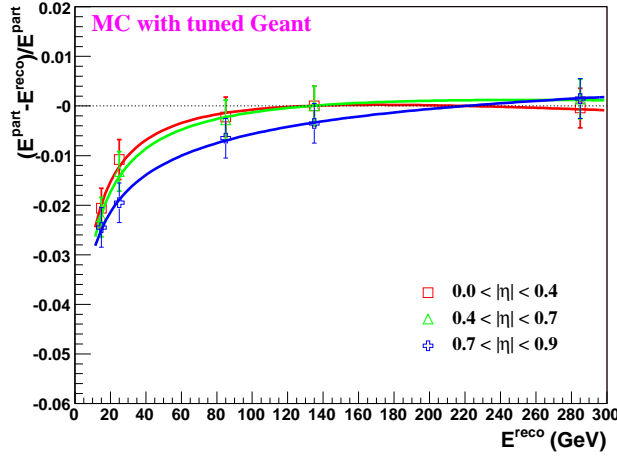


**Figure 3.31** Photon energy scale correction for the MC with tuned GEANT.

For  $H \rightarrow \gamma\gamma$  search, general full MC are used, since we mainly deal with the high energy ( $p_T > 50$  GeV) photons, where we would expect such photon-to-electron energy scale over-correction is negligible.



## Chapter 4 $H \rightarrow \gamma\gamma$ search

In the standard model (SM), the  $H \rightarrow \gamma\gamma$  branching ratio is very small. For instance, the branching ratio is about 0.22% for a Higgs boson with a mass of 130 GeV. However, in some models beyond the SM, the  $H \rightarrow \gamma\gamma$  branching ratio can be enhanced significantly<sup>[10]</sup>. The idea of the fermiophobic Higgs, which assumes zero couplings of the Higgs to the fermions, has been tested at LEP<sup>[39]</sup> and the Tevatron<sup>[40]</sup>. In this thesis, we examine the inclusive diphoton dataset ( $\gamma\gamma+X$ ) and search for high mass resonances. The SM Higgs is used as the signal model for reference, and this analysis is a forerunner to the leading low-mass Higgs analysis at the LHC<sup>[41,42]</sup>. There are several sizable sources of Higgs boson production within the SM (Section 1.2). In this thesis, gluon gluon fusion (GF), associated production (VH) and vector boson fusion (VBF) (see Figure 4.1) are taken into account, with corresponding cross sections as predicted by the SM<sup>[4–6]</sup>. The result of the search is interpreted as upper limits on the production cross section times the branching ratio ( $H \rightarrow \gamma\gamma$ ) relative to the SM prediction for different assumed Higgs masses. Later, the results is extended to the particular fermiophobic Higgs scenario.

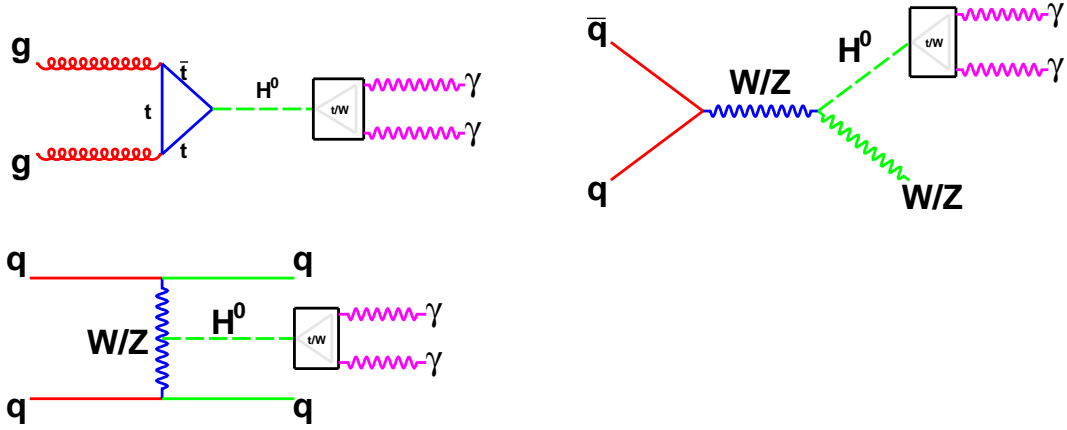


**Figure 4.1** Dominant SM Higgs production used in this analysis.

#### 4.1 Data and Monte Carlo samples

The data used in this analysis were collected by the DØ detector between July 2002 and December 2008 (see Fig. 4.2). We use events collected with using triggers requiring at least two clusters of energy in the EM calorimeter (calorimeter-only diem triggers). The total integrated luminosity of the sample is  $4.2 \pm 0.3 \text{ fb}^{-1}$  [43].

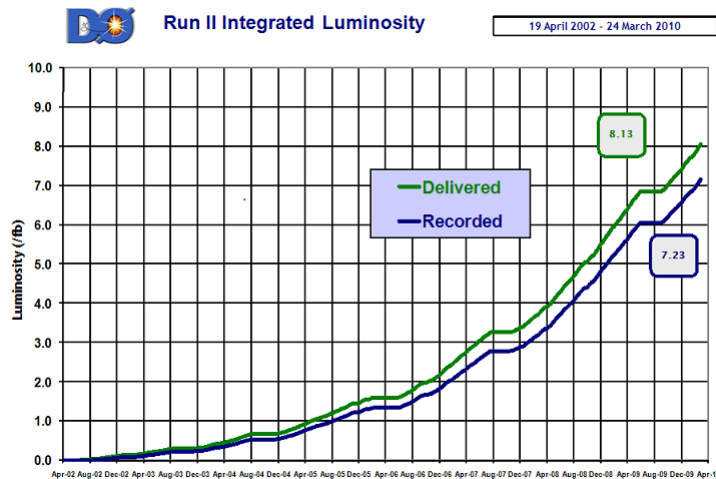


**Figure 4.2** DØ Run II integrated luminosity vs. time.

DØ trigger system has three distinct levels: L1/L2/L3. The first stage (L1) comprises a collection of hardware trigger ele-

ments that provide a trigger accept rate of about 2 kHz. In the second stage (L2), hardware engines and embedded microprocessors associated with specific subdetectors provide information to a global processor to construct a trigger decision based on individual objects as well as object correlations, which has an accept rate of approximately 1 kHz. Candidates passed by L1 and L2 are sent to a farm of Level 3 (L3) microprocessors with reducing the rate to about 50Hz.

There are 6 trigger lists: v8-11,v12,v13,v14,v15 and v16, used in this analysis, corresponding to the data taking period. Each trigger list is a combination of the L1, L2 and L3, with requiring at least two clusters of energy in the EM calorimeter with loose shower shape requirements and varying  $p_T$  thresholds between 15 GeV and 25 GeV. The corresponding trigger efficiency is measured from  $Z \rightarrow ee$  data events, and for v8-v14 is estimated to be 100% at a precision of 0.1% [44]. For v15 and v16 the trigger efficiency is found to be greater than 98% for a di-em invariant mass  $M_{ee} = 50$  GeV and increases to about 100% at  $M_{ee} = 90$  GeV. The dependence of the trigger efficiency on  $M_{ee}$  is shown in Figure 4.3 and parameterized as

$$\varepsilon_{trigger}^{v15,16}(M_{ee}) = 0.5 \cdot p_2 \cdot (1.0 + \text{TMath::Erf}((M_{ee} - p_0)/(\sqrt{2} \cdot p_1))) \quad (4.1)$$

where

$$p_0 = -16.39, \quad p_1 = 34.55, \quad p_2 = 0.9995 \quad (4.2)$$

All MC samples used in this analysis are generated using

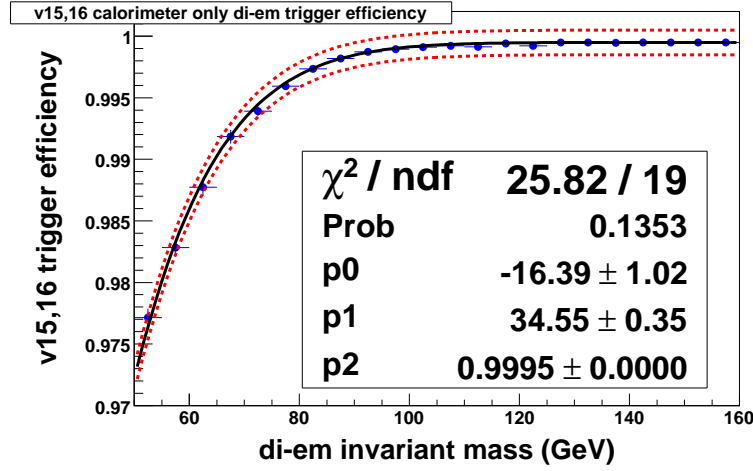


**Figure 4.3** V15 and v16 calorimeter-only di-em trigger efficiency as a function of di-em invariant mass, where the two dotted lines illustrate the assigned 0.1% uncertainty.

PYTHIA<sup>[13]</sup> with CTEQ6L<sup>[14]</sup> parton distribution functions (PDFs), and processed through a GEANT based<sup>[32]</sup> simulation of the DØ detector and the same reconstruction software as the data. Signal samples are generated separately for GF, VH and VBF production and normalized using the theoretical cross sections<sup>[45–47]</sup> and branching ratio predictions from HDECAY<sup>[7]</sup>. The SM Higgs samples are produced for different assumed masses. The corresponding cross section values of GF, VH and VBF are shown in Table 4.11. The natural width of the Higgs boson is negligible compared to the effect of the detector resolutions. The width of the reconstructed invariant mass distribution is dominated by the detector resolution and is about 3 GeV for a Higgs mass of 100 GeV.

mass (GeV)	GF(NNLO)	WH(NNLO)	ZH(NNLO)	VBF(NLO)	BR
100	1.723	0.2861	0.1668	0.0995	0.001531
105	1.516	0.2432	0.1431	0.0918	0.001718
110	1.339	0.2077	0.1233	0.0842	0.001901
115	1.188	0.1781	0.1067	0.0764	0.002064
120	1.058	0.1532	0.0926	0.0693	0.002187
125	0.946	0.1322	0.0806	0.0651	0.002246
130	0.847	0.1145	0.0704	0.0604	0.002229
135	0.762	0.0994	0.0616	0.0557	0.002124
140	0.688	0.0866	0.0541	0.0509	0.001943
145	0.622	0.0756	0.0476	0.0475	0.001693
150	0.563	0.0661	0.0420	0.0441	0.001394

**Table 4.1** Cross section(pb) and branching ratio(BR) for the signal samples. Signal with mass greater than 150 GeV is not considered due to its BR.

## 4.2 Event selection

In this analysis, events are selected by requiring at least two photon candidates with transverse momentum  $p_T > 25$  GeV and  $|\eta| < 1.1$ . Furthermore, the detailed cuts (Chapter 3) on these photon candidates are:

- EM energy fraction:  $f_{EM} > 0.97$
- Calorimeter isolation:  $f_{iso} < 0.10$
- Tracker isolation:  $p_{T\text{trk}}^{\text{sum}} < 2$  GeV
- EM shower shape:  $sigphi < 14$  cm<sup>2</sup>
- Photon ANN:  $O_{NN} > 0.1$
- No-track matching:  $P_{trk} < 0.0$  and  $D_{hor} > 0.9$

As discussed in Chapter 3, the corresponding efficiencies for these requirements are fairly independent on the photon  $p_T$  and  $\eta$ , especially for the high  $p_T$  ( $> 50$  GeV) photons.

The overall selection efficiency (see Table 4.2) for the three signal processes (GF, VH, VBF) is similar, and about 20%. The efficiency loss is mainly due to the geometry acceptance requirement.

	100GeV	110GeV	120GeV	130GeV	140GeV	150GeV
$\epsilon_{sel}$ (GF)	0.195±0.001	0.200±0.001	0.207±0.001	0.213±0.001	0.216±0.001	0.219±0.001
$\epsilon_{sel}$ (VH)	0.185±0.001	0.195±0.001	0.203±0.001	0.209±0.001	0.218±0.001	0.219±0.001
$\epsilon_{sel}$ (VBF)	0.198±0.001	0.211±0.001	0.218±0.001	0.226±0.001	0.233±0.001	0.238±0.001

**Table 4.2** Event selection efficiencies ( $\epsilon_{sel}$ ) with its statistical error from gluon fusion (GF), associated production (VH) and vector boson fusion (VBF) respectively.

### 4.3 Backgrounds

There are three major sources of background: (i) Drell-Yan events (see Fig. 4.4), when both electrons are misidentified as photons due to the tracking inefficiencies. This contribution is estimated by using Monte Carlo simulations; (ii)  $\gamma$ +jet and di-jet events (see Figs. 4.5), where the jet(s) are mis-identified as photon(s). This contribution is estimated from data by using a  $4 \times 4$  matrix method. (iii) direct di-photon events (see Fig. 4.7), we also estimate its contribution from data by using a side-band fitting method.

#### 4.3.1 Drell-Yan $Z/\gamma^* \rightarrow ee$ contributions

We use  $Z/\gamma^* \rightarrow ee$  PYTHIA full MC samples to estimate the Drell-Yan contribution. The NNLO  $p\bar{p} \rightarrow Z/\gamma^* \rightarrow ee$  cross sections<sup>[48]</sup> are used for the absolute normalization. From the  $Z/\gamma^* \rightarrow ee$  MC samples, we find that 2.0 – 4.0 % (depending on the  $\phi$ ) of the electrons can satisfy the photon selection requirements described in Section 3.5.2 due to tracking inefficiencies. The total background contribution from the Drell-Yan process is found to be  $216.3 \pm 43.4$  events.

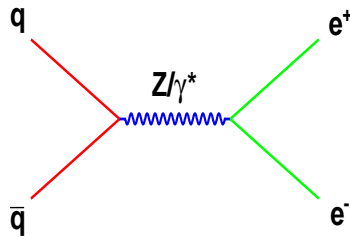


**Figure 4.4** Main Feynman diagram for the  $Z/\gamma^* \rightarrow ee$  production.

### 4.3.2 $\gamma$ +jet and di-jet background

We estimate the  $\gamma$  + jet and di-jet contributions from the data with the final event selection applied (see section 4.2) by using a  $4 \times 4$  matrix background subtraction method<sup>[49]</sup>.

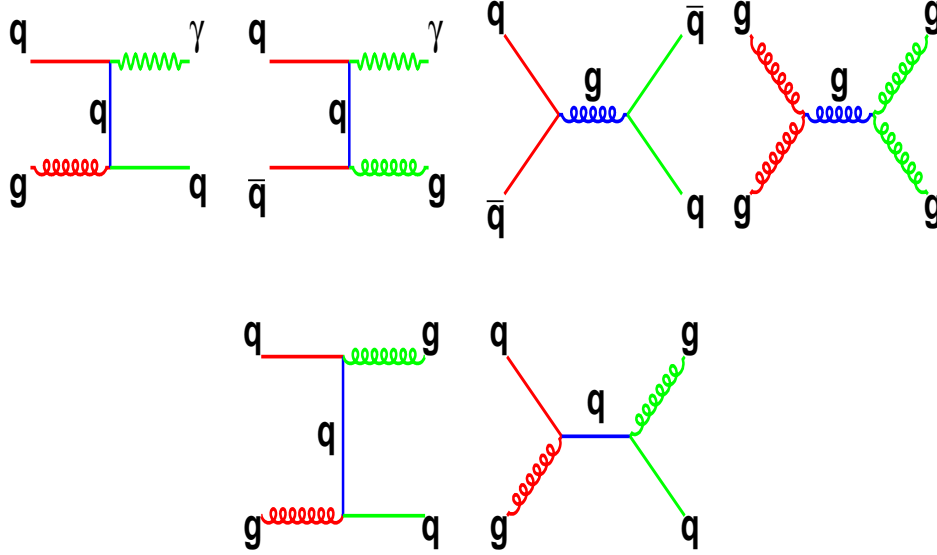


**Figure 4.5** Main Feynman diagram for  $\gamma$ +jet and di-jet production.

In this analysis, we use  $O_{NN} = 0.75$  as a boundary to classify the candidates into four categories:

- $N_{pp}$  of them have both photon candidates with  $O_{NN} > 0.75$ ;
- $N_{pf}$  of them have the leading photon candidate with  $O_{NN} > 0.75$ , but the sub-leading  $O_{NN} < 0.75$ ;
- $N_{fp}$  vice versa;
- $N_{ff}$  of them have both photon candidates with  $O_{NN} < 0.75$ ;

The pass-fail vector  $(N_{pp}, N_{pf}, N_{fp}, N_{ff})$  thus obtained is related with the  $(N_{\gamma\gamma}, N_{\gamma j}, N_{j\gamma}, N_{jj})$  vector as follows:



$$\begin{pmatrix} N_{ff} \\ N_{fp} \\ N_{pf} \\ N_{pp} \end{pmatrix} = E \times \begin{pmatrix} N_{jj} \\ N_{j\gamma} \\ N_{\gamma j} \\ N_{\gamma\gamma} \end{pmatrix} \quad (4.3)$$

where the  $N_{\gamma\gamma}$  is the number of  $\gamma+\gamma$  events,  $N_{\gamma j}$  and  $N_{j\gamma}$  are the number of  $\gamma$ +jet events and  $N_{jj}$  is the number of di-jet events.

The  $4 \times 4$  matrix  $E$  is defined as:

$$\begin{pmatrix} (1 - \epsilon_{j1})(1 - \epsilon_{j2}) & (1 - \epsilon_{j1})(1 - \epsilon_{\gamma2}) & (1 - \epsilon_{\gamma1})(1 - \epsilon_{j2}) & (1 - \epsilon_{\gamma1})(1 - \epsilon_{\gamma2}) \\ (1 - \epsilon_{j1})\epsilon_{j2} & (1 - \epsilon_{j1})\epsilon_{\gamma2} & (1 - \epsilon_{\gamma1})\epsilon_{j2} & (1 - \epsilon_{\gamma1})\epsilon_{\gamma2} \\ \epsilon_{j1}(1 - \epsilon_{j2}) & \epsilon_{j1}(1 - \epsilon_{\gamma2}) & \epsilon_{\gamma1}(1 - \epsilon_{j2}) & \epsilon_{\gamma1}(1 - \epsilon_{\gamma2}) \\ \epsilon_{j1}\epsilon_{j2} & \epsilon_{j1}\epsilon_{\gamma2} & \epsilon_{\gamma1}\epsilon_{j2} & \epsilon_{\gamma1}\epsilon_{\gamma2} \end{pmatrix} \quad (4.4)$$

where  $\epsilon_{\gamma1}$  and  $\epsilon_{\gamma2}$  are the fractions of the leading and sub-leading photons that have passed the event selection and have  $O_{NN} > 0.75$ , and  $\epsilon_{j1}$  and  $\epsilon_{j2}$  are the fractions of jets that have passed the event selection and have  $O_{NN} > 0.75$ . The photon efficiency ( $\epsilon_{\gamma}$ ) is estimated using DPP MC and corrected for small differences between data and the simulation measured in pure samples of photon events from radiative  $Z$  decays  $Z \rightarrow \ell^+ \ell^- \gamma$  ( $\ell = e, \mu$ ). The jet efficiency ( $\epsilon_j$ ) is estimated using di-jet MC enriched in jets misidentification as photons, and cross-checked in jet samples in data. Both efficiencies are parameterized as a function of photon pseudorapidity (see Section 3.5.3).

The method is used on an event by event basis. For each event, if there are no Drell-Yan events, the pass-fail 4-vector  $(N_{pp}, N_{pf}, N_{fp}, N_{ff})$  has four possibilities  $(1,0,0,0)$ ,  $(0,1,0,0)$ ,  $(0,0,1,0)$ ,  $(0,0,0,1)$ ; if we consider Drell-Yan events, the vector can be writ-

ten as  $(1-\epsilon_{DY}^{pp}, 0, 0, 0), (0, 1-\epsilon_{DY}^{pf}, 0, 0), (0, 0, 1-\epsilon_{DY}^{fp}, 0), (0, 0, 0, 1-\epsilon_{DY}^{ff})$ , where the  $\epsilon_{DY}^{pp}$ ,  $\epsilon_{DY}^{fp}$ ,  $\epsilon_{DY}^{pf}$  and  $\epsilon_{DY}^{ff}$  are the ratio of Drell-Yan events (estimated from MC) and data events in different situations (see Appendix 8.1).

Thus the  $(N_{\gamma\gamma}, N_{\gamma j}, N_{j\gamma}, N_{jj})$  can be obtained by solving the linear equation 4.3. Table 4.3 shows the results after applying the method on the real data.

Total	7939
Total - $N_{DY}$	7722.7
$N_{\gamma\gamma}$	$4538.8 \pm 144.7$
$N_{\gamma j} + N_{j\gamma}$	$2189.0 \pm 170.3$
$N_{jj}$	$994.9 \pm 106.6$
non- $\gamma\gamma$	$3183.9 \pm 200.9$

**Table 4.3** The number of  $\gamma\gamma$ ,  $\gamma$ +jet, di-jet and non- $\gamma\gamma$  ( sum of  $\gamma$ +jet and di-jet ) events in the data samples from the  $4 \times 4$  matrix method. The quoted uncertainties are statistical only.

We reverse the event selection  $O_{NN}$  cut (0.1) on one of the two photon candidates to get an enriched non- $\gamma\gamma(\gamma$ +jet,di-jet) sample from data. Fig. 4.6 shows that the shape of the di-photon mass distribution from such “reversed-ONN” sample is in good agreement with the results from the  $4 \times 4$  matrix method.

Given the good agreement between the shape from the two orthogonal samples and the low statistics of the results from the matrix method, we use the “reversed-ONN” sample to determine the shape of the non- $\gamma\gamma$  background. In order to smooth out statistical fluctuations, we fit the mass distribution with an exponential function  $f(M_{non}) = \exp(p_0 \cdot M_{non}^2 + p_1 \cdot M_{non} + p_2)$  with  $M_{non}$  denoting the mass of the two photon candidates. The estimation of the total number of non- $\gamma\gamma$  events from the  $4 \times 4$

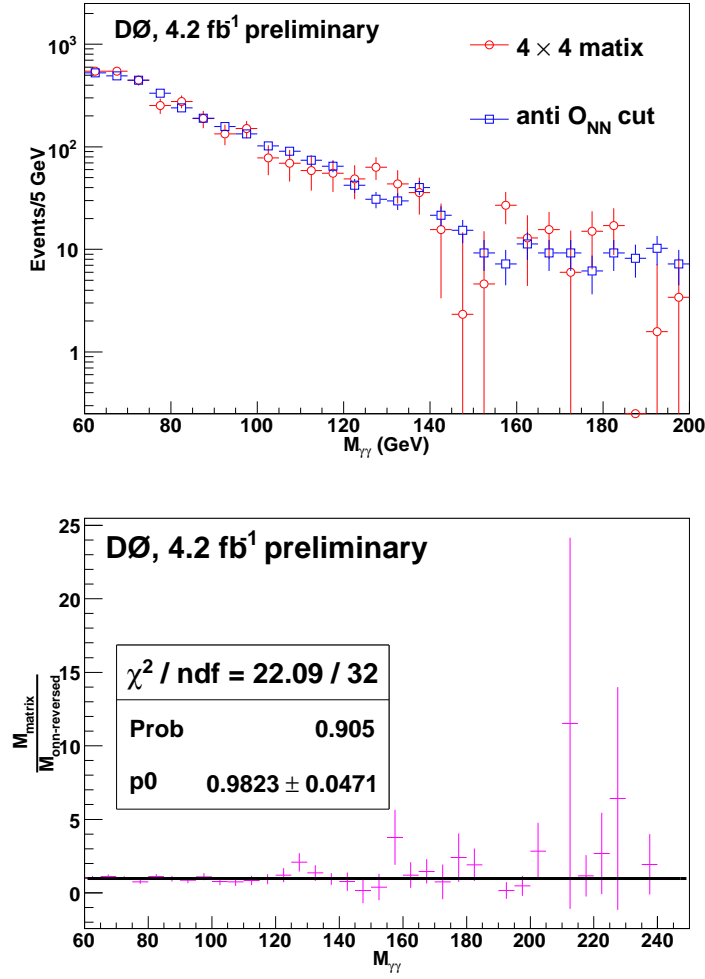


**Figure 4.6** Non- $\gamma\gamma$  component invariant mass distribution from  $4 \times 4$  matrix background subtraction and from reversing the  $O_{NN}$  cut. The area of both histograms are normalized to unity.

matrix method is used to fix the normalization. The systematic uncertainty from the shape function is taken into account when calculating the limits<sup>[?]</sup>.

#### 4.3.3 Direct photon pair production

Due to the poor model of the DPP production (Section 1.3), we use the side-band fitting method to estimate the DPP production from real data after having subtracted the non- $\gamma\gamma$  (estimated from data by using  $4 \times 4$  matrix method) and Drell-Yan (estimated from MC) components.

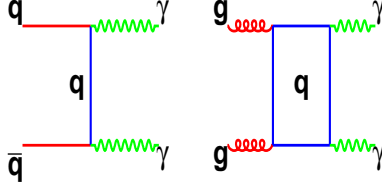


**Figure 4.7** Main Feynman diagram for the direct photon pair production.

Fig. 4.8 shows the comparison of di-photon invariant mass between the background-subtracted data ( $\gamma\gamma$  component) and DPP full PYTHIA MC, where the NLO cross section from DIPHOX<sup>[16]</sup> is used for absolute normalization. Fig. 4.9 shows the comparison of the differential cross sections ( $d\sigma/dM_{\gamma\gamma}$ ) in PYTHIA and DIPHOX. The ratio between the two differential cross section is arbitrarily parameterized as:

$$\frac{d\sigma_{diphox}^{NLO}/dM}{d\sigma_{pythia}^{LO}/dM}(M_{\gamma\gamma}) = p_0 \cdot M_{\gamma\gamma}^6 + p_1 \cdot M_{\gamma\gamma}^5 + p_2 \cdot M_{\gamma\gamma}^4 + p_3 \cdot M_{\gamma\gamma}^3 + p_4 \cdot M_{\gamma\gamma}^2 + p_5 \cdot M_{\gamma\gamma} + p_6 \quad (4.5)$$

and is applied on the PYTHIA LO cross section.

For each assumed Higgs mass( $M_H$ ), we use the simple exponential function  $f(M_{\gamma\gamma}) = \exp(p_0 \cdot M_{\gamma\gamma}^2 + p_1 \cdot M_{\gamma\gamma} + p_2)$  to fit the di-photon mass distribution in the  $[70, 200]$  GeV range outside of the signal mass region ( $M_H - 15$  GeV,  $M_H + 15$  GeV). We then extrapolate the function to the signal region and the fit result is taken as the direct photon pair production contribution. The uncertainty from the fitting function is estimated as

$$\begin{aligned} \sigma_{f(M_{\gamma\gamma})}^2 &= \left(\frac{\partial f}{\partial p_0}\right)^2 \cdot (\sigma_{p_0})^2 + \left(\frac{\partial f}{\partial p_1}\right)^2 \cdot (\sigma_{p_1})^2 + \left(\frac{\partial f}{\partial p_2}\right)^2 \cdot (\sigma_{p_2})^2 \\ &+ 2 \cdot \frac{\partial f}{\partial p_0} \frac{\partial f}{\partial p_1} \cdot Cov(p_0, p_1) + 2 \cdot \frac{\partial f}{\partial p_1} \frac{\partial f}{\partial p_2} \cdot Cov(p_1, p_2) \end{aligned}$$

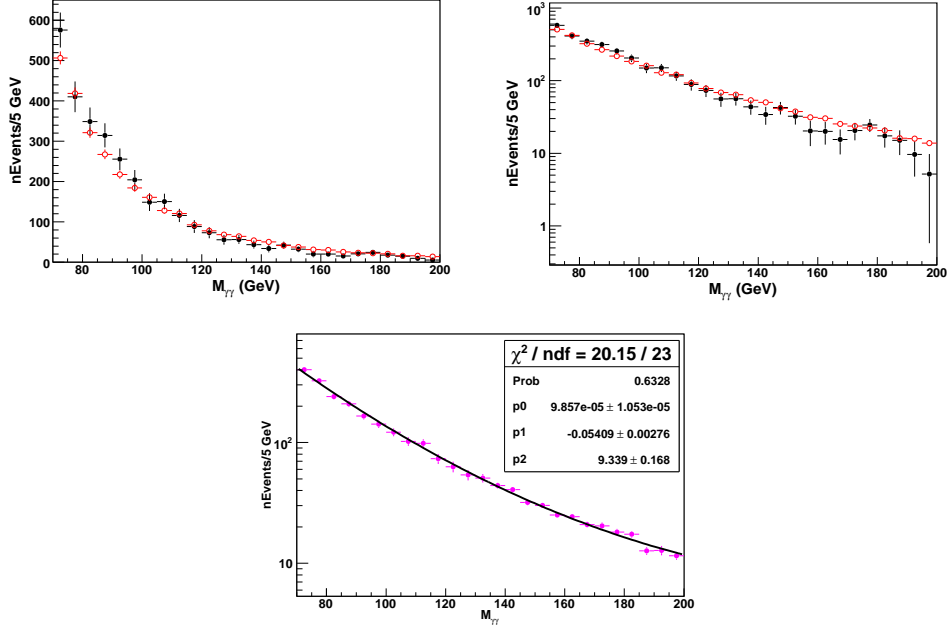


**Figure 4.8** Top-left plot show the diphoton invariant mass distribution of  $\gamma\gamma$  component of data and DPP MC. Top-right plot is the log scale of the left plot. Bottom plot shows the results of using the exponential function described below on the DPP MC after normalization.

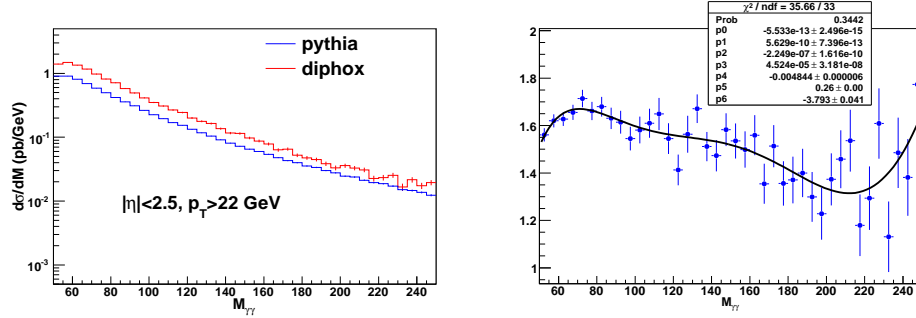


**Figure 4.9** Differential cross sections ( $\frac{d\sigma}{dM_{\gamma\gamma}}$ ) (left) and the ratio (right) between DIPHOX and PYTHIA.

$$+ 2 \cdot \frac{\partial f}{\partial p_0} \frac{\partial f}{\partial p_2} \cdot \text{Cov}(p_0, p_2) \quad (4.6)$$

We test the simple fitting function on the DPP full MC (shown in Fig. 4.8), and Figs. 4.10 - 4.11 show the corresponding results from the background subtracted data events.

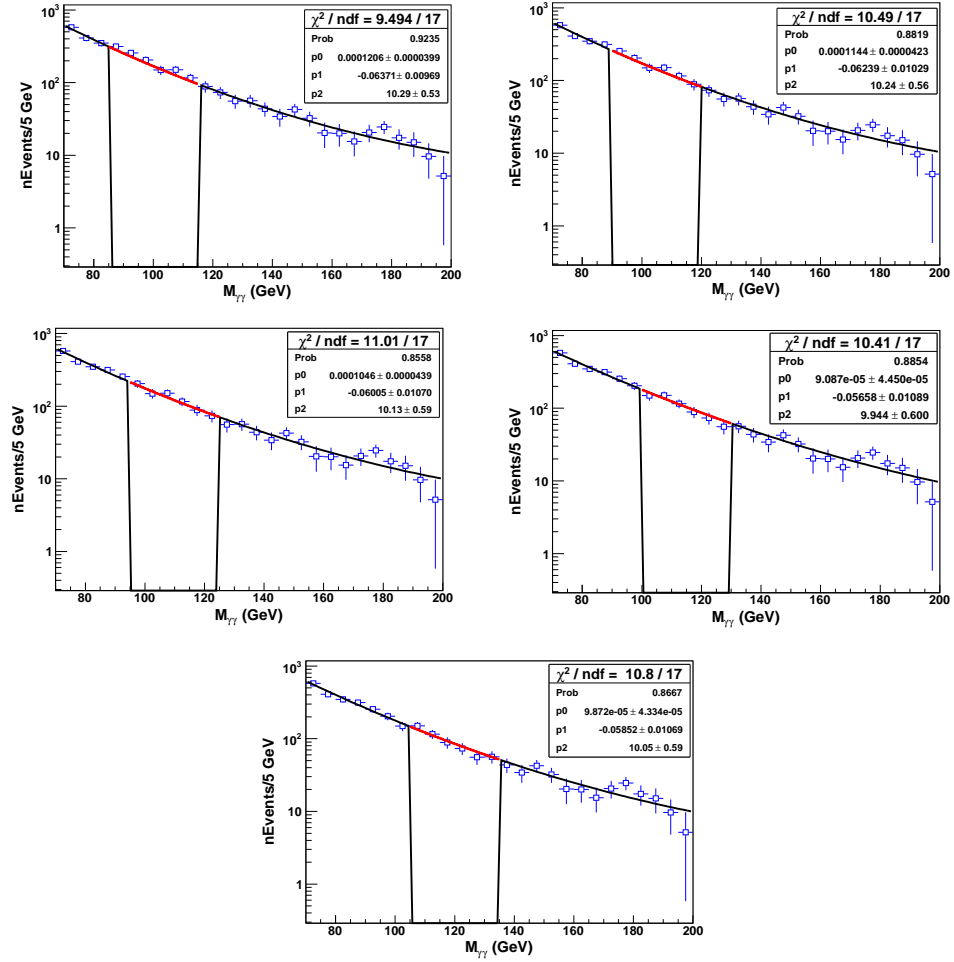


**Figure 4.10** Side-band fitting results from background subtracted data events for  $100 \leq M_H \leq 120$  GeV mass regions.

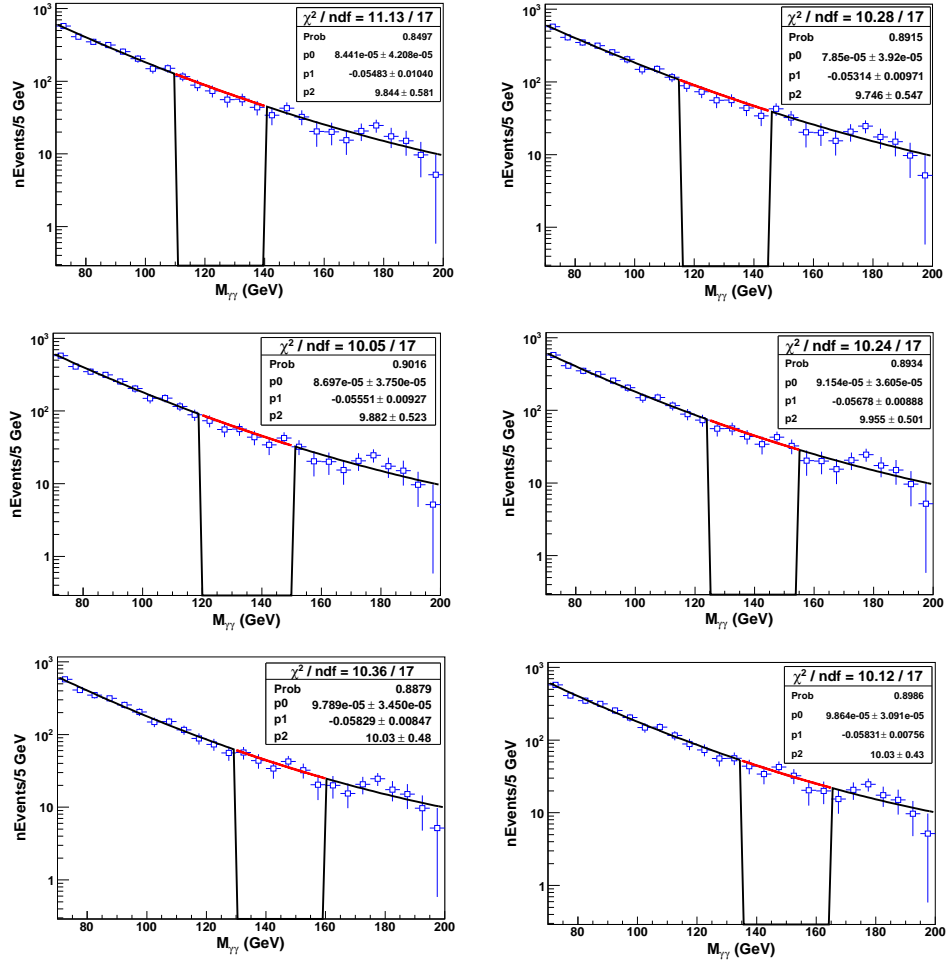


**Figure 4.11** Side-band fitting results from background subtracted data events for  $125 \leq M_H \leq 150$  GeV mass regions.

#### 4.4 Systematic uncertainties

Except the uncertainties from the event selection efficiency described in Section 3.5, some others have been considered in this analysis are:

- the 6.1%<sup>[43]</sup> uncertainty on the total luminosity;
- the influence of the parton distribution functions (PDF) uncertainty on the acceptance is 1.7% - 2.2% depending on the Higgs mass, estimated from CTEQ6M<sup>[14]</sup> error functions;
- the shape systematic uncertainty from the photon energy scale uncertainty detailedly described in Appendix 8.2;
- the difference between PYTHIA and SHERPA NLO on the acceptance is 0.01%-2.23% depending the Higgs mass, estimated by reweighting the Higgs boson  $p_T$  of the PYTHIA signal sample to the SHERPA, such  $p_T$  reweighting would not affect the di-photon invariant mass shape, more details can be found in Appendix 8.3;
- the shape systematic uncertainty from the fitting function on  $O_{NN}$ -reversed sample as described in section 4.3.2. The shape uncertainty would affect the shape of the non- $\gamma\gamma$  component, and further affect the shape of DPP component. We treat the effects on the non- $\gamma\gamma$  component and DPP component as correlated when setting the limits, more details can be found in Appendix 8.4;
- the uncertainty of the  $4 \times 4$  matrix background subtraction,



its source is the uncertainty of the  $O_{NN} > 0.75$  efficiencies for the photon and photon-like jets, where we adopt the difference in the number of background events from the mean efficiencies and the plus(minus) uncertainties as the systematic uncertainty. We treat its effect as correlated between the non- $\gamma\gamma$  component and DPP component, more details can be found in Appendix 8.5;

- the systematic uncertainty from the side-band fitting of DPP component as Eq. 4.6 shows.

Table 4.4 lists all the systematic uncertainties of this analysis:

source	uncertainty	signal	Drell-Yan	non- $\gamma\gamma$	DPP
luminosity	6.1%	✓	✓	-	-
trigger	0.1%	✓	✓	-	-
PDF for $H \rightarrow \gamma\gamma$ acceptance	1.7 - 2.2%	✓	-	-	-
H $p_T$ reweight on $H \rightarrow \gamma\gamma$ acceptance	0.01 - 2.23%	✓	-	-	-
photon ID efficiency	2.9%	✓	✓	-	-
$Z/\gamma^*(ee)$ cross section	3.9%	-	✓	-	-
photon energy scale	-	shape	-	-	-
$4 \times 4$ matrix background subtraction	-	-	-	14.3%	shape
non- $\gamma\gamma$ shape	-	-	-	shape	shape
side-band fitting	-	-	-	-	shape

**Table 4.4** Uncertainties of SM  $H \rightarrow \gamma\gamma$  are listed.

## 4.5 Final event distributions and Limits

### 4.5.1 Final event distributions

For illustration, we show the di-photon invariant mass ( $M_{\gamma\gamma}$ ) distribution of the events in data together with those of the background estimation for the mass region  $70 \text{ GeV} \leq M_{\gamma\gamma} \leq 200 \text{ GeV}$  in Fig. 4.12, where the Drell-Yan is estimated from MC, the non- $\gamma\gamma$  component is estimated from data by using  $4 \times 4$  matrix method and the direct photon pair production is estimated from data by using side-band fitting for  $130 \pm 15 \text{ GeV}$  mass window.

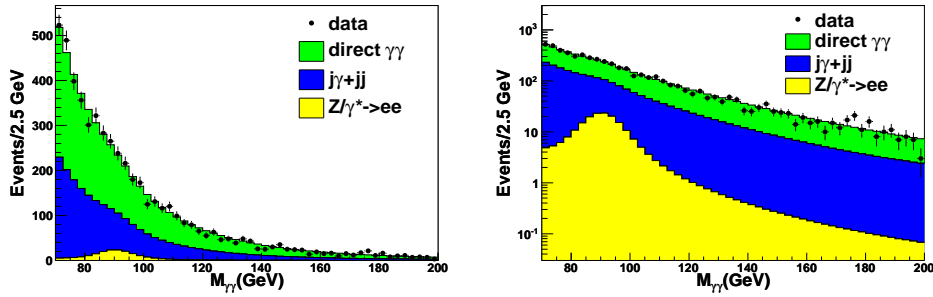


**Figure 4.12** Left plot shows the invariant mass distribution of two photon candidates in mass region  $70 \text{ GeV} \leq M_{\gamma\gamma} \leq 200 \text{ GeV}$ , right plot is the corresponding log scale distribution.

Figs. 4.13 and 4.14 show the final invariant mass of the two photon candidates in the interval of  $(M_H - 15 \text{ GeV}, M_H + 15 \text{ GeV})$  for each assumed Higgs mass. Figs. 4.15 and 4.16 are basically the same plot as Figs. 4.13 and 4.14 except adding the uncertainties on the total background. Table 4.5 shows the corresponding number of events in data, the background estimation and the signal for different Higgs masses.

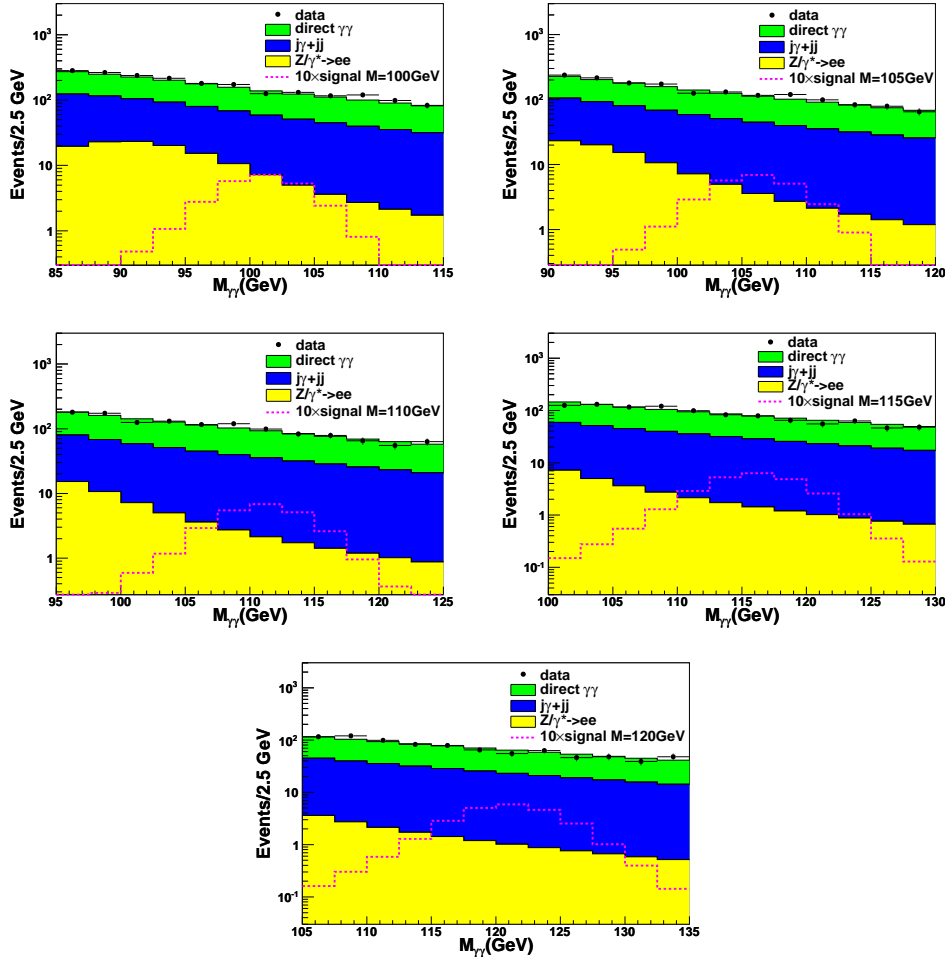


**Figure 4.13** Invariant mass distribution of the two photon candidates in mass interval of  $(M_H - 15 \text{ GeV}, M_H + 15 \text{ GeV})$  for 100 to 120 GeV Higgs mass with 2.5 GeV step for each mass bin. The  $Z/\gamma^* \rightarrow ee$  contribution has been smoothened by fitting the mass distribution with a Breit-Wigner function convoluted with a Gaussian resolution function plus an exponential background (see Appendix 8.1). The  $j\gamma + jj$  and direct  $\gamma\gamma$  contributions are obtained using the template and side-band fitting methods described in the previous section.

	100GeV	110GeV	120GeV	130GeV	140GeV	150GeV
$Z/\gamma^* \rightarrow ee$	$134.2 \pm 27.4$	$52.8 \pm 11.5$	$17.2 \pm 4.8$	$8.6 \pm 3.3$	$5.2 \pm 2.4$	$3.4 \pm 1.5$
$\gamma j + jj$	$712.4 \pm 101.9$	$455.0 \pm 65.1$	$298.8 \pm 42.7$	$201.8 \pm 28.9$	$140.1 \pm 20.0$	$100.1 \pm 14.3$
direct $\gamma\gamma$	$1080.4 \pm 95.6$	$764.2 \pm 61.9$	$538.9 \pm 41.2$	$404.1 \pm 28.0$	$280.1 \pm 19.4$	$207.2 \pm 13.9$
total background	$1927.0 \pm 35.4$	$1272.0 \pm 21.0$	$854.9 \pm 14.2$	$614.5 \pm 10.0$	$425.4 \pm 6.9$	$310.7 \pm 5.0$
data	2029	1289	861	567	412	295
signal	$2.53 \pm 0.18$	$2.53 \pm 0.18$	$2.38 \pm 0.17$	$2.01 \pm 0.14$	$1.45 \pm 0.10$	$0.87 \pm 0.06$

**Table 4.5** The number of events in data, signal and the background estimation in the mass interval of  $(M_H - 15 \text{ GeV}, M_H + 15 \text{ GeV})$  from 100 GeV to 150 GeV with 10 GeV step, where the systematic uncertainties have been included for both signal and background, the correlation between the different backgrounds has been considered when calculating the error for the total background.

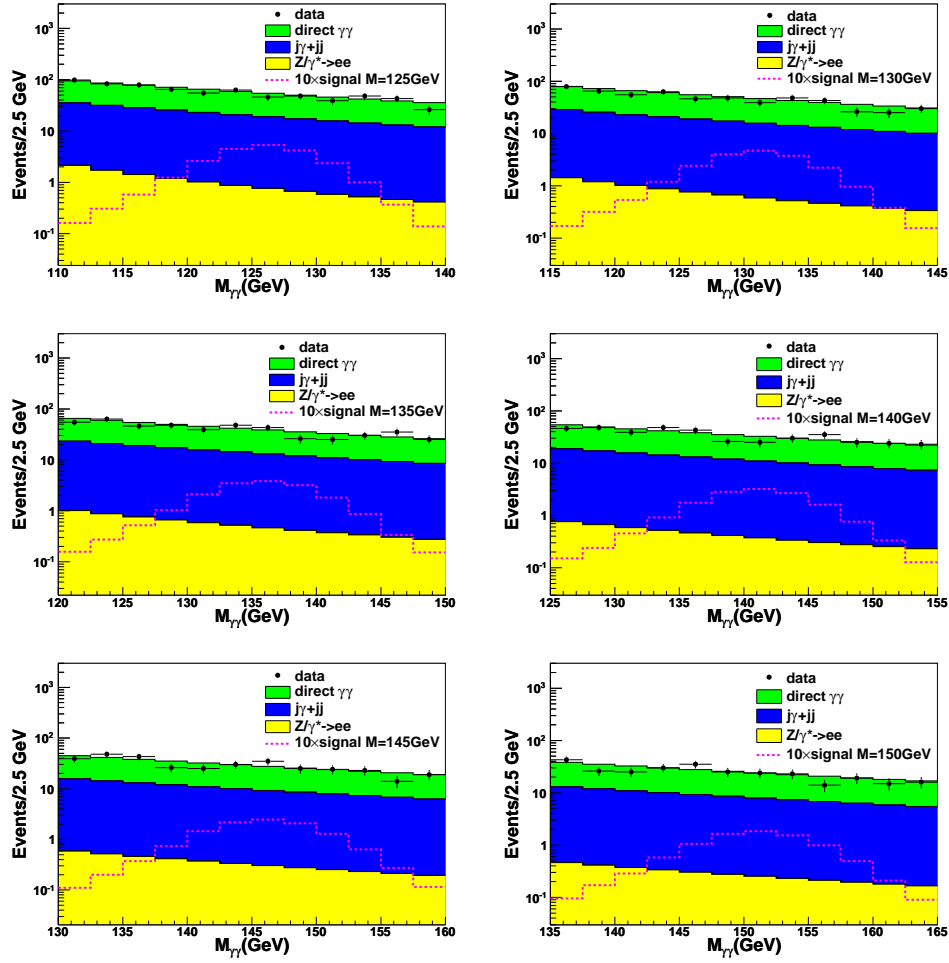


**Figure 4.14** Invariant mass distribution of the two photon candidates in mass interval of  $(M_H - 15 \text{ GeV}, M_H + 15 \text{ GeV})$  for 125 to 150 GeV Higgs mass with 2.5 GeV step for each mass bin.

	105GeV	115GeV	125GeV	135GeV	145GeV
$Z/\gamma^* \rightarrow ee$	$94.2 \pm 19.8$	$28.3 \pm 6.7$	$11.8 \pm 3.8$	$6.6 \pm 2.7$	$4.2 \pm 1.9$
$\gamma j + j j$	$567.3 \pm 81.1$	$367.4 \pm 52.5$	$244.7 \pm 35.0$	$167.5 \pm 24.0$	$118.0 \pm 16.9$
direct $\gamma\gamma$	$906.7 \pm 76.6$	$655.5 \pm 50.4$	$468.8 \pm 33.9$	$333.6 \pm 23.2$	$238.3 \pm 16.3$
total background	$1568.2 \pm 27.8$	$1051.2 \pm 17.0$	$725.2 \pm 12.1$	$507.8 \pm 8.2$	$360.5 \pm 5.8$
data	1625	1030	694	483	351
signal	$2.49 \pm 0.17$	$2.44 \pm 0.17$	$2.17 \pm 0.15$	$1.70 \pm 0.12$	$1.15 \pm 0.08$

**Table 4.6** Number of events in data, signal and the background estimation in the mass interval of  $(M_H - 15 \text{ GeV}, M_H + 15 \text{ GeV})$  from 105 GeV to 145 GeV with 10 GeV step.

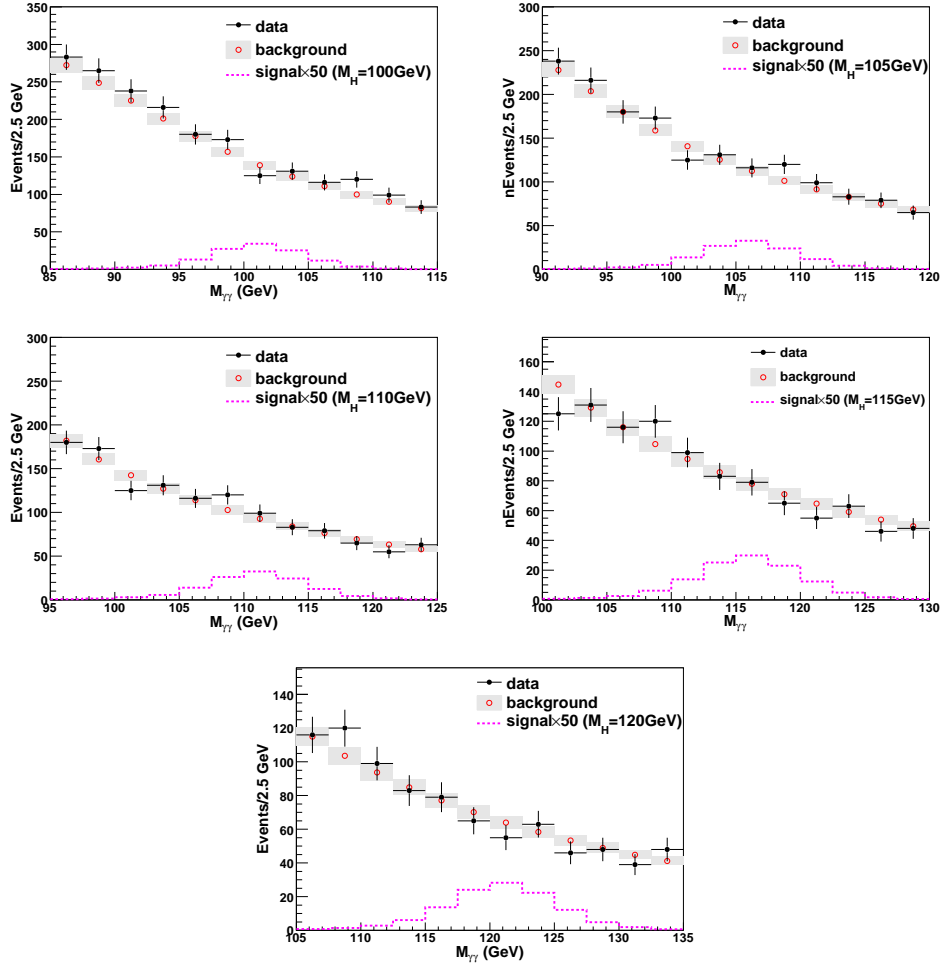


**Figure 4.15** Invariant mass distribution of the two photon candidates in mass interval of  $(M_H - 15 \text{ GeV}, M_H + 15 \text{ GeV})$  for 100 to 120 GeV Higgs mass with 2.5 GeV step for each mass bin after adding the statistical and systematic uncertainties on the total background.

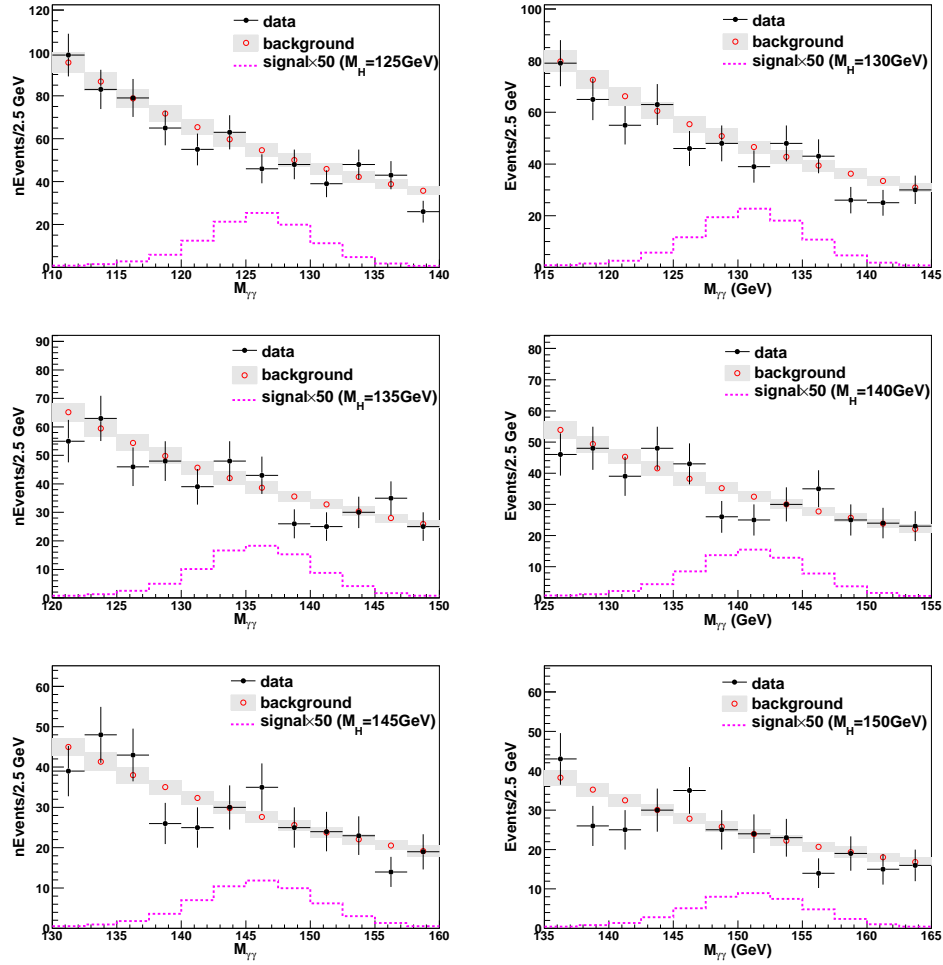


**Figure 4.16** Invariant mass distribution of the two photon candidates in mass interval of  $(M_H - 15\text{ GeV}, M_H + 15\text{ GeV})$  for 125 to 150 GeV Higgs mass with 2.5 GeV step for each mass bin after adding the statistical and systematic uncertainties on the total background.

#### 4.5.2 Limit setting

Since there is no excess observed above the background expectation, we proceed to set upper limits on the Higgs production cross section times branching ratio for Higgs decaying into a pair of photons. The distributions of invariant mass of the two photon candidates in the interval of  $(M_H - 15 \text{ GeV}, M_H + 15 \text{ GeV})$  (shown in Figs. 4.13 and 4.14) are used for this purpose. Limits are calculated at the 95% confidence level using the modified frequentist CLs approach with a Poisson log-likelihood ratio test statistic<sup>[50,51]</sup>. The impact of systematic uncertainties is incorporated via convolution of the Poisson probability distributions corresponding to the different sources of systematic uncertainty. The correlation in systematic uncertainties are maintained between signal and backgrounds.

In this analysis, we use the diphoton invariant mass as the discriminant for limit setting. We find that the selection efficiency varies smoothly and the diphoton mass resolution is almost constant ( $\sim 3 \text{ GeV}$ ). Therefore, we could get the 2.5 GeV interpolated mass points by using the current available 5 GeV step signal MC samples. By doing so, we interpolate two things:

- acceptance: as shown in Table 4.2, the maximum difference between two masses differing by 10 GeV is 5%, so a linear interpolation of the kind we make should be precise to the sub-percent level;
- mass template: we can perform a worst-case scenario where

we compare the actual template with the predicted one from mass points 10 GeV away, which is interpolation over a range a x4 larger than actually used. Fig. 4.17 shows that the predicted mass distribution for  $M_H=110$  GeV based on the existing  $M_H=100$  and 120 GeV templates is in good agreement with the actual one. Therefore, we have carried out this works even better for our 2.5 GeV interpolation.

More details can be found in Appendix 8.6.

Tables 4.7 and 4.8 show the limits on  $\sigma \times BR$  for the different Higgs masses. Tables 4.9 and 4.10 show the limits on  $\sigma \times BR$  relative to the SM prediction for different Higgs masses. The corresponding graphs are displayed in Fig. 4.18.

Higgs mass (GeV)	100	102.5	105	107.5	110	112.5	115	117.5	120	122.5	125
observed limits (fb)	93.9	98.4	102.9	108.5	86.1	68.8	46.3	38.1	36.0	35.3	30.0
expected limits (fb)	74.5	69.6	66.1	61.9	58.1	55.8	53.9	51.6	48.1	46.8	45.2

**Table 4.7** 95% C.L. limits on  $\sigma \times BR$  for the different Higgs masses from 100 GeV to 125 GeV.

Higgs mass (GeV)	127.5	130	132.5	135	137.5	140	142.5	145	147.5	150
observed limits (fb)	30.5	29.4	30.9	30.6	27.2	26.7	30.5	33.2	33.4	27.0
expected limits (fb)	43.6	41.0	40.4	38.3	37.2	34.3	34.1	32.2	31.7	29.7

**Table 4.8** 95% C.L. limits on  $\sigma \times BR$  for the different Higgs masses from 127.5 GeV to 150 GeV.

Higgs mass (GeV)	100	102.5	105	107.5	110	112.5	115	117.5	120	122.5	125
observed limits	29.7	31.4	33.0	35.2	28.3	22.9	15.8	13.3	13.1	13.2	11.9
expected limits	23.6	22.2	21.2	20.1	19.1	18.6	18.5	18.0	17.5	17.6	17.9

**Table 4.9** 95% C.L. limits on  $\sigma \times BR$  relative to the SM prediction for different Higgs masses from 100 GeV to 125 GeV.



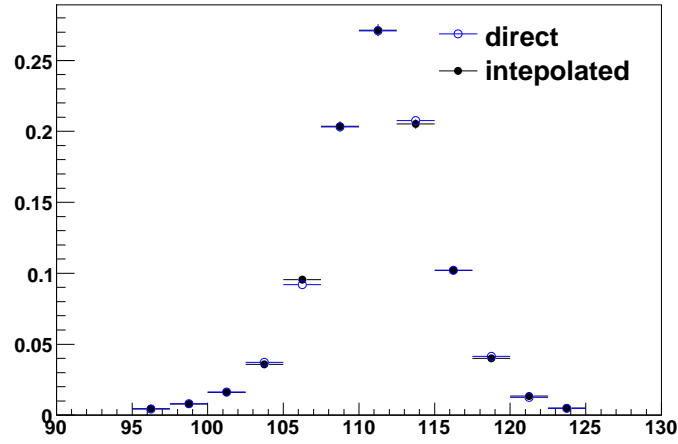


**Figure 4.17** The predicted (interpolated) diphoton invariant distribution for  $M_H = 110$  GeV based on the existing  $M_H = 100$  and  $120$  GeV templates versus the actual one (direct).

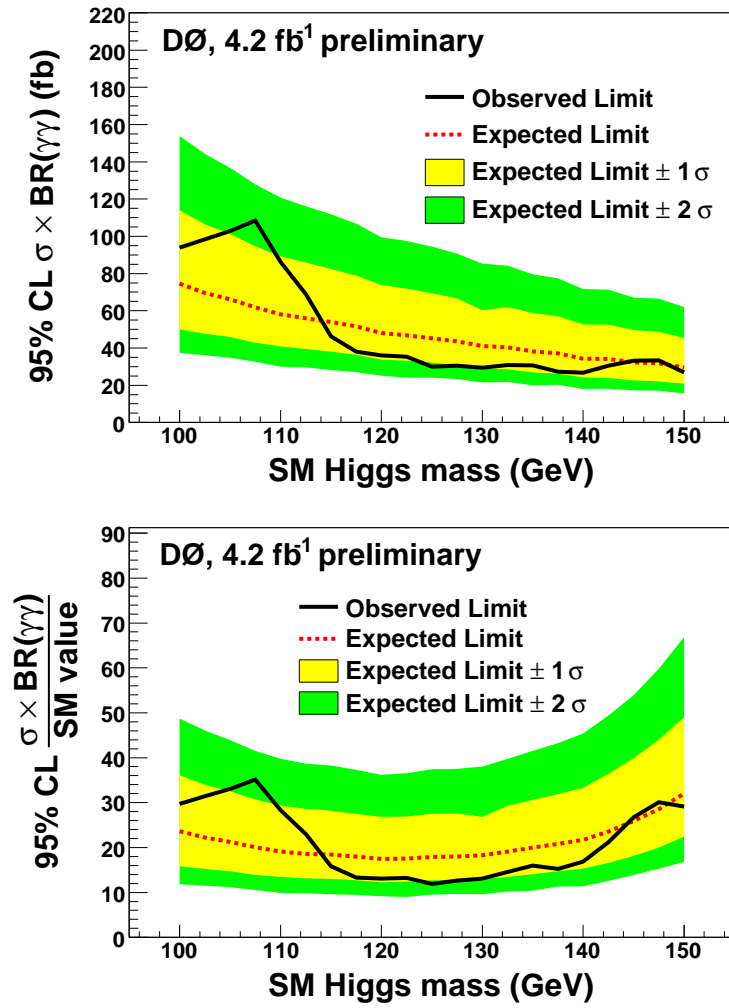


**Figure 4.18** 95% C.L. limits on the  $\sigma \times BR$  (top) and on the  $\sigma \times BR$  relative to the SM prediction (bottom) as a function of Higgs mass.

Higgs mass (GeV)	127.5	130	132.5	135	137.5	140	142.5	145	147.5	150
observed limits	12.6	13.1	14.6	16.0	15.2	16.9	21.2	26.8	30.1	29.1
expected limits	18.0	18.3	19.1	20.0	20.8	21.7	23.6	25.9	28.5	32.0

**Table 4.10** 95% C.L. limits on  $\sigma \times BR$  relative to the SM prediction for different Higgs masses from 127.5 GeV to 150 GeV.

## 4.6 Fermiophobic $H \rightarrow \gamma\gamma$ search

For a Fermiophobic Higgs boson ( $h_f$ ), there are no couplings to fermions, the  $\gamma\gamma$  branching ratio is almost an order of magnitude larger (see Table. 4.11) than the SM ones.  $h_f$  has SM-like production cross sections, except the gluon fusion diagram is absent. Thus it is produced mainly in associations with vector bosons ( $h_f + V \rightarrow \gamma\gamma + V$ ,  $V = W, Z$ ) or through the vector boson fusion process (VBF  $h_f \rightarrow \gamma\gamma$ ). A distinctive feature of these production mechanisms is that the Higgs boson is produced with large  $p_T$  of diphoton system ( $p_T^{\gamma\gamma}$ ) (see Fig. 4.19). Therefore, a cut on the  $p_T^{\gamma\gamma}$  can be very effective at suppressing the background while keeping most of the signal.

### 4.6.1 Data, MC samples and Event selection

In this section, we present the extension of the previous SM Higgs search in diphoton final states using  $4.2 \text{ fb}^{-1}$  of data (described in the above sections and documented in<sup>[52]</sup>) to a Fermiophobic Higgs scenario. The data and MC samples, all analysis cuts, background estimation procedures, and sources of systematic uncertainties are identical to those described in Ref.<sup>[52]</sup>, with the following two exceptions:

- the photon  $p_T$  has been lowered from 25 to 20 GeV. The main reason is that a Fermiophobic Higgs boson can be significantly lighter than in the SM. The lowered cut also helps to reduce the kinematic bias in the diphoton mass spectrum and thus allows us to slightly extend the range used for side-

band fitting to lower masses.

- we require in addition  $p_T^{\gamma\gamma} > 35$  GeV. This cut is justified given the main production mechanism for a Fermiophobic Higgs boson and produces a significant reduction of the background while keeping most of the signal. This is the same cut as applied in a previous DØ publication<sup>[40]</sup> and has not been reoptimized.

Table 4.12 shows the overall selection efficiency for the VH and VBF signal processes.

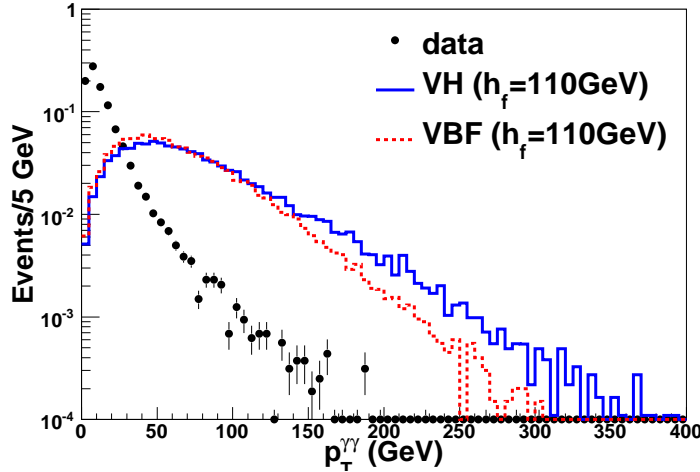


**Figure 4.19**  $p_T$  of di-photon system ( $p_T^{\gamma\gamma}$ ) distribution from data and 110 GeV associated production and vector boson fusion signal. All histograms are normalized to unity.

#### 4.6.2 Backgrounds

We use the  $Z/\gamma^* \rightarrow ee$  PYTHIA Monte Carlo samples to estimate the Drell-Yan contribution. The  $Z$   $p_T$  spectrum is reweighted in PYTHIA for each event to measured data in order to properly model the efficiency of the  $p_T^{\gamma\gamma}$  cut. After normalizing to the  $4.2 \text{ fb}^{-1}$  luminosity, its contribution is estimated to be  $25.7 \pm 2.3$

$m_{h_f}$ (GeV)	$Wh_f(\text{NNLO})$	$Zh_f(\text{NNLO})$	$VBF(\text{NLO})$	$BR(h_f \rightarrow \gamma\gamma)$
80	0.581	0.313	0.141	0.70
90	0.406	0.223	0.119	0.41
100	0.2861	0.1668	0.0995	0.18
110	0.2077	0.1233	0.0842	0.062
120	0.1532	0.0926	0.0693	0.028
130	0.1145	0.0704	0.0604	0.019
140	0.0866	0.0541	0.0508	0.0061
150	0.0661	0.0420	0.0441	0.0020

**Table 4.11** Cross section (pb) and branching ratio (BR) for a Fermiophobic Higgs boson. Signal with mass greater than 150 GeV is not considered due to its small BR.

	80GeV	90GeV	100GeV	110GeV	120GeV	130GeV	140GeV	150GeV
$\epsilon_{sel}(\text{VH})$	$0.117 \pm 0.001$	$0.132 \pm 0.001$	$0.148 \pm 0.001$	$0.156 \pm 0.001$	$0.161 \pm 0.001$	$0.168 \pm 0.001$	$0.176 \pm 0.001$	$0.176 \pm 0.001$
$\epsilon_{sel}(\text{VBF})$	$0.133 \pm 0.001$	$0.144 \pm 0.001$	$0.152 \pm 0.001$	$0.160 \pm 0.001$	$0.164 \pm 0.001$	$0.169 \pm 0.001$	$0.170 \pm 0.001$	$0.173 \pm 0.001$

**Table 4.12** Event selection efficiencies( $\epsilon_{sel}$ ) with their statistical errors for signal.

(stat.) events. To smooth out the statistical fluctuation for the final limits setting, we use a Gaussian convoluted with a Breit-Wigner and add an exponential function to fit the final invariant mass distribution. Due to the poor statistics after all event selection (see top plot of Fig. 4.20, we use the invariant mass distribution without  $D_{hor} < 0.9$  requirement as a template to do the fitting (see bottom plot of Fig. 4.20).

The  $\gamma$ +jet and di-jet background (non- $\gamma\gamma$ ) is measured using the  $4 \times 4$  matrix method (see Table. 4.13) with using the shape got from reversed-ONN samples, as described in Section 4.3.2. Fig. 4.21 shows the corresponding results.

The DPP contribution is estimated from the data after subtracting the non- $\gamma\gamma$  and Drell-Yan components using the side-band fitting method. The diphoton mass range considered as a side-band is (60, 180) GeV, with the exception of the search win-

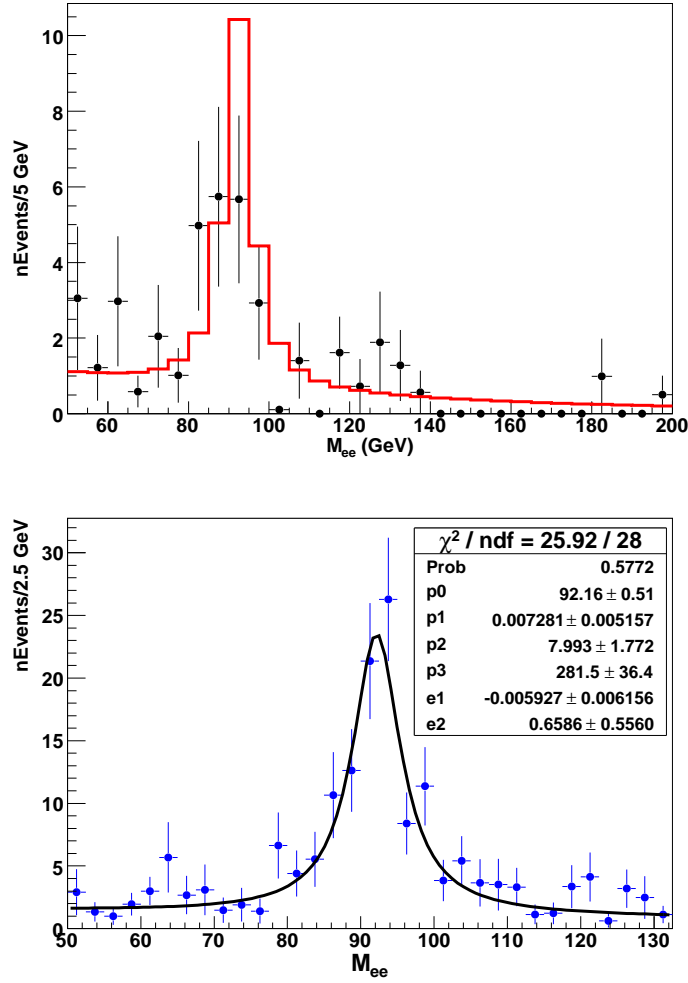


**Figure 4.20** Normalized invariant mass distribution from  $Z/\gamma^* \rightarrow ee$  contribution (top). and the invariant mass template fitting after removing the  $D_{hor} < 0.9$  requirement.

dow, which is defined to be  $M_{h_f} \pm 10$  GeV. Please note that this is different than in Ref. [52], where the side-band was (70, 200) GeV and the search window was  $M_H \pm 15$  GeV. The main reason for the change is the limited data statistics in this analysis after the application of the  $p_T^{\gamma\gamma} > 35$  GeV cut, which forces us to try to make use of as many data points as possible to minimize the statistical fluctuations in the predicted background. The sensitivity loss from using a narrower search window had been estimated during a previous study [52] and shown to be negligible. We continue

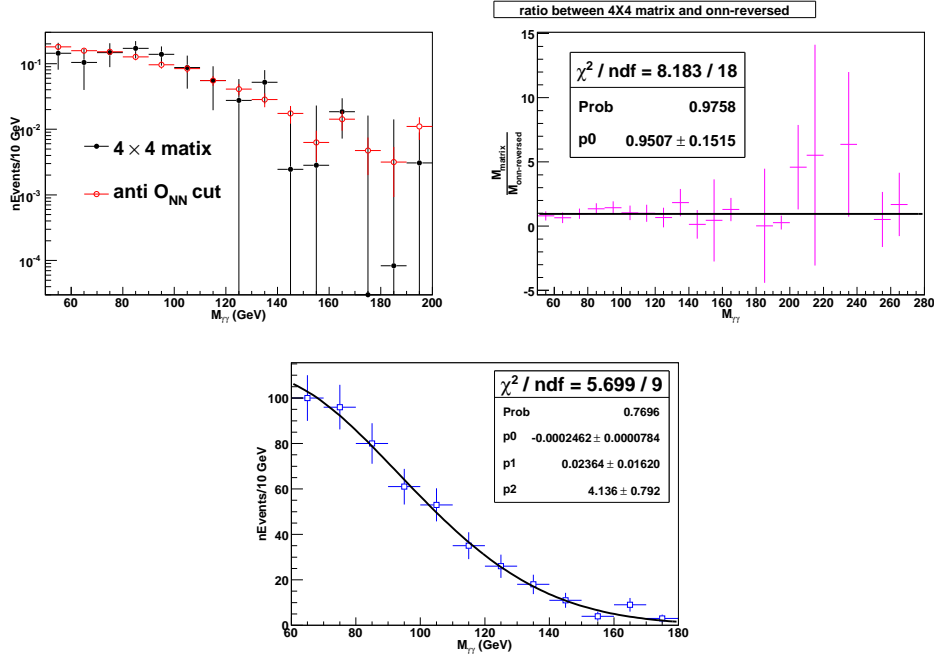


**Figure 4.21** Top-left plot shows the non- $\gamma\gamma$  component invariant mass from the  $4 \times 4$  matrix background subtraction and reversing the  $O_{NN}$  cut. Top-right plot shows the corresponding ratio for the two distributions shown in the left plot. Bottom plot shows the fitting results on the samples by reversing the  $O_{NN}$  cut.

Total	1084
Total - $N_{DY}$	1058.3
$N_{\gamma\gamma}$	$745.0 \pm 56.9$
non- $\gamma\gamma$	$313.3 \pm 52.9$

**Table 4.13** The number of  $\gamma\gamma$  and non- $\gamma\gamma$  ( sum of  $\gamma$ +jet and di-jet ) events in the data samples from the  $4 \times 4$  matrix method. The quoted uncertainties include statistical uncertainties only.

to fit the side-band with an exponential function, as in Ref.<sup>[52]</sup>.

Figs. 4.22 and 4.23 show the results.

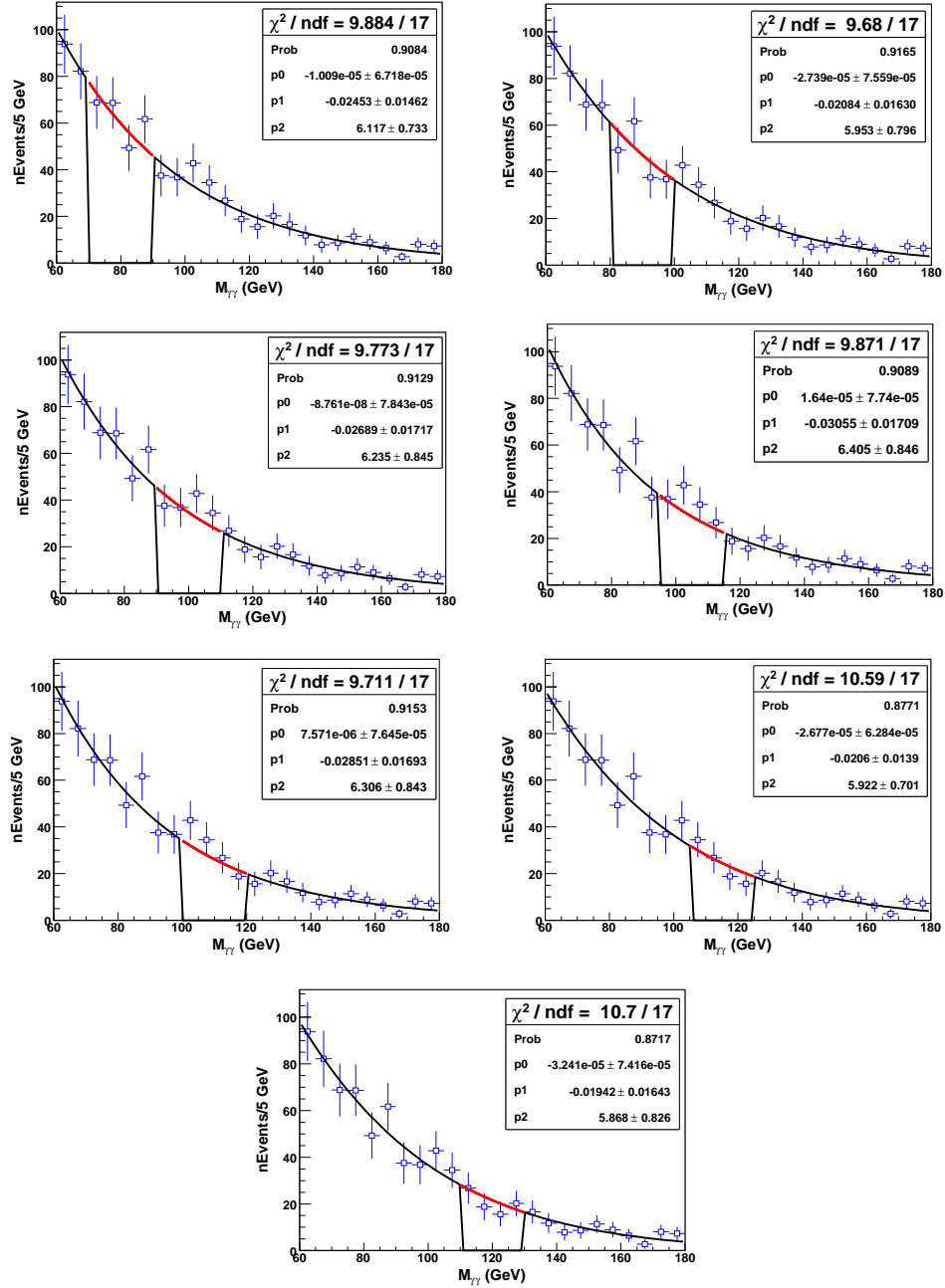


**Figure 4.22** Side-band fitting results for 80 GeV (top left) to 120 GeV (bottom right) mass regions.



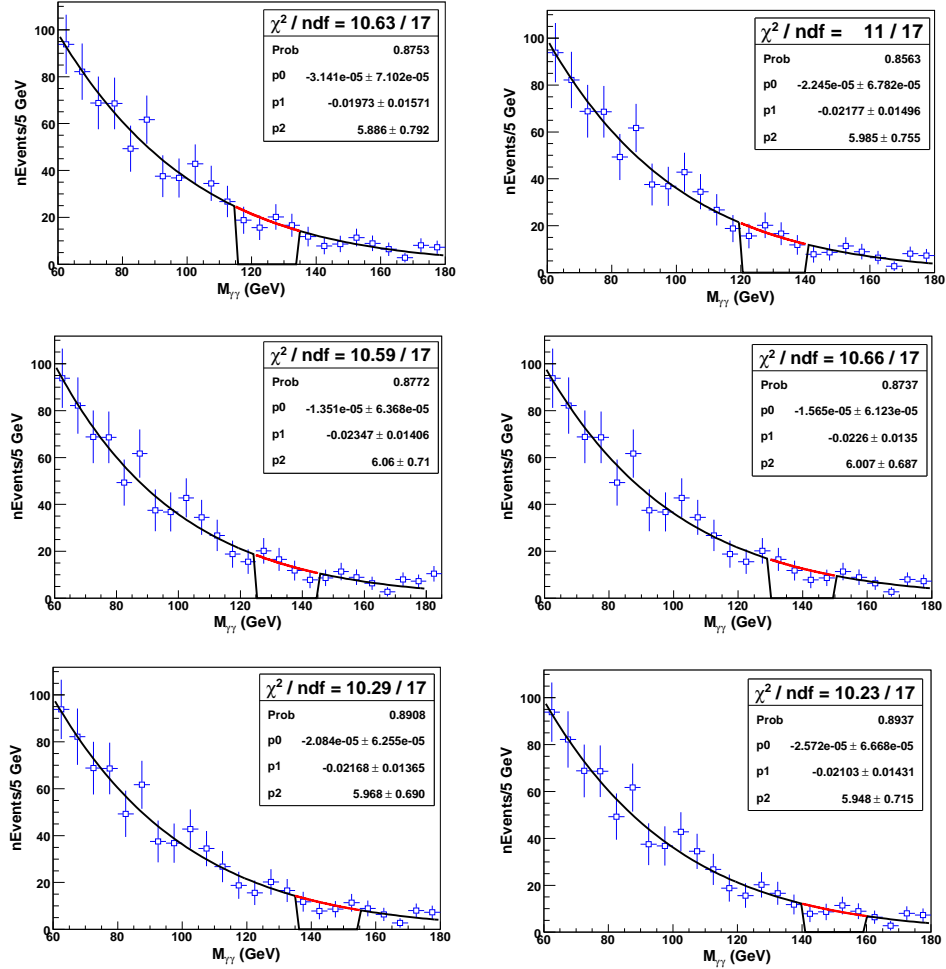


**Figure 4.23** Side-band fitting results for 125 GeV (top left) to 150 GeV (bottom right) mass regions.

## 4.6.3 Final event distributions and limits

For illustration, we show the invariant mass distribution of the events in data together with those of the background estimation for the mass region  $[60 \text{ GeV}, 180 \text{ GeV}]$  in Fig. 4.24, where the Drell-Yan is estimated from MC, the non- $\gamma\gamma$  component is estimated from data by using  $4 \times 4$  matrix method and the direct photon pair production is estimated from data by using side-band fitting for  $130 \pm 10 \text{ GeV}$  mass window. Figs. 4.25 and 4.28 show

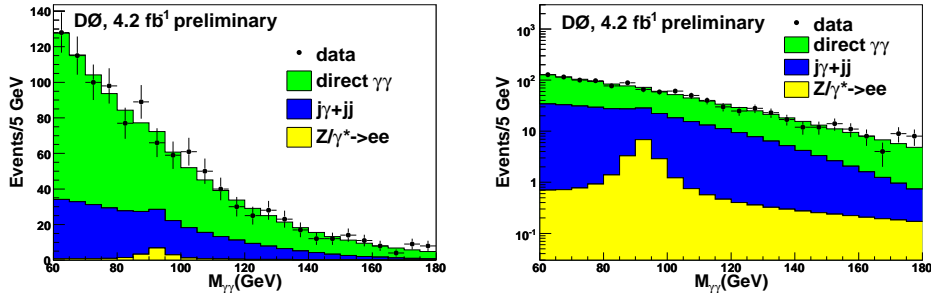


**Figure 4.24** Left plot shows the invariant mass distribution of the photon candidates in mass region  $60 \text{ GeV} \leq M_{\gamma\gamma} \leq 180 \text{ GeV}$ , right plot is the corresponding log scale distribution.

the final invariant mass of the two photon candidates in the interval of  $(M_{h_f} - 10 \text{ GeV}, M_{h_f} + 10 \text{ GeV})$  for each assumed Higgs mass.

Table 4.14 shows the corresponding number of events in data, the background estimation and the signal events for different Higgs masses.

$M_{h_f}(\text{GeV})$	$Z/\gamma^* \rightarrow ee$	$\gamma j+jj$	QCD $\gamma\gamma$	total background	data
80	$6.4 \pm 1.4$	$109.2 \pm 23.3$	$241.6 \pm 15.8$	$357.2 \pm 9.4$	364
90	$14.4 \pm 2.9$	$91.2 \pm 19.4$	$190.9 \pm 13.3$	$296.6 \pm 8.5$	291
100	$11.7 \pm 2.3$	$72.7 \pm 15.5$	$140.2 \pm 10.7$	$224.6 \pm 7.3$	236
102.5	$8.5 \pm 1.7$	$68.1 \pm 14.5$	$131.1 \pm 10.1$	$207.7 \pm 6.8$	219
105	$5.4 \pm 1.1$	$63.7 \pm 13.6$	$118.7 \pm 9.4$	$187.9 \pm 6.3$	210
107.5	$3.8 \pm 0.8$	$59.3 \pm 12.6$	$111.0 \pm 8.9$	$174.2 \pm 5.9$	188
110	$3.0 \pm 0.6$	$55.1 \pm 11.7$	$105.6 \pm 8.4$	$163.8 \pm 5.5$	181
112.5	$2.5 \pm 0.5$	$51.1 \pm 10.9$	$98.8 \pm 7.8$	$152.4 \pm 5.2$	172
115	$2.2 \pm 0.5$	$47.2 \pm 10.0$	$99.1 \pm 7.2$	$148.5 \pm 4.6$	145
117.5	$2.0 \pm 0.4$	$43.4 \pm 9.2$	$92.7 \pm 6.7$	$138.1 \pm 4.3$	131
120	$1.8 \pm 0.4$	$39.9 \pm 8.5$	$87.2 \pm 6.4$	$128.9 \pm 4.2$	123
122.5	$1.7 \pm 0.4$	$36.5 \pm 7.7$	$81.5 \pm 5.8$	$119.6 \pm 3.9$	114
125	$1.6 \pm 0.4$	$33.3 \pm 7.1$	$75.7 \pm 5.3$	$110.5 \pm 3.5$	106
127.5	$1.5 \pm 0.4$	$30.3 \pm 6.4$	$70.7 \pm 4.9$	$102.4 \pm 3.2$	105
130	$1.4 \pm 0.4$	$27.4 \pm 5.8$	$65.0 \pm 4.4$	$93.8 \pm 2.9$	93
132.5	$1.3 \pm 0.4$	$24.8 \pm 5.3$	$60.7 \pm 4.1$	$86.8 \pm 2.7$	89
135	$1.3 \pm 0.4$	$22.4 \pm 4.7$	$57.0 \pm 3.7$	$80.6 \pm 2.5$	80
137.5	$1.2 \pm 0.3$	$20.1 \pm 4.3$	$53.2 \pm 3.4$	$74.6 \pm 2.3$	72
140	$1.1 \pm 0.3$	$18.0 \pm 3.8$	$51.1 \pm 3.2$	$70.3 \pm 2.2$	64
142.5	$1.1 \pm 0.3$	$16.1 \pm 3.4$	$47.8 \pm 2.9$	$65.0 \pm 2.1$	57
145	$1.1 \pm 0.2$	$14.3 \pm 3.0$	$44.0 \pm 2.7$	$59.4 \pm 2.0$	55
147.5	$1.0 \pm 0.2$	$12.7 \pm 2.7$	$41.1 \pm 2.5$	$54.8 \pm 1.9$	50
150	$1.0 \pm 0.2$	$11.2 \pm 2.4$	$37.1 \pm 2.4$	$49.4 \pm 1.9$	49

**Table 4.14** Number of events in data, signal and the background estimation in the mass interval of  $(M_{h_f} - 15 \text{ GeV}, M_{h_f} + 15 \text{ GeV})$ , where the systematic uncertainties have been included for the background, the correlation between the different backgrounds has been considered when calculating the error for the total background.

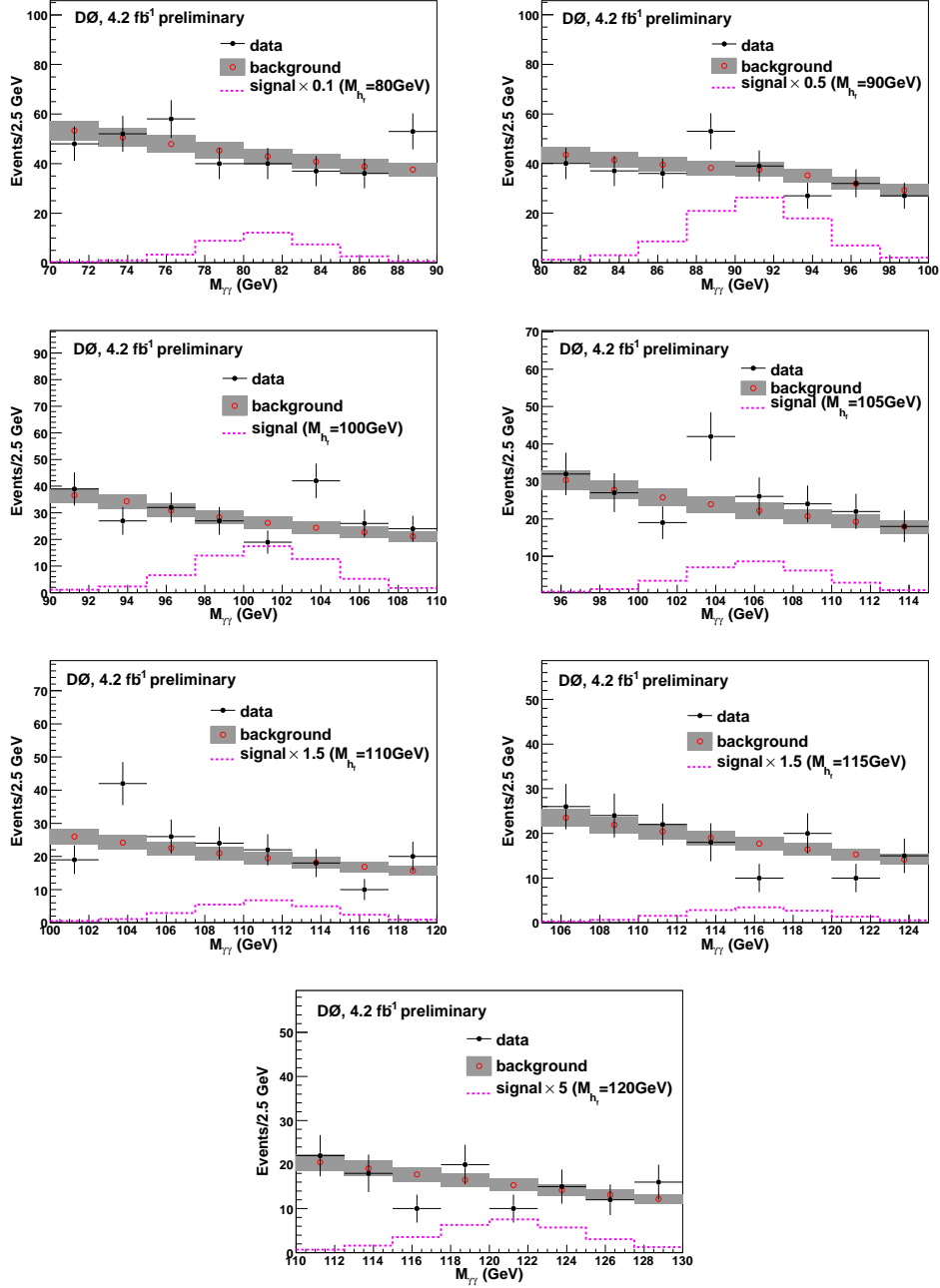


**Figure 4.25** Invariant mass distribution of the two photon candidates in mass interval of  $(M_{h_f} - 10 \text{ GeV}, M_{h_f} + 10 \text{ GeV})$  for 80 (top left) to 120 GeV (bottom) Higgs mass in 5 GeV step for each mass bin after adding the systematic uncertainties on the total background.

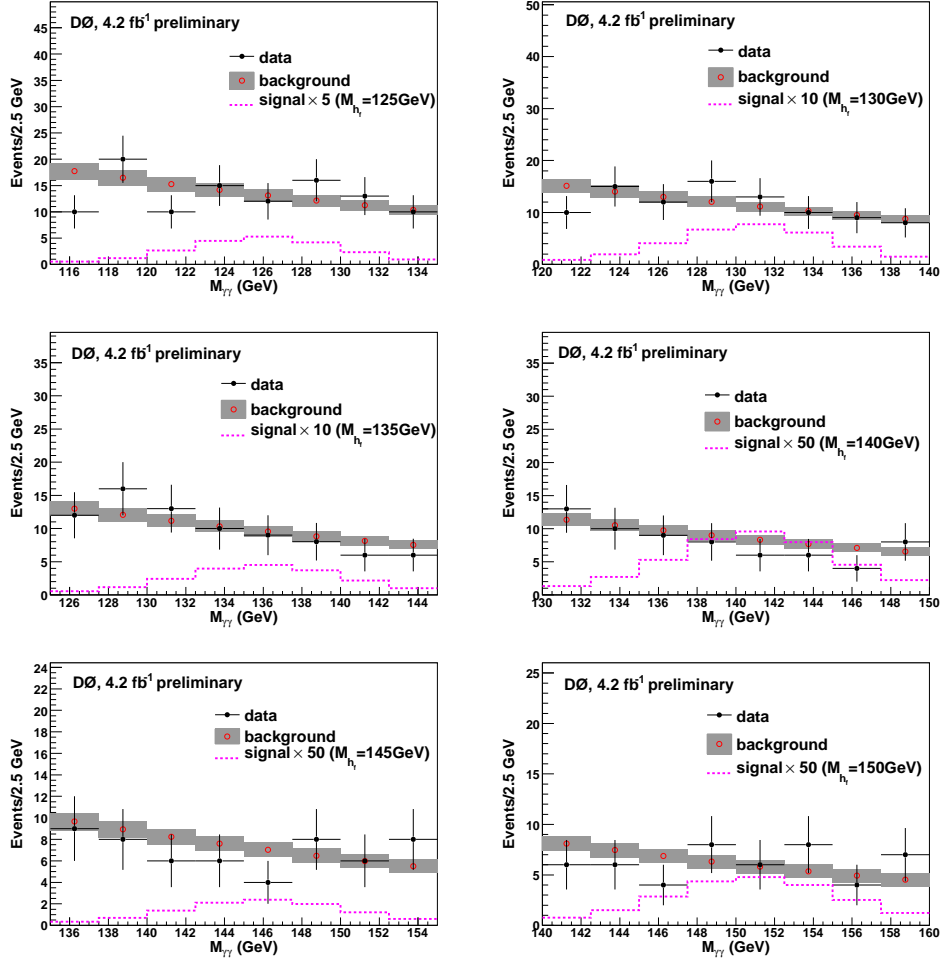


**Figure 4.26** Invariant mass distribution of the two photon candidates in mass interval of  $(M_{h_f} - 10 \text{ GeV}, M_{h_f} + 10 \text{ GeV})$  for 125 (top left) to 150 GeV (bottom) Higgs mass in 5 GeV step for each mass bin after adding the systematic uncertainties on the total background.

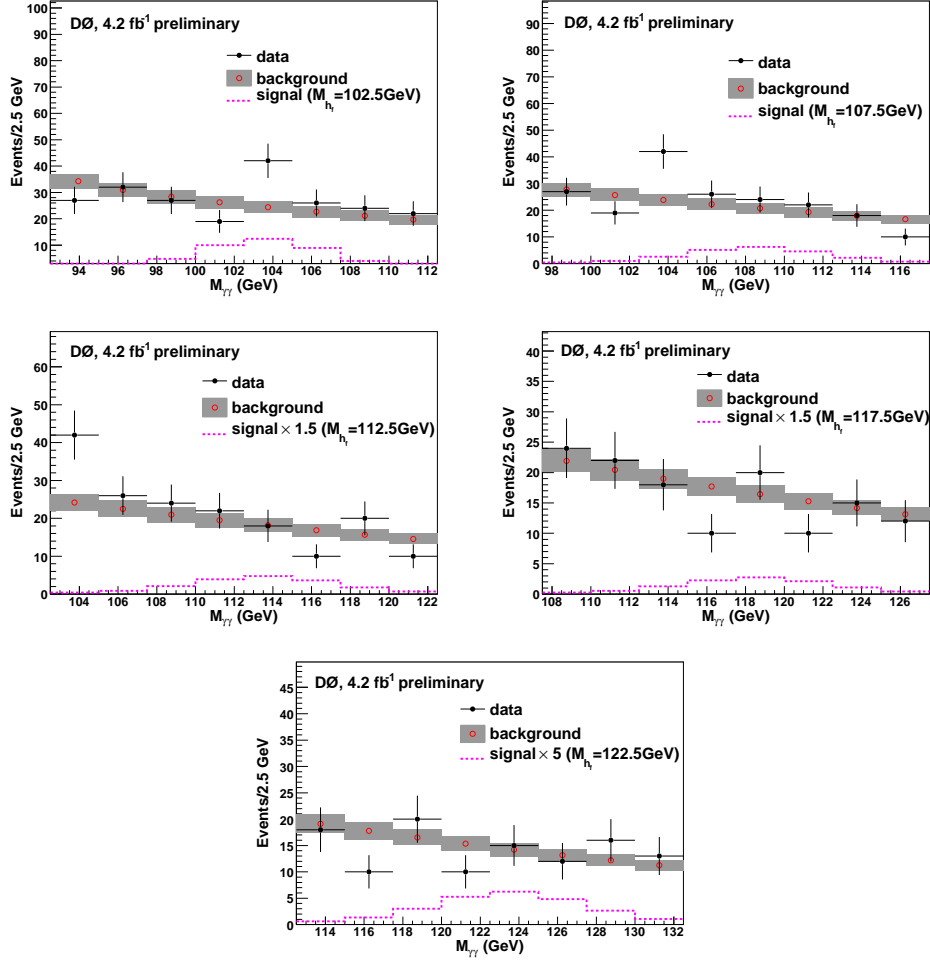


**Figure 4.27** Invariant mass distribution of the two photon candidates in mass interval of  $(M_{h_f} - 10 \text{ GeV}, M_{h_f} + 10 \text{ GeV})$  for the interpolated 102.5 (top left) to 122.5 GeV (bottom) Higgs mass in 5 GeV step for each mass bin after adding the systematic uncertainties on the total background.

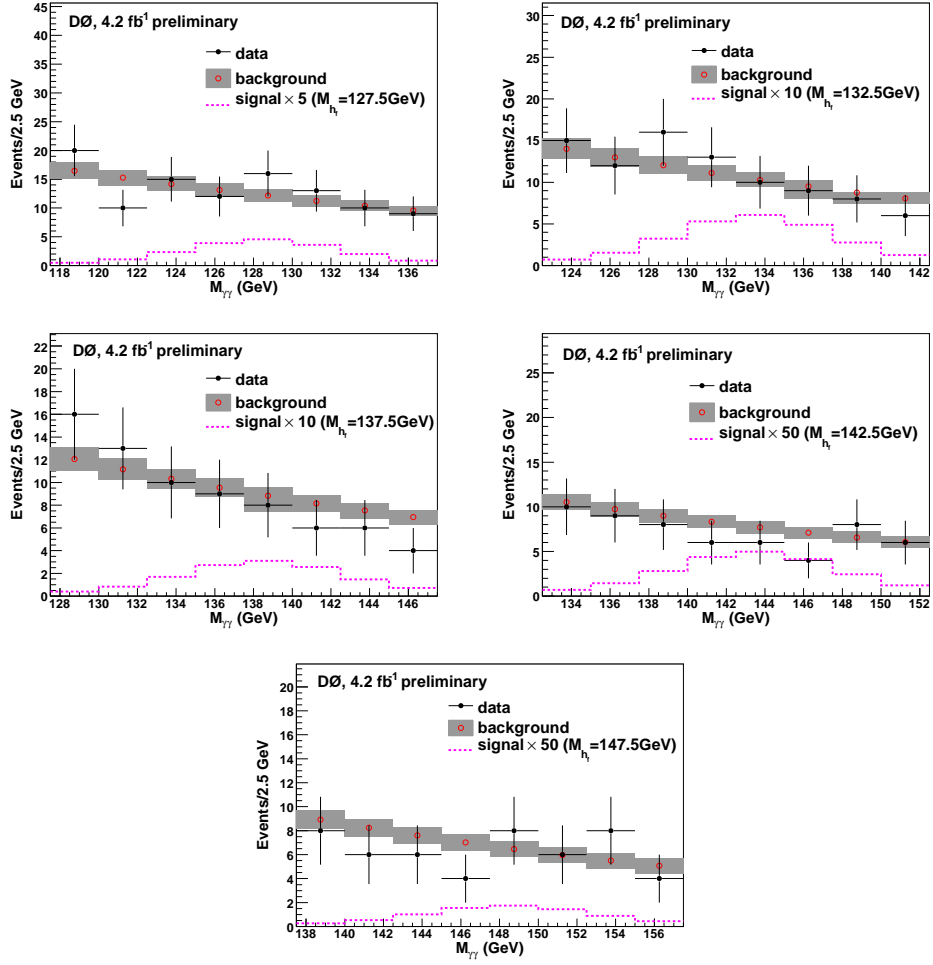


**Figure 4.28** Invariant mass distribution of the two photon candidates in mass interval of  $(M_{h_f} - 10 \text{ GeV}, M_{h_f} + 10 \text{ GeV})$  for the interpolated 127.5 (top left) to 147.5 GeV (bottom) Higgs mass in 5 GeV step for each mass bin after adding the systematic uncertainties on the total background.

We proceed to set upper limits on the Higgs production cross section times branching ratio for Higgs decaying into a pair of photons. The distributions of invariant mass of the two photon candidates in the interval of  $(M_{h_f} - 10 \text{ GeV}, M_{h_f} + 10 \text{ GeV})$  (shown in Figs. 4.25 – 4.28) are used for this purpose. Limits are calculated at the 95% confidence level using the modified frequentist CLs approach with a Poisson log-likelihood ratio test statistic. The impact of systematic uncertainties is incorporated via convolution of the Poisson probability distributions corresponding to the different sources of systematic uncertainty. The correlation in systematic uncertainties are maintained between signal and backgrounds. Table 4.15 and Fig. 4.18(top) show the limits on  $\sigma \times BR(h_f \rightarrow \gamma\gamma)$  for the different Higgs masses. By assuming the SM cross section for the associated and vector boson fusion Higgs production mechanisms, we derive upper limits on the  $BR(h_f \rightarrow \gamma\gamma)$  as a function of Higgs mass (see Fig. 4.18(bottom)). As it can be appreciated, this search considerably extends the range excluded by LEP and a previous DØ result.

$M_{h_f}$	80	90	100	102.5	105	107.5	110	112.5	115	117.5	120
$\sigma \times BR_{obs} \text{ (fb)}$	46.5	61.9	54.3	71.7	80.8	63.7	45.4	33.1	24.3	22.7	23.3
$\sigma \times BR_{exp} \text{ (fb)}$	58.9	51.5	40.2	38.9	37.8	35.5	33.7	33.6	33.0	31.5	29.7

**Table 4.15** 95% C.L. limits on  $\sigma \times BR$  for different fermiophobic Higgs masses from 80 GeV to 120 GeV.

$M_{h_f}$	122.5	125	127.5	130	132.5	135	137.5	140	142.5	145	147.5	150
$\sigma \times BR_{obs} \text{ (fb)}$	26.3	30.6	33.4	31.6	27.5	21.8	17.5	14.7	14.3	16.4	18.1	18.7
$\sigma \times BR_{exp} \text{ (fb)}$	29.4	28.1	27.0	25.4	24.8	23.9	23.0	21.9	21.3	20.7	20.0	22.2

**Table 4.16** 95% C.L. limits on  $\sigma \times BR$  for different fermiophobic Higgs masses from 122.5 GeV to 150 GeV.



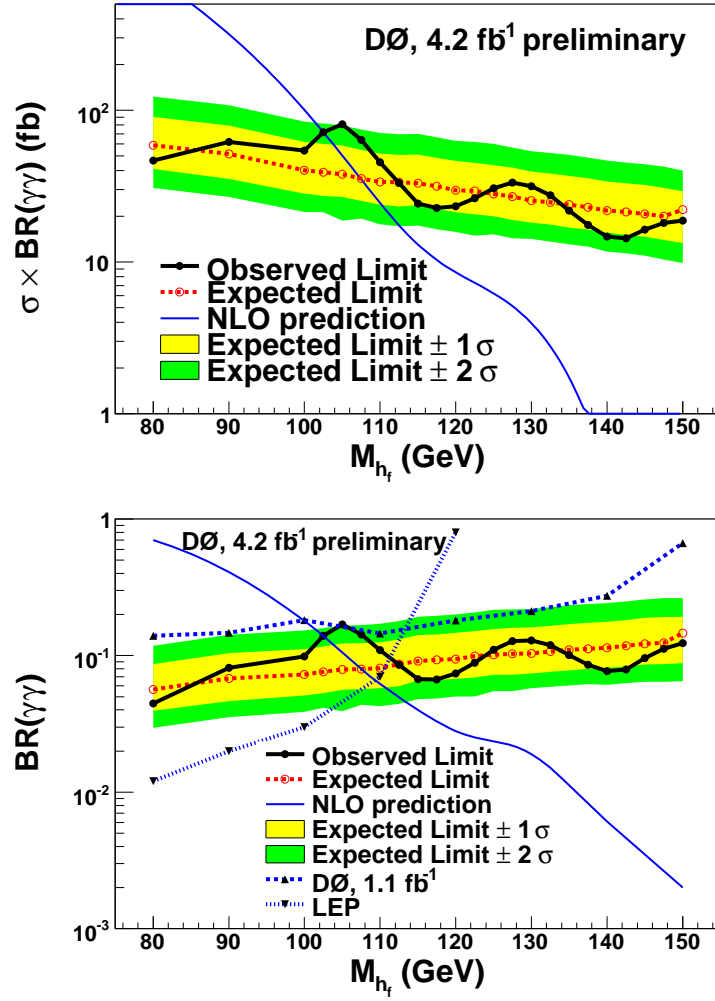


**Figure 4.29** 95% C.L. limits on  $\sigma \times BR$  (top) and  $BR$  (bottom) as a function of fermiophobic Higgs mass.



## Chapter 5 Direct photon pair production differential cross section measurement

As discussed in Section 1.3, especially illustrated by the latest  $D\bar{O} \ H \rightarrow \gamma\gamma$  search results (Chapter 4), we know the DPP production with large diphoton invariant mass ( $M_{\gamma\gamma}$ ) constitutes a large and irreducible background to searches for the Higgs boson and other new phenomena. Thus, precise measurements of the diphoton differential production cross sections for various kinematic variables and the validation of theoretical predictions understanding are extremely important.

In addition, DPP production is interesting in its own right, and is used to check the validity of the predictions of pQCD and soft-gluon resummation methods implemented in theoretical calculations. Measurements involving the diphoton final state have been previously carried out at fixed-target<sup>[53,54]</sup> and collider experiments<sup>[55–57]</sup>. However, the large integrated luminosity accumulated by the  $D\bar{O}$  experiment in  $p\bar{p}$  collisions at  $\sqrt{s} = 1.96$  TeV at the Fermilab Tevatron Collider allows us to perform precise measurements of several observables in kinematic regions previously unexplored, as well as, for the first time, the measurement of double differential cross sections for this process.

In this chapter, we will present the latest and first DPP cross section measurements at  $D\bar{O}$  with using  $4.2 \text{ fb}^{-1}$  data. We measure single differential isolated DPP production cross sections

(see Eq. 5.1) in bins of the diphoton invariant mass ( $M_{\gamma\gamma}$ ), the total transverse momentum of diphoton system ( $p_T^{\gamma\gamma}$ ), the azimuthal angle ( $\Delta\phi_{\gamma\gamma}$ ) and the polar scattering angle ( $\cos\theta^*$ ) between the two photons (Here  $\theta^*$  is defined as  $\tanh(\eta^*)$ , where  $\eta^* = (\eta_1 - \eta_2)/2$  with  $\eta_{1(2)}$  being the pseudorapidity of the (next-to-) highest  $p_T$  photon.). The results are compared with theoretical predictions from three theoretical codes, RESBOS<sup>[15]</sup>, DIPHOX<sup>[16]</sup> and PYTHIA<sup>[13]</sup>.

$$\frac{d\sigma}{dX} = \frac{N_{data} - N_{bkg}}{L \cdot A_{cc} \cdot \epsilon_{trigger} \cdot \epsilon_{sel} \cdot \Delta X} \quad (5.1)$$

where

- $X$  is the measured kinematic variable of interest;
- $N_{data}$  is the number of data events;
- $N_{bkg}$  is the number of background events;
- $L$  is the instantaneous luminosity;
- $A_{cc}$  is the acceptance;
- $\epsilon_{trigger}$  is the trigger efficiency;
- $\epsilon_{sel}$  is the di-photon selection efficiency;
- $\Delta X$  is the bin width for the variable  $X$ .

## 5.1 Review of previous Tevatron Run II measurements

The first Run II measurements of DPP cross sections are published by CDF with using 207  $pb^{-1}$  data set<sup>[57]</sup>. It has 889

diphoton candidates after requiring transverse momentum  $p_T > 14$  (13) GeV for the highest (next-to-highest)  $p_T$  photon candidate,  $|\eta_{1(2)}| < 0.9$  and isolation energy less than 1 GeV.

The measured cross section as a function of diphoton mass is shown in Fig. 5.1, which shows agreement between data and NLO theoretical predictions. However, due to the poor statistics, the data and theory comparison is limited to the  $M_{\gamma\gamma} < 100$  GeV phase space, which is lower than the crucial  $M_{\gamma\gamma} > 100$  GeV region to the current Higgs and NP search. Also, the inset plot shows the  $gg$  contribution is important to the low  $M_{\gamma\gamma}$  region. Furthermore, they also measured the differential cross sections as a function of diphoton transverse momentum ( $q_T$ ) and azimuthal angle between the two photons ( $\Delta\phi_{\gamma\gamma}$ ). The corresponding results could be found in Figs. 5.2 and 5.3. As one can see, at low to moderate  $q_T$  and  $\Delta\phi_{\gamma\gamma}$  greater than  $\pi/2$ , where the effects of soft gluon emission are important, the data turns to agree with RESBOS. By contrast, in the large  $q_T$ ,  $\Delta\phi_{\gamma\gamma}$  less than  $\pi/2$  and low  $M_{\gamma\gamma}$ , the data turns to agree with DIPHOX, which has full NLO fragmentation contributions.

Overall, the results shows the need of the resummed full NLO calculation for achieving better agreement between the data and theoretical predictions.

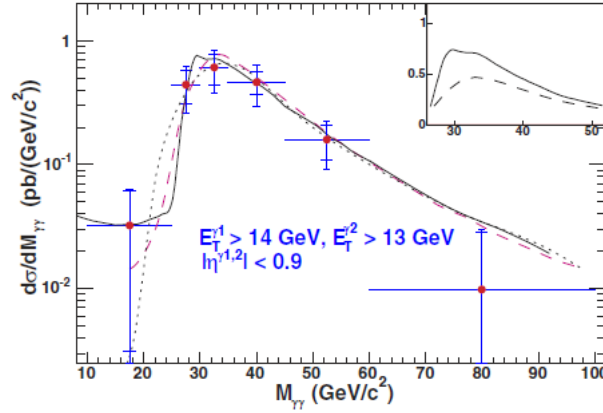


**Figure 5.1** The  $\gamma\gamma$  mass distribution from the CDF Run II data, along with predictions from DIPHOX (solid line), RESBOS (dashed line), and PYTHIA (dot-dashed line). The PYTHIA predictions have been scaled by a factor of 2. The inset shows, on a linear scale, the total  $\gamma\gamma$  cross section in DIPHOX with (solid line)/without (dashed line) the  $gg$  contribution.

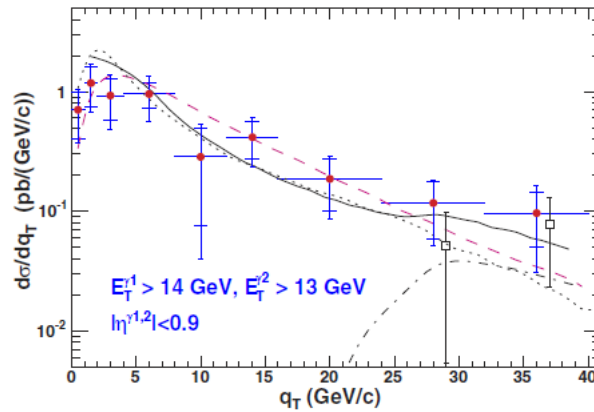


**Figure 5.2** The  $\gamma\gamma$   $q_T$  distribution from the CDF Run II data, along with predictions from DIPHOX (solid line), RESBOS (dashed line), and PYTHIA (dot-dashed line). The PYTHIA predictions have been scaled by a factor of 2. Also shown, at larger  $q_T$ , are the DIPHOX prediction (dotted line) and the CDF Run II data (open squares: shifted to the right by 1 GeV for visibility) for the configuration where the two photons are required to have  $\Delta\phi_{\gamma\gamma} < 2$  rad..

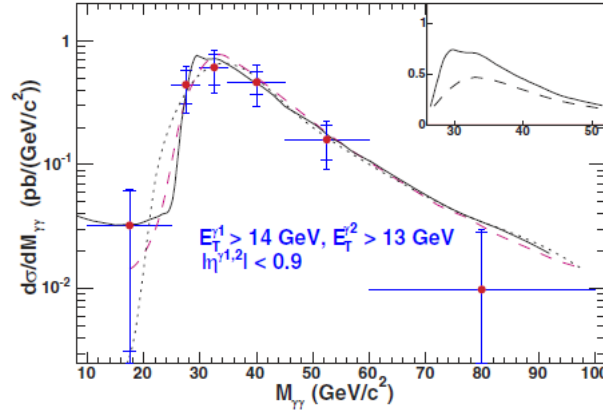


**Figure 5.3** The azimuthal angle between the two photons ( $\Delta\phi_{\gamma\gamma}$ ) from the CDF Run II data, along with predictions from DIPHOX (solid line), RESBOS (dashed line), and PYTHIA (dot-dashed line). The PYTHIA predictions have been scaled by a factor of 2.

## 5.2 Data samples

The data used in this analysis were collected by the DØ detector between August 2006 and June 2009. We use the same calorimeter only di-em triggers as the  $H \rightarrow \gamma\gamma$  search (see Section 4.1). Events with only good luminosity blocks and run number are used. Runs during which the tracking system or the calorimeter was not fully functional are removed. The total integrated luminosity of the sample is  $4.2 \pm 0.3 \text{ fb}^{-1}$ . The corresponding trigger efficiency  $\epsilon_{trigger}$  as a function of leading and sub-leading EM cluster  $E_T$  is shown in Fig. 5.4, which is calculated using  $Z \rightarrow ee$  data (Section 4.1) and found to be very high, varied as 94–100%. It is used in Eq. 5.1 to calculate cross sections and also to weight MC events to calculate acceptance and efficiencies.

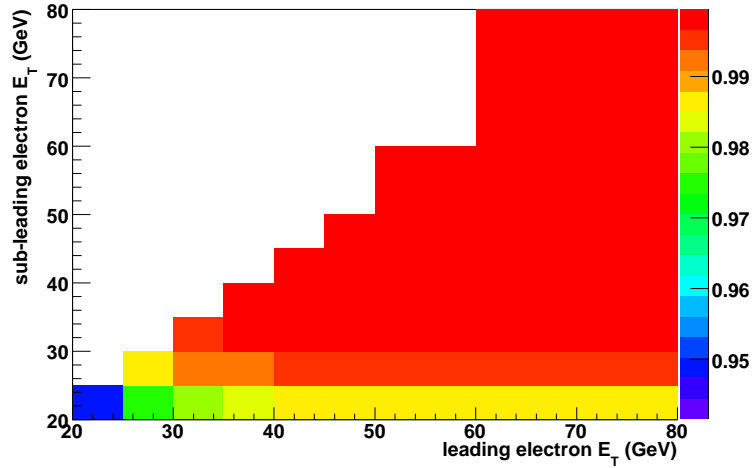


**Figure 5.4** v15 and v16 calorimeter-only di-em trigger efficiency as a function of leading and sub-leading EM cluster  $E_T$ .



### 5.3 Event selection and binning

#### 5.3.1 Event selection and selection efficiencies

The vertex selection is important for the photon involved analyzes (see Section 3.1), especially for the diphoton final states. In this analysis, the primary vertex with the maximum number of tracks ( $maxtrk$ ) associated to it is selected for each event, and the  $z$ -coordinate of this vertex ( $z_{vtx}$ ) is required to be within 60 cm from the geometrical center of the detector. It should be noted that for diphoton events the default primary vertex from d0reco does not always match the best primary vertex with respect to which the photon 4-momentum are computed). Therefore, a revertexing of the photon candidates to the selected vertex is required. All photon kinematic variables ( $p_T$ ,  $\eta$ ,  $\phi$  etc) are recalculated with respect to the new  $maxtrk$  vertex. As shown in Section 3.1, the vertex with largest track multiplicity has a higher probability to match the true hard scatter vertex. Table 5.1 shows the fraction of events where the reconstructed vertex, either the one largest track multiplicity ( $maxtrk$ ) or default one with lowest minbias probability, are matched to the true one as well as the  $maxtrk$  vertex matched to the default one within  $|dz| < 1$  cm using  $Z \rightarrow ee$  data, MC and DPP PYTHIA full MC events. To get better agreement with data, the MC events are reweighted according to the number of vertexes observed in data. Also, in order to choose the  $maxtrk$  vertex in the  $Z \rightarrow ee$  events (in both data and MC) we have subtracted 2 tracks from  $Z$ -boson pointing to the vertex. One can see that for just 65% diphoton events

the default reco vertex matches within  $|dz| < 1$  cm with the true vertex while this fraction increases to 80% for the *maxtrk* vertex. Thus, the new vertexing algorithm has much better performance for diphoton events. Also Fig. 5.5 shows the primary vertex selection efficiency versus mass from PYTHIA MC samples with using the new and default d0reco vertex, which demonstrates such efficiency is pretty high ( $\sim 100\%$ ) for both cases, and gives us the hints that the mis-vertexing rate dominates in the systematics by comparison with the primary vertex selection efficiency.

To estimate such mis-vertexing rate in data for the *maxtrk* vertex in the diphoton events, we have considered  $Z \rightarrow ee$  data events and required very tight quality cuts for the two electron tracks pointing to the default vertex (in such a way it can be treated as a “true” vertex). Then we have estimated how often the *maxtrk* vertex (with subtracted 2 tracks) in the event agrees within  $|dz| < 1$  cm with the “true” one. We have found that it happens in about 65% cases. We use this number in Section 5.4 when we calculate diphoton acceptance, assigning a 23% uncertainty (obtained from  $80/65=1.23$ ) for this mis-vertexing rate.

$ dz $	Zee data	Zee MC	DPP MC
$dz_{def,true}$	-	80%	65%
$dz_{maxtrk,true}$	-	80%	80%
$dz_{def,maxtrk}$	65%	80%	80%

**Table 5.1** Fraction of events by requiring the distance in  $z$  ( $dz$ ) between true vertex and default vertex or the vertex with maximum multiplicity (*maxtrk*) within  $|dz| < 1$  cm.

Except the above primary vertex selection requirement, in this analysis, at least two EM cluster are selected in each event.

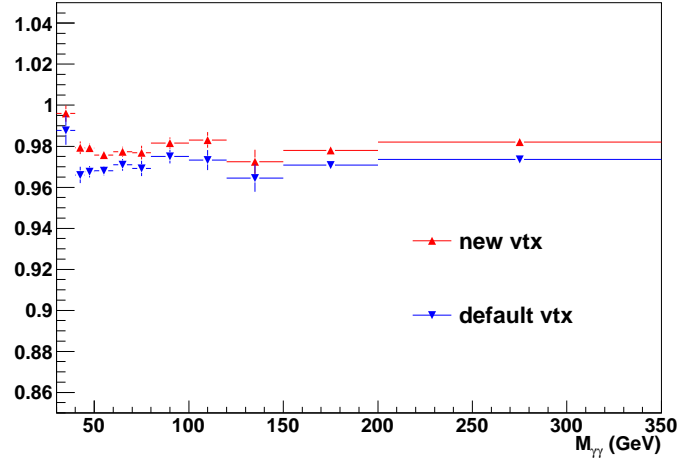


**Figure 5.5** Primary vertex selection efficiency with requiring  $z_{vtx} < 60$  cm versus the di-photon mass with using the maxtrk (new) and reco vertex.

The leading and sub-leading (in  $p_T$ ) EM clusters should both satisfy:

- $|\eta| < 0.9$
- be in calorimeter fiducial region
- leading photon  $E_T^1 > 21.0$  GeV and sub-leading photon  $E_T^2 > 20.0$  GeV
- EM energy fraction:  $f_{EM} > 0.97$
- Calorimeter isolation:  $f_{iso} < 0.07$
- Tracker isolation:  $p_{T\text{trk}}^{\text{sum}} < 1.5$  GeV
- EM shower shape:  $sigphi < 18$  cm<sup>2</sup>
- Photon ANN:  $O_{NN} > 0.3$
- No-track matching:  $P_{trk} < 0.0$  and  $D_{hor} > 0.9$
- $\Delta R_{\gamma\gamma} > 0.4$

- $M_{\gamma\gamma} > p_T^{\gamma\gamma}$ .

, where we have limited our phase space to the  $M_{\gamma\gamma} > p_T^{\gamma\gamma}$  region. This requirement significantly reduces contribution from fragmentation processes and thus reduce dependence of predictions on tunable isolation parameters and factorization scale. It restricts data-to-theory comparisons to region where theory is best understood and uncertainties are smaller. More related discussion could be found in Ref.<sup>[15]</sup>.

After applying all the above event selection cuts and corresponding scale factors (Section 3.5), the overall diphoton selection efficiency was estimated using pythia DPP sample. The efficiency as a function of  $M_{\gamma\gamma}, p_T^{\gamma\gamma}, \Delta\phi_{\gamma\gamma}$  and  $\cos\theta^*$  is shown in Fig. 5.6. The corresponding systematic uncertainties are shown in Table 5.2.

sources	systematic uncertainty (%)
General ID efficiency	1.0
“No-track match” efficiency	2.0
$O_{NN} > 0.3$ efficiency	1.5
difference between e and $\gamma$	1.0
Total	2.9

**Table 5.2** The systematic uncertainty for per-photon selection efficiencies.

### 5.3.2 Binning

The data must be binned appropriately. There are two major guidelines to define the appropriate binning:

- The first one is very straightforward, it is the statistics of the data events. We require that the estimated number of equivalent diphoton events per bin is  $> 10$ , so that  $\sqrt{\sum w_i^2}$

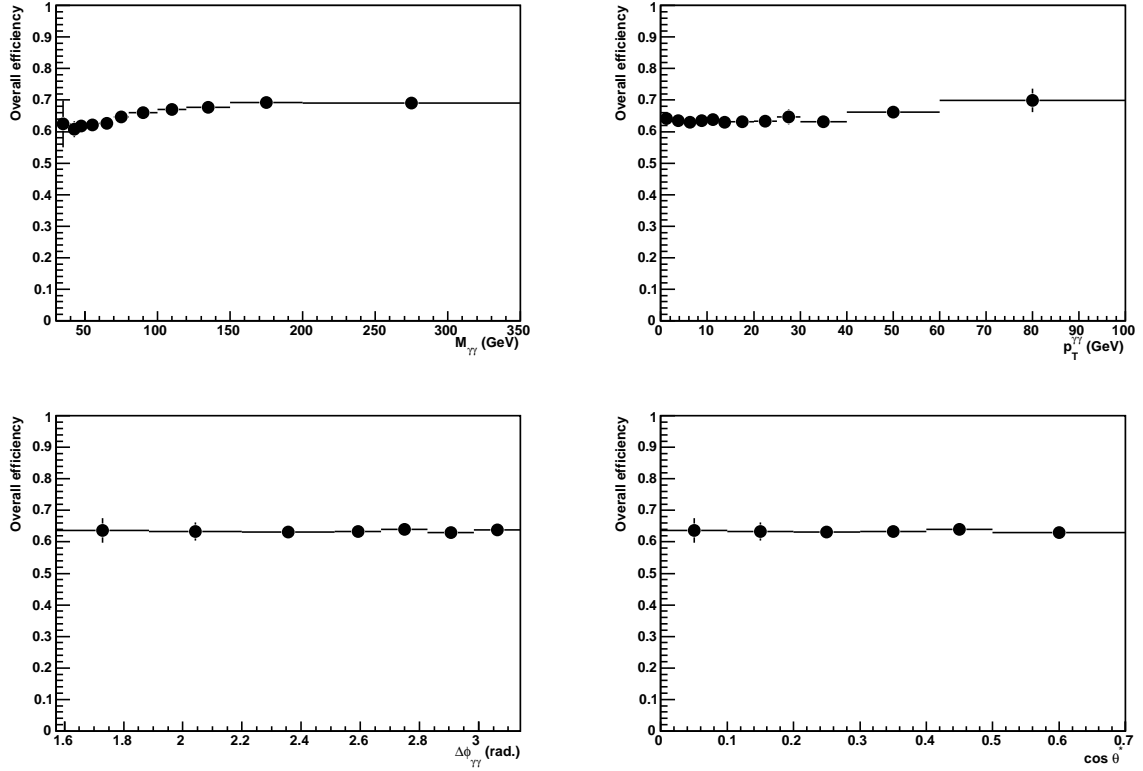


**Figure 5.6** Overall diphoton selection efficiency (with only statistical uncertainty) versus  $M_{\gamma\gamma}$ ,  $p_T^{\gamma\gamma}$ ,  $\Delta\phi_{\gamma\gamma}$  and  $\cos\theta^*$ .

is a good approximation to the statistical error in the bin. Here  $w_i$  is the event-by-event diphoton weight computed by the 4x4 matrix method (see Section 4.3.2).

- The other is the bin purity, which would give one an idea about the migration across the bins. It is desirable to have bin purities of the order of 50% or larger (see Appendix 8.7).

The binning we used are the following:

- 10 bins used for  $M_{\gamma\gamma}$  distribution (15 GeV bin width from 30 to 45 GeV, 5 GeV bin width from 45 to 50 GeV, 10 GeV bin width from 50 to 80 GeV, 20 GeV bin width from 100 to 120 GeV, 30 GeV bin width from 120 to 150 GeV, 50 GeV

bin width from 150 to 200 GeV and then 150 GeV bin width from 200 to 350 GeV);

- 12 bins used for  $p_T^{\gamma\gamma}$  distribution (2.5 GeV bin width from 0 to 15 GeV, 5 GeV bin width from 15 to 30 GeV, 10 GeV bin width from 30 to 40 GeV, 20 GeV bin width from 40 to 60 GeV and then 40 GeV bin width from 60 to 100 GeV);
- 7 bins used for  $\Delta\phi_{\gamma\gamma}$  distribution (0.1 $\pi$  bin width from 0.5 $\pi$  to 0.8 $\pi$ , 0.05 $\pi$  bin width from 0.8 $\pi$  to  $\pi$ );
- 6 bins used for  $\cos\theta^*$  distribution (0.1 bin width from 0 to 0.5 and 0.2 bin width from 0.5 to 0.7).

#### 5.4 Acceptance

The acceptance is calculated as:

$$Acc = \frac{N_{reco}^{bin\ i}}{N_{gen}^{bin\ i}} \quad (5.2)$$

for four variables:  $M_{\gamma\gamma}$ ,  $p_T^{\gamma\gamma}$ ,  $\Delta\phi_{\gamma\gamma}$  or  $\cos\theta^*$ ,  $N_{reco}^{bin\ i}$  and  $N_{gen}^{bin\ i}$  are number of events in bin  $i$  at the reconstruction level and the generator level.

The generator level events are required to have  $p_T^{1(2)} > 21$  (20) GeV,  $|\eta^{1(2)}| < 0.9$ ,  $M(\gamma\gamma) > p_T^{\gamma\gamma}$ ,  $\Delta R_{\gamma\gamma} > 0.4$ ,  $\sum_{particles}^{\Delta R < 0.4} p_T < 2.5$  GeV ( $\sum_{particles}^{\Delta R < 0.4} p_T$  is the scalar sum of all stable particles generated around the photon candidate within  $\Delta R < 0.4$ ). At the reconstructed level we require photons with  $p_T^{1(2)} > 21$  (20) GeV,  $|\eta^{1(2)}| < 0.9$ ,  $|\eta_{det}^{1(2)}| < 0.9$ ,  $f_{EM} > 0.90$ ,  $f_{iso} < 0.20$ ,

in CC calorimeter fiducial regions, also with  $M_{\gamma\gamma} > p_T^{\gamma\gamma}$  and  $30 < M_{\gamma\gamma} < 350$  GeV.

The acceptance and related systematic uncertainties are calculated using the events generated with RESBOS and also using the parameterized fast MC simulation (Section 3.6) (in this case,  $N_{reco}^{bini}$  corresponds to the number of events obtained in a given bin  $i$  after the fast MC simulation).

In the fast MC simulation, photons are extrapolated from the (randomized by a Gaussian) primary vertex position to the position of the third layer of the electromagnetic calorimeter. Photons are then scaled and smeared according to the measured energy scale and resolution and also angular resolution. The test of fast MC for the electron energy resolution and energy scale is shown in Section 3.6.4 using  $Z \rightarrow ee$  events. It also shows a comparison of electron and photon resolutions and confirms their good agreement. Photon reconstruction efficiencies described in Section 3.5 and the trigger efficiency (Fig. 5.4) measured from data are applied to the fast MC parameterization.

The phimod shift due to the position bias on the reconstruction EM cluster is also applied<sup>[58]</sup>. The default RMS of the beamspot position used in the fast MC simulation is 25 cm, the photon energy scale is 1.003 and the constant term for the energy resolution is 2.25%<sup>[58]</sup>. The  $\eta$  and  $E$ -dependent sampling term determined by the  $W$  mass group is used<sup>[58]</sup>. These smearing numbers have been re-tuned based on Run IIb data (Section 3.6.4).

A size of the bin-to-bin migration effect for the chosen binning is studied in Appendix 8.7.

As we mentioned above, for the acceptance calculation we have used the events simulated with the NLO predictions based on RESBOS. Since for the acceptance vs.  $M_{\gamma\gamma}$ ,  $\Delta\phi_{\gamma\gamma}$ ,  $p_T^{\gamma\gamma}$  and  $\cos\theta^*$  the correct spectrum over these variables is important (to better take into account the bin-by-bin migration effects), we have calculated acceptance in two steps:

- First, we have calculated acceptance using the default RESBOS and then used it together with luminosity, efficiencies and the di-photon purity (Section 5.5) to obtain the preliminary cross-sections.
- Then we have re-weighted the RESBOS events according to the observed difference, which is shown in Fig. 8.21 of Appendix 8.8.

Then for the final acceptance we have used individually re-weighted spectra for each of the four variables. The overall acceptance for all the four variables is shown in Fig. 5.7. Also, Figs. 8.24 – 8.28 compare results for the acceptances when we used for a given variable the reweighted events using the spectra for all the four variables. The comparison with the default acceptance, based on the non-reweighted RESBOS, is also shown. One can see that for almost all the cases those variations agree within 3-4%.

The smearing parameters in the fast MC simulation can af-



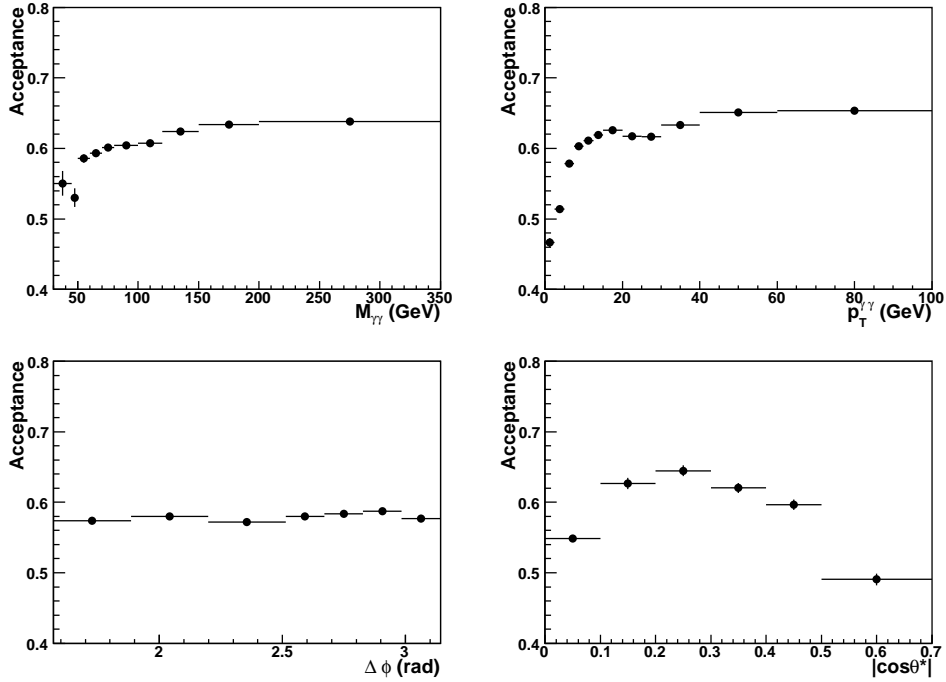


**Figure 5.7** Acceptance as a function of  $M_{\gamma\gamma}$ ,  $p_T^{\gamma\gamma}$ ,  $\Delta\phi_{\gamma\gamma}$  and  $\cos\theta^*$ .

fect the bin-to-bin migration at the detector (reco) level, and thus change the final unfolded distributions. To estimate the systematic uncertainties, we allow these parameters to vary by one standard deviation and regenerate the detector level distributions and obtain new unfolded distributions. The differences between the unfolded results using the varied parameters and the default parameters are assigned as the systematic uncertainties. The uncertainties on these parameters are mainly obtained from collider data and  $W$  boson mass analysis[58].

We vary the RMS of beamspot position by  $\pm 10\%$  (“Vtx Resol” uncertainty), the photon energy scale by  $\pm 0.5\%$  (“E Scale” uncertainty), the constant term for the energy resolution by  $\pm 5\%$  (“E Resol” uncertainty) and the phimod shift by  $\pm 20\%$  to esti-

mate the uncertainties on the acceptance (“PhiMod” uncertainty)<sup>[58]</sup>. The default mis-vertexing rate used in the fast MC simulation is 65%, and we vary it with a relative uncertainty of  $\pm 23\%$  (see Table 5.1) to estimate the systematic uncertainty (“Vtx MisMatching” uncertainty). The systematic uncertainties on the four distributions are shown in Tables 5.3, 5.4, 5.5 and 5.6 respectively.

As expected, due to the requirement that both photons must be in the fiducial region of the CC EM calorimeter, the overall acceptance is dominated by the  $\phi$  fiducial requirement, which is expected to be around 64% for two photons (Briefly, the DØ calorimeter in the central (CC) region is splitted in detector  $\phi$  in 32 modules with cracks between them (Section 2.2.3). We call region “fiducial in  $\phi$ ”, if the EM cluster position (at EM3) in  $\phi$  is located by  $\geq 0.02$  from the crack. Thus, applying requirement “fiducial in  $\phi$ ” for each module we “lose”  $\sim 0.04/0.20 = 20\%$  of the acceptance per EM object). That is really the case for MC. For data, due to data/MC difference in implementation of the charge collection in liquid argon, and energy leakage to the crack, we have different shifts of the EM cluster position with respect to the crack (more in MC then in data). Therefore, we have to apply the correction factor found from the tracks/EMclusters in  $Z \rightarrow ee$  events. This factor is 13–14% and increases our acceptance in  $\phi$  from 0.64 to 0.73. The distributions for four variables are shown in Fig. 5.8. The parameterizations used in the fast MC simulation is based on studies done in  $W$  boson mass group<sup>[58]</sup>.

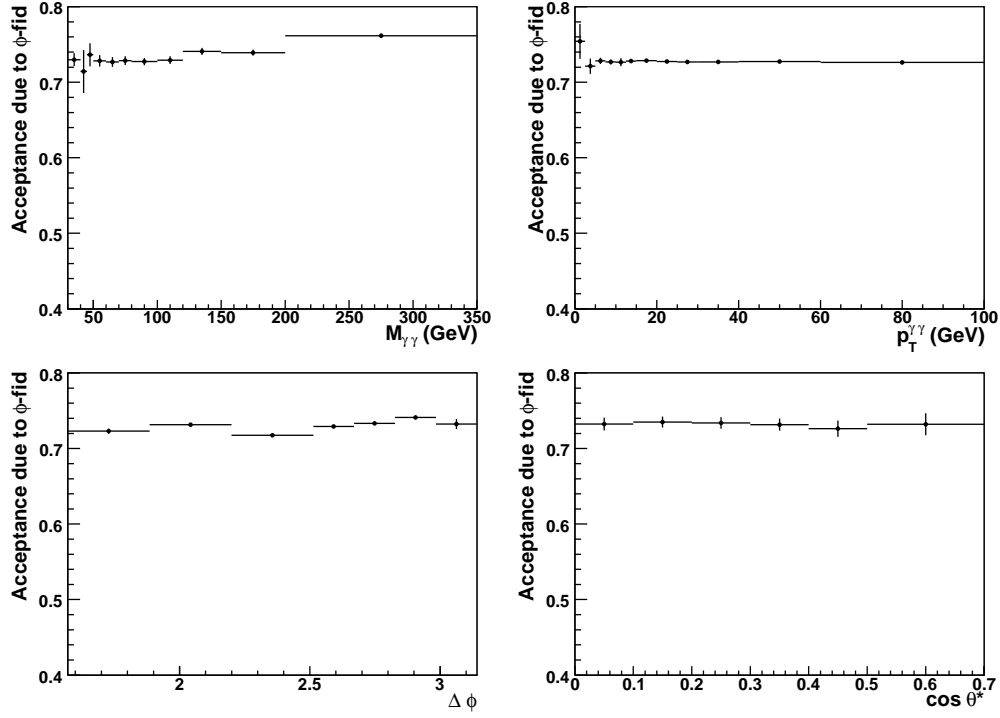


**Figure 5.8** Acceptance due to  $\phi$ -fiducial requirement as a function of  $M_{\gamma\gamma}$ ,  $p_T^{\gamma\gamma}$ ,  $\Delta\phi$  and  $\cos\theta^*$ .

$M_{\gamma\gamma}$ bin	Acc	Stat (%)	Vtx Reso (%)	Vtx MisMatching (%)	E Scale (%)	E Reso (%)	PhiMod (%)	Overall syst.(%)
0	0.55	1.17	-1.61	1.65	-0.15	0.10	2.07	3.09
			1.80	-6.13	-0.94	-0.07	-2.30	-6.76
1	0.53	2.47	-1.82	3.24	1.24	-0.04	1.86	4.33
			0.24	-3.99	-1.99	-0.01	-1.96	-4.87
2	0.59	1.02	-1.45	1.82	1.35	-0.02	1.77	3.22
			1.88	-0.46	-0.90	0.06	-1.90	-2.86
3	0.59	0.83	-1.46	0.22	1.72	0.04	1.87	2.94
			1.38	-0.48	-1.54	-0.03	-2.00	-2.91
4	0.60	0.80	-1.75	0.66	1.23	-0.02	1.77	2.85
			1.52	0.67	-1.39	0.00	-2.09	-3.01
5	0.60	0.62	-1.51	-0.83	1.44	0.02	1.67	2.80
			1.58	-0.39	-1.42	0.06	-1.94	-2.90
6	0.61	0.68	-1.57	0.28	1.29	-0.02	1.80	2.73
			1.62	0.73	-1.21	-0.06	-2.12	-3.02
7	0.62	0.61	-1.44	0.28	1.48	0.03	1.71	2.69
			1.44	0.23	-1.40	0.01	-1.90	-2.78
8	0.63	0.53	-1.55	0.55	1.38	0.02	1.74	2.76
			1.63	0.33	-1.37	-0.00	-1.86	-2.85
9	0.64	0.40	-1.53	-0.12	1.59	-0.01	1.56	2.70
			1.45	-1.37	-1.63	-0.01	-1.83	-3.16

**Table 5.3** Acceptance with statistical and systematic uncertainties (in %) in  $M_{\gamma\gamma}$  bins. The two numbers in each box correspond to  $+1\sigma$  and  $-1\sigma$  variations.

$p_T^{\gamma\gamma}$ bin	Acc	Stat (%)	Vtx Reso (%)	Vtx MisMatching (%)	E Scale (%)	E Reso (%)	PhiMod (%)	Overall syst.(%)
0	0.46	1.60	-1.60	3.46	0.99	-0.08	1.45	4.20
			0.77	-7.95	-0.59	0.16	-1.48	-8.14
1	0.51	0.42	-2.14	5.65	1.07	-0.09	1.95	6.44
			2.57	-2.14	-0.96	0.12	-2.16	-4.09
2	0.58	0.26	-1.59	1.13	1.38	-0.03	1.80	2.99
			1.64	-0.35	-1.25	-0.01	-1.97	-2.87
3	0.60	0.34	-1.68	-0.16	1.35	0.05	1.78	2.80
			1.15	0.26	-1.31	-0.04	-2.05	-2.70
4	0.61	0.23	-1.38	-0.77	1.44	0.07	1.75	2.77
			1.36	0.61	-1.49	-0.06	-2.10	-2.98
5	0.62	0.24	-1.14	-1.42	1.57	0.04	1.79	3.00
			1.09	0.78	-1.50	-0.01	-2.00	-2.84
6	0.63	0.20	-1.23	-1.27	1.51	0.04	1.74	2.91
			1.18	1.74	-1.59	-0.05	-2.00	-3.30
7	0.62	0.24	-1.22	-1.40	1.62	0.01	1.80	3.06
			1.09	1.02	-1.66	-0.04	-2.06	-3.04
8	0.62	0.27	-1.19	-0.99	1.60	0.07	1.81	2.87
			1.01	1.26	-1.62	-0.00	-2.06	-3.08
9	0.63	0.23	-1.18	-1.26	1.74	0.04	1.81	3.05
			1.18	0.97	-1.72	-0.05	-2.03	-3.07
10	0.65	0.23	-1.16	-1.01	1.76	0.03	1.78	2.94
			1.11	0.83	-1.77	-0.02	-2.00	-3.01
11	0.65	0.31	-1.22	-0.49	1.95	0.02	1.83	2.98
			1.28	1.33	-1.90	-0.02	-2.14	-3.41

**Table 5.4** Acceptance with statistical and systematic uncertainties (in %) in  $p_T^{\gamma\gamma}$  bins. The two numbers in each box correspond to  $+1\sigma$  and  $-1\sigma$  variations.

$\Delta\phi$ bin	Acc	Stat (%)	Vtx Reso (%)	Vtx MisMatching (%)	E Scale (%)	E Reso (%)	PhiMod (%)	Overall syst.(%)
0	0.57	0.44	-1.68	0.41	1.67	0.01	1.86	3.04
			1.49	-1.45	-1.69	-0.02	-2.10	-3.41
1	0.58	0.33	-1.57	0.91	1.72	-0.00	1.68	3.01
			1.57	-1.14	-1.73	0.02	-1.92	-3.23
2	0.57	0.20	-1.64	1.15	1.70	-0.01	1.90	3.24
			1.57	-1.25	-1.71	0.03	-2.19	-3.43
3	0.58	0.21	-1.68	1.17	1.51	-0.01	1.80	3.12
			1.52	-1.20	-1.58	0.00	-1.98	-3.19
4	0.58	0.17	-1.57	0.97	1.43	-0.01	1.67	2.87
			1.53	-1.49	-1.55	0.01	-1.92	-3.26
5	0.59	0.15	-1.61	1.46	1.46	-0.01	1.63	3.09
			1.54	-1.10	-1.40	0.02	-1.86	-3.00
6	0.57	0.94	-1.48	1.15	1.20	0.00	1.75	2.83
			1.28	-0.75	-1.08	0.02	-1.99	-2.71

**Table 5.5** Acceptance with statistical and systematic uncertainties (in %) in  $\Delta\phi_{\gamma\gamma}$  bins. The two numbers in each box correspond to  $+1\sigma$  and  $-1\sigma$  variations.

$\cos \theta^*$ bin	Acc	Stat (%)	Vtx Reso (%)	Vtx MisMatching (%)	E Scale (%)	E Reso (%)	PhiMod (%)	Overall syst.(%)
0	0.58	1.28	-1.19	2.82	1.27	-0.06	1.71	3.73
			1.52	-1.41	-1.22	0.02	-2.00	-3.13
1	0.60	1.24	-1.43	1.81	1.09	-0.02	1.82	3.14
			0.97	-1.86	-1.38	-0.00	-1.90	-3.15
2	0.60	1.22	-1.24	0.65	1.50	0.07	1.75	2.69
			1.30	-0.12	-1.22	0.04	-1.95	-2.65
3	0.60	0.98	-1.61	0.14	1.60	0.00	1.65	2.81
			1.26	-2.09	-1.39	0.02	-1.93	-3.41
4	0.57	1.29	-1.95	-0.39	1.44	-0.02	1.88	3.09
			1.64	-0.14	-1.06	0.04	-1.99	-2.79
5	0.49	1.54	-2.60	0.45	1.40	0.02	1.83	3.51
			2.64	1.24	-1.28	-0.00	-2.12	-3.82

**Table 5.6** Acceptance with statistical and systematic uncertainties (in %) in  $\cos \theta^*$  bins. The two numbers in each box correspond to  $+1\sigma$  and  $-1\sigma$  variations.

## 5.5 Backgrounds

There are two major sources of background events to the DPP production: (i) Drell-Yan events, (see Fig. 4.4) when both electrons are misidentified as photons due to the tracking inefficiencies. This contribution is estimated by using Monte Carlo simulations (with SF from Section 3.5); (ii)  $\gamma$ +jet and di-jet events (see Fig. 4.5), where the jet(s) are mis-identified as photon(s). This contribution is estimated from data by using the  $4 \times 4$  matrix method (see Section 4.3.2). The minor  $W + jet/\gamma$  background with  $W \rightarrow e\nu$  decay has been estimated from MC and found to be negligible.

### 5.5.1 Drell-Yan $Z/\gamma^* \rightarrow ee$ contributions

We use  $Z/\gamma^* \rightarrow ee$  PYTHIA MC samples to estimate Drell-Yan contribution. The NNLO  $p\bar{p} \rightarrow Z/\gamma^* \rightarrow ee$  cross section is used for the absolute normalization and the generator level  $Z/\gamma^*$  boson  $p_T$  has been re-weighted to the measured data distribution. The expected number of events from Drell-Yan process in the whole invariant mass region 30–350 GeV is  $161 \pm 10$  (stat).

### 5.5.2 $\gamma$ +jet and di-jet background

We estimate the contributions from  $\gamma$ +jet and di-jet events in data using a  $4 \times 4$  matrix background subtraction method (see Section 4.3.2). The corresponding results is shown in Table 5.7.

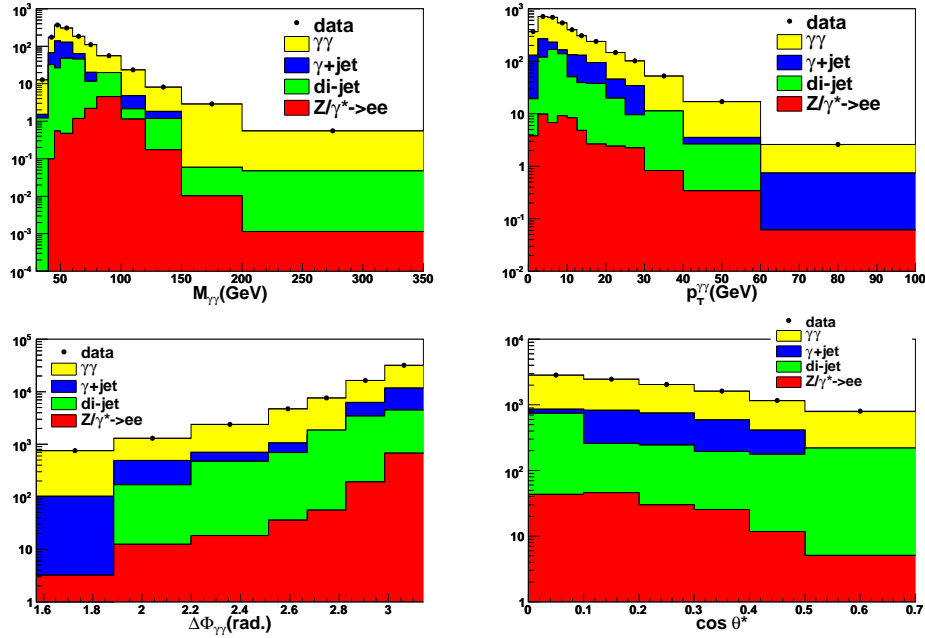
### 5.5.3 Di-photon purity

Fig. 5.9 shows contributions from signal and different backgrounds as they are determined using the matrix method in data

Total	10938
Total - $N_{DY}$	10777
$N_{\gamma\gamma}$	$7307 \pm 312$
$N_{\gamma j + j\gamma}$	$1791 \pm 411$
$N_{jj}$	$1679 \pm 281$
$N_{non-\gamma\gamma}$	$3470 \pm 498$

**Table 5.7** The total numbers of  $\gamma\gamma$ ,  $\gamma j + j\gamma$ ,  $jj$  and non- $\gamma\gamma$  (equal to  $\gamma j + j\gamma + jj$ ) events in the data samples from the  $4 \times 4$  matrix method. The quoted uncertainties include statistical uncertainties only.

in the bins of  $M_{\gamma\gamma}$ ,  $p_T^{\gamma\gamma}$ ,  $\Delta\phi_{\gamma\gamma}$  and  $\cos\theta^*$ .



**Figure 5.9** Contributions from signal and different types of background events in data in the bins of  $M_{\gamma\gamma}$ ,  $p_T^{\gamma\gamma}$ , azimuthal angle  $\Delta\phi_{\gamma\gamma}$  and polar angle  $\cos\theta^*$ .

After subtracting the non- $\gamma\gamma$  and Drell-Yan backgrounds, we measure the  $\gamma\gamma$  purity (= the fraction of signal events in data), which is defined as

$$\text{Purity} = \frac{N_{data} - N_{non-\gamma\gamma} - N_{DY}}{N_{data}} \quad (5.3)$$

The purity as a function of  $M_{\gamma\gamma}$ ,  $p_T^{\gamma\gamma}$ ,  $\Delta\phi_{\gamma\gamma}$  and  $\cos\theta^*$  are shown in Fig. 5.10.

In Appendix 8.9 we are doing cross-check of the purities found by two-dimensional fitting of the photon ANN outputs (each dimension correspond to one di-photon candidate) for diphoton, dijet and photon-jet events in each bin of  $M_{\gamma\gamma}$ ,  $\Delta\phi_{\gamma\gamma}$ ,  $p_T^{\gamma\gamma}$  and  $\cos\theta^*$ . We get a confirmation of the found purities within fitting uncertainties.

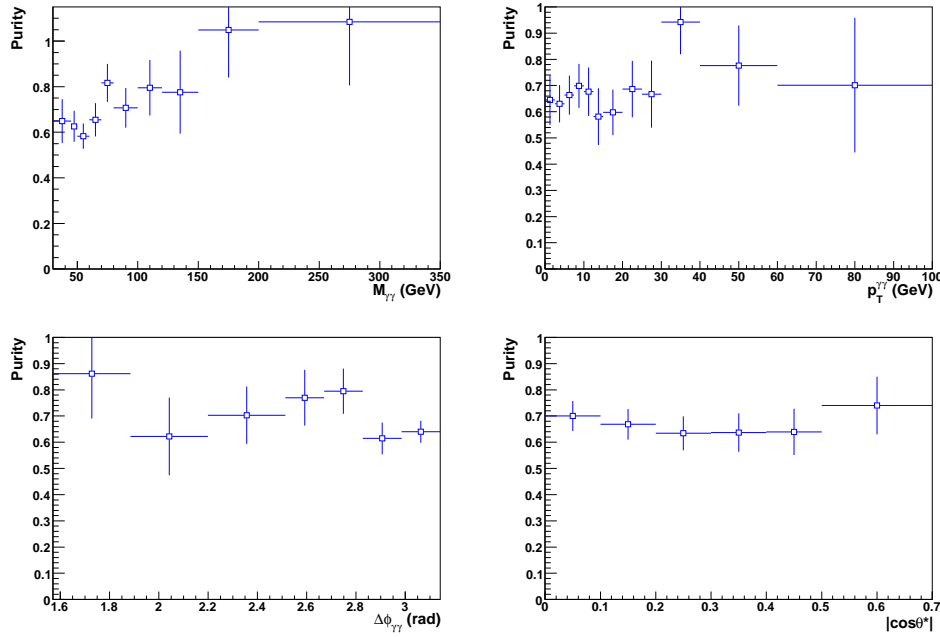


**Figure 5.10**  $\gamma\gamma$  purity as a function of  $M_{\gamma\gamma}$ ,  $\Delta\phi_{\gamma\gamma}$ ,  $p_T^{\gamma\gamma}$  and  $\cos\theta^*$ . The shown uncertainties are statistical only.

## 5.6 Photon energy scale correction

Due to photon will deposit less energy in the dead material, we need correct the over-correction caused by the electron energy scale derived from  $Z \rightarrow ee$  data (Section 3.6.4). Except this, another effect that influences the energy correction is caused by an admixture of background electromagnetic jets remaining after application of the photon ID cuts. These em-jets, after interaction with the matter upstream of the calorimeter and being registered



in the cone of  $\Delta R = 0.2$ , show a shift to smaller  $E$  values than the true photon signal in the same  $E^{\text{reco}}$  bin<sup>[38]</sup>. To select in data for the mass bins, the bin center that is related with photon events we weighted in each event the mass with a factor  $\omega_i = N_{\gamma\gamma}^i$  from Eq. 4.3:

$$M_{\gamma\gamma} = \sum M_i \omega_i / \sum \omega_i \quad (5.4)$$

where  $M_{\gamma\gamma}$  corresponds to the di-photon invariant mass in a given bin and the sum runs over the events in a given bin.

## 5.7 Systematics

Tables 5.8, 5.9, 5.10 and 5.11 summarize all the main systematic uncertainties in the measurements of the four differential cross sections. The columns of the tables correspond to the sources which are the photon purity, trigger  $\epsilon_t$  and photon  $\epsilon_s^\gamma$  selection efficiencies, photon acceptance ( $Acpt$ ) and luminosity ( $Lum$ ). The photon purity uncertainty is the dominant uncertainty for this analysis, its source is the uncertainty of the  $O_{NN} > 0.6$  efficiencies for the photon and photon-like jets, where we adopt the difference in the number of events from mean efficiencies and plus(minus) uncertainties as the systematic uncertainty, more details could be found in Appendix 8.10. The total uncertainty is calculated by adding them in quadrature by considering the both, up and down directions (for instance, for the first mass bin the total “up” systematic uncertainty is  $25.3\% = (13.7 * 13.7 + 14.1 * 14.1 + 3.1 * 3.1 + 2.0 * 2.0 + 4.1 * 4.1 + 6.1 * 6.1)^{1/2}\%$ .) The uncertainties due to photon selection efficiency and luminosity can be considered as a normalization ones and give 7.3% in total.

**Table 5.8** Systematic uncertainties (%) due to purity, photon acceptance ( $Acpt$ ), trigger  $\epsilon_t$ , photon  $\epsilon_s^\gamma$  selection efficiencies and luminosity ( $Lum$ ) in  $M_{\gamma\gamma}$  bins.

$M_{\gamma\gamma}$ bin (GeV)	$N_{\gamma\gamma}^{\epsilon_\gamma \pm 1.5\%}$	$N_{\gamma\gamma}^{\epsilon_j \pm 10.0\%}$	$Acpt$	$\epsilon_t$	$\epsilon_s^\gamma$	$Lum$	Total syst.
30 – 45	13.7 -11.4	14.1 -19.9	3.1 -6.8	2.0	4.1	6.1	+ 21.4 - 25.3
45 – 50	13.6 -11.3	10.1 -12.5	4.3 -4.9	1.0	4.1	6.1	+ 19.0 - 19.1
50 – 60	13.6 -11.3	8.6 -10.0	3.2 -2.9	0.5	4.1	6.1	+ 18.0 - 17.0
60 – 70	13.6 -11.3	7.5 -8.4	2.9 -2.9	0.5	4.1	6.1	+ 17.5 - 16.2
70 – 80	13.6 -11.3	6.4 -6.8	2.9 -3.0	0.5	4.1	6.1	+ 17.0 - 15.4
80 – 100	13.6 -11.3	4.9 -4.5	2.8 -2.9	0.5	4.1	6.1	+ 16.4 - 14.5
100 – 120	13.6 -11.3	3.5 -1.6	2.7 -3.0	0.5	4.1	6.1	+ 16.1 - 13.9
120 – 150	13.5 -11.2	2.9 -1.1	2.7 -2.8	0.0	4.1	6.1	+ 15.9 - 13.7
150 – 200	13.6 -11.3	3.8 -3.4	2.8 -2.9	0.0	4.1	6.1	+ 16.2 - 14.2
200 – 350	13.5 -11.2	2.5 -1.4	2.7 -3.2	0.0	4.1	6.1	+ 15.8 - 13.8

**Table 5.9** Systematic uncertainties (%) in  $p_T^{\gamma\gamma}$  bins.

$p_T^{\gamma\gamma}$ bin (GeV)	$N_{\gamma\gamma}^{\epsilon_\gamma \pm 1.5\%}$	$N_{\gamma\gamma}^{\epsilon_j \pm 10.0\%}$	$Acpt$	$\epsilon_t$	$\epsilon_s^\gamma$	$Lum$	Total syst.
0.0 – 2.5	13.7 -11.3	8.3 -10.1	4.2 -8.1	0.5	4.1	6.1	+ 18.1 - 18.7
2.5 – 5.0	13.6 -11.3	7.9 -9.2	6.4 -4.1	0.5	4.1	6.1	+ 18.5 - 16.8
5.0 – 7.5	13.6 -11.3	7.5 -8.1	3.0 -2.9	0.5	4.1	6.1	+ 17.4 - 16.0
7.5 – 10.0	13.6 -11.3	8.0 -9.4	2.8 -2.7	0.5	4.1	6.1	+ 17.6 - 16.6
10.0 – 12.5	13.7 -11.4	7.6 -8.6	2.8 -3.0	0.5	4.1	6.1	+ 17.5 - 16.3
12.5 – 15.0	13.6 -11.3	7.9 -9.4	3.0 -2.8	0.5	4.1	6.1	+ 17.6 - 16.7
15.0 – 20.0	13.6 -11.3	7.9 -9.1	2.9 -3.3	0.5	4.1	6.1	+ 17.6 - 16.6
20.0 – 25.0	13.6 -11.3	8.8 -11.2	3.1 -3.0	0.5	4.1	6.1	+ 18.1 - 17.8
25.0 – 30.0	13.6 -11.3	8.9 -10.9	2.9 -3.1	0.5	4.1	6.1	+ 18.0 - 17.6
30.0 – 40.0	13.5 -11.2	8.3 -9.8	3.0 -3.1	0.5	4.1	6.1	+ 17.8 - 16.9
40.0 – 60.0	13.5 -11.3	7.4 -7.9	2.9 -3.0	0.5	4.1	6.1	+ 17.3 - 15.9
60.0 – 100.0	13.7 -11.4	11.2 -15.8	3.0 -3.4	0.5	4.1	6.1	+ 19.4 - 21.1

**Table 5.10** Systematic uncertainties (%) in  $\Delta\phi_{\gamma\gamma}$  bins.

$\Delta\phi_{\gamma\gamma}$ bin (rad)	$N_{\gamma\gamma}^{\epsilon_{\gamma}} \pm 1.5\%$	$N_{\gamma\gamma}^{\epsilon_j} \pm 10.0\%$	$Acpt$	$\epsilon_t$	$\epsilon_s^{\gamma}$	$Lum$	Total syst.
$0.5 \cdot \pi - 0.6 \cdot \pi$	13.6 -11.3	11.0 -15.5	3.0 -3.4	0.5	4.1	6.1	+ 19.2 - 20.8
$0.6 \cdot \pi - 0.7 \cdot \pi$	13.6 -11.3	7.7 -8.5	3.0 -3.2	0.5	4.1	6.1	+ 17.5 - 16.2
$0.7 \cdot \pi - 0.8 \cdot \pi$	13.6 -11.3	7.4 -8.4	3.2 -3.4	0.5	4.1	6.1	+ 17.5 - 16.2
$0.8 \cdot \pi - 0.85 \cdot \pi$	13.6 -11.3	9.6 -12.8	3.1 -3.2	0.5	4.1	6.1	+ 18.5 - 18.9
$0.85 \cdot \pi - 0.9 \cdot \pi$	13.6 -11.3	7.3 -7.9	2.9 -3.3	0.5	4.1	6.1	+ 17.3 - 15.9
$0.9 \cdot \pi - 0.95 \cdot \pi$	13.6 -11.3	7.7 -8.7	3.1 -3.0	0.5	4.1	6.1	+ 17.5 - 16.3
$0.95 \cdot \pi - \pi$	13.6 -11.3	7.1 -7.4	2.8 -2.7	0.5	4.1	6.1	+ 17.3 - 15.6

**Table 5.11** Systematic uncertainties (%) in  $|\cos\theta^*|$  bins.

$ \cos\theta^* $ bin (rad)	$N_{\gamma\gamma}^{\epsilon_{\gamma}} \pm 1.5\%$	$N_{\gamma\gamma}^{\epsilon_j} \pm 10.0\%$	$Acpt$	$\epsilon_t$	$\epsilon_s^{\gamma}$	$Lum$	Total syst.
$0.0 - 0.1$	13.7 -11.3	8.0 -9.2	3.7 -3.1	0.5	4.1	6.1	+ 17.8 - 16.7
$0.1 - 0.2$	13.7 -11.3	7.0 -7.2	3.1 -3.1	0.5	4.1	6.1	+ 17.3 - 15.6
$0.2 - 0.3$	13.6 -11.3	7.6 -8.6	2.7 -2.7	0.5	4.1	6.1	+ 17.5 - 16.2
$0.3 - 0.4$	13.6 -11.3	7.2 -7.7	2.8 -3.4	0.5	4.1	6.1	+ 17.3 - 15.9
$0.4 - 0.5$	13.5 -11.2	7.3 -7.7	3.1 -2.8	0.5	4.1	6.1	+ 17.3 - 15.7
$0.5 - 0.7$	13.3 -11.1	7.2 -7.7	3.5 -3.8	0.5	4.1	6.1	+ 17.2 - 15.8

## 5.8 Correction of theory for MPI and hadronization effects

NLO QCD theoretical cross sections with which we compare our data do not include correction for contributions from additional parton interactions (“MPI effect”) as well as corrections for hadronization effect.

It should be important not only for jet-based cross sections but also for the  $e/\gamma$  ones due to the additional contribution to the EM isolation cone. The size of these corrections strongly depends on the isolation conditions.

To estimate such corrections we used Tunes A as one of the best for old MPI models and Tune S0 as a representative of the new MPI models<sup>[60]</sup>. These tunes are good approximations to the CDF minbias data for a distribution of “average charged  $p_T$  vs. track multiplicity”<sup>[61]</sup>. So, Tunes A and S0 have been chosen for our following estimates.

In Fig. 5.11 we have shown distributions of total  $p_T$  sum in the photon isolation cone ( $\Delta R < 0.4$ ) for the di-photon events simulated with PYTHIA in the four cases: (1) without hadronization and MPI effects (but with ISR/FSR), (2) with hadronization, but without MPI; (3a) with MPI Tune A and (3b) with MPI Tune S0. From analysis and comparison of those events we can conclude that (a) additional parton interactions lead to a noticeable  $p_T$  increase in the isolation cone; (b) the change of shape is consistent between the two tunes and (c) contribution from the hadronization effect is negligible as compared with MPI one, being about 0.7% and 0.5% for the 2 GeV and 2.5 GeV isolations.

As we found, the relative isolation requires strongly  $p_T$  dependent correction for the theory. More importantly, those corrections also strongly vary in the  $M_{\gamma\gamma}, p_T^{\gamma\gamma}, \Delta\phi_{\gamma\gamma}$  bins. As compared to them, the absolute isolation leads to the correction that are almost flat for those variables. The left plot in Fig. 5.12 shows the efficiency to pass the isolation cut  $sumPT < 2.5$  GeV due to ISR/FSR (red circles) and due to ‘ISR/FSR + MPI + hadronization effects in  $p_T^{\gamma}$  bins. To estimate just the correction caused by the MPI + hadronization we need to find a difference between the two curves. The results is shown on the right plot of Fig. 5.12.

Since we measure  $d\sigma/dM_{\gamma\gamma}, d\sigma/dp_T^{\gamma\gamma}, d\sigma/d\Delta\phi_{\gamma\gamma}$  and  $d\sigma/d\cos\theta^*$  differential cross sections, we would like to know how big those corrections should be for the theory in bins of our measurable quantities. The results are shown on the four plots of Fig. 5.13. From Figs. 5.12 and 5.13 we can see that Tunes A and S0 give very close results. To parameterize the corrections, we fitted points for Tune A in Fig. 5.13. The results are shown on the plots. We can see that the required correction varies between 4 – 6%.

Analogously, we have parameterized correction for the theory for the 2D cross sections, in the three mass intervals. Results are shown in Fig. 5.14.

Those parameterizations are applied to theory and used in the next section when we compare our measurements with theory.

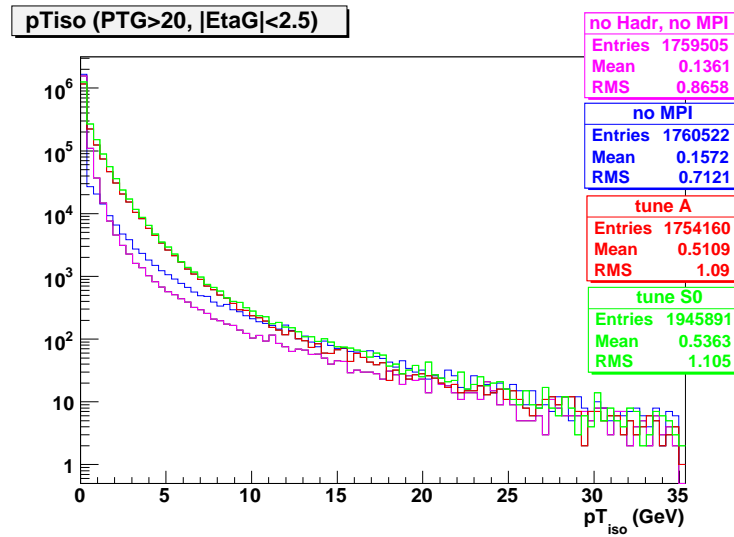


**Figure 5.11** Total  $p_T$  sum in the photon isolation cone ( $\Delta R < 0.4$ ) for the diphoton events ( $pT_{iso}$ ) simulated with PYTHIA in the four cases: (1) without hadronization and MPI effects (but with ISR/FSR), (2) with hadronization, but without MPI; (3a) with MPI Tune A and (3b) with MPI Tune S0.

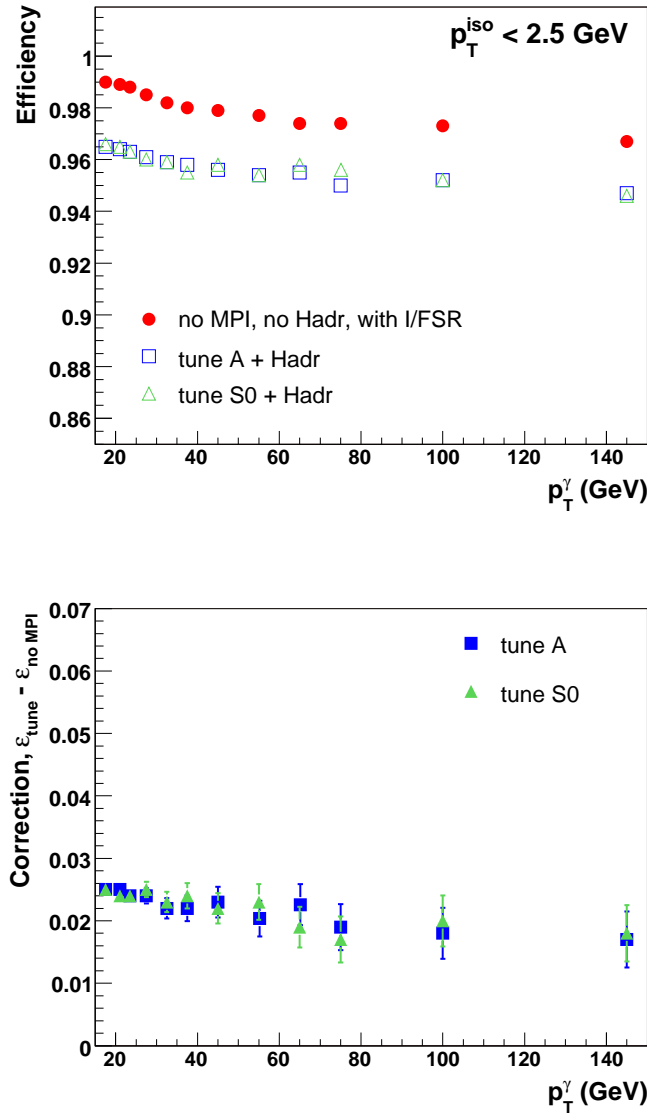


**Figure 5.12** Left: Efficiency to pass the isolation cut  $p_T^{iso} < 2.5$  GeV due to ISR/FSR (red circles) and due to 'ISR/FSR + MPI + hadronization effects in  $p_T^\gamma$  bins. Right: Corrections to the NLO QCD predictions due to MPI and hadronization effects in bins of  $p_T^\gamma$ .



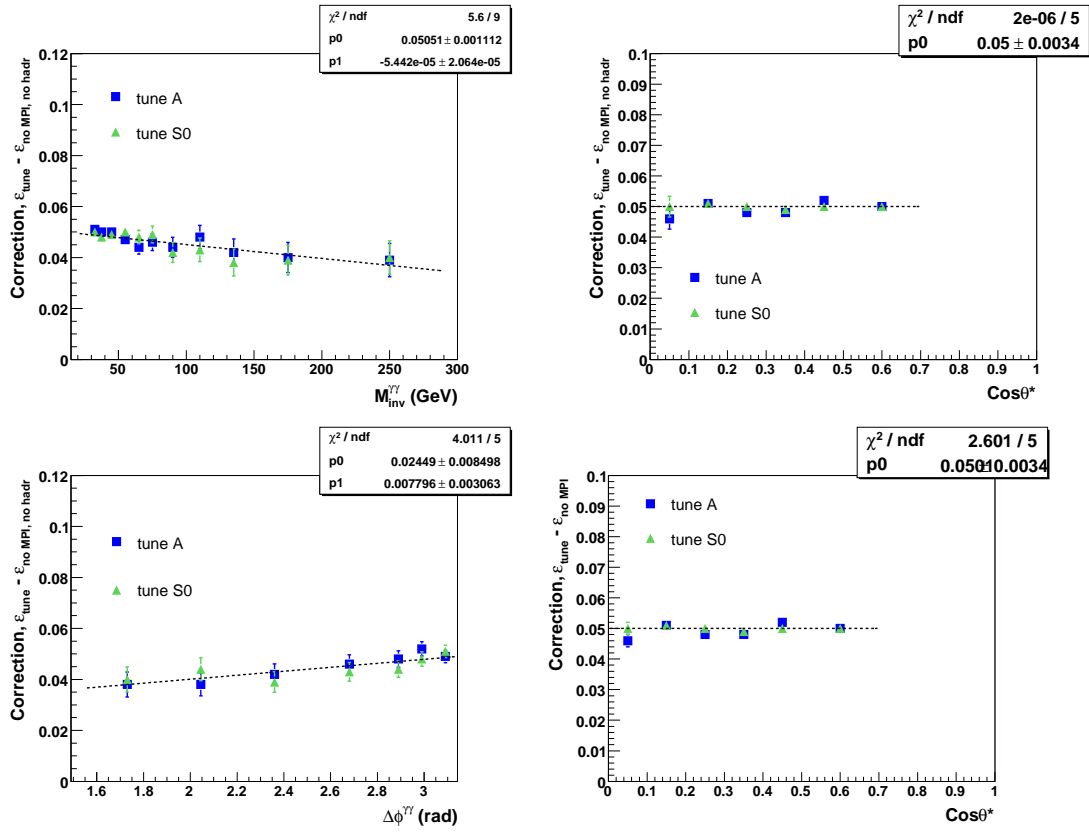


**Figure 5.13** Corrections to the NLO QCD predictions due to MPI and hadronization effects in bins of  $M_{\gamma\gamma}$ ,  $p_T^{\gamma\gamma}$ ,  $\Delta\phi_{\gamma\gamma}$  and  $\cos\theta^*$  with tunes A and S0.

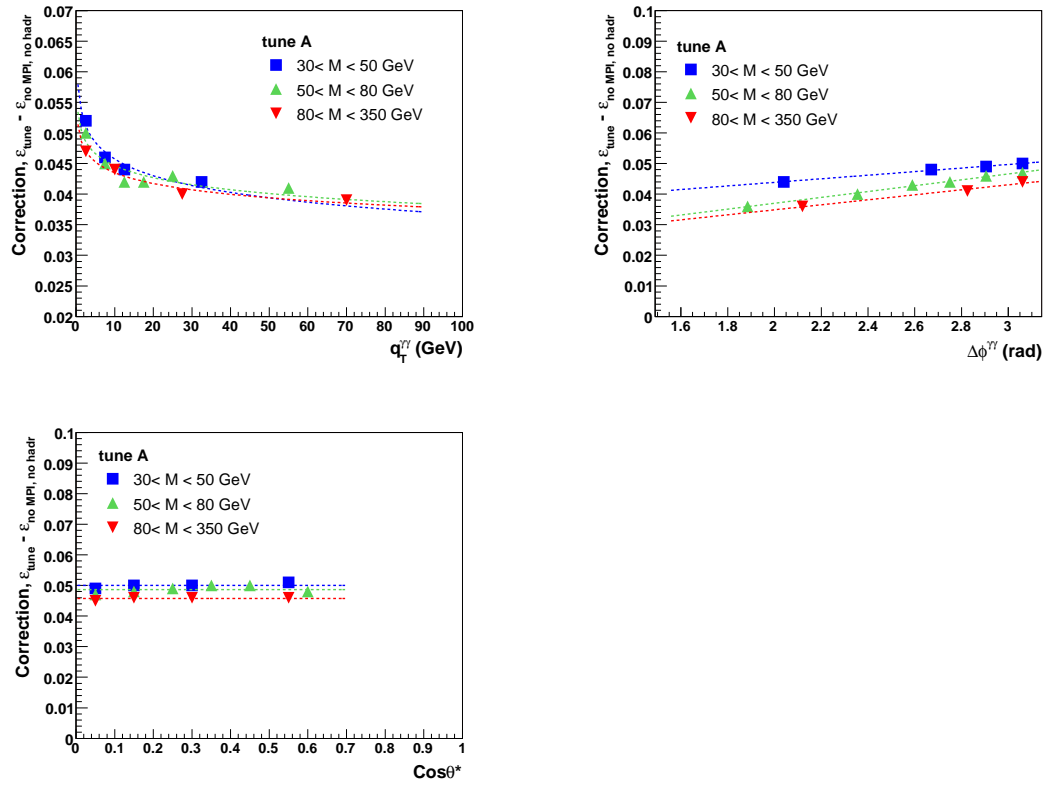


**Figure 5.14** Corrections to the NLO QCD predictions due to MPI and hadronization effects in bins of  $p_T^{\gamma\gamma}$ ,  $\Delta\phi_{\gamma\gamma}$  and  $\cos\theta^*$  with tunes A for the three mass intervals.

## 5.9 Comparison with Theory

In this section we compare the four measured differential cross sections,  $d\sigma/M_{\gamma\gamma}$ ,  $d\sigma/p_T^{\gamma\gamma}$ ,  $d\sigma/\Delta\phi^{\gamma\gamma}$  and  $d\sigma/|\cos\theta^*|$  with analogous predicted by RESBOS, DIPHOX and PYTHIA. These results are shown in Tables 5.12, 5.13, 5.14 and 5.15. The statistical uncertainties  $\delta_{stat}$  in those tables are caused by statistics in data and MC used to calculate  $N_{\gamma\gamma}$  events in the 4x4 matrix method and also statistical uncertainty in the acceptance calculation (Tables 5.3–5.6). The systematic uncertainties  $\delta_{syst}$  are obtained from the total uncertainties in Tables 5.8, 5.9, 5.10 and 5.11. All the uncertainties are also summarized in Fig. 5.15. The results for the four cross sections are also shown at four plots of Fig. 5.16 as absolute values in bins of the four variables on the top plots and as the data/theory ratios on the bottom plots. The inner line for the error bars in data points shows the statistical uncertainty, while the outer line shows the total (statistic and systematic added in quadrature) uncertainty after subtraction of the 7.4% normalization uncertainty (caused by luminosity and diphoton selection efficiency). The RESBOS and DIPHOX predictions are corrected for effects from the underlying events as described in Section 5.8 and shown in Figs 5.11–5.13. The scale uncertainty in the theory predictions are obtained with DIPHOX and caused by simultaneous variation of the three scales renormalization  $\mu$ , fragmentation and factorization scales (the latter two are taken to be equal and denoted as  $M_F$ ) with respect to the central predictions with all the scales equal to  $M_{\gamma\gamma}$ . The theoretical scale

uncertainties are also shown separately in Fig. 5.17. The predictions in DIPHOX and RESBOS are done using CTEQ6.6M PDF and tune A (with CTEQ5L PDF) in PYTHIA, v6.420. The scale uncertainties are shown as dash-dotted lines and the PDF uncertainties by the shaded regions. The ratios between DIPHOX, PYTHIA and RESBOS predictions are also shown.

Fig. 5.18 shows a ratio of theoretical NLO predictions with HERA2001 and MSTW2008 PDFs to those with CTEQ6.6M PDF (taken as a default). One can see that largest variations for all the four variables do not exceed 10%. We have also considered PYTHIA predictions with tune A in which we replaced the default CTEQ5L PDF by CTEQ6L1 set. The results are shown in Fig. 5.19. By comparing those ratios with Fig. 5.16 one can conclude that tune A with CTEQ6L1 is closer to our data. A comparison of predictions with the default tune A to those with tune Perugia0 (that uses CTEQ5L PDF) is also shown.

The results obtained (see Fig. 5.16) show that none of the theoretical predictions considered is able to describe the data well in all kinematic regions of the four variables. RESBOS shows the best agreement with data, although systematic discrepancies are observed at low  $M_{\gamma\gamma}$ , high  $p_T^{\gamma\gamma}$ , and low  $\Delta\phi_{\gamma\gamma}$ . However, the agreement between RESBOS and data is fair at intermediate  $M_{\gamma\gamma}$  (50 – 80 GeV), and good at high  $M_{\gamma\gamma}$  (> 80 GeV). The large discrepancy between RESBOS and DIPHOX in some regions of the phase space is due to absence of all-order soft-gluon resummation and accounting  $gg \rightarrow \gamma\gamma$  contribution just at LO in DIPHOX.

**Table 5.12**  $d\sigma/dM_{\gamma\gamma}$  (pb/GeV) cross section with uncertainties.

$M_{\gamma\gamma}$ (GeV)	$\langle M_{\gamma\gamma} \rangle$ (GeV)	$N_{data}$	$N_{\gamma\gamma}$	$d\sigma/dM_{\gamma\gamma}$ (pb/GeV)				DIPHOX	RESBOS	PYTHIA
				Data	$\delta_{stat}$ (%)	$\delta_{syst}$ (%)	$\delta_{total}$ (%)			
30 – 45	43.0	998	648	3.11e-02	15.2	+ 21.4/- 25.3	+ 25.5/- 28.9	2.04e-02	1.94e-02	1.24e-02
45 – 50	47.6	1846	1156	1.74e-01	11.2	+ 19.0/- 19.1	+ 20.8/- 20.9	1.12e-01	1.22e-01	7.38e-02
50 – 60	54.7	3073	1791	1.19e-01	9.6	+ 18.0/- 17.0	+ 19.0/- 18.1	9.32e-02	1.09e-01	6.06e-02
60 – 70	64.6	1851	1212	7.89e-02	11.2	+ 17.5/- 16.2	+ 19.4/- 18.2	5.63e-02	6.82e-02	3.58e-02
70 – 80	74.6	1104	902	5.61e-02	10.2	+ 17.0/- 15.4	+ 18.4/- 17.0	3.36e-02	4.09e-02	2.13e-02
80 – 100	88.6	1123	794	2.39e-02	12.3	+ 16.4/- 14.5	+ 19.2/- 17.5	1.75e-02	2.13e-02	1.14e-02
100 – 120	108.9	470	374	1.12e-02	15.3	+ 16.1/- 13.9	+ 20.9/- 19.3	8.18e-03	9.84e-03	5.65e-03
120 – 150	132.9	246	191	03.65e-03	23.4	+ 15.9/- 13.7	+ 27.3/- 26.2	3.89e-03	4.53e-03	2.85e-03
150 – 200	170.7	144	151	1.67e-03	19.9	+ 16.2/- 14.2	+ 24.6/- 23.3	1.50e-03	1.74e-03	1.22e-03
200 – 350	248.8	83	90	3.30e-04	25.7	+ 15.8/- 13.8	+ 29.3/- 28.3	3.28e-04	3.53e-04	2.93e-04

**Table 5.13**  $d\sigma/dp_T^{\gamma\gamma}$  (pb/GeV) cross section with uncertainties.

$p_T^{\gamma\gamma}$ (GeV)	$\langle p_T^{\gamma\gamma} \rangle$ (GeV)	$N_{data}$	$N_{\gamma\gamma}$	$d\sigma/dp_T^{\gamma\gamma}$ (pb/GeV)				DIPHOX	RESBOS	PYTHIA
				Data	$\delta_{stat}$ (%)	$\delta_{syst}$ (%)	$\delta_{total}$ (%)			
0.0 – 2.5	1.5	918	592	1.93e-01	14.8	+ 18.1/- 18.7	+ 22.2/- 22.7	3.34e-01	2.63e-01	2.55e-01
2.5 – 5.0	3.7	1789	1122	3.34e-01	11.4	+ 18.5/- 16.8	+ 20.4/- 19.0	3.95e-01	3.30e-01	2.39e-01
5.0 – 7.5	6.2	1726	1149	3.06e-01	11.2	+ 17.4/- 16.0	+ 19.4/- 18.1	1.76e-01	2.41e-01	1.29e-01
7.5 – 10.0	8.7	1344	935	2.38e-01	12.0	+ 17.6/- 16.6	+ 20.0/- 19.2	1.08e-01	1.73e-01	7.93e-02
10.0 – 12.5	11.2	995	663	1.66e-01	13.8	+ 17.5/- 16.3	+ 21.1/- 20.1	7.43e-02	1.28e-01	5.24e-02
12.5 – 15.0	13.7	768	444	1.10e-01	18.8	+ 17.6/- 16.7	+ 24.7/- 24.0	5.43e-02	9.57e-02	3.66e-02
15.0 – 20.0	17.3	1190	719	8.80e-02	14.5	+ 17.6/- 16.6	+ 21.6/- 20.8	3.72e-02	6.34e-02	2.33e-02
20.0 – 25.0	22.3	733	506	6.30e-02	15.6	+ 18.1/- 17.8	+ 22.7/- 22.5	2.42e-02	3.98e-02	1.36e-02
25.0 – 30.0	27.3	509	337	4.20e-02	19.3	+ 18.0/- 17.6	+ 25.4/- 25.0	1.70e-02	2.57e-02	8.24e-03
30.0 – 40.0	34.3	522	499	2.99e-02	12.9	+ 17.8/- 16.9	+ 20.7/- 20.0	1.02e-02	1.39e-02	3.76e-03
40.0 – 60.0	47.8	340	269	7.58e-03	19.5	+ 17.3/- 15.9	+ 25.0/- 24.1	3.90e-03	4.72e-03	9.02e-04
60.0 – 100.0	73.4	104	74	9.92e-04	36.4	+ 19.4/- 21.1	+ 40.6/- 41.4	8.03e-04	9.20e-04	1.07e-04

**Table 5.14**  $d\sigma/d\Delta\phi_{\gamma\gamma}$  (pb/rad.) cross section with uncertainties.

$\Delta\phi_{\gamma\gamma}$ (rad.)	$\langle \Delta\phi_{\gamma\gamma} \rangle$ (rad.)	$N_{data}$	$N_{\gamma\gamma}$	$d\sigma/d\Delta\phi_{\gamma\gamma}$ (pb/rad)				DIPHOX	RESBOS	PYTHIA
				Data	$\delta_{stat}$ (%)	$\delta_{syst}$ (%)	$\delta_{total}$ (%)			
$0.5 \cdot \pi - 0.6 \cdot \pi$	1.7	237	205	4.32e-01	19.7	+ 19.2/- 20.8	+ 26.5/- 27.7	1.10e-01	1.31e-01	2.28e-02
$0.6 \cdot \pi - 0.7 \cdot \pi$	2.1	408	253	5.30e-01	24.0	+ 17.5/- 16.2	+ 28.8/- 28.0	1.96e-01	2.70e-01	8.45e-02
$0.7 \cdot \pi - 0.8 \cdot \pi$	2.4	750	530	1.15	15.5	+ 17.5/- 16.2	+ 22.2/- 21.2	3.86e-01	6.38e-01	2.32e-01
$0.8 \cdot \pi - 0.85 \cdot \pi$	2.6	746	579	2.43	13.7	+ 18.5/- 18.9	+ 21.8/- 22.1	7.46e-01	1.34	5.08e-01
$0.85 \cdot \pi - 0.9 \cdot \pi$	2.8	1192	959	3.99	10.8	+ 17.3/- 15.9	+ 19.1/- 17.8	1.40	2.49	9.33e-01
$0.9 \cdot \pi - 0.95 \cdot \pi$	2.9	2582	1594	6.70	9.8	+ 17.5/- 16.3	+ 18.7/- 17.6	3.50	5.25	2.47
$0.95 \cdot \pi - \pi$	3.1	5023	3188	1.34e+01	6.6	+ 17.3/- 15.6	+ 17.0/- 15.3	4.06e+01	1.33e+01	1.01e+01

**Table 5.15**  $d\sigma/d\cos\theta^*$  (pb) cross section with uncertainties.

$ \cos\theta^* $	$\langle  \cos\theta^*  \rangle$	$N_{data}$	$N_{\gamma\gamma}$	$d\sigma/d \cos\theta^* $ (pb)				DIPHOX	RESBOS	PYTHIA
				Data	$\delta_{stat}$ (%)	$\delta_{syst}$ (%)	$\delta_{total}$ (%)			
0.0 – 0.1	0.05	2840	1989	1.38e+01	8.3	+ 17.8/- 16.7	+ 18.7/- 17.6	8.02	9.22	5.28
0.1 – 0.2	0.15	2461	1645	1.00e+01	8.8	+ 17.3/- 15.6	+ 18.4/- 16.9	7.05	7.96	4.50
0.2 – 0.3	0.25	2038	1292	7.78	10.3	+ 17.5/- 16.2	+ 19.4/- 18.2	6.15	7.00	3.98
0.3 – 0.4	0.35	1625	1035	6.38	11.5	+ 17.3/- 15.9	+ 19.9/- 18.7	5.22	5.90	3.44
0.4 – 0.5	0.45	1168	747	4.77	13.8	+ 17.3/- 15.7	+ 21.3/- 20.1	3.99	4.54	2.70
0.5 – 0.7	0.57	804	595	2.35	15.0	+ 17.2/- 15.8	+ 22.0/- 20.9	1.97	2.16	1.36

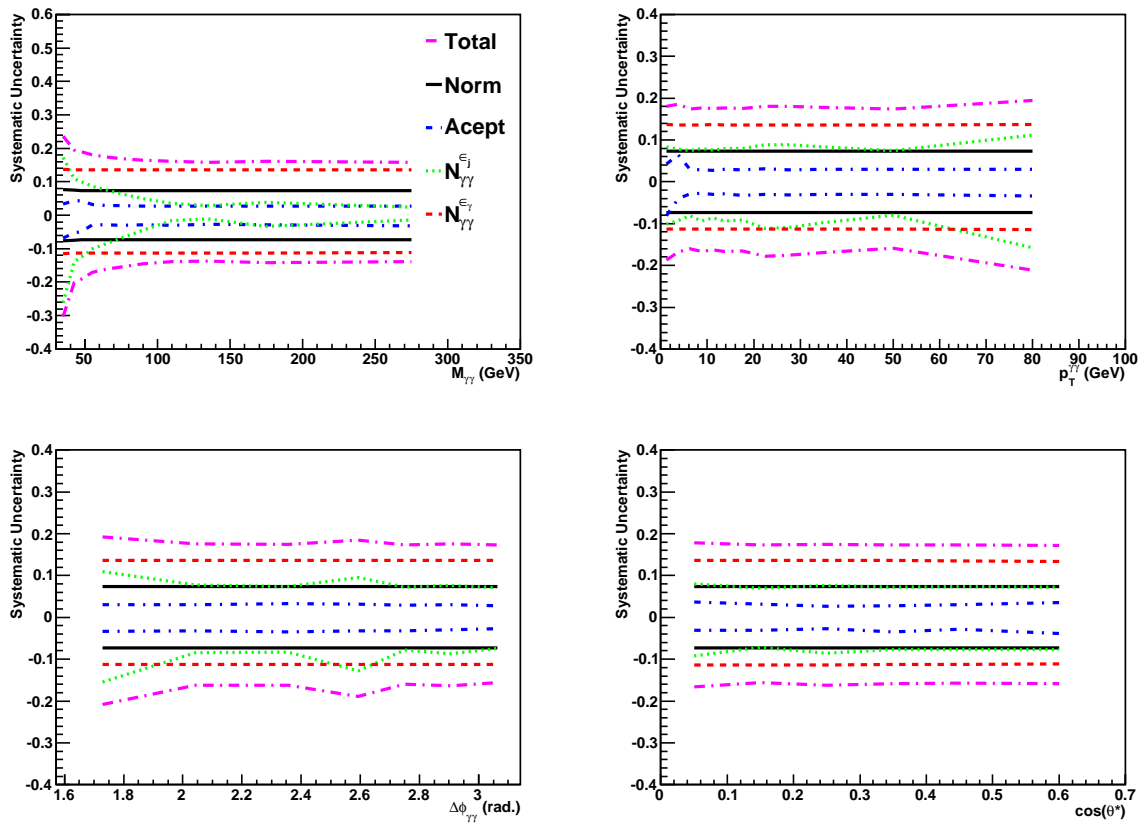


**Figure 5.15** The main sources of systematic uncertainties for the four cross sections (see also Tables 5.8– 5.11).

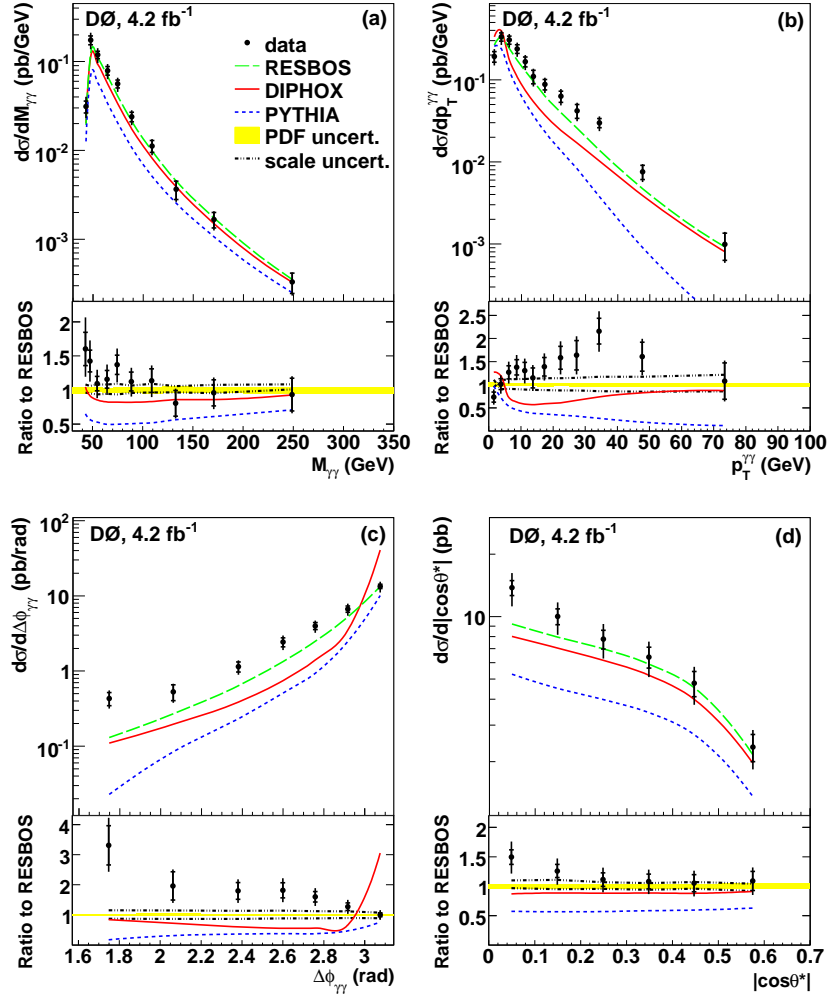


**Figure 5.16** The differential cross sections as a function of  $M_{\gamma\gamma}$ ,  $p_T^{\gamma\gamma}$ ,  $\Delta\phi_{\gamma\gamma}$  and  $\cos\theta^*$  from data (black points) and theory predictions (curves) are shown on the left plots. The right plots show the ratio of data and DIPHOX, PYTHIA predictions to the RESBOS predictions. The inner line for the error bars in data points shows the statistical uncertainty, while the outer line shows the total (statistic and systematic added in quadrature) uncertainty after subtraction of the 7.4% normalization uncertainty. The predictions in DIPHOX and RESBOS are done using CTEQ6.6M PDF and using Tune A (with CTEQ5L PDF) in PYTHIA. The scale uncertainties are shown as dash-dotted lines and the PDF uncertainties by the shaded regions.

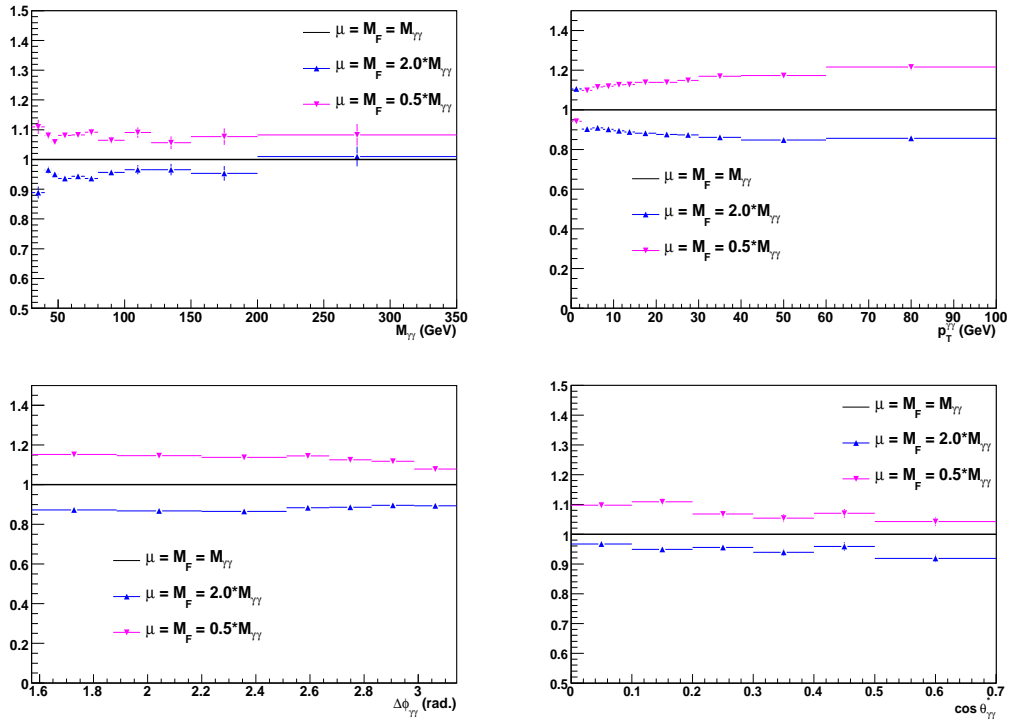


**Figure 5.17** Theoretical uncertainties caused by variation of the three scales.



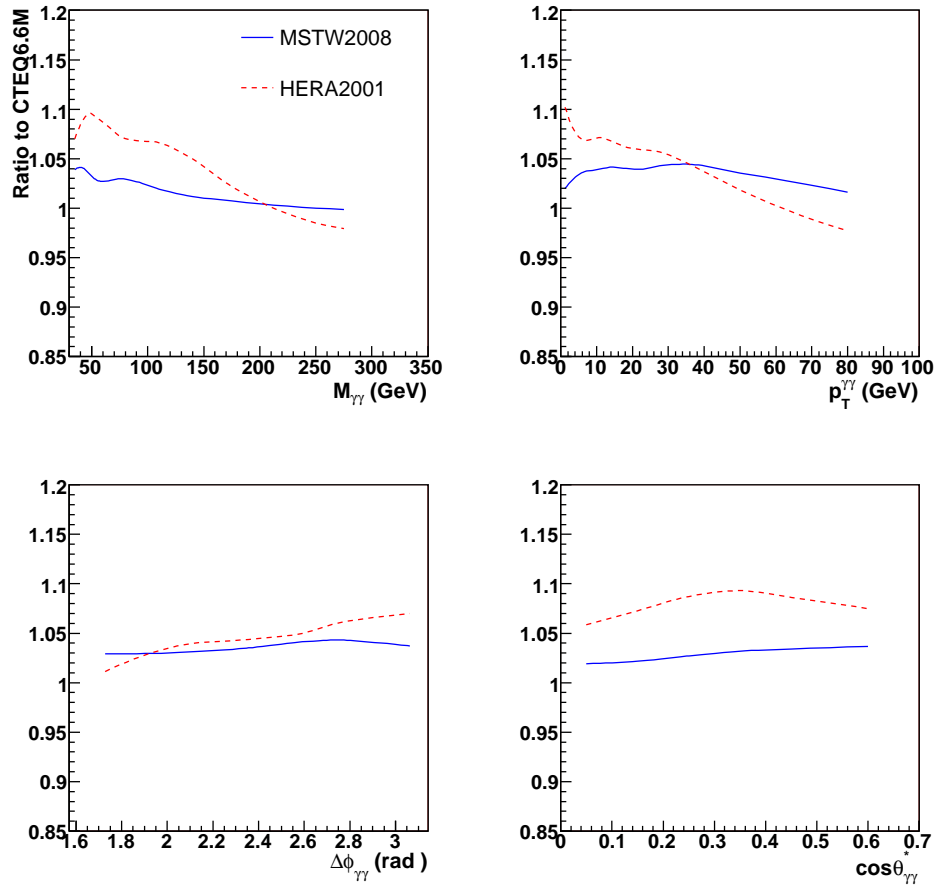


**Figure 5.18** Ratio of theoretical NLO predictions with HERA2001 (dashed line) and MSTW2008 PDFs (full line) to those with CTEQ6.6M PDF (default).

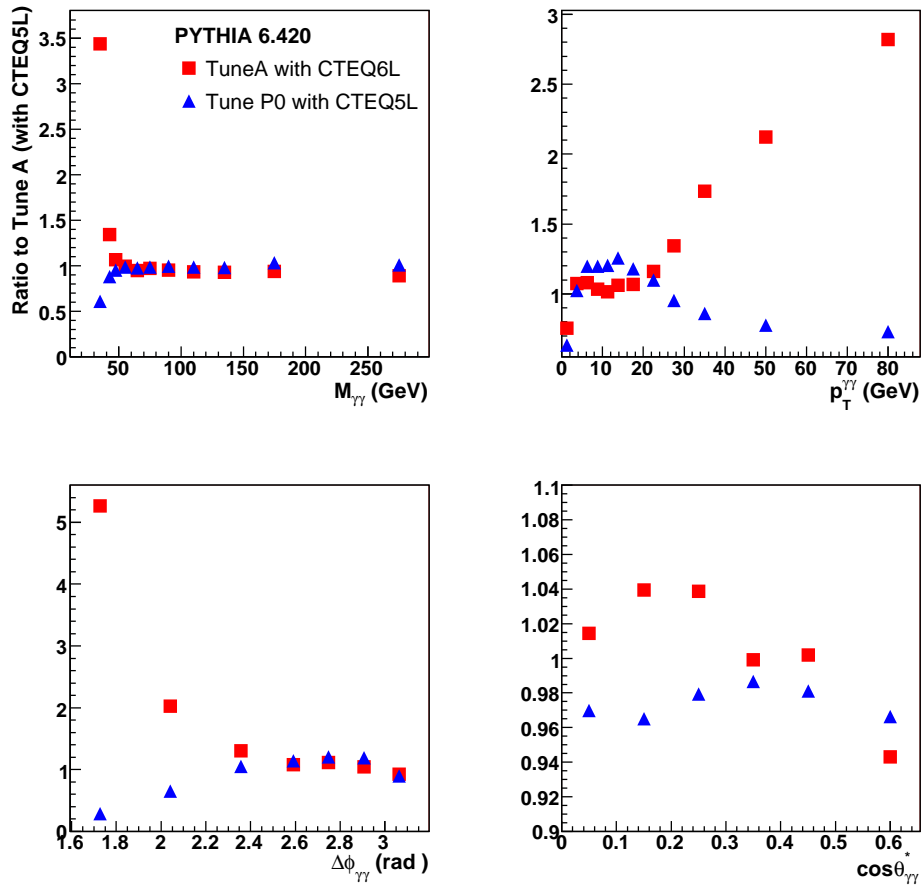


**Figure 5.19** The ratio of PYTHIA predictions done with Tune A and using CTEQ6L1 as well as with Tune Perugia0 to those with Tune A and CTEQ5L (default).

## 5.10 Closure tests

We use the RESBOS via fast MC to measure the acceptance (Section 5.4). To demonstrate there is no visible model-dependence for such measurement, we have made a closure test by comparing directly the true and unfolded RESBOS cross sections and did it in two iterations.

First, we have used the default RESBOS (called "*Resbos<sub>0</sub>*") to calculate the initial acceptance ( $Acc_0$ ) using our fast simulation. This acceptance have been applied to unfold the data spectra. Then we have re-weighted *Resbos<sub>0</sub>* (each kinematic variable individually, see Fig. 8.21) to the unfolded data spectra (and get "*Resbos<sub>1</sub>*") and recalculated acceptance again ( $Acc_1$ ). This iteration is also described in details in Section 5.4 and Appendix 8.8. As we explained, we use acceptance  $Acc_1$  to calculate the final cross sections. As we showed in the note (see Fig. 8.24), the difference between  $Acc_0$  and  $Acc_1$  is small ( $<3-4\%$  across all the bins for all the four variables). This difference is directly extrapolated to the difference in the unfolded spectra at the "truth level". To show this, we unfolded smeared *Resbos<sub>0</sub>* events with  $Acc_1$  and compared with *Resbos<sub>0</sub>* "truth" cross sections in Fig. 5.20.

One can see that the difference between the two sets of cross sections is same as the difference between  $Acc_0$  and  $Acc_1$ , i.e.  $<3-5\%$ .

It is clear that one can continue reweighting to get even more accurate acceptance and check stability of the results. So, we

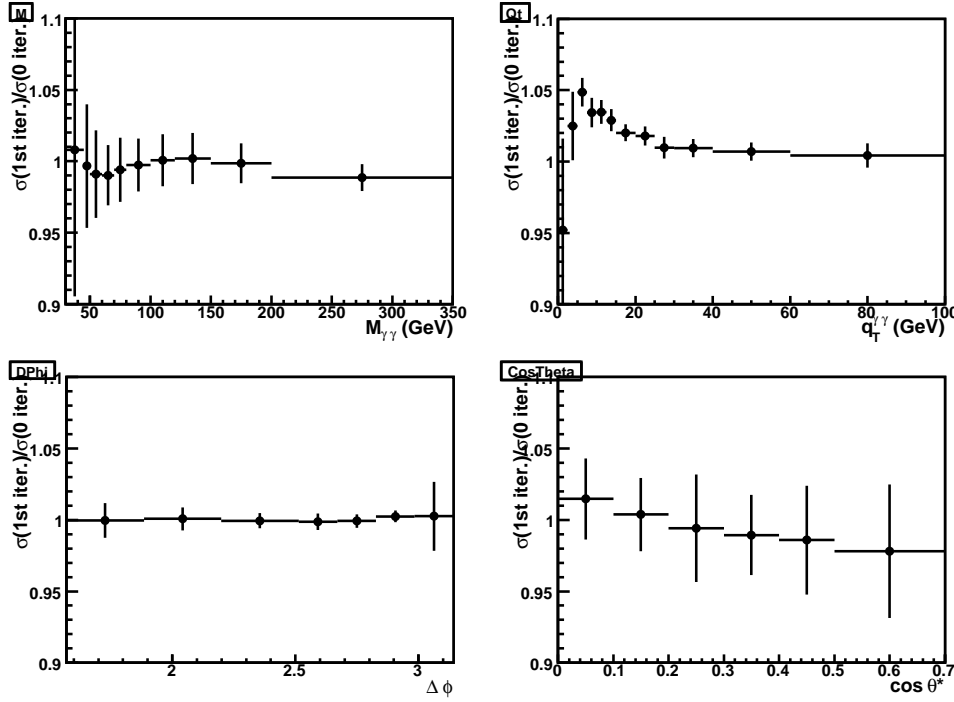


**Figure 5.20** The ratio between unfolded smeared  $Resbos_0$  and  $Resbos_0$  "truth" cross sections. Here " $\sigma(0th - iteration)$ " simply means (non-reweighted/default)  $Resbos_0$  "truth" cross section, while " $\sigma(1st - iteration)$ " means the unfolded smeared  $Resbos_0$  events with  $Acc_1$ .

reweighted  $Resbos_1$  events to our final experimental results (i.e. made 2nd iteration and obtained " $Resbos_2$ "), then smeared them through the fast simulation and calculated  $Acc_2$ . Now we apply  $Acc_2$  to unfold the smeared  $Resbos_1$  events and compared with the true  $Resbos_1$  spectra. The results are shown in Fig. 5.21.

As one can see, the true cross sections are calculated now even more accurately, specifically within 1-2%, which can be treated as the systematics. It also tells us that the procedure of re-weighting to data is converging and that  $Acc_1$ , obtained even after the 1st reweighting to data, and used for the final results, is stable within same 1-2%.

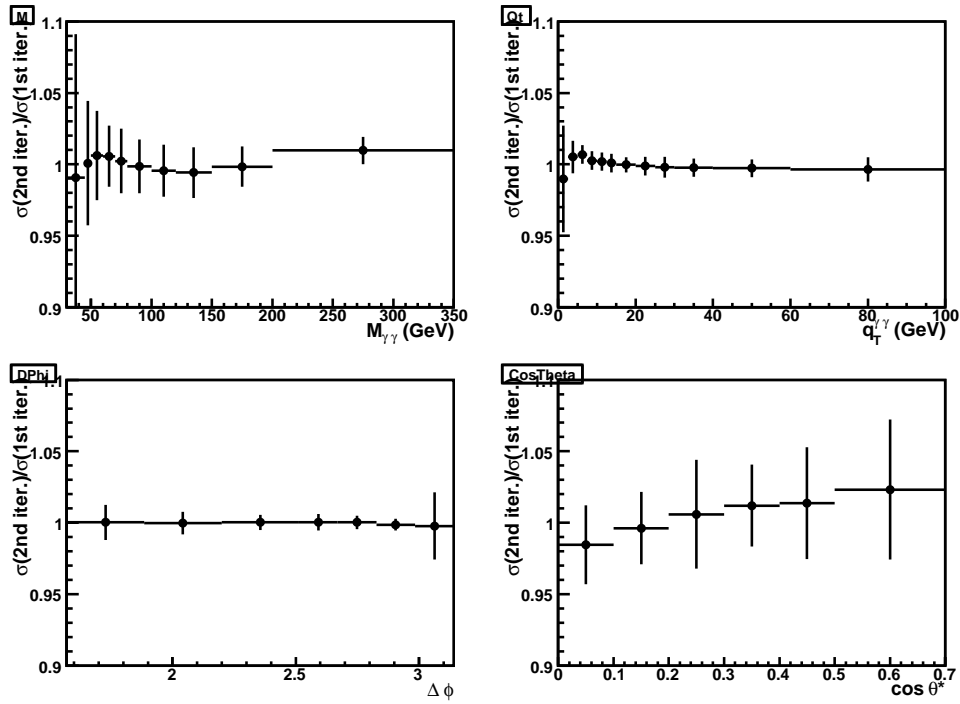


**Figure 5.21** The ratio between unfolded smeared  $Resbos_1$  and  $Resbos_1$  "truth" cross sections. Here " $\sigma(1th - iteration)$ " simply means (non-reweighted/default)  $Resbos_1$  "truth" cross section, while " $\sigma(2nd - iteration)$ " means the unfolded smeared  $Resbos_1$  events with  $Acc_2$ .

We also run PYTHIA events through the fast MC simulation and get the "data" distributions after smearing. We then use exactly the same two-step iterative procedure as we used for the real data measurement (RESBOS + fast MC simulation) to get the unfolded distribution and compare the unfolded distribution with the input distribution. We compared the unfolded cross section using the default RESBOS for the acceptance calculation and then compare with the truth PYTHIA distributions, the ratios can be found in Fig. 5.22.

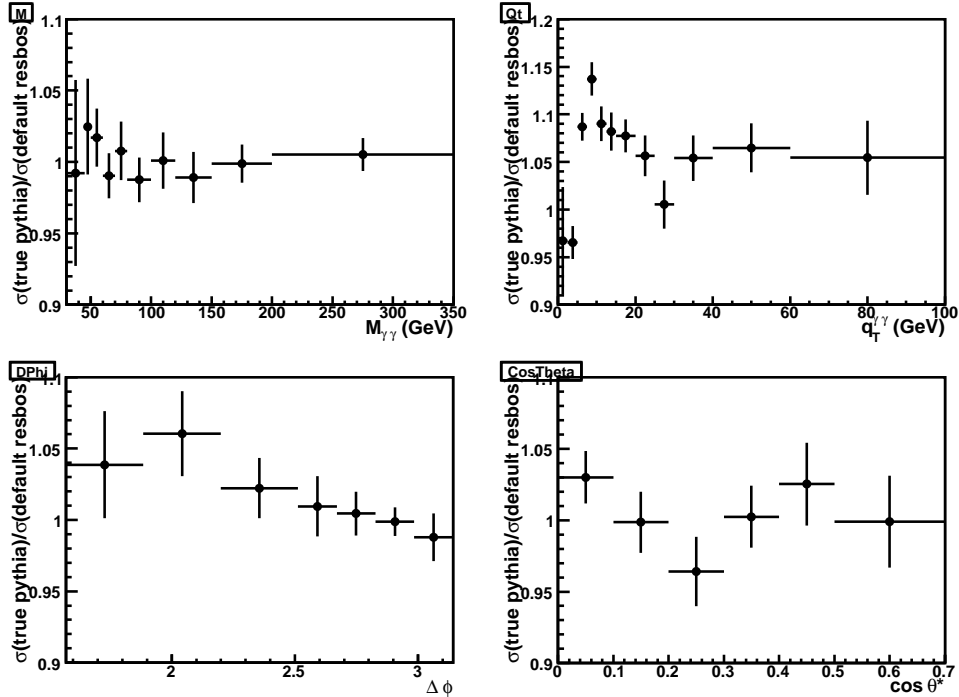


**Figure 5.22** The ratio between unfolded smeared PYTHIA cross section with using default RESBOS for the acceptance calculation and truth PYTHIA cross sections.

Since the same fast MC simulation is used, the difference that we observed here is mainly due to the input generator distributions. We then reweight the input RESBOS distribution according to the ratio of the measured cross section and the input PYTHIA distribution and recalculate the acceptance. We then cal-

culate the ratios of the measured distributions from the second step to the truth PYTHIA distributions, they can be found in Fig. 5.23.

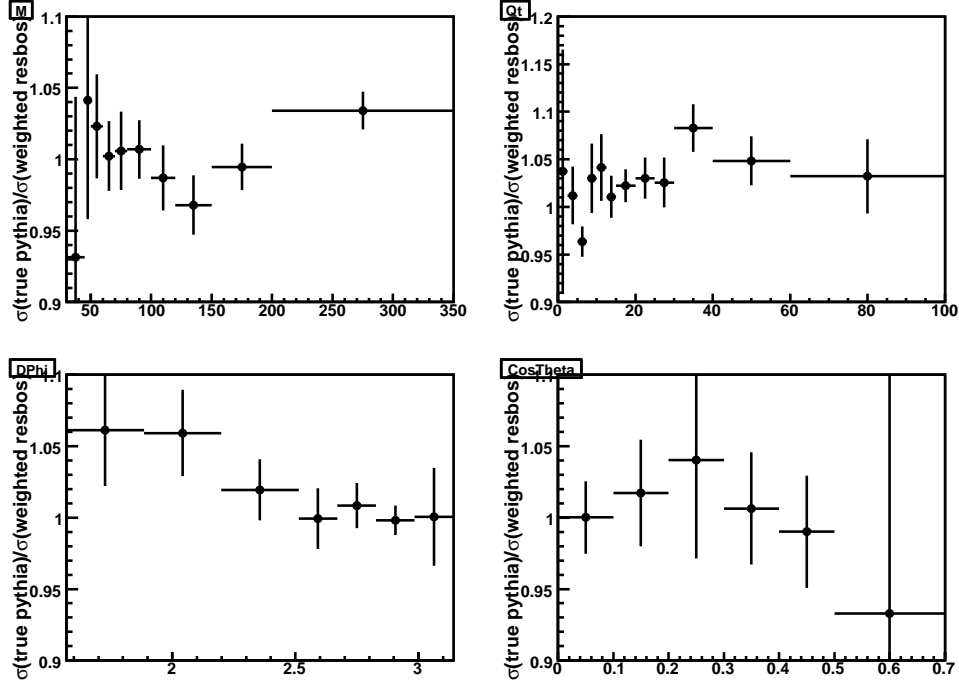
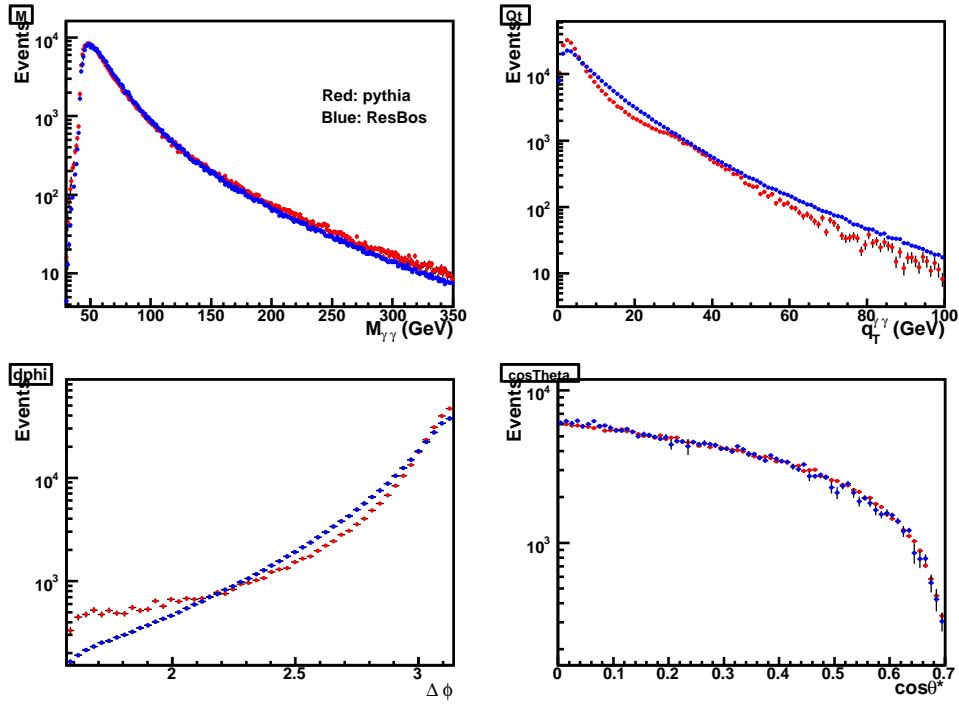


**Figure 5.23** The ratio between unfolded smeared PYTHIA cross section with using default RESBOS for the acceptance calculation and truth PYTHIA cross sections, where the input RESBOS distributions have been reweighted to the input PYTHIA distributions.

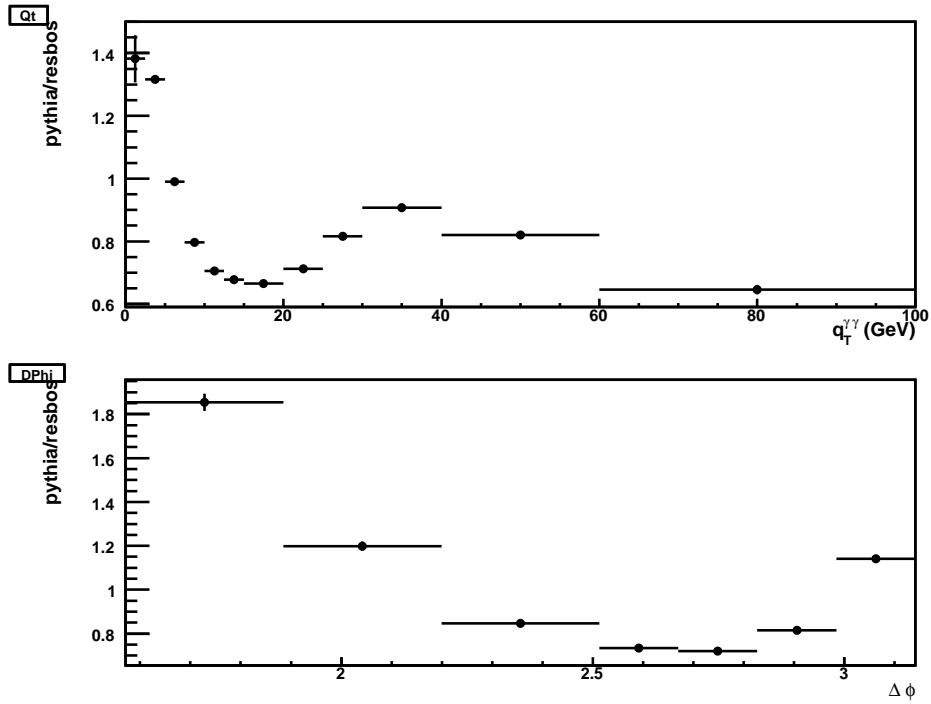
The bias we observed is  $<5\%$  for most bins in all four distributions.

Fig. 5.24 shows the comparison of the default resbos and pythia distributions (normalized to each other) for all four variables, as you can see, the biggest discrepancies come from the  $p_T^{\gamma\gamma}$  and  $\Delta\phi_{\gamma\gamma}$  distributions as we expected, the  $M_{\gamma\gamma}$  and  $|\cos\theta^*|$  distributions are close to each other in PYTHIA and RESBOS. The ratios between RESBOS and PYTHIA truth distributions for  $p_T^{\gamma\gamma}$  and  $\Delta\phi_{\gamma\gamma}$  can be found in Fig. 5.25.

As we can see, the difference can be as large as 80%. How-



**Figure 5.24** The comparison of the default RESBOS and PYTHIA distributions.



**Figure 5.25** The comparison of the default RESBOS and PYTHIA distributions.



ever, with just two-step iterative corrections, we can correct the differences to less than 5%. RESBOS is quite close to data spectra already with just default settings (closer than PYTHIA and RESBOS to PYTHIA), that is why should expect a faster convergence to a stable result and that what we have seen in the previous closure test.

## 5.11 Measurement of double differential cross sections

Further insight on the dependence of the  $p_T^{\gamma\gamma}$ ,  $\Delta\phi_{\gamma\gamma}$ , and  $\cos\theta^*$  kinematic distributions on the mass scale can be gained through the measurement of double differential cross sections. For this purpose, in this section we describe results of the measurement of double (2D) differential cross sections  $d^2\sigma/dM_{\gamma\gamma}dp_T^{\gamma\gamma}$ ,  $d^2\sigma/dM_{\gamma\gamma}d\Delta\phi_{\gamma\gamma}$  and  $d^2\sigma/dM_{\gamma\gamma}d|\cos\theta^*|$  in three  $M_{\gamma\gamma}$  bins: 30 – 50 GeV, 50 – 80 GeV and 80 – 350 GeV. They can be considered as an extension and re-iteration of the single (1D) differential cross section measurements  $d\sigma/dp_T^{\gamma\gamma}$ ,  $d\sigma/d\Delta\phi_{\gamma\gamma}$  and  $d\sigma/d|\cos\theta^*|$  described in the previous sections, that are now done in the three diphoton mass  $dM_{\gamma\gamma}$  intervals, 30 – 50 GeV, 50 – 80 GeV and 80 – 350 GeV. In this case, Eq. 5.1 requires a slight modification as

$$\frac{d^2\sigma}{dXdM} = \frac{N_{data} - N_{bkg}}{L \cdot A_{cc} \cdot \epsilon_{trigger} \cdot \epsilon_{sel} \cdot \Delta X \cdot \Delta M} \quad (5.5)$$

where  $\Delta X$  and  $\Delta M$  are the bin widths for the variable  $X$  and  $M_{\gamma\gamma}$ , correspondingly.

### 5.11.1 Acceptances

To measure acceptances, we use the parameterized fact MC with RESBOS events as in input, in the same way how it was done for the single differential cross sections, described in section 5.4, Specifically, for this aim we used initially the re-weighted RESBOS according to data/RESBOS ratios shown in Fig. 5.16. These acceptances are shown by open blue points in Fig. 5.26. The first

column corresponds to the acceptances for the three mass bins for the  $p_T^{\gamma\gamma}$  variable, the second column to  $\Delta\phi_{\gamma\gamma}$  and the third one to  $\cos\theta^*$ . We used these acceptances to calculate preliminary cross sections. Then, using new ratios data/RESBOS for each variable and the mass bin, we re-weighted RESBOS once more and made final calculation of the acceptances. They are shown by filled black points on the same plots of Fig. 5.26. As one can see, for the 2D case (obtained with the two iterations) acceptances changed, however the size of the changes is within 4–5%.

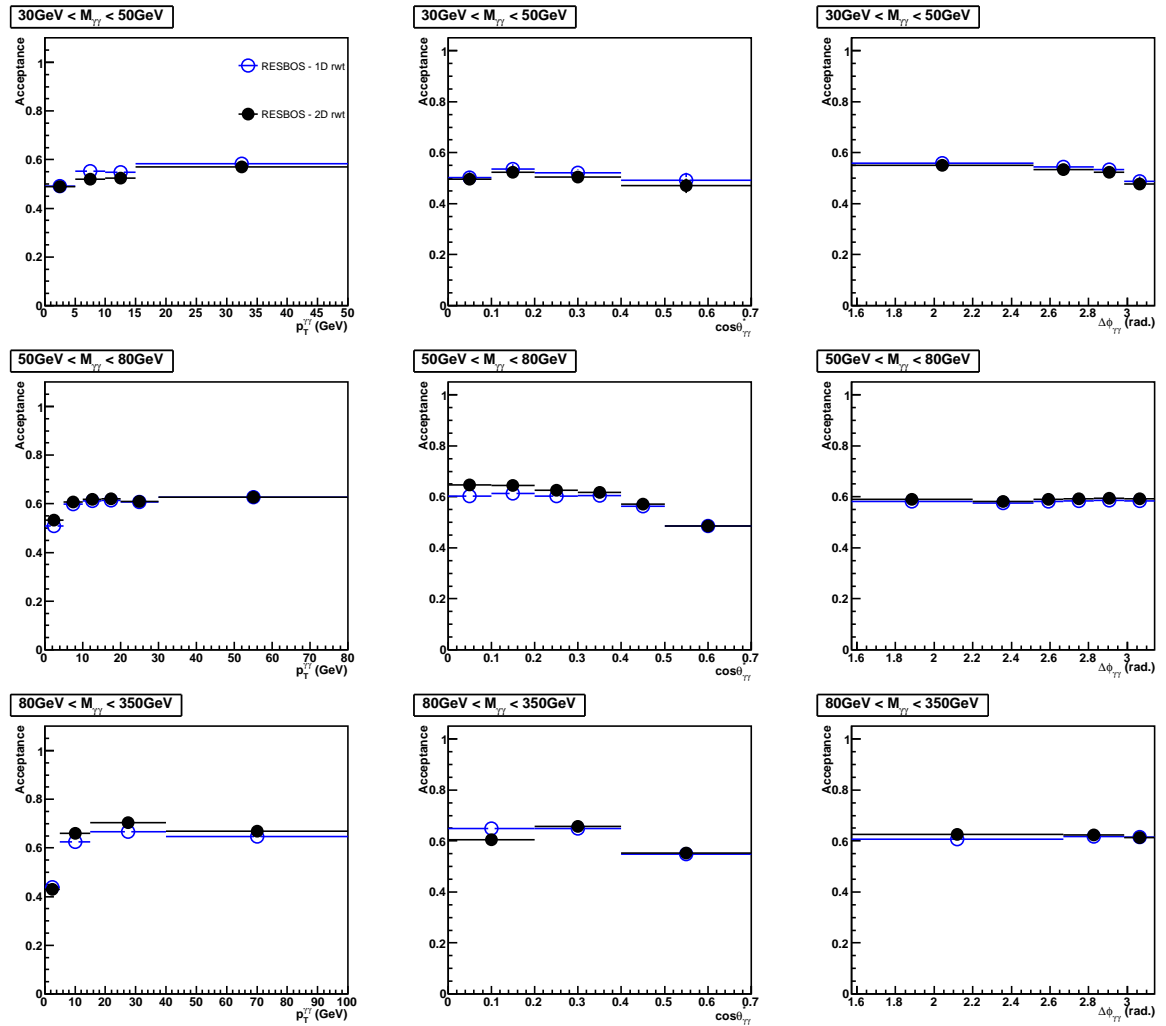


**Figure 5.26** Acceptances for  $p_T^{\gamma\gamma}$ ,  $\cos\theta^*$  and  $\Delta\phi_{\gamma\gamma}$  variables in the three mass bins. Statistical uncertainties only are shown on the plots.

The systematic uncertainties for the acceptance is calculated

analogously to those obtained in Tables 5.4–5.6 (for 1D cross sections). They are shown for all the nine ( $3 \text{ variables} \times 3 \text{ mass bins}$ ) cases in Appendix 8.11. Appendix 8.12 shows comparison of the RESBOS re-weighted to data (as described above) with the background subtracted data for all those cases. As in case of Fig. 8.22 (done for 1D cross sections), from Figs. 8.33 – 8.35 we can see a good agreement between fast MC and data that again gives us confidence about correct simulation of the detector effects in the fast MC.

#### 5.11.2 Selection efficiencies

The diphoton selection efficiencies are calculated by analogy to Section 5.3.1. They are shown in Fig. 5.27. The sources and values of overall systematic uncertainties are the same as shown in Table 5.2. One can see that efficiencies grow slowly from 60–62% at  $30 < M_{\gamma\gamma} < 50 \text{ GeV}$  to 68–70% at  $80 < M_{\gamma\gamma} < 350 \text{ GeV}$  bins in good agreement with the “efficiency vs. mass” dependence shown on the left upper plot of Fig. 5.6.

#### 5.11.3 Diphoton purity

The fractions of the diphoton events in data are calculated bin-by-bin using the matrix method, also applied for the 1D results of Section 5.5.3. The obtained diphoton purities are shown in Fig. 5.28. One can see that the purities slowly grow from  $30 < M_{\gamma\gamma} < 50 \text{ GeV}$  to  $80 < M_{\gamma\gamma} < 350 \text{ GeV}$  mass bins. The source of the systematic uncertainties is related again with the efficiency to pass photon ANN cut  $O_{NN} > 0.6$  that are about

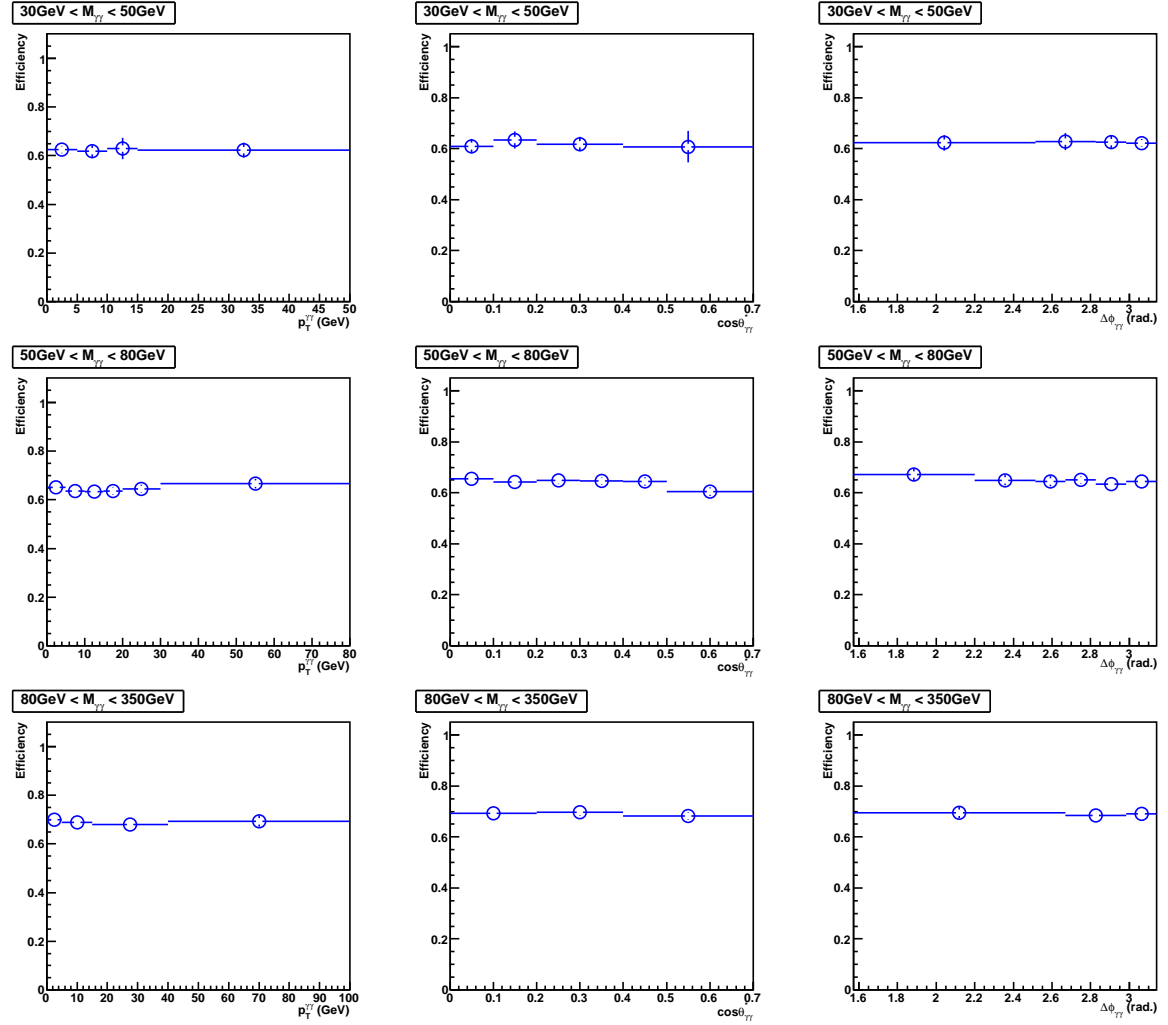


**Figure 5.27** Diphoton selection efficiency. Statistical uncertainties only are shown on the plots.

11–13% for  $N_{\gamma\gamma}$  due to the photon efficiency ( $\varepsilon_\gamma$ ) and varied between 2–26% due to the jet efficiency ( $\varepsilon_j$ ) as shown the second and third columns of Tables 5.9–5.11.

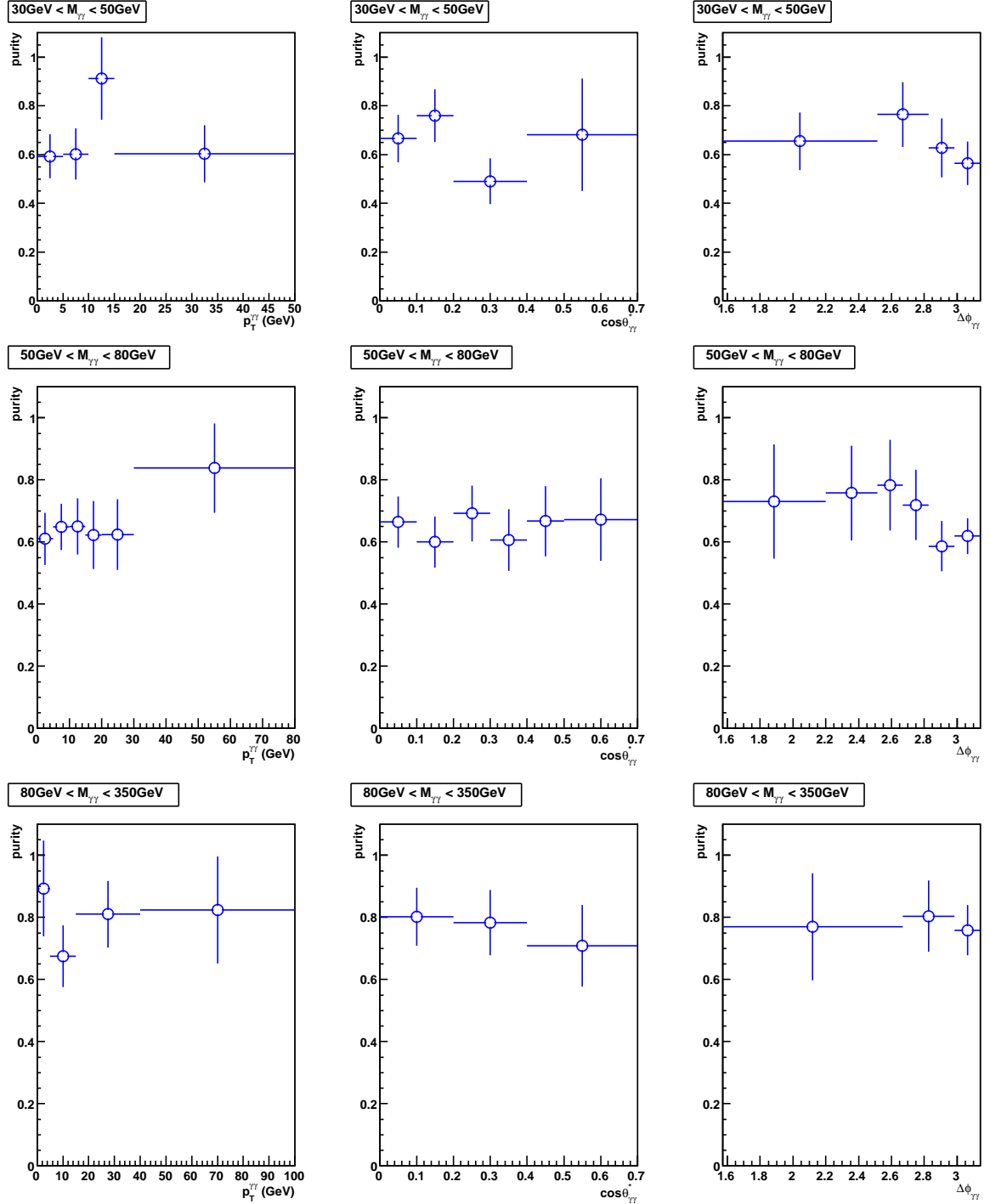


**Figure 5.28** Diphoton fraction (purity) in data. Statistical uncertainties only are shown on the plots.

#### 5.11.4 Double differential cross sections and comparison with theory

Combining results on the acceptance, selection efficiency and the diphoton purity, described above, we can calculate double differential cross sections  $d^2\sigma/dM_{\gamma\gamma}dp_T^{\gamma\gamma}$ ,  $d^2\sigma/dM_{\gamma\gamma}d\Delta\phi_{\gamma\gamma}$  and  $d^2\sigma/dM_{\gamma\gamma}d\cos\theta^*$  using Eq. 5.5. The results are shown in Tables 5.16 – 5.18 for  $d^2\sigma/dM_{\gamma\gamma}dp_T^{\gamma\gamma}$ , in Tables 5.19 – 5.21 for  $d^2\sigma/dM_{\gamma\gamma}d\Delta\phi_{\gamma\gamma}$  and in Tables 5.22 – 5.24 for  $d^2\sigma/dM_{\gamma\gamma}d\cos\theta^*$  cross sections. By analogy to Section 5.9, the results are also compared to the predictions done with RESBOS, DIPHOX and PYTHIA. The results for the cross sections are also shown at plots of Fig. 5.29–5.31. The RESBOS and DIPHOX predictions are corrected for effects from the underlying events as described in Section 5.8 and shown in Fig. 5.14.

With the 2D cross sections we can better see effects of the data/theory disagreement we have seen earlier in Section 5.9. Specifically, one can see that data/RESBOS ratios in bin  $30 < M_{\gamma\gamma} < 50$  GeV reach a factor 2-2.4 at large  $p_T^{\gamma\gamma}$  or small  $\Delta\phi_{\gamma\gamma}$  values and about constant, at about 1.7, in bins of  $\cos\theta^*$ . The level of disagreement becomes smaller at  $50 < M_{\gamma\gamma} < 80$  GeV mass bin and we see that data and RESBOS agree within uncertainties at the last mass bin  $80 < M_{\gamma\gamma} < 350$  GeV.

These 2D cross sections results confirm that the largest discrepancies between data and RESBOS for each of the kinematic variables originate from the lowest  $M_{\gamma\gamma}$  region ( $M_{\gamma\gamma} < 50$  GeV). As shown in Fig. 1.6, this is the region where the contribution from  $gg \rightarrow \gamma\gamma$  is expected to be largest. The discrepancies be-

tween data and RESBOS are reduced in the intermediate  $M_{\gamma\gamma}$  region (50 – 80 GeV), and a quite satisfactory description of all kinematic variables is achieved for the  $M_{\gamma\gamma} > 80$  GeV region, the relevant region for the Higgs boson and new phenomena searches. However, it should be pointed out that at the Tevatron, DPP production at high masses is strongly dominated by  $q\bar{q}$  annihilation, in contrast with the LHC, where the contribution from  $gg$  and  $qg$  initiated process will be significant. It remains to be seen whether the addition of NNLO corrections to RESBOS, as done in<sup>[62]</sup>, will improve the description of the high  $p_T^{\gamma\gamma}$  (low  $\Delta\phi_{\gamma\gamma}$ ) spectrum at low  $M_{\gamma\gamma}$ .

**Table 5.16**  $d^2\sigma/dM_{\gamma\gamma}dp_T^{\gamma\gamma}$  cross section with uncertainties in 30 GeV <  $M_{\gamma\gamma}$  < 50 GeV region.

$p_T^{\gamma\gamma}$ (GeV)	$\langle p_T^{\gamma\gamma} \rangle$ (GeV)	$N_{data}$	$N_{\gamma\gamma}$	$d^2\sigma/dM_{\gamma\gamma}dp_T^{\gamma\gamma}$ (pb/GeV <sup>2</sup> )						
				Data	$\delta_{stat}$ (%)	$\delta_{syst}$ (%)	$\delta_{total}$ (%)	DIPHOX	PYTHIA	RESBOS
0.0 – 5.0	2.4	1097	650	5.11e-03	15.2	+ 16.6/- 14.3	+ 22.5/- 20.9	6.04e-03	3.66e-03	4.64e-03
5.0 – 10.0	7.0	810	488	3.65e-03	17.5	+ 16.1/- 14.1	+ 23.8/- 22.4	1.46e-03	1.11e-03	2.35e-03
10.0 – 15.0	12.2	325	296	2.16e-03	18.6	+ 16.0/- 14.1	+ 24.5/- 23.4	4.24e-04	3.58e-04	8.71e-04
15.0 – 50.0	23.4	612	369	3.58e-04	19.4	+ 15.9/- 14.1	+ 25.1/- 24.0	1.01e-04	6.22e-05	1.67e-04

**Table 5.17**  $d^2\sigma/dM_{\gamma\gamma}dp_T^{\gamma\gamma}$  cross section with uncertainties in 50 GeV <  $M_{\gamma\gamma}$  < 80 GeV region.

$p_T^{\gamma\gamma}$ (GeV)	$\langle p_T^{\gamma\gamma} \rangle$ (GeV)	$N_{data}$	$N_{\gamma\gamma}$	$d^2\sigma/dM_{\gamma\gamma}dp_T^{\gamma\gamma}$ (pb/GeV <sup>2</sup> )						
				Data	$\delta_{stat}$ (%)	$\delta_{syst}$ (%)	$\delta_{total}$ (%)	DIPHOX	PYTHIA	RESBOS
0.0 – 5.0	2.8	1301	794	3.68e-03	13.8	+ 16.0/- 15.2	+ 21.1/- 20.5	6.07e-03	4.21e-03	5.07e-03
5.0 – 10.0	7.3	1827	1185	4.92e-03	11.5	+ 15.8/- 13.8	+ 19.6/- 17.9	2.74e-03	1.92e-03	4.06e-03
10.0 – 15.0	12.3	1103	717	2.93e-03	13.9	+ 15.9/- 13.8	+ 21.1/- 19.6	1.35e-03	8.37e-04	2.33e-03
15.0 – 20.0	17.3	733	457	1.86e-03	17.6	+ 15.9/- 13.8	+ 23.7/- 22.3	7.57e-04	4.10e-04	1.29e-03
20.0 – 30.0	24.1	647	404	8.22e-04	18.3	+ 16.1/- 13.8	+ 24.4/- 23.0	3.76e-04	1.70e-04	5.81e-04
30.0 – 80.0	39.8	417	349	1.34e-04	17.2	+ 15.8/- 13.8	+ 23.4/- 22.1	5.47e-05	1.33e-05	6.81e-05



**Table 5.18**  $d^2\sigma/dM_{\gamma\gamma}dp_T^{\gamma\gamma}$  cross section with uncertainties in  $80 \text{ GeV} < M_{\gamma\gamma} < 350 \text{ GeV}$  region.

$p_T^{\gamma\gamma}$ (GeV)	$\langle p_T^{\gamma\gamma} \rangle$ (GeV)	$N_{data}$	$N_{\gamma\gamma}$	$d^2\sigma/dM_{\gamma\gamma}dp_T^{\gamma\gamma}$ (pb/GeV $^2$ )						
				Data	$\delta_{stat}$ (%)	$\delta_{syst}$ (%)	$\delta_{total}$ (%)	DIPHOX	PYTHIA	RESBOS
0.0 – 5.0	2.8	309	276	1.64e-04	17.2	+ 20.1/- 23.6	+ 26.4/- 29.2	2.23e-04	1.76e-04	1.93e-04
5.0 – 15.0	9.3	768	518	1.02e-04	14.8	+ 16.0/- 14.4	+ 21.8/- 20.7	8.45e-05	6.79e-05	1.18e-04
15.0 – 40.0	24.3	736	596	4.46e-05	13.2	+ 17.8/- 16.4	+ 22.1/- 21.1	2.23e-05	1.37e-05	3.56e-05
40.0 – 100.0	58.1	253	209	6.67e-06	20.9	+ 16.1/- 14.0	+ 26.4/- 25.1	4.53e-06	1.07e-06	5.48e-06

**Table 5.19**  $d^2\sigma/dM_{\gamma\gamma}d\Delta\phi_{\gamma\gamma}$  cross section with uncertainties in  $30 \text{ GeV} < M_{\gamma\gamma} < 50 \text{ GeV}$  region.

$\Delta\phi_{\gamma\gamma}$	$\langle\Delta\phi_{\gamma\gamma}\rangle$	$N_{data}$	$N_{\gamma\gamma}$	$d^2\sigma/dM_{\gamma\gamma}d\Delta\phi_{\gamma\gamma}$ (pb/GeV/rad.)						
				Data	$\delta_{stat}$ (%)	$\delta_{syst}$ (%)	$\delta_{total}$ (%)	DIPHOX	PYTHIA	RESBOS
$0.5\cdot\pi-0.8\cdot\pi$	2.2	606	397	1.47e-02	18.1	+ 15.9/- 14.2	+ 24.1/- 23.0	3.71e-03	2.33e-03	6.16e-02
$0.8\cdot\pi-0.9\cdot\pi$	2.7	519	397	4.54e-02	17.3	+ 16.1/- 14.1	+ 23.7/- 22.3	1.13e-02	9.73e-03	2.25e-02
$0.9\cdot\pi-0.95\cdot\pi$	2.9	643	403	9.45e-02	19.3	+ 16.4/- 14.1	+ 25.3/- 23.9	3.90e-02	3.18e-02	5.76e-02
$0.95\cdot\pi-\pi$	3.1	1076	607	1.56e-01	16.2	+ 16.4/- 14.4	+ 23.1/- 21.7	4.75e-01	1.12e-01	1.47e-01

**Table 5.20**  $d^2\sigma/dM_{\gamma\gamma}d\Delta\phi_{\gamma\gamma}$  cross section with uncertainties in  $50 \text{ GeV} < M_{\gamma\gamma} < 80 \text{ GeV}$  region.

$\Delta\phi_{\gamma\gamma}$	$\langle\Delta\phi_{\gamma\gamma}\rangle$	$N_{data}$	$N_{\gamma\gamma}$	$d^2\sigma/dM_{\gamma\gamma}d\Delta\phi_{\gamma\gamma}$ (pb/GeV/rad.)						
				Data	$\delta_{stat}$ (%)	$\delta_{syst}$ (%)	$\delta_{total}$ (%)	DIPHOX	PYTHIA	RESBOS
$0.5\cdot\pi-0.7\cdot\pi$	2.0	263	192	6.18e-03	25.2	+ 15.9/- 13.8	+ 29.8/- 28.7	2.35e-03	6.92e-04	3.00e-03
$0.7\cdot\pi-0.8\cdot\pi$	2.4	379	287	1.94e-02	20.2	+ 15.9/- 13.8	+ 25.7/- 24.5	7.09e-03	4.01e-03	1.16e-02
$0.8\cdot\pi-0.85\cdot\pi$	2.6	427	334	4.49e-02	18.7	+ 15.9/- 13.8	+ 24.5/- 23.2	1.43e-02	9.36e-03	2.56e-02
$0.85\cdot\pi-0.9\cdot\pi$	2.8	697	501	6.64e-02	15.7	+ 15.9/- 13.8	+ 22.4/- 20.9	2.72e-02	1.75e-02	4.86e-02
$0.9\cdot\pi-0.95\cdot\pi$	2.9	1486	872	1.18e-01	13.7	+ 16.0/- 13.8	+ 21.1/- 19.5	6.72e-02	4.55e-02	1.04e-01
$0.95\cdot\pi-\pi$	3.1	2776	1718	2.30e-01	9.4	+ 15.9/- 13.9	+ 18.4/- 16.7	6.79e-01	1.67e-01	2.47e-01

**Table 5.21**  $d^2\sigma/dM_{\gamma\gamma}d\Delta\phi_{\gamma\gamma}$  cross section with uncertainties in  $80 \text{ GeV} < M_{\gamma\gamma} < 350 \text{ GeV}$  region.

$\Delta\phi_{\gamma\gamma}$	$\langle\Delta\phi_{\gamma\gamma}\rangle$	$N_{data}$	$N_{\gamma\gamma}$	$d^2\sigma/dM_{\gamma\gamma}d\Delta\phi_{\gamma\gamma}$ (pb/GeV/rad.)						
				Data	$\delta_{stat}$ (%)	$\delta_{syst}$ (%)	$\delta_{total}$ (%)	DIPHOX	PYTHIA	RESBOS
$0.5\cdot\pi-0.85\cdot\pi$	2.4	253	195	3.63e-04	22.4	+ 18.4/- 15.6	+ 29.0/- 27.3	2.08e-04	8.38e-05	2.85e-04
$0.85\cdot\pi-0.95\cdot\pi$	2.9	642	516	3.44e-03	14.2	+ 16.1/- 13.9	+ 21.5/- 19.9	1.86e-03	1.18e-04	2.94e-03
$0.95\cdot\pi-\pi$	3.1	1171	888	1.19e-02	10.7	+ 16.0/- 13.8	+ 19.2/- 17.4	3.76e-02	9.57e-03	1.26e-02

**Table 5.22**  $d^2\sigma/dM_{\gamma\gamma}d|\cos\theta^*|$  cross section with uncertainties in  $30 \text{ GeV} < M_{\gamma\gamma} < 50 \text{ GeV}$  region.

$ \cos\theta^* $	$\langle  \cos\theta^*  \rangle$	$N_{data}$	$N_{\gamma\gamma}$	$d^2\sigma/dM_{\gamma\gamma}d \cos\theta^* $ (pb/GeV)						
				Data	$\delta_{stat}$ (%)	$\delta_{syst}$ (%)	$\delta_{total}$ (%)	DIPHOX	PYTHIA	RESBOS
0.0 – 0.1	0.05	963	641	2.55e-01	15.3	+ 17.3/- 13.8	+ 23.1/- 20.6	1.37e-01	9.02e-02	1.49e-01
0.1 – 0.2	0.15	758	576	2.09e-01	14.6	+ 15.9/- 14.5	+ 21.6/- 20.6	1.13e-01	7.26e-02	1.18e-01
0.2 – 0.4	0.28	935	459	8.84e-02	19.4	+ 15.8/- 15.6	+ 25.0/- 24.9	7.40e-02	4.74e-02	7.64e-02
0.4 – 0.7	0.44	188	128	1.80e-02	34.5	+ 19.0/- 14.5	+ 39.4/- 37.4	1.12e-02	6.83e-03	1.02e-02

**Table 5.23**  $d^2\sigma/dM_{\gamma\gamma}d|\cos\theta^*|$  cross section with uncertainties in 50 GeV <  $M_{\gamma\gamma}$  < 80 GeV region.

$ \cos\theta^* $	$\langle \cos\theta^* \rangle$	$N_{data}$	$N_{\gamma\gamma}$	$d^2\sigma/dM_{\gamma\gamma}d \cos\theta^* $ (pb/GeV)						
				Data	$\delta_{stat}$ (%)	$\delta_{syst}$ (%)	$\delta_{total}$ (%)	DIPHOX	PYTHIA	RESBOS
0.0 – 0.1	0.05	1404	932	1.77e-01	12.5	+ 16.1/- 14.0	+ 20.4/- 18.8	1.28e-01	8.19e-02	1.58e-01
0.1 – 0.2	0.15	1287	772	1.50e-01	13.8	+ 16.1/- 13.8	+ 21.2/- 19.5	1.16e-01	7.16e-02	1.41e-01
0.2 – 0.3	0.25	1114	771	1.53e-01	13.1	+ 16.1/- 13.9	+ 20.8/- 19.1	1.06e-01	6.65e-02	1.29e-01
0.3 – 0.4	0.35	944	573	1.15e-01	16.4	+ 15.8/- 13.8	+ 22.8/- 21.5	9.52e-02	6.22e-02	1.14e-01
0.4 – 0.5	0.45	726	485	1.06e-01	17.0	+ 16.1/- 13.9	+ 23.4/- 22.0	7.98e-02	5.37e-02	9.52e-02
0.5 – 0.7	0.58	553	371	5.08e-02	19.9	+ 17.3/- 14.2	+ 26.3/- 24.4	4.16e-02	2.83e-02	4.49e-02

**Table 5.24**  $d^2\sigma/dM_{\gamma\gamma}d\cos\theta^*$  cross section with uncertainties in 80 GeV <  $M_{\gamma\gamma}$  < 350 GeV region.

$ \cos\theta^* $	$\langle \cos\theta^* \rangle$	$N_{data}$	$N_{\gamma\gamma}$	$d^2\sigma/dM_{\gamma\gamma}d \cos\theta^* $ (pb/GeV)						
				Data	$\delta_{stat}$ (%)	$\delta_{syst}$ (%)	$\delta_{total}$ (%)	DIPHOX	PYTHIA	RESBOS
0.0 – 0.2	0.10	889	713	7.58e-03	11.7	+ 17.2/- 14.3	+ 20.8/- 18.4	5.08e-03	3.57e-03	5.89e-03
0.2 – 0.4	0.30	670	525	5.11e-03	13.4	+ 15.8/- 13.7	+ 20.7/- 19.2	4.42e-03	3.09e-03	5.11e-03
0.4 – 0.7	0.53	505	358	2.82e-03	18.6	+ 16.1/- 14.0	+ 24.6/- 23.2	2.93e-03	2.10e-03	3.42e-03

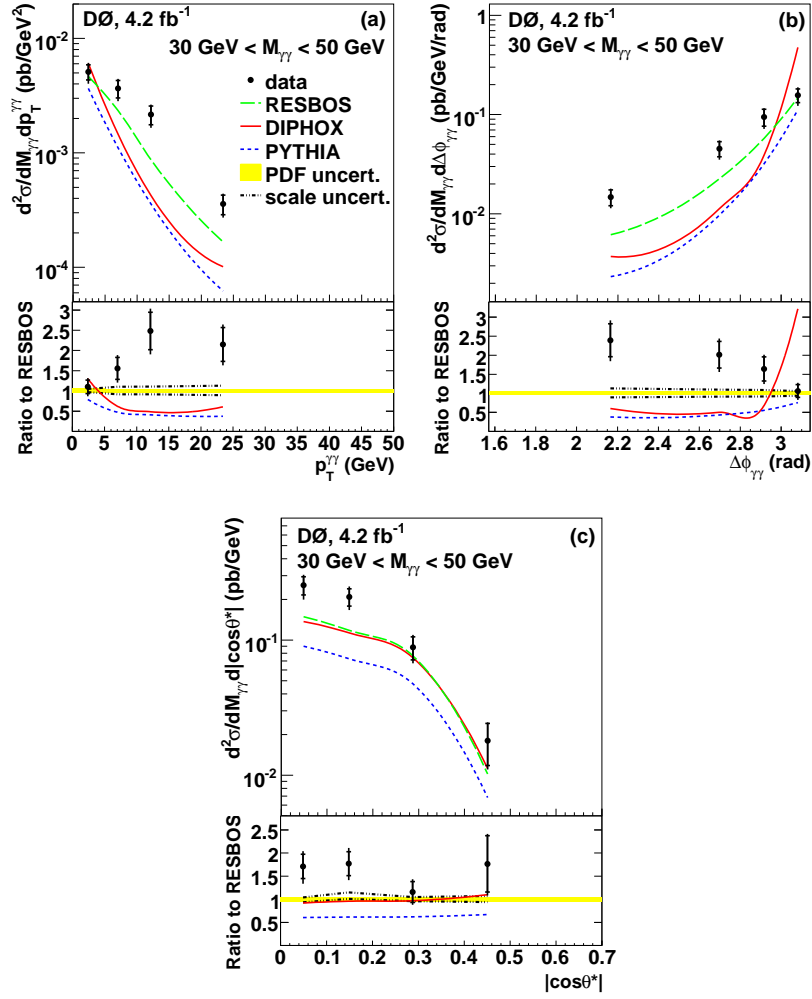


**Figure 5.29** The measured double differential diphoton production cross sections as functions of (a)  $p_T^{\gamma\gamma}$ , (b)  $\Delta\phi_{\gamma\gamma}$  and (c)  $\cos\theta^*$  for the diphoton mass bin  $30 < M_{\gamma\gamma} < 50$  GeV.

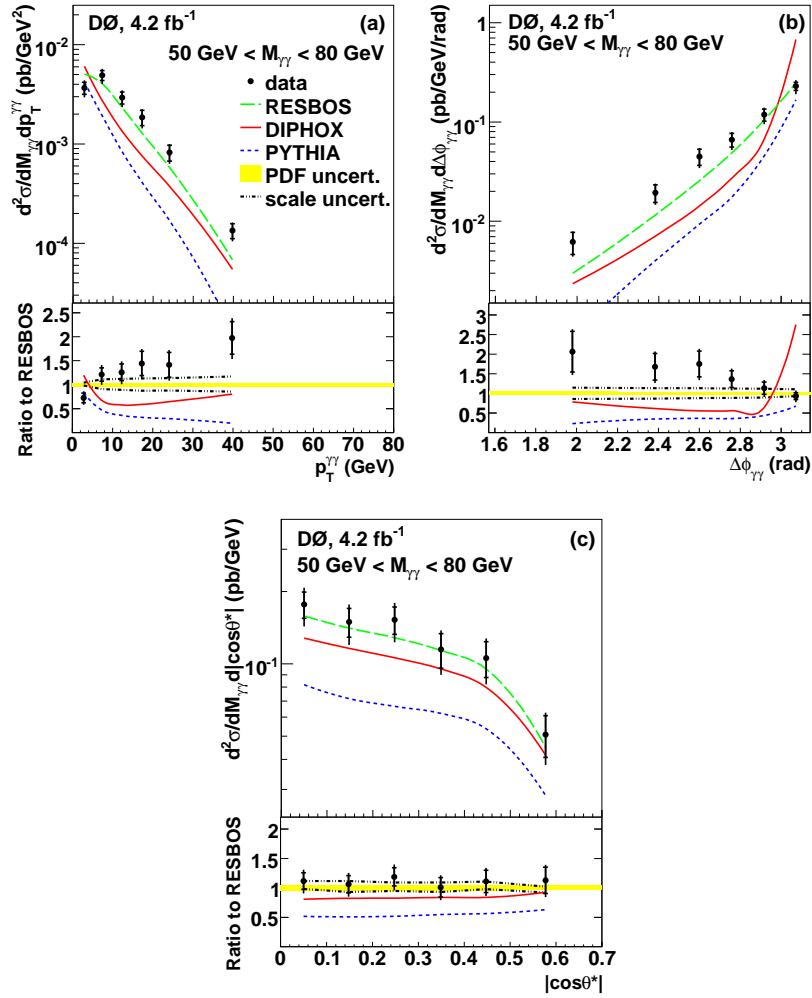


**Figure 5.30** The measured double differential diphoton production cross sections as functions of (a)  $p_T^{\gamma\gamma}$ , (b)  $\Delta\phi_{\gamma\gamma}$  and (c)  $\cos\theta^*$  for the diphoton mass bin  $50 < M_{\gamma\gamma} < 80$  GeV.

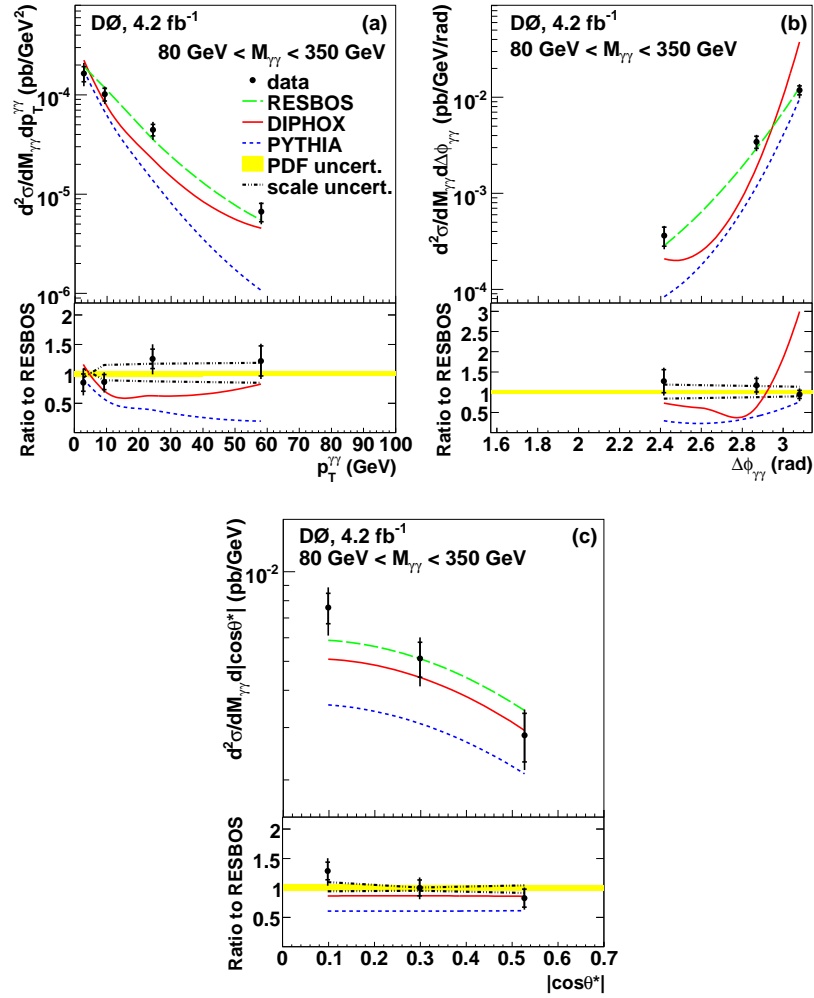


**Figure 5.31** The measured double differential diphoton production cross sections as functions of (a)  $p_T^{\gamma\gamma}$ , (b)  $\Delta\phi_{\gamma\gamma}$  and (c)  $\cos\theta^*$  for the diphoton mass bin  $80 < M_{\gamma\gamma} < 350$  GeV.



## Chapter 6 Conclusion

In this thesis, we present a search for a Higgs boson in the diphoton final state using  $4.2 \pm 0.3 \text{ fb}^{-1}$  of the DØ Run II data, collected at the Fermilab Tevatron collider from April 2002 to December 2008. Good agreement between the data and the SM background prediction is observed. Since there is no evidence for new physics, we set 95% C.L. limits on the production cross section times the branching ratio ( $\sigma \times BR(H \rightarrow \gamma\gamma)$ ) relative to the SM-like Higgs prediction for different assumed Higgs masses. The observed limits ( $\frac{\sigma(limit)}{\sigma(SM)}$ ) range from 11.9 to 35.2 for Higgs masses from 100 to 150 GeV, while the expected limits range from 17.5 to 32.0. By comparison with the published  $2.7 \text{ fb}^{-1}$  results<sup>[9]</sup>, the limits are improved by about 20%, as expected from the luminosity increase. This search is also interpreted in the context of a particular fermiophobic Higgs model. The corresponding results have reached the same sensitivity as a single LEP experiment, setting a lower limit on the fermiophobic Higgs of  $M_{h_f} > 102.5 \text{ GeV}$  ( $M_{h_f} > 107.5 \text{ GeV}$  expected). We provide access to the  $M_{h_f} > 125 \text{ GeV}$  region which was inaccessible at LEP. We are slightly below the combined LEP limit ( $M_{h_f} > 109.7 \text{ GeV}$ ), however, the combined Tevatron limit could potentially exceed it.

We also present the precise measurement of the DPP single differential cross sections as a function of the diphoton mass,

the transverse momentum of the diphoton system, the azimuthal angle between the photons, and the polar scattering angle of the photons, as well as the double differential cross sections considering the last three kinematic variables in three diphoton mass bins, using  $4.2\text{ fb}^{-1}$  data. These results are the first of their kind at DØ, and in fact the double differential measurements are the first of their kind at Tevatron.

The measured cross sections are compared to predictions from RESBOS, DIPHOX and PYTHIA, showing the necessity of including higher order corrections beyond NLO as well as the resummation to all orders of soft and collinear initial state gluons. These results allow the tuning of the theoretical predictions for this process, which is of great relevance for improving the sensitivity of searches for the Higgs boson and other new phenomena at the Tevatron and the LHC.

As one can see, the  $H \rightarrow \gamma\gamma$  channel can be used to increase the overall sensitivity of the SM Higgs boson search program at the Tevatron<sup>[11]</sup>, especially for the difficult intermediate mass region ( $110 < M_H < 140\text{ GeV}$ ) and allows new physics models predicting an enhanced  $H \rightarrow \gamma\gamma$  BR to be probed. For the current  $H \rightarrow \gamma\gamma$  search (see Chapter 4), only the diphoton mass distribution is used for the final limits setting, due to the imperfect theoretical prediction of the major and irreducible DPP background. To understand this important background, we later do the precise measurement on its differential cross sections (see Chapter 5). The results show that RESBOS agrees with data very



well in the  $M_{\gamma\gamma}$  region of interest. Thus, one could employ multivariate techniques to allow use of additional information beyond  $M_{\gamma\gamma}$  in the final limit setting, for instance, the transverse momentum of the diphoton system, to improve the sensitivity to the Higgs boson searches (as well as other diphoton resonances).

As well as using a multivariate technique with the better predicted DPP production, there are also other areas in which the overall  $H \rightarrow \gamma\gamma$  sensitivity can be improved, namely:

- Add more data events;
- Add the CC-EC sub-composition, the overall acceptance could be increased by  $\sim 50\%$ ;
- Use the CPS-pointing technique to reduce the mis-vertex rate;
- Improve the energy resolution using the energy deposited in the CPS. The current preliminary results from the single electron MC (see Fig. 6.1) shows  $> 10\%$  improvement;
- Develop more powerful photon ID variables with using FPS;

Thus, with the full  $10\text{ fb}^{-1}$  data events, we expect  $\sim 50\%$  improvement from the additional integrated luminosity, along with a further  $50\%$  gain from adding all the above improvements, in particular the use of a multivariate technique in the limit setting. The expected limits on  $\sigma \times BR$  over the SM prediction would then be expected less than 10 for the intermediate mass region ( $110 < M_H < 140\text{ GeV}$ ).

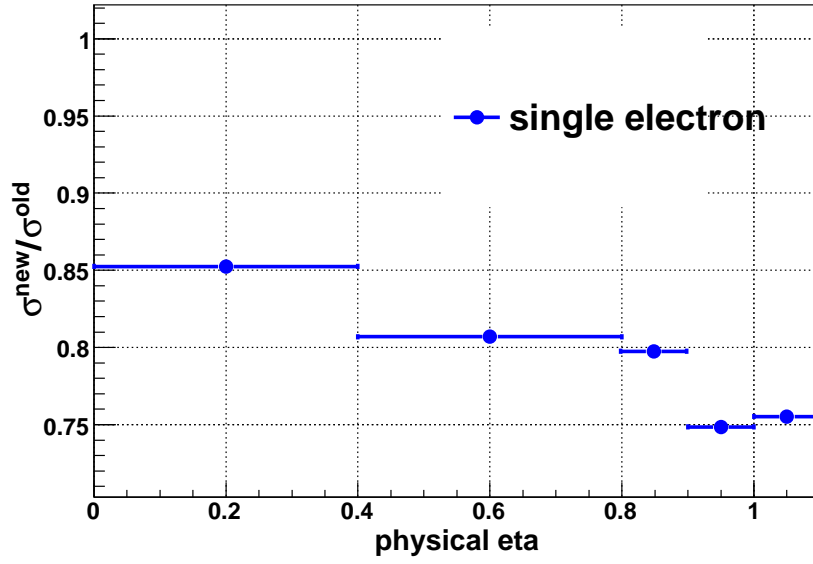


**Figure 6.1** Energy resolution improvement as a function of electron rapidity from  $E = 45$  GeV single electron MC events, where  $\sigma^{\text{old}}$  is from the default energy resolution with using the 4 EM layer energy deposition, the  $\sigma^{\text{new}}$  is obtained with additionally using the energy deposited in CPS.

## Chapter 7 Bibliography

- [1] The ALEPH, DELPHI, L3 and OPAL Collaborations, and the LEP Working Group for Higgs Boson Searches, *Phys. Lett. B* **565**, 61 (2003).
- [2] The ALEPH, CDF, DØ DELPHI, L3, OPAL, and SLD Collaborations, the LEP Electroweak Working Group, the Tevatron Electroweak Working Group, and the SLD Electroweak and Heavy Flavour Groups, arXiv:0911.2604 [hep-ex] (2009).
- [3] DØ and CDF collaborations, *Phys. Rev. Lett.* **104**, 061802 (2010).
- [4] S. Catani *et al.*, *JHEP* **0307**, 028 (2003).
- [5] U. Aglietti *et al.*, arXiv:hep-ph/0610033 (2006).
- [6] K.A. Assamagan *et al.*, arXiv:hep-ph/0406152 (2004).
- [7] A. Djouadi, J. Kalinowski and M. Spira, *Comput. Phys. Commun.* **108**, 56 (1998).
- [8] G. Aad *et al.* (ATLAS Collaboration), arXiv:0901.0512[hep-ex] (2009); G.L. Bayatian *et al.* (CMS Collaboration), *J. Phys. G* **34**, 995 (2007).
- [9] V.M. Abazov *et al.* (DØ Collaboration), *Phys. Rev. Lett.* **102**, 231801 (2009). X. Bu *et al.*, DØ note 5734 (2008).

- [10] S. Mrenna and J. Wells, Phys. Rev. D **63**, 015006 (2001); and references therein.
- [11] The TEVNPHWorking Group, for the CDF and DØ Collaborations, arXiv:0903.4001 [hep-ex] (2009).
- [12] See e.g. G.F. Giudice, R. Rattazzi, Phys. Rept. **322**, 419 (1999); M.C. Kumar, P. Mathews, V. Ravindran and A. Tripathi Phys. Lett. B **672**, 45 (2009); and references therein.
- [13] T. Sjöstrand *et al.*, arXiv:hep-ph/0108264 (2001).
- [14] W.K. Tung *et al.*, JHEP **0702**, 052 (2007).
- [15] C. Balazs, E.L. Berger, P. Nadolsky and C.-P. Yuan, Phys. Rev. D **76**, 013009 (2007); and references therein.
- [16] T. Binoth, J. Ph.Guillet, E. Pilon, and M. Werlen, Eur. Phys. J. C **16**, 311 (2000).
- [17] M. Syphers, Fermilab Accelerator Division, Accelerator Concepts, Version 3.0 (2002).
- [18] Fermilab Accelerator Division Document Databases, <http://beamdocs.fnal.gov/DocDB//Static/Lists//FullList.html>
- [19] S. Abachi *et al.* (DØ Collaboration), The DØ Detector, Nucl. Instr. and Methods, A338, 185 (1994).
- [20] V. Abazov *et. al.*, The Upgraded DØ Detector, Nucl. Instrum. Methods Phys. Res., A565, 463 (2006).
- [21] DØ Collaboration, Calorimeter Electronics Upgrade for Run 2, (1998).

- [22] DØ Upgrade Collaboration, “DØ Silicon Tracker Technical Design Report”, [http://www-d0.fnal.gov/trigger/stt/smt/smt\\_tdr.ps](http://www-d0.fnal.gov/trigger/stt/smt/smt_tdr.ps).
- [23] D. Adams et al. (DØ Collaboration), The D0 Upgrade: Central Fiber Tracker, Technical Design Report, DØ note 4164 (1999).
- [24] M. Adams et al. (DØ Collaboration), Central Fiber Tracker Technical Design Report, DØ note 3014 (1996).
- [25] DØ Collaboration, The DØ Upgrade: Forward Preshower, Muon System and Level 2 Trigger, DØ note 2894 (1996).
- [26] B. Abbott et al. (DØ Collaboration), Measurement of the  $W$  boson mass, Phys. Rev. D **58**, 092003 (1998).
- [27] A. Schwartzman and M. Narain, Vertex Fitting by means of the Kalman Filter technique, DØ note 3907 (2001).
- [28] A. Schwartzman and M. Narain, Probabilistic Primary Vertex Selection, DØ note 4042 (2002).
- [29] X. Bu *et al.* “Artificial neural network using central preshower detector information for electron and photon selection”, DØ Note 5650 (2008).
- [30] V.M. Abazov *et al.* (DØ Collaboration), Phys. Lett. B **653**, 378 (2007).

- [31] G. C. Blazey *et al.*, "Run II Jet Physics: Proceedings of the Run II QCD and Weak Boson Physics Workshop", arXiv:hep-ex/0005012 (2000).
- [32] R. Brun and F. Carminati, CERN Program Library Long Writeup W5013 (1993); we use GEANT version v3.21.
- [33] "Jet Energy Scale Determination at DØ Run II", [http://www-d0.fnal.gov/physid/jes/d0\\_private/certified/certified\\_jes.html](http://www-d0.fnal.gov/physid/jes/d0_private/certified/certified_jes.html)
- [34] Jet Energy Scale group, DØ Note 5382 (2007).
- [35] Tim Andeen and Alex Melnitchouk, Measurement of Electron Energy Scale and Offset with  $Z \rightarrow ee$  Full Monte Carlo and Data, DØ Note 5662 (2009).
- [36] C. Fabjan and F. Gianotti, Calorimetry for particle physics, Rev. Mod. Phys., Vol.75 (2003).
- [37] A. Melnitchouk, M. Wetstein, Determination of the constant term of the electron resolution, DØ Note 5879 (2009).
- [38] V. Abazov *et al.* (DØ collaboration), Phys. Lett. B **666**, 435 (2008); Phys. Rev. Lett. **102**, 192002 (2009).
- [39] A. Heister *et al.* (ALEPH Collaboration), Phys. Lett. B **544**, 16 (2002);  
P. Abreu *et al.* (DELPHI Collaboration), Phys. Lett. B **507**, 89 (2001); Eur. Phys. J. C **35**, 313, (2004);  
G. Abbiendi *et al.* (OPAL Collaboration), Phys. Lett. B **544**,

- 44 (2002);  
P. Achard *et al.* (L3 Collaboration), Phys. Lett. B **534**, 28 (2002); Phys. Lett. B **568**, 191 (2003);  
LEP (LEP Higgs Working Group) hep-ex/0107035, (2001).
- [40] B. Abbott *et al.* (DØ Collaboration), Phys. Rev. Lett. **82**, 2244 (1999);  
T. Affolder *et al.* (CDF Collaboration), Phys. Rev. D **64**, 092002 (2001);  
V.M. Abazov *et al.* (DØ Collaboration), Phys. Rev. Lett. **101**, 051801 (2008);  
T. Aaltonen *et al.* (CDF Collaboration), Phys. Rev. Lett. **103**, 061803 (2009).
- [41] ATLAS Calorimeter Performance, TDR-1, CERN/LHCC 96-40, December 1996.
- [42] CMS ECAL Technical Design Report, CERN/LHCC 97-33, CMS TDR 4, 15 December 1997.
- [43] T. Andeen *et al.*, FERMILAB-TM-2365 (2007).
- [44] L. Han, Y. Liu, H. Yin and J. Zhu, “Measurement of the forward-backward charge asymmetry in  $Z/\gamma^* + Z \rightarrow e^+e^- + X$  events produced at  $\sqrt{s} = 1.96$  TeV, DØ Note 5603 (2008).
- [45] S. Catani *et al.*, JHEP 0307, 028 (2003).
- [46] U. Aglietti *et al.*, arXiv:hep-ph/0610033 (2006).

- [47] K.A. Assamagan et al., arXiv:hep-ph/0406152 (2004).
- [48] R. Hamberg, W. L. van Neerven and T. Matsuura, Nucl. Phys. B **359**, 343 (1991) [Erratum-ibid. B **644**, 403 (2002)].
- [49] Y. Liu, Ph.D. thesis, Fermilab [FERMILAB-THESIS-2004-37] (2004).
- [50] W. Fisher, FERMILAB-TM-2386-E (2006).
- [51] T. Junk, Nucl. Instrum. Meth. A **434**, 435 (1999); A. Read, CERN 2000-005 (30 May 2000).
- [52] X. Bu *et al.*, “Search for the standard model Higgs boson in di-photon final states at DZero with  $4.2 \text{ fb}^{-1}$  of data”, DØ Note 5846 (2008).
- [53] E. Bonvin et al. (WA70 Collaboration), Z. Phys. C 41, 591 (1989); Phys. Lett. B 236, 523 (1990).
- [54] M. Begel, Ph.D. Thesis, University of Rochester (1999), FERMILAB-THESIS-1999-05.
- [55] C. Albajar et al. (UA1 Collaboration), Phys. Lett. B 209, 385 (1988).
- [56] J. Alitti et al. (UA2 Collaboration), Phys. Lett. B 288, 386 (1992).
- [57] F. Abe et al. (CDF Collaboration), Phys. Rev. Lett. 70, 2232 (1993); D. Acosta et al. (CDF Collaboration), Phys. Rev. Lett. 95, 022003 (2005).



- [58] T. Andeen *et al.*, DØ note 5868.
- [59] R. Barlow, C. Beeston, *Comp.Phys.Comm.* **77** (1993)219-228. See also p.120-131 of HBOOK manual.
- [60] T. Sjostrand and P. Skands, *JHEP* (2004) 0403.
- [61] D.Wicke, P.Skands, hep-ph:0807.3248
- [62] Q.-H. Cao, C.-R. Chen, C. Schmidt, and C.-P. Yuan, arXiv:0909.2305 [hep-ph] (2009).



## Chapter 8 Appendices

### 8.1 $Z/\gamma^* \rightarrow ee$ background

The number of data events are split to the four categories as described in Section 4.3.2 in different mass bin. The number of normalized Drell-Yan events is estimated from MC as described in Section 4.3.1. The electron  $O_{NN} > 0.75$  efficiency is found to be  $0.63 \pm 0.01$  ( $\epsilon_{O_{NN}}^e$ ) from  $Z \rightarrow ee$  data after all event selection described in Section 4.2. Thus the fraction of Drell-Yan events in four different categories are calculated as

$$\begin{aligned}\epsilon_{DY}^{pp} &= \frac{N_{DY}}{N_{pp}} \times \epsilon_{O_{NN}}^e \cdot \epsilon_{O_{NN}}^e \\ \epsilon_{DY}^{pf} &= \frac{N_{DY}}{N_{pf}} \times \epsilon_{O_{NN}}^e \cdot (1.0 - \epsilon_{O_{NN}}^e) \\ \epsilon_{DY}^{fp} &= \frac{N_{DY}}{N_{fp}} \times (1.0 - \epsilon_{O_{NN}}^e) \cdot \epsilon_{O_{NN}}^e \\ \epsilon_{DY}^{ff} &= \frac{N_{DY}}{N_{ff}} \times (1.0 - \epsilon_{O_{NN}}^e) \cdot (1.0 - \epsilon_{O_{NN}}^e)\end{aligned}\tag{8.1}$$

To smoothen out the statistical fluctuation for the final limits setting, we use the Gaussian convoluted the Breit-Wigner and plus the exponential function ( $p_3 * TMath::Voigt(M_{diem} - p_0, p_1, p_2, 4) + \exp(e_1 * M_{diem} + e_2)$ ) to fit the final invariant mass distribution. Fig. 8.1 shows the corresponding results.

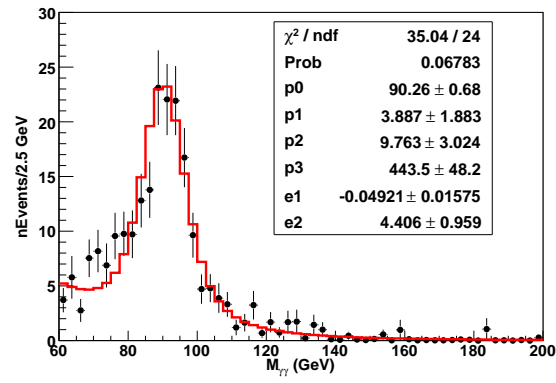


**Figure 8.1** Normalized invariant mass distribution from  $Z/\gamma^* \rightarrow ee$  contribution.

## 8.2 Photon energy scale

We use the same event selection (Section 4.2) requirement except reversing the track match cut to select two electrons from Zee data and full PYTHIA MC samples, the invariant mass distribution is shown in Fig. 8.2. The data and MC distribution agree very well, and we choose 0.3% as the electron energy scale uncertainty by comparing the mass value between the data and MC. Since electrons lose more energy in dead material than photons, the electron energy scale corrections effectively "overcorrect" the photon energies, so another 0.5% photon-to-electron energy scale uncertainty is also taken into account, a comparison of the reconstructed and particle-level electron/photon energies as a function of the reconstructed energy for different scenarios has been detailedly studied by the Ref.<sup>[33]</sup>, where the 0.5% is chosen for the particular photon  $E_T$  region ( $50 \text{ GeV} < E_T < 100 \text{ GeV}$ ). The final photon energy scale uncertainty is taken as the quadrature of the above two uncertainties, and we apply the uncertainty to the 4-momentum of the photons for our signal MC samples, then we treat the corresponding shape change (see Figs. 8.3 and 8.4) as the systematic uncertainties when calculating the final limits.

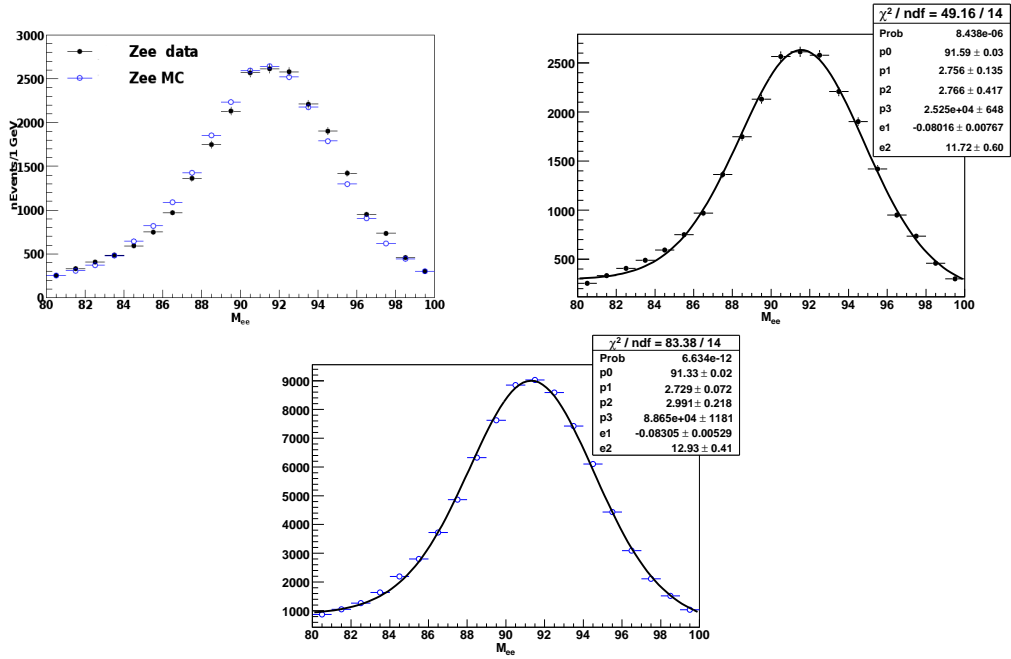


**Figure 8.2** Left plot is the invariant mass distribution of the two electrons candidates for the Zee data and MC, middle and right plots show the corresponding fitting results for the data and MC respectively, where the fitting function is  $p_3 * TMath::Voigt(M_{ee} - p_0, p_1, p_2, 4) + \exp(e_1 * M_{ee} + e_2)$ .

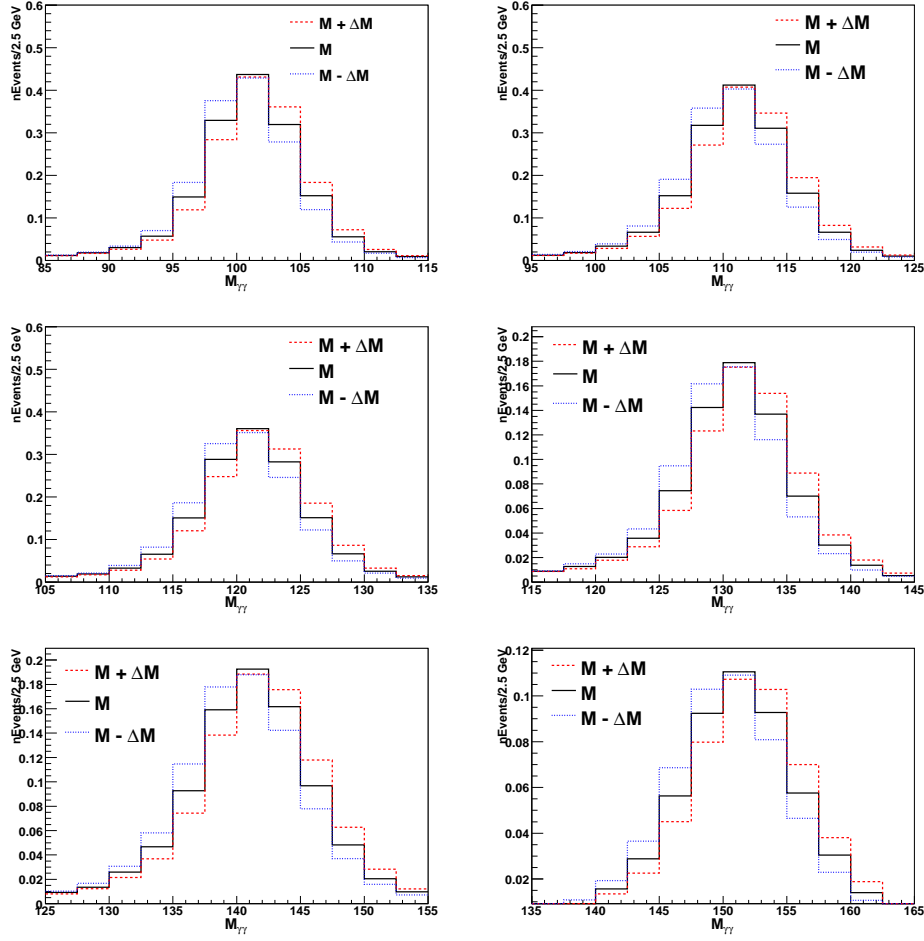


**Figure 8.3** Invariant mass distribution of the two photon candidates for the Higgs MC samples in mass interval of  $(M_H - 15 \text{ GeV}, M_H + 15 \text{ GeV})$  for 100 (top-left), 110 (top-right), 120 (middle-left), 130 (middle-right), 140 (bottom-left), and 150 (bottom-right) GeV Higgs mass with 2.5 GeV step for each mass bin. The dotted lines show the positive (red) and negative (blue) shape systematic uncertainties from photon energy scale.

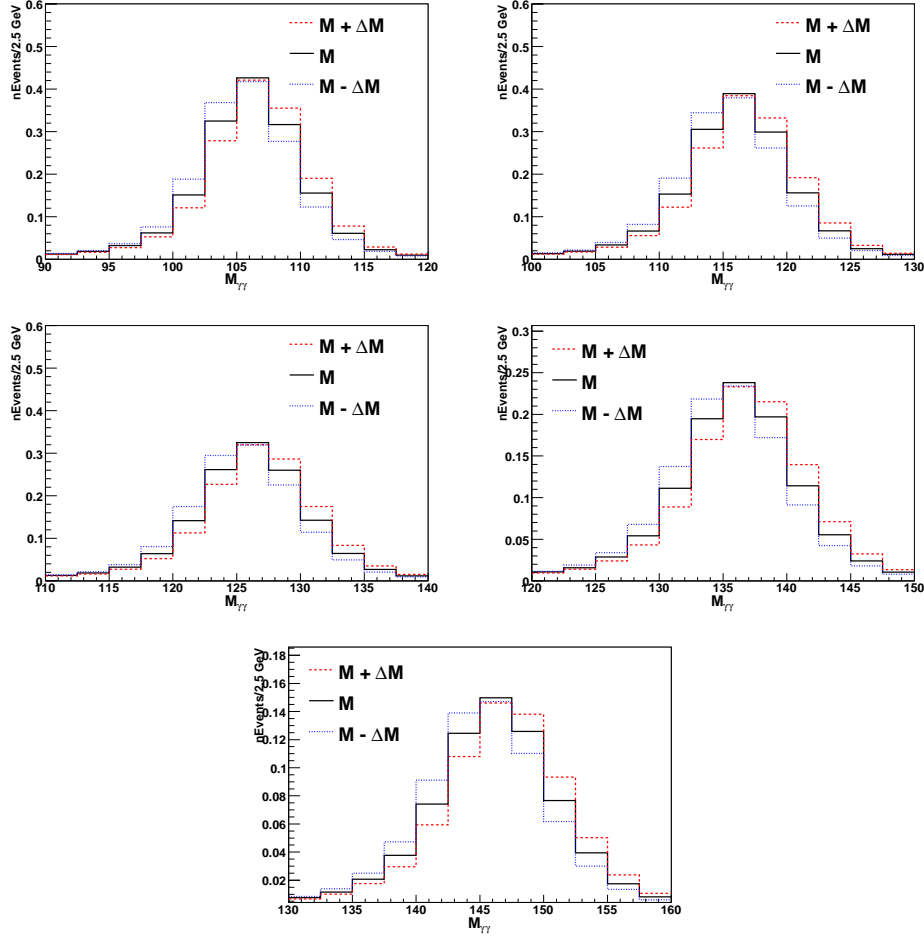


**Figure 8.4** Invariant mass distribution of the two photon candidates for the Higgs MC samples in mass interval of  $(M_H - 15 \text{ GeV}, M_H + 15 \text{ GeV})$  for 105 (top-left), 115 (top-right), 125 (middle-left), 135 (middle-right), 145 (bottom) GeV Higgs mass with 2.5 GeV step for each mass bin. The dotted lines show the positive (red) and negative (blue) shape systematic uncertainties from photon energy scale.



### 8.3 $H p_T$ reweighting

In order to estimate the difference between PYTHIA and SHERPA NLO, the  $H p_T$  is reweighted according to the SHERPA. Such weight effect has been checked on the acceptance and the diphoton invariant mass for GF signal. Table 8.1 shows the acceptance change after adding the weight, the effect is negligible in the high mass region. Fig. 8.5 shows the ratio for the diphoton invariant mass between with and without such weight, from the plots we can see all ratios are almost flat.

mass (GeV)	100	110	120	130	140	150
$\delta_{acc}$	0.023	0.018	0.011	0.009	0.004	0.0001

**Table 8.1** Relative acceptance change for each mass points.

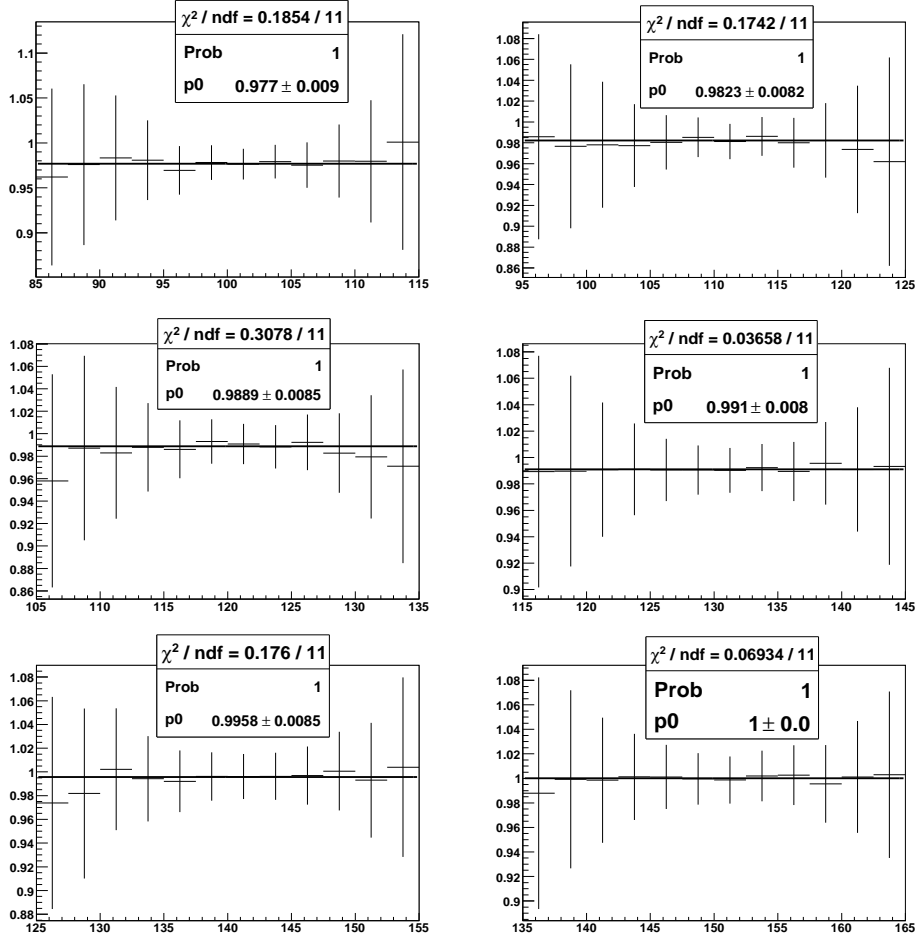


**Figure 8.5** The ratio for the invariant mass distribution of the two photon candidates for the Higgs MC samples between with and without  $H p_T$  weight in mass interval of  $(M_H - 15 \text{ GeV}, M_H + 15 \text{ GeV})$  for 100 (top-left), 110 (top-right), 120 (middle-left), 130 (middle-right), 140 (bottom-left), and 150 (bottom-right) GeV, where the uncertainty maybe overestimated since the statistical uncertainties are treated as uncorrelated for the original two mass distributions.

#### 8.4 Fitting function from $O_{NN}$ -reversed sample

The systematic uncertainty ( $\Delta \mathbf{f}$ ) of the fitting function ( $\mathbf{f}$ ) from  $O_{NN}$ -reversed sample used to predict the shape of non- $\gamma\gamma$  component as section 4.3.2 described affects the shape of the non- $\gamma\gamma$  component, thus further affects the shape of the direct  $\gamma\gamma$  contribution. We measure the  $\Delta \mathbf{f}$  effect on the non- $\gamma\gamma$  component and direct  $\gamma\gamma$  contribution in each different mass interval. Figs. 8.6 and 8.7 show the corresponding results. For limits calculation, we take into account the shapes from  $\mathbf{f} \pm \Delta \mathbf{f}$  as the systematic uncertainties, and treat their effects as correlated between the non- $\gamma\gamma$  component and direct  $\gamma\gamma$  contribution.

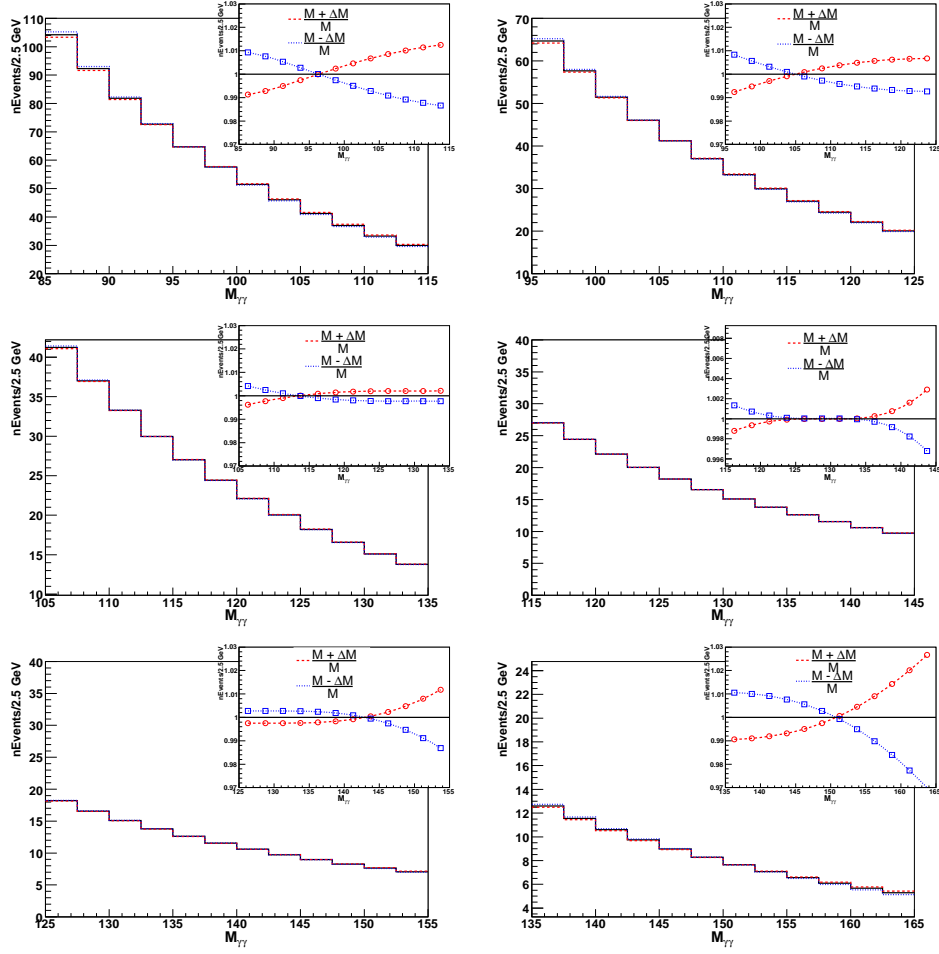


**Figure 8.6** Invariant mass distribution of the two photon candidates for the non- $\gamma\gamma$  component in mass interval of  $(M_H-15 \text{ GeV}, M_H+15 \text{ GeV})$  for 100 (top-left), 110 (top-right), 120 (middle-left), 130 (middle-right), 140 (bottom-left), and 150 (bottom-right) GeV Higgs mass with 2.5 GeV step for each mass bin. The dotted lines show the positive (red) and negative (blue) shape systematic uncertainties from the fitting function of  $O_{NN}$ -reversed sample.

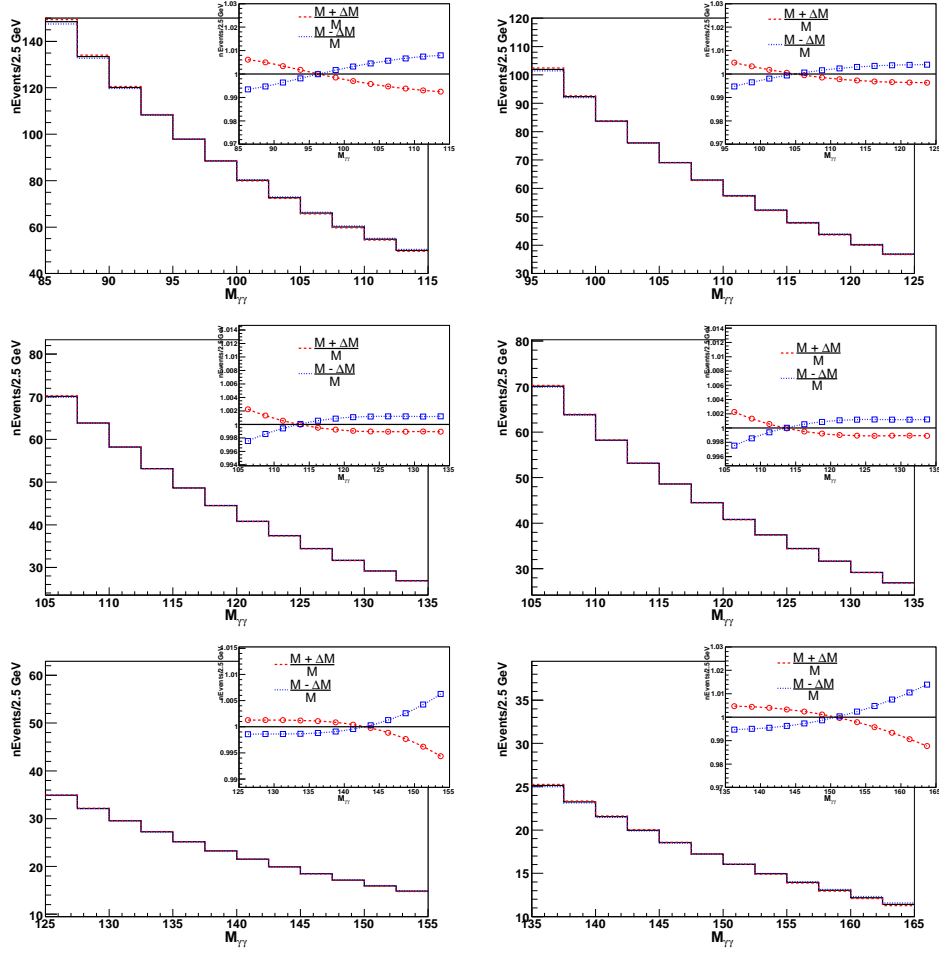


**Figure 8.7** Invariant mass distribution of the two photon candidates for the direct  $\gamma\gamma$  contribution in mass interval of  $(M_H-15 \text{ GeV}, M_H+15 \text{ GeV})$  for 100 (top-left), 110 (top-right), 120 (middle-left), 130 (middle-right), 140 (bottom-left), and 150 (bottom-right) GeV Higgs mass with 2.5 GeV step for each mass bin. The dotted lines show the positive (red) and negative (blue) shape systematic uncertainties from the fitting function of  $O_{NN}$ -reversed sample.

### 8.5 $4 \times 4$ matrix background subtraction

The uncertainty of the  $O_{NN} > 0.75$  efficiencies for the photon and photon-like jets is the source of the  $4 \times 4$  matrix background subtraction uncertainty. We adopt the difference in the number of background events from the mean efficiencies and the plus(minus) uncertainties as the systematic uncertainty. Table 8.2 shows the corresponding three systematic uncertainties for the non- $\gamma\gamma$  component, we take the total quadrature of the three as the final systematic for non- $\gamma\gamma$  normalization, thus this uncertainty would further affect the shape of the direct  $\gamma\gamma$  component. We treat its effect correlated between the non- $\gamma\gamma$  component and direct  $\gamma\gamma$  component. The effects are measured for each mass interval, the corresponding results are shown in Figs. 8.8 – 8.11.

stat.	5.6%
$\epsilon_\gamma \pm 2\%$	12.0%
$\epsilon_j \pm 10\%$	5.4%
total	14.3%

**Table 8.2** Systematic uncertainties for the non- $\gamma\gamma$  component.

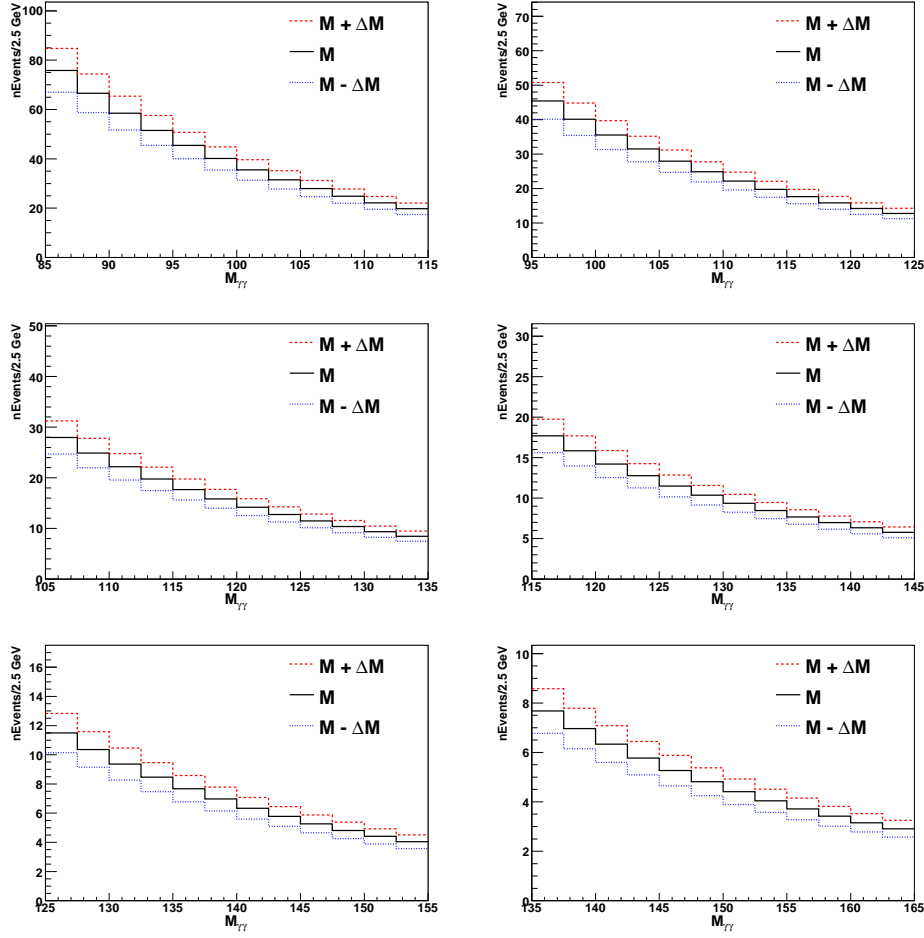


**Figure 8.8** Invariant mass distribution of the two photon candidates for the non- $\gamma\gamma$  component in mass interval of  $(M_H-15 \text{ GeV}, M_H+15 \text{ GeV})$  for 100 (top-left), 110 (top-right), 120 (middle-left), 130 (middle-right), 140 (bottom-left), and 150 (bottom-right) GeV Higgs mass with 2.5 GeV step for each mass bin. The dotted lines show the positive (red) and negative (blue) shape systematic uncertainties from  $4 \times 4$  matrix background subtraction.

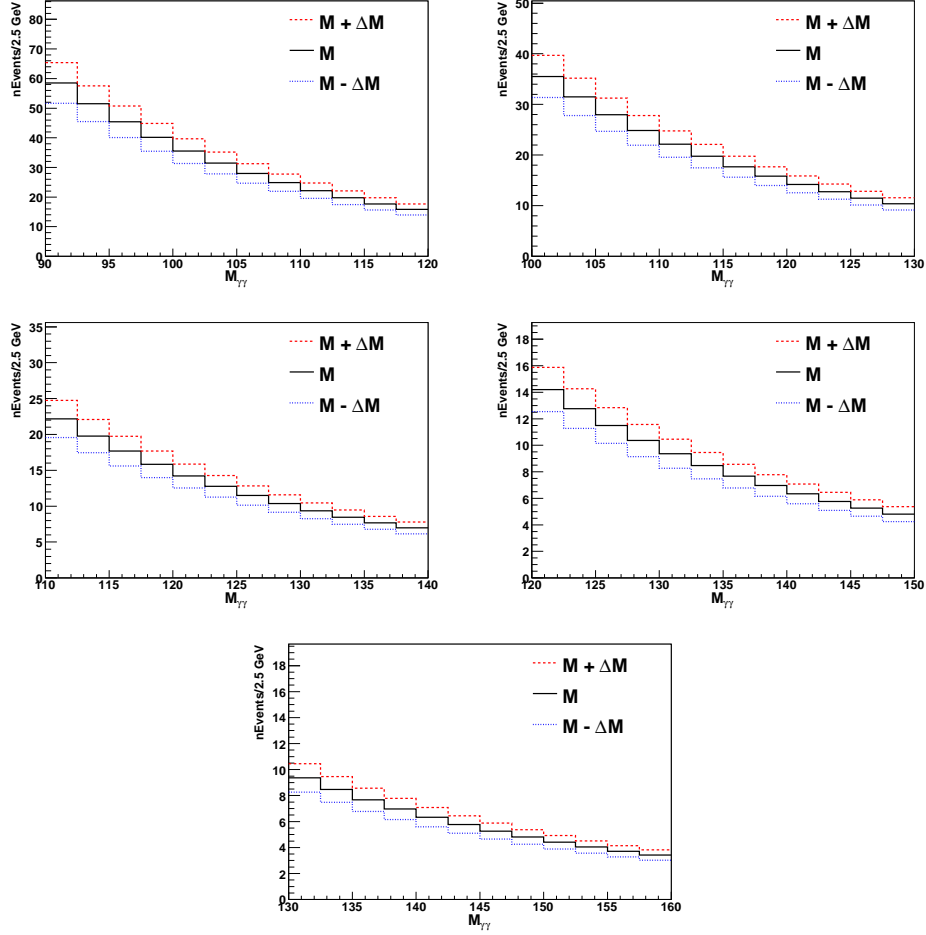


**Figure 8.9** Invariant mass distribution of the two photon candidates for the non- $\gamma\gamma$  component in mass interval of  $(M_H - 15 \text{ GeV}, M_H + 15 \text{ GeV})$  for 105 (top-left), 115 (top-right), 125 (middle-left), 135 (middle-right), 145 (bottom) GeV Higgs mass with 2.5 GeV step for each mass bin. The dotted lines show the positive (red) and negative (blue) shape systematic uncertainties from  $4 \times 4$  matrix background subtraction.



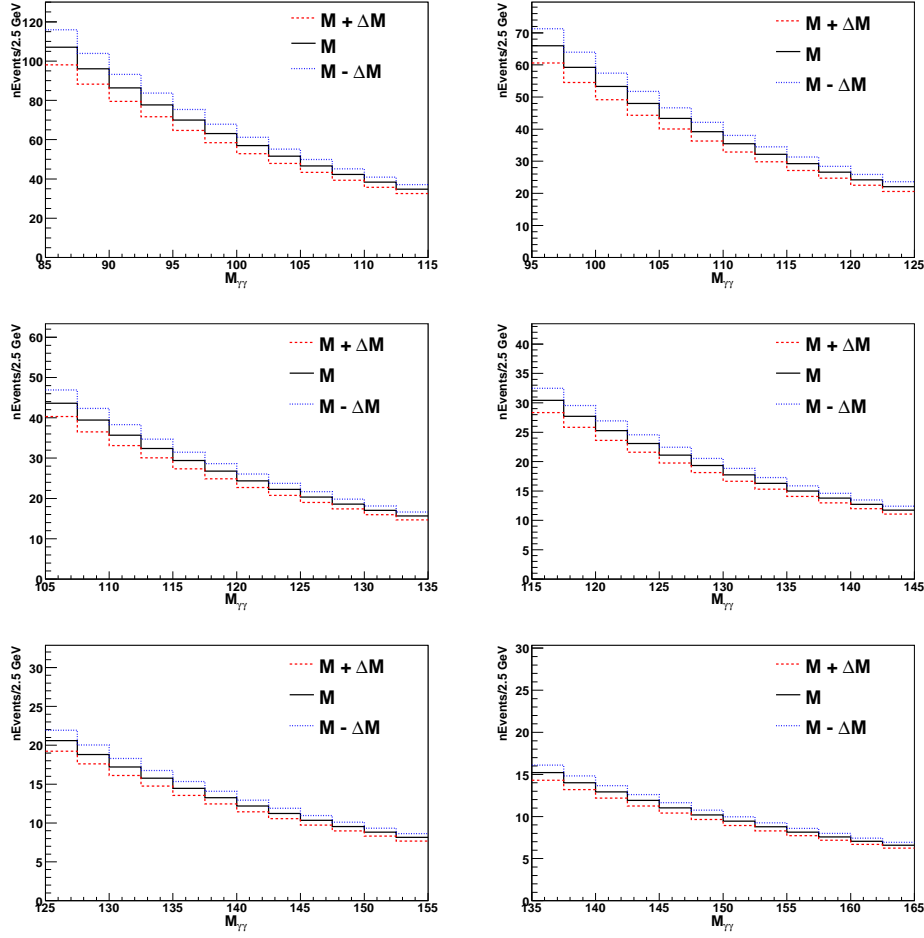


**Figure 8.10** Invariant mass distribution of the two photon candidates for the direct  $\gamma\gamma$  component in mass interval of ( $M_H - 15 \text{ GeV}$ ,  $M_H + 15 \text{ GeV}$ ) for 100 (top-left), 110 (top-right), 120 (middle-left), 130 (middle-right), 140 (bottom-left), and 150 (bottom-right) GeV Higgs mass with 2.5 GeV step for each mass bin. The dotted lines show the positive (red) and negative (blue) shape systematic uncertainties from  $4 \times 4$  matrix background subtraction.

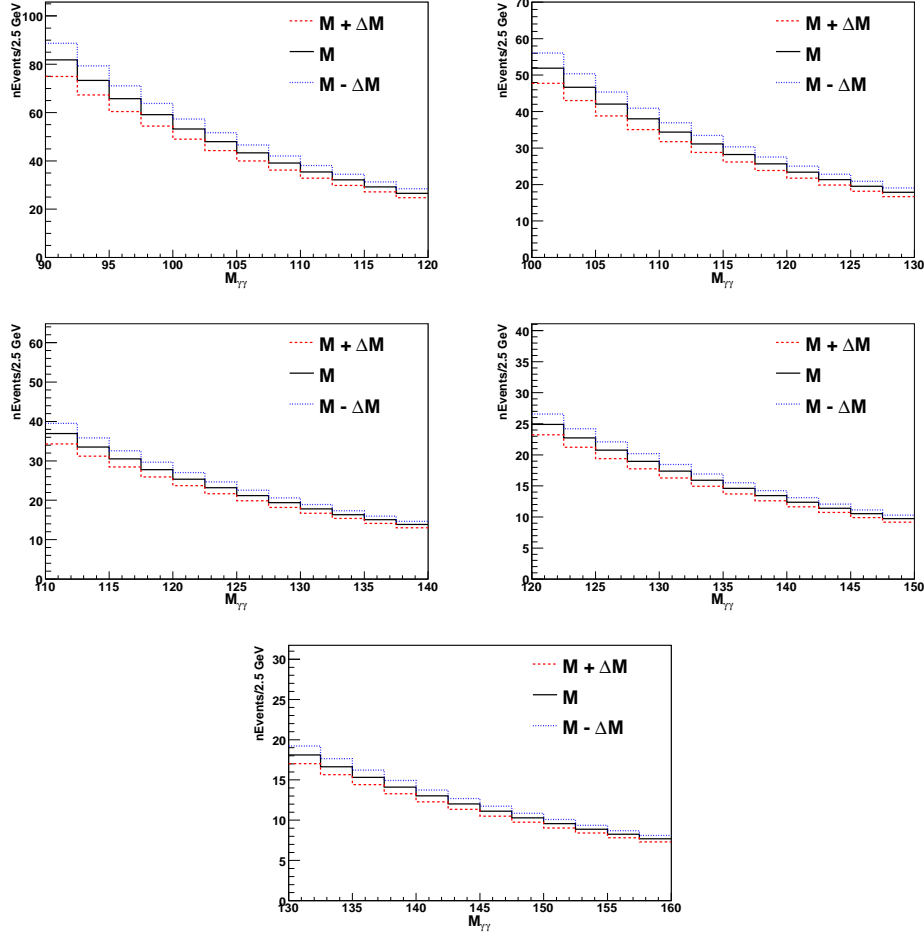


**Figure 8.11** Invariant mass distribution of the two photon candidates for the direct  $\gamma\gamma$  component in mass interval of  $(M_H - 15 \text{ GeV}, M_H + 15 \text{ GeV})$  for 105 (top-left), 115 (top-right), 125 (middle-left), 135 (middle-right), 145 (bottom) GeV Higgs mass with 2.5 GeV step for each mass bin. The dotted lines show the positive (red) and negative (blue) shape systematic uncertainties from  $4 \times 4$  matrix background subtraction.

## 8.6 Interpolated signal mass points

For now, we have 5GeV step signal MC samples, to get the interpolated signal mass points we shift the both low and high mass points. For instance, to get the 102.5 GeV signal mass distribution, we shift the 100 GeV signal mass by plusing 2.5 GeV and shift the 105 GeV signal mass by minusing 2.5 GeV, then use the average as the 102.5 GeV mass distribution, where assume the event selection efficiency of the average mass point is equal to the half of the sum of plus and minus 2.5 GeV mass points. Before doing the shifting, we use the integrated luminosity, number of signal sample events, trigger efficiency and scale factors to normalize the signal mass distributions. After doing the shifting we compare the mass distribution from 100 GeV plus 2.5GeV, 105 GeV minus 2.5 GeV and the average in Figs. 8.12 – 8.17. Finally, we redo the normalization on the average mass distribution by adding the values of  $\sigma \times \text{BR}$  ( see Table 8.3). Table 8.4 shows the number of data, signal and background events for these interpolated signal mass points, the corresponding distributions are shown in Figs. 8.18 and 8.19 .

mass (GeV)	ggH(NNLO)	WH(NNLO)	ZH(NNLO)	VBF(NLO)	BR
102.5	1.5512	0.2637	0.1544	0.0952	0.001623
107.5	1.3640	0.2247	0.1328	0.0878	0.001810
112.5	1.2043	0.1922	0.1146	0.0809	0.001988
117.5	1.0674	0.1651	0.0993	0.0746	0.002132
122.5	0.9493	0.1423	0.0864	0.0688	0.002224
127.5	0.8471	0.1230	0.0753	0.0634	0.002246
132.5	0.7583	0.1066	0.0658	0.0585	0.002187
137.5	0.6809	0.0927	0.0577	0.0539	0.002045
142.5	0.6129	0.0809	0.0507	0.0497	0.001825
147.5	0.5528	0.0707	0.0447	0.0458	0.001546

**Table 8.3** Cross section(pb) and Branching ratio(BR) for the signal samples.

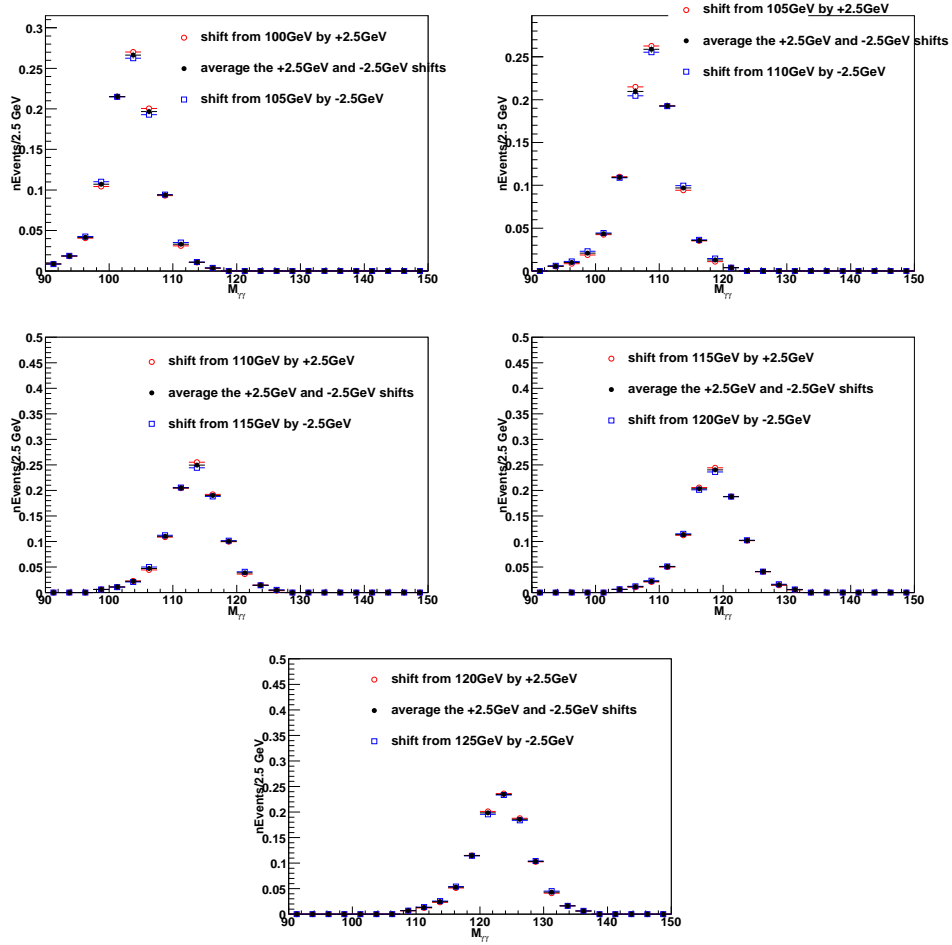


**Figure 8.12** Shifting comparison for GF from 102.5 GeV to 122.5 GeV.

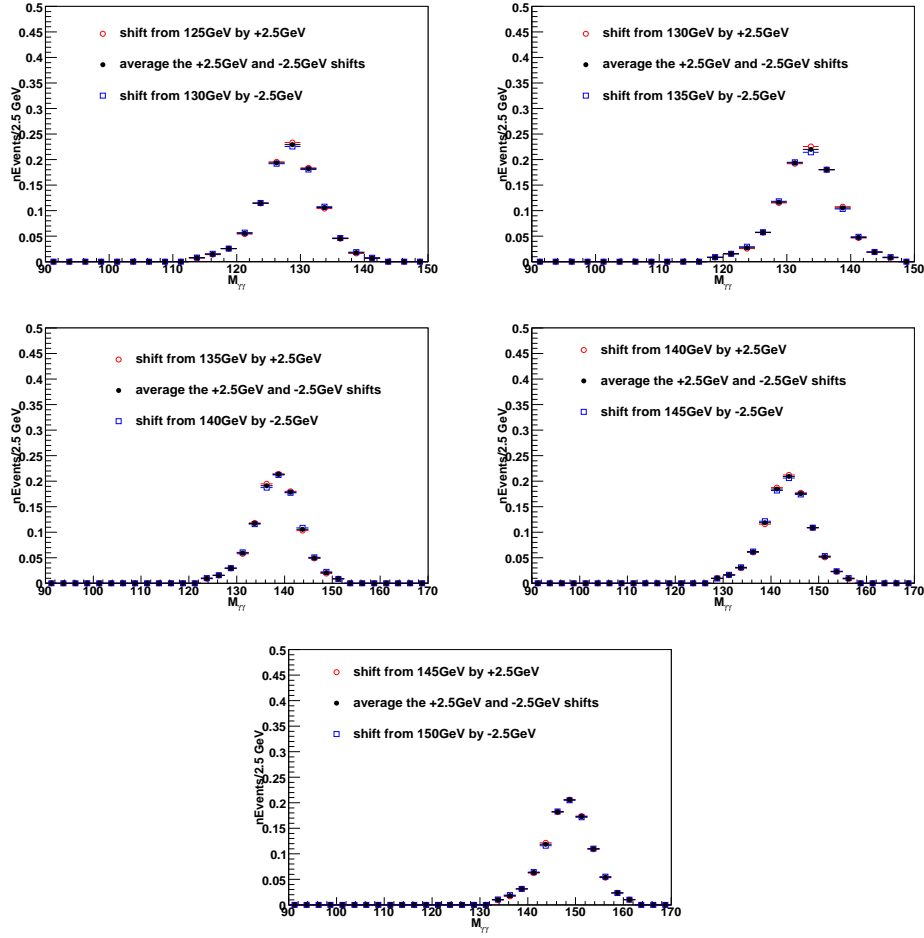


**Figure 8.13** Shifting comparison for GF from 127.5 GeV to 147.5 GeV.

$M_{\text{Higgs}}(\text{GeV})$	$Z/\gamma^* \rightarrow ee$	$\gamma j + jj$	direct $\gamma\gamma$	total background	data	signal
102.5	$116.0 \pm 24.0$	$635.2 \pm 90.8$	$977.6 \pm 85.4$	$1728.8 \pm 31.7$	1825	$2.50 \pm 0.18$
107.5	$72.0 \pm 15.3$	$507.6 \pm 72.6$	$823.0 \pm 68.7$	$1402.6 \pm 23.9$	1442	$2.50 \pm 0.18$
112.5	$38.3 \pm 8.6$	$408.5 \pm 58.4$	$696.1 \pm 55.8$	$1142.9 \pm 18.6$	1155	$2.49 \pm 0.17$
117.5	$21.7 \pm 5.6$	$331.0 \pm 47.3$	$599.2 \pm 45.6$	$951.9 \pm 15.7$	944	$2.42 \pm 0.17$
122.5	$14.1 \pm 4.3$	$270.1 \pm 38.6$	$493.6 \pm 37.4$	$777.8 \pm 13.2$	788	$2.28 \pm 0.16$
127.5	$10.0 \pm 3.5$	$222.0 \pm 31.7$	$430.7 \pm 30.9$	$662.7 \pm 11.2$	620	$2.09 \pm 0.15$
132.5	$7.5 \pm 2.8$	$183.7 \pm 26.3$	$372.2 \pm 25.5$	$563.4 \pm 9.2$	523	$1.85 \pm 0.13$
137.5	$5.8 \pm 2.5$	$153.1 \pm 21.9$	$307.8 \pm 21.2$	$466.7 \pm 7.6$	452	$1.58 \pm 0.11$
142.5	$4.6 \pm 2.1$	$128.5 \pm 18.4$	$259.0 \pm 17.8$	$392.1 \pm 6.3$	380	$1.30 \pm 0.09$
147.5	$3.7 \pm 1.9$	$108.6 \pm 15.5$	$221.1 \pm 15.1$	$333.4 \pm 5.4$	327	$1.00 \pm 0.07$

**Table 8.4** Number of events in data, signal and the background estimation in the mass interval of  $(M_H - 15 \text{ GeV}, M_H + 15 \text{ GeV})$ .

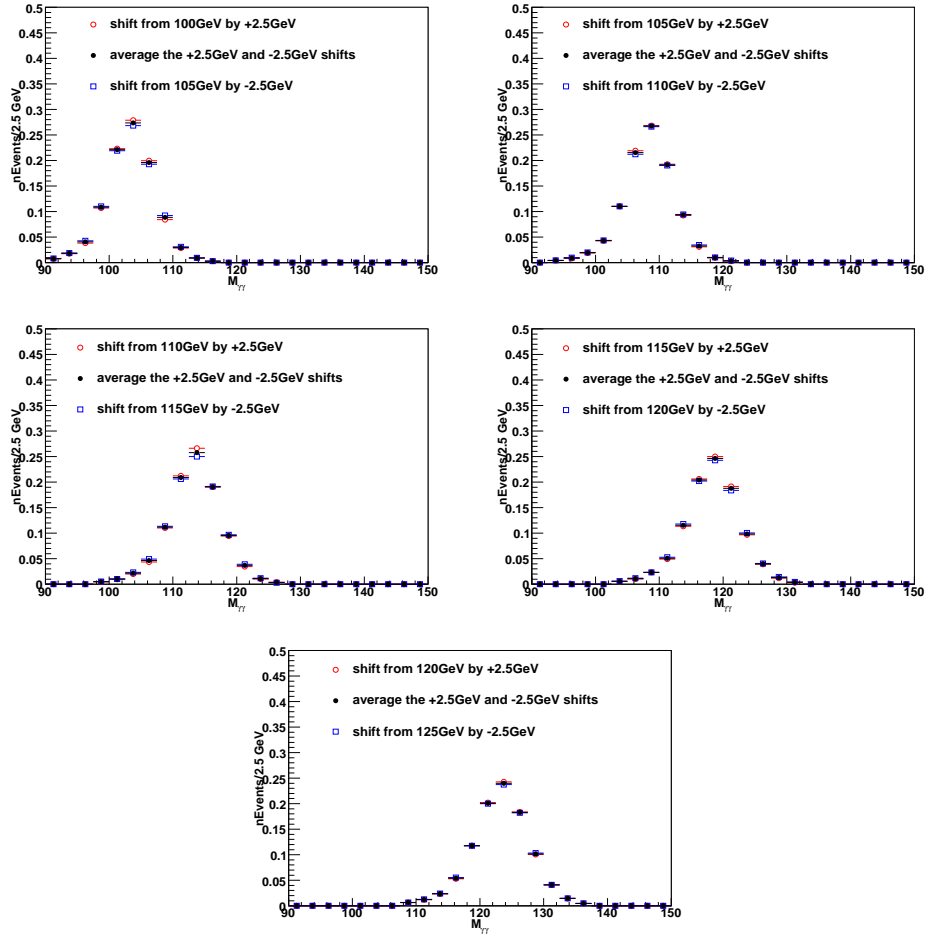


**Figure 8.14** Shifting comparison for VH from 102.5 GeV to 122.5 GeV.

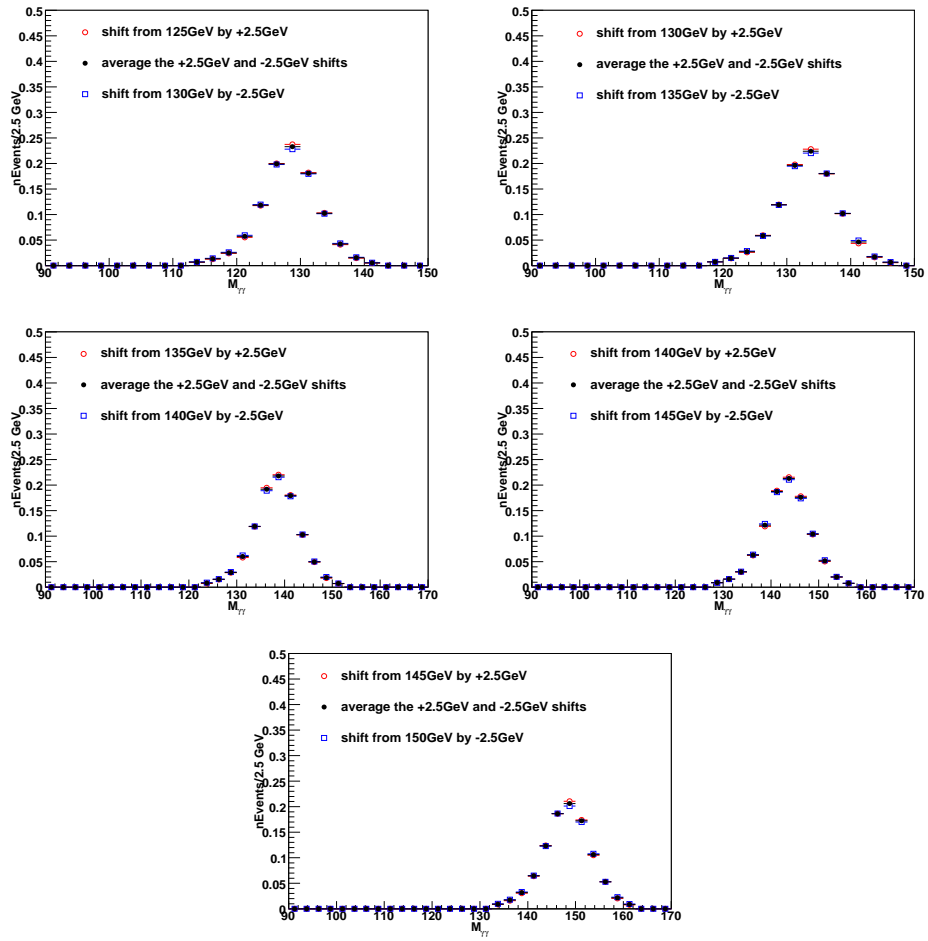


**Figure 8.15** Shifting comparison for  $VH$  from 127.5 GeV to 147.5 GeV.

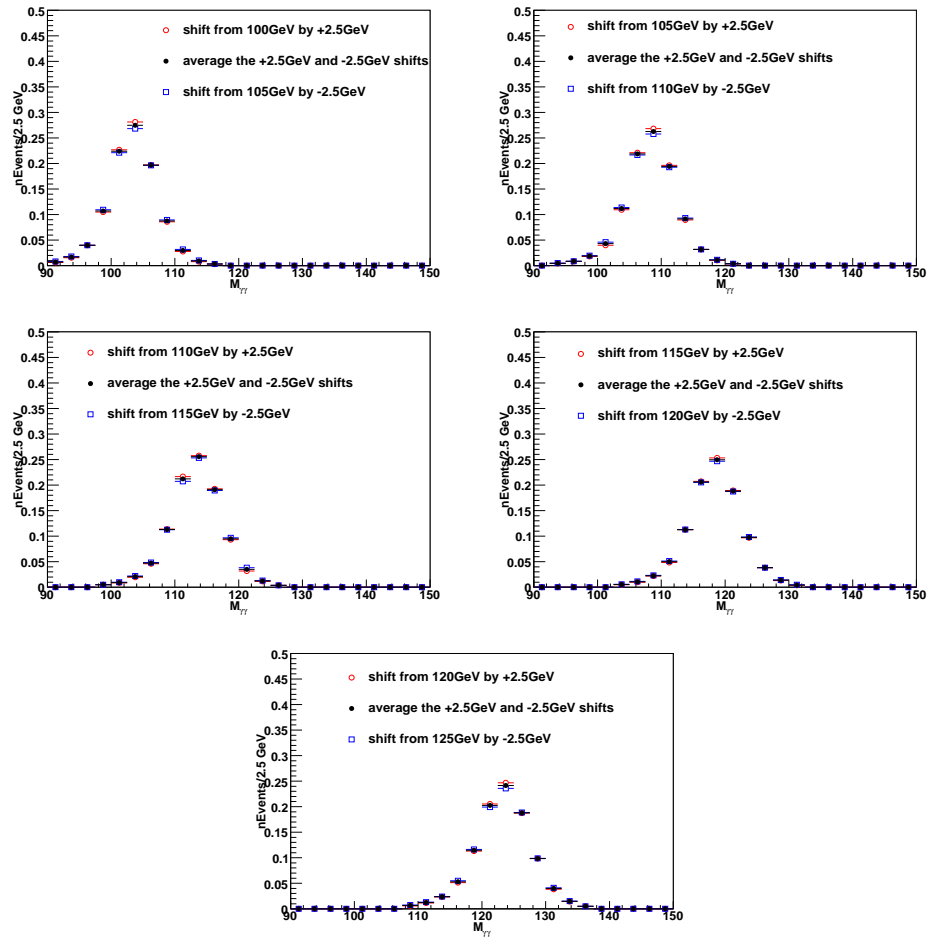


Figure 8.16 Shifting comparison for VBF.



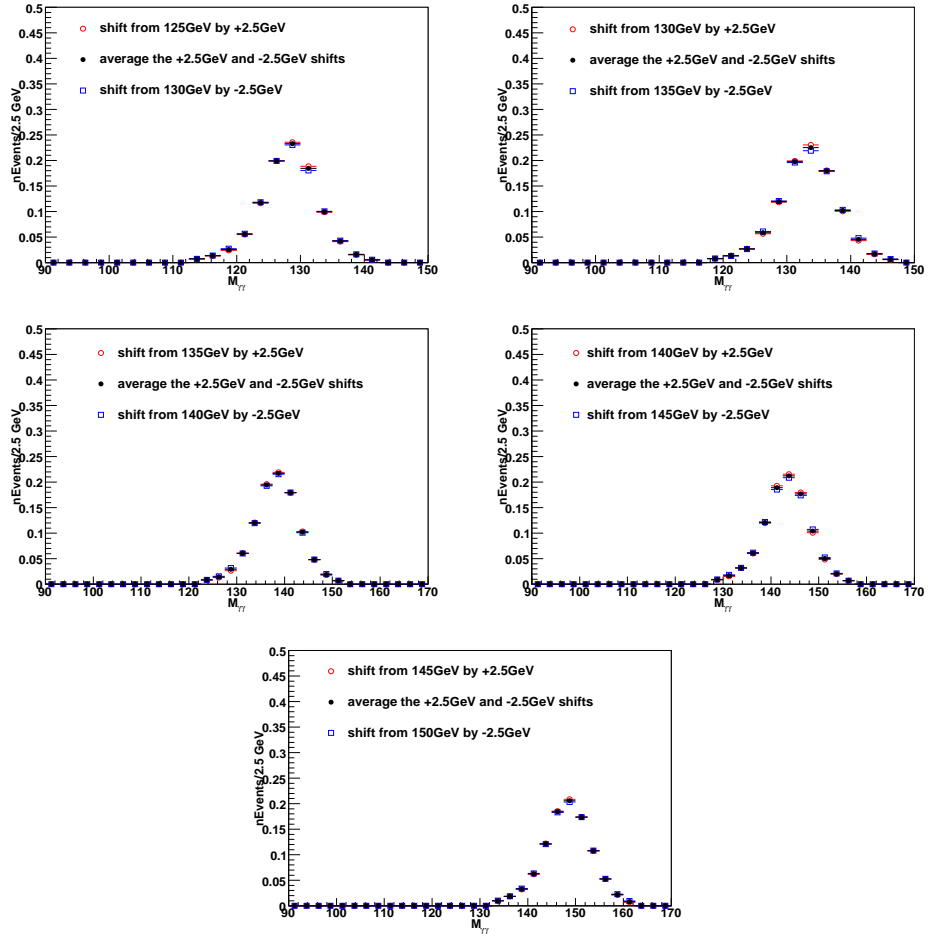
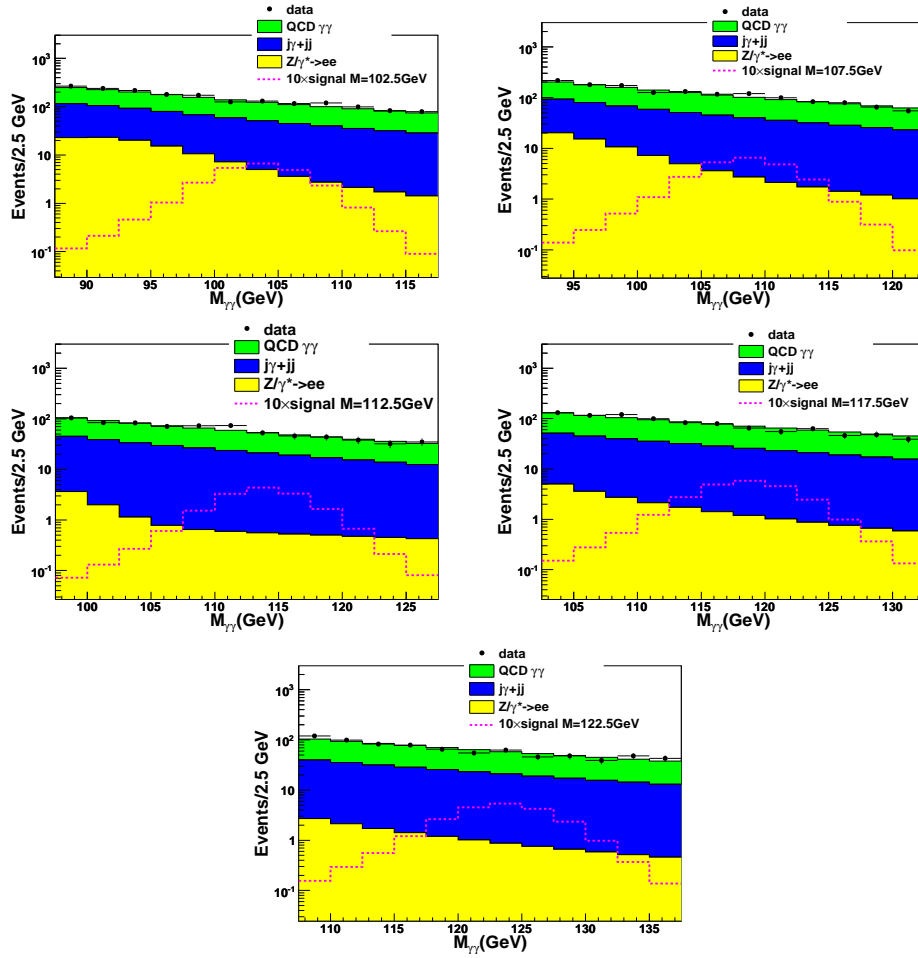
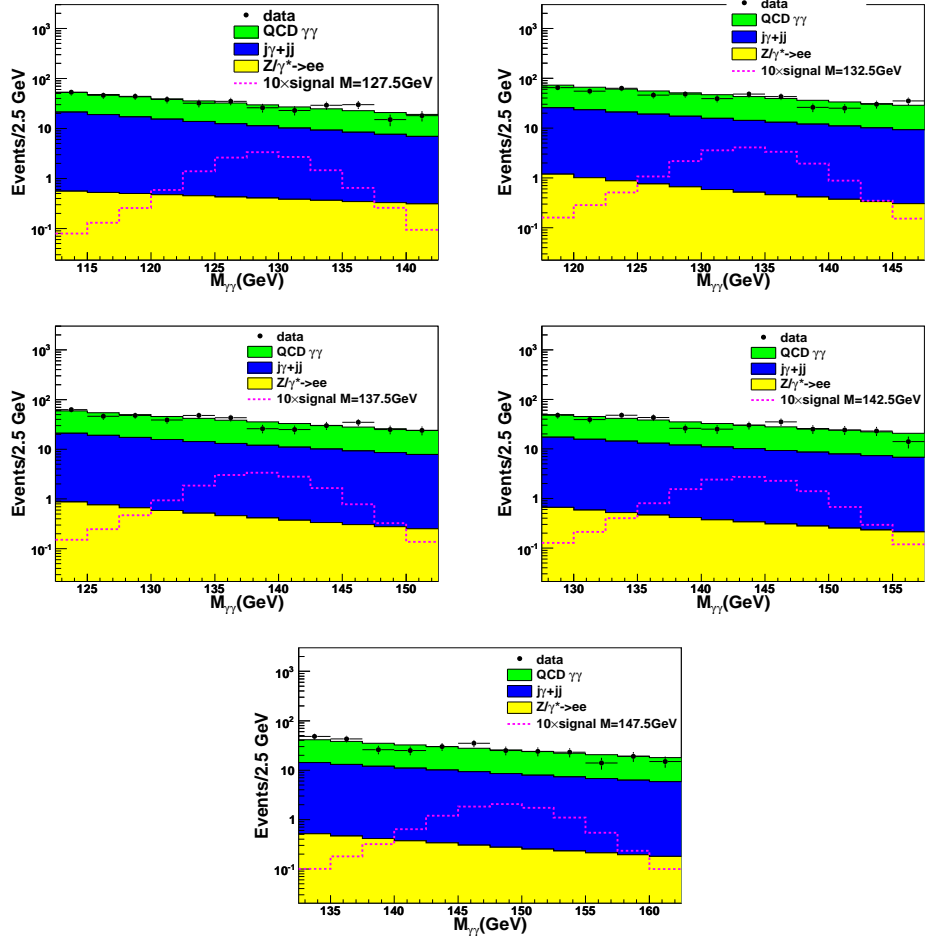


Figure 8.17 Shifting comparison for VBF.



**Figure 8.18** Invariant mass distribution of the two photon candidates in mass interval of  $(M_H - 15 \text{ GeV}, M_H + 15 \text{ GeV})$  for 102.5 to 122.5 GeV Higgs mass with 2.5 GeV step for each mass bin.



**Figure 8.19** Invariant mass distribution of the two photon candidates in mass interval of  $(M_H - 15 \text{ GeV}, M_H + 15 \text{ GeV})$  for 127.5 to 147.5 GeV Higgs mass with 2.5 GeV step for each mass bin.

## 8.7 Bin-by-bin purity

Here we define two variables that reflect the bin-to-bin migration since the generator level distribution in one bin can have the reconstructed distribution in a different bin. These variables are purity  $P$

$$P = N(\text{gen bin } i \text{ and reco bin } i) / N(\text{reco bin } i)$$

and efficiency

$$\text{Eff} = N(\text{gen bin } i \text{ and reco bin } i) / N(\text{gen bin } i)$$

Here  $N(\text{gen bin } i \text{ and reco bin } i)$  is the number of events with both generator level and reconstructed level information in bin  $i$ , while  $N(\text{reco bin } i)$  is the number of events reconstructed in bin  $i$  and  $N(\text{gen bin } i)$  is the number of events generated in bin  $i$ . With this definition, the efficiency provides information on the fraction of events at the truth level that remain in the same bin at the reconstructed level, whereas the purity refers to the fraction of events at the reconstructed level which came from the same bin at the truth level. The bin-by-bin acceptance (Section 5.4) is given by the ratio of bin efficiency and purity.

The bin-to-bin purity and efficiency distributions for all four variables are shown in Fig. 8.20.

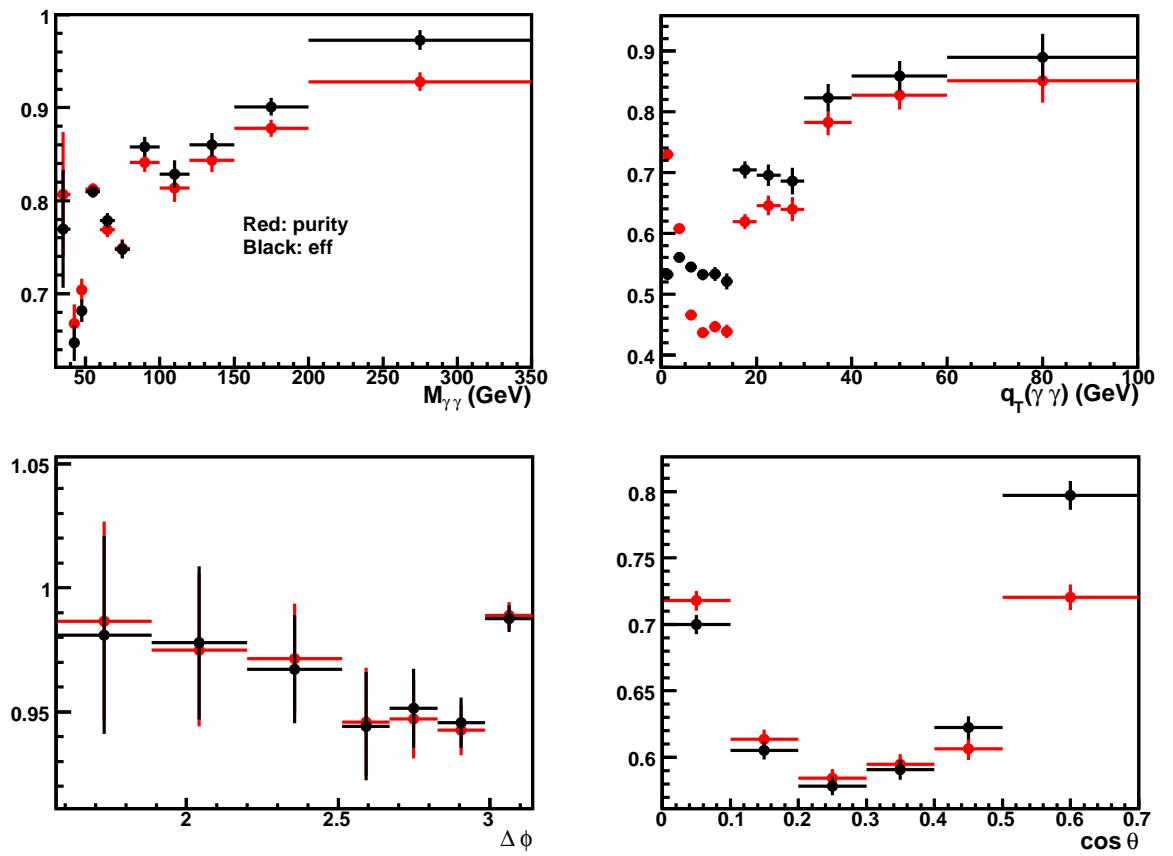


**Figure 8.20** Bin-to-bin migration purity and efficiency as a function of  $M_{\gamma\gamma}$ ,  $p_T^{\gamma\gamma}$ ,  $\Delta\phi_{\gamma\gamma}$  and  $\cos\theta^*$ .

## 8.8 Unfolded results using different re-weightings to data

In this section we compare results on the acceptance calculation after re-weighting RESBOS spectra in  $M_{\gamma\gamma}$ ,  $p_T^{\gamma\gamma}$ ,  $\Delta\phi_{\gamma\gamma}$  and  $\cos\theta^*$  to data. For this aim we used the ratio of data/theory cross sections obtained with a regular (non-reweighted RESBOS) which are fitted with smooth functions, as shown in Fig. 8.21 (exclusion is the first mass bin for which we used direct ratio data/RESBOS: see also Fig. 8.29).

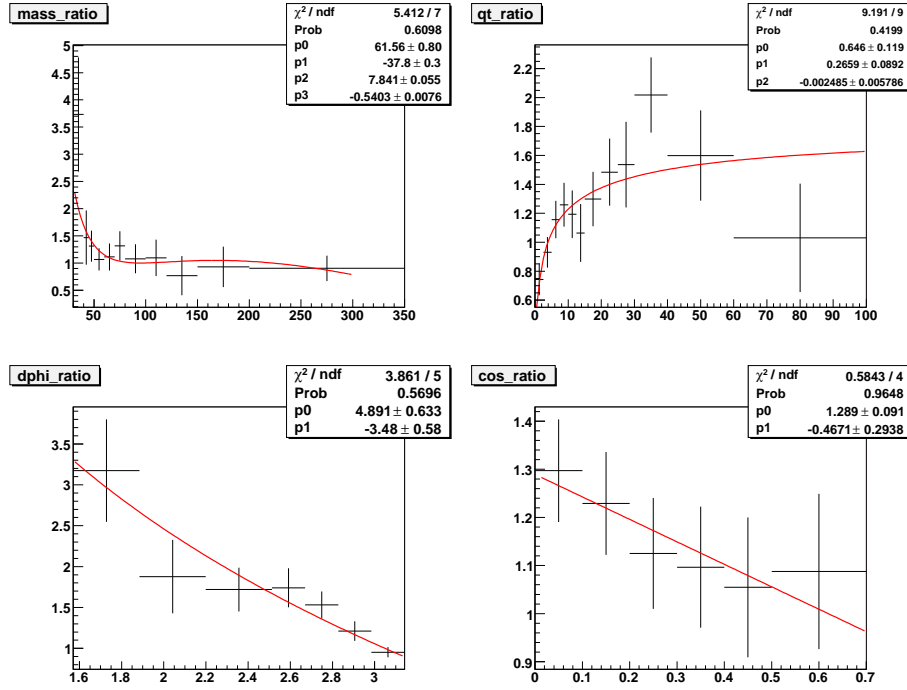


**Figure 8.21** The ratio between the RESBOS predictions and the data cross sections for which the acceptance is calculated using fast MC (section 5.4) and non-reweighted RESBOS.

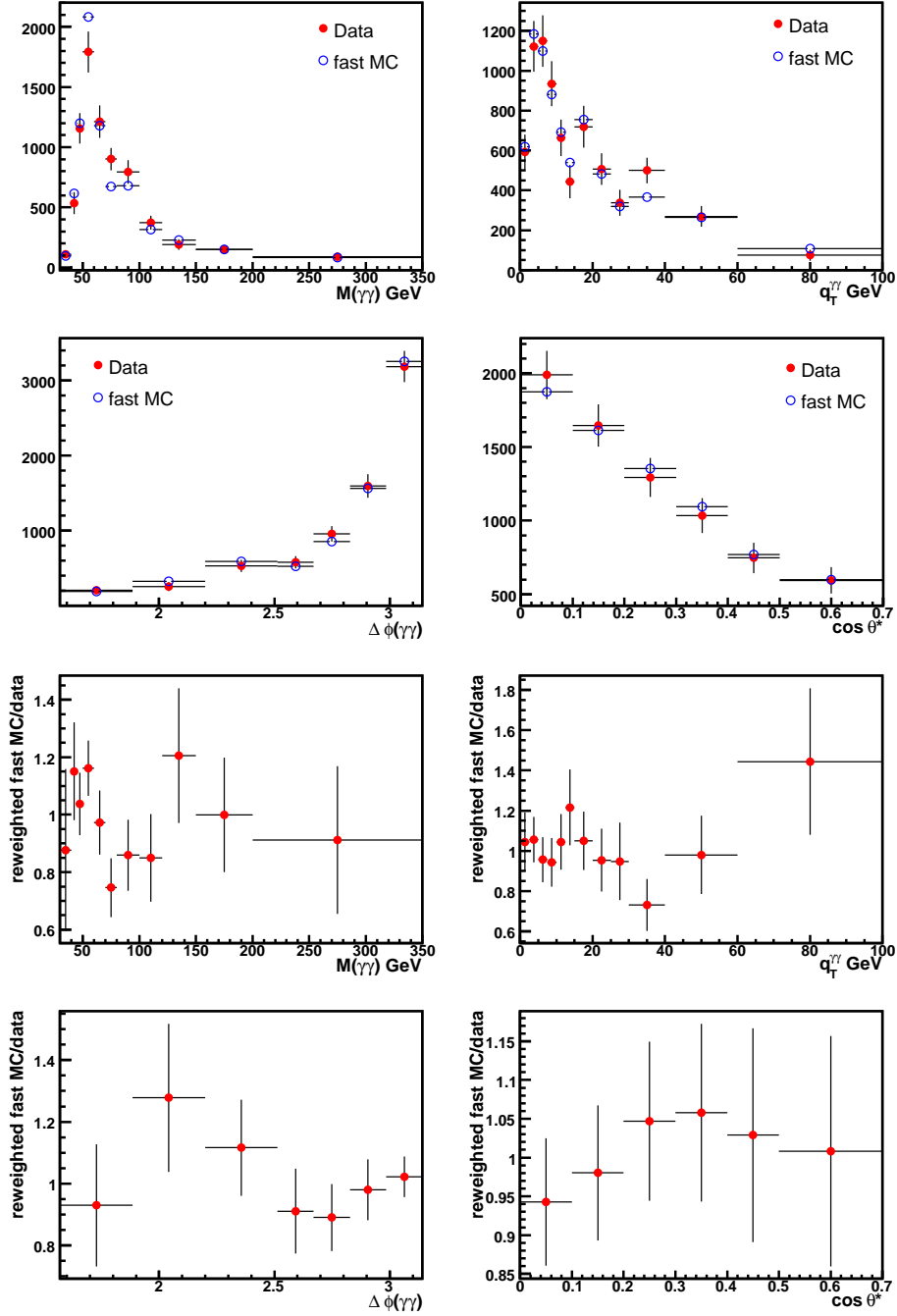
Then, we re-calculate each of the four acceptances using either  $M_{\gamma\gamma}$  or  $p_T^{\gamma\gamma}$  or  $\Delta\phi_{\gamma\gamma}$  or  $\cos\theta^*$  spectra for the re-weightings. The comparison between the background-subtracted data distributions and the smeared distributions from the generator-level-reweighted resbos fast MC simulation can be found in Fig. 8.22.

Good agreements are observed which give us confidence about the fast MC simulation and also the generator-level-reweighted resbos.

Fig. 8.23 shows a comparison between the background-subtracted data distributions and the smeared distributions from the generator-level-reweighted RESBOS fast MC simulation for leading and sub-leading photon  $p_T$ : two upper plots show the actual distributions and two bottom show the ratios RESBOS/data. Just statistical uncertainties are shown (i.e. one needs to keep in mind additional 12–17% caused by the di-photon events purity used in the background subtraction). One can see that the RESBOS predictions describe the data very well.

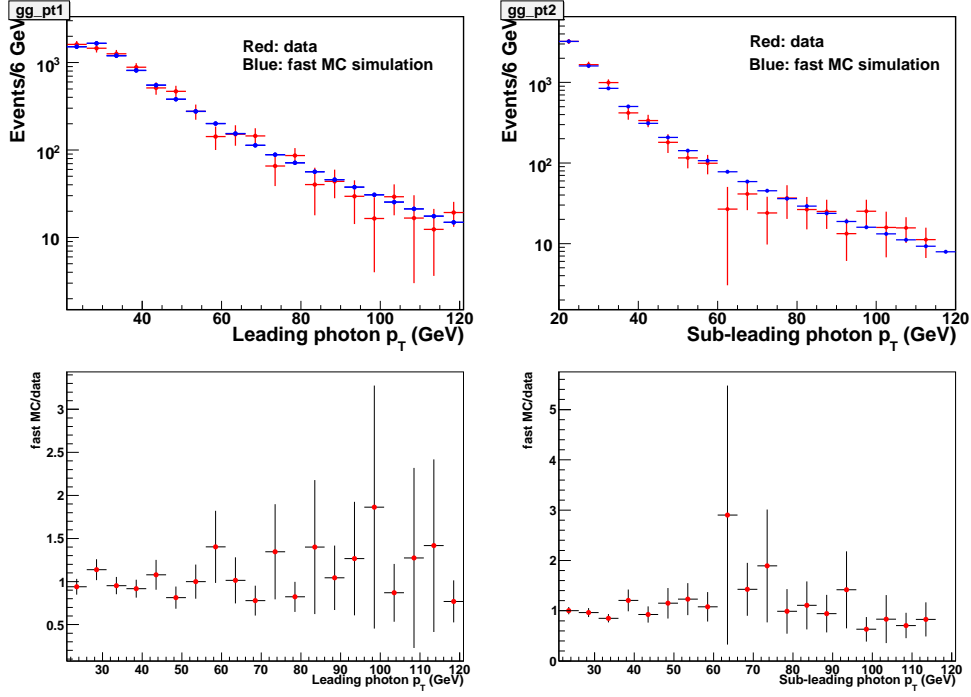
The results for the acceptances using the generator-level-reweighted resbos fast MC simulation are shown in Fig. 8.24. The results are also presented in Figs. 8.25 – 8.28 as ratios acceptance calculated with the reweightings to  $M_{\gamma\gamma}$  or  $p_T^{\gamma\gamma}$  or  $\Delta\phi_{\gamma\gamma}$  or  $\cos\theta^*$  spectra to the acceptance with default RESBOS. One can see that results with various reweightings are pretty consistent with each other within 3 – 4%,

Fig. 8.29 compares the mass acceptances calculated either with smooth reweighting function for all the bins shown in the upper left plot of Fig. 8.21 or with the smooth reweighting for all the bins excepting the 1st one, where we used the RESBOS/data ratio (=3.8) directly. One can see that the two acceptances are in agreement and differ just in the 1st and 2nd bins by about (relative) 8–10% much smaller for all other bins. Due to the large



**Figure 8.22** Comparisons between the background-subtracted data distributions and the smeared distributions from the generator-level-reweighted resbos fast MC simulation.





**Figure 8.23** Comparisons between the background-subtracted data distributions and the smeared distributions from the generator-level-reweighted resbos fast MC simulation for leading and sub-leading photon  $p_T$ : two upper plots show the actual distributions and two bottom show the ratios  $\text{resbos}/\text{data}$ . Just statistical uncertainties are shown.

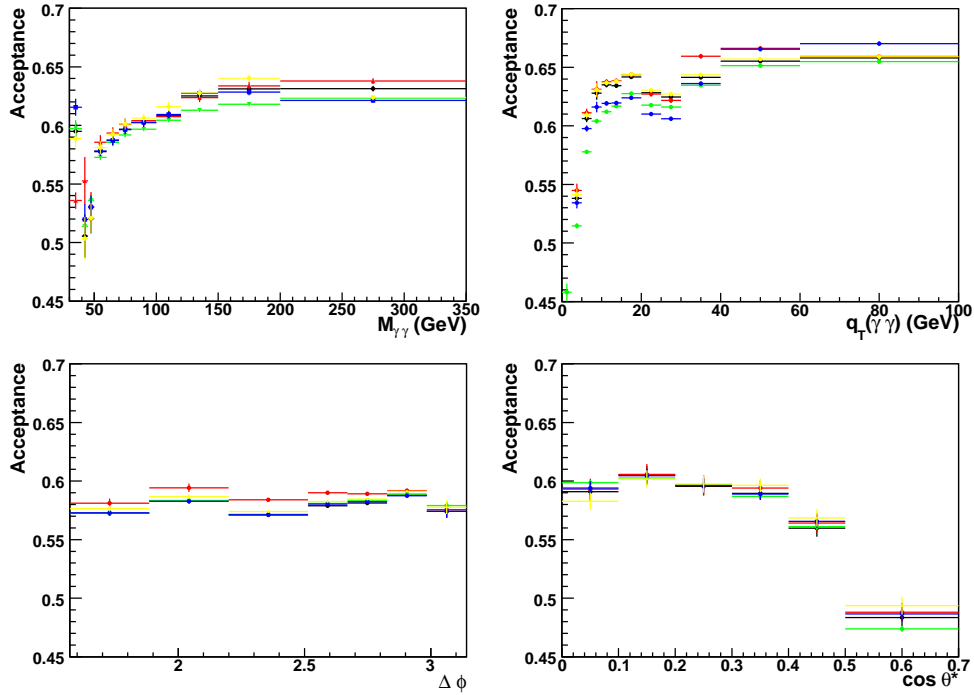


**Figure 8.24** Acceptance calculation with different re-weightings of RESBOS to data. Here the black points are the default RESBOS spectra (without any reweighting), red points are with mass reweighting, green ones are with  $p_T^{\gamma\gamma}$  reweighting, blue ones are with  $\Delta\phi_{\gamma\gamma}$  reweighting and yellow ones are with  $\cos\theta^*$  reweighting.

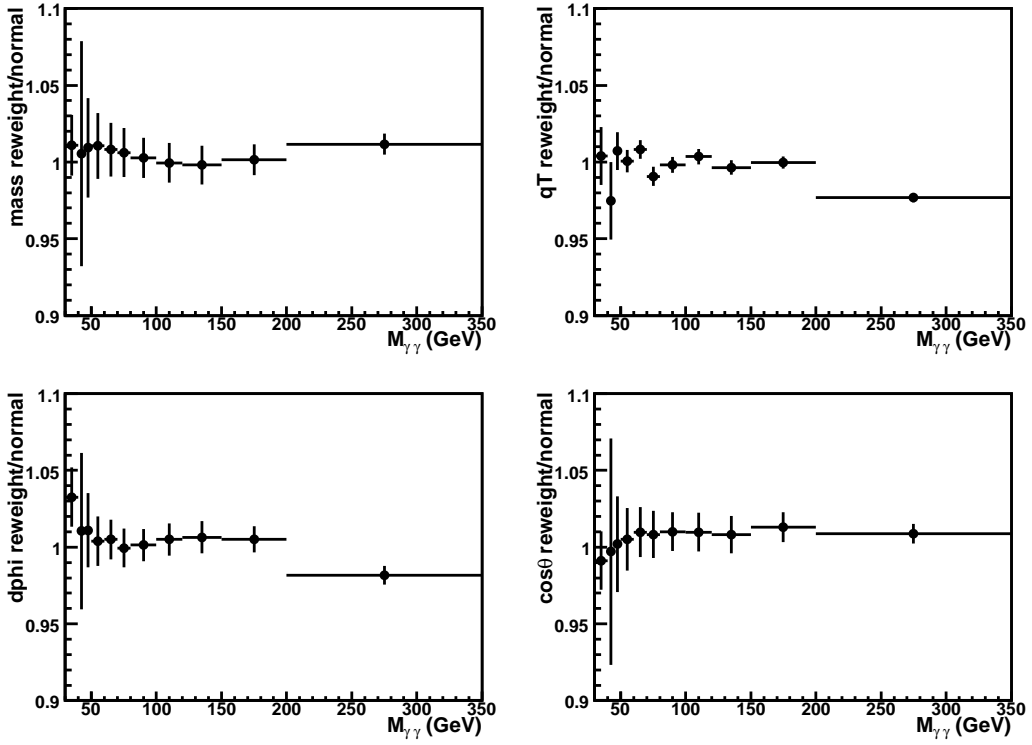


**Figure 8.25** Ratio of the acceptance calculated with the reweightings to  $M_{\gamma\gamma}$  or  $p_T^{\gamma\gamma}$  or  $\Delta\phi_{\gamma\gamma}$  or  $\cos\theta^*$  spectra to the acceptance with default RESBOS for  $M_{\gamma\gamma}$ .

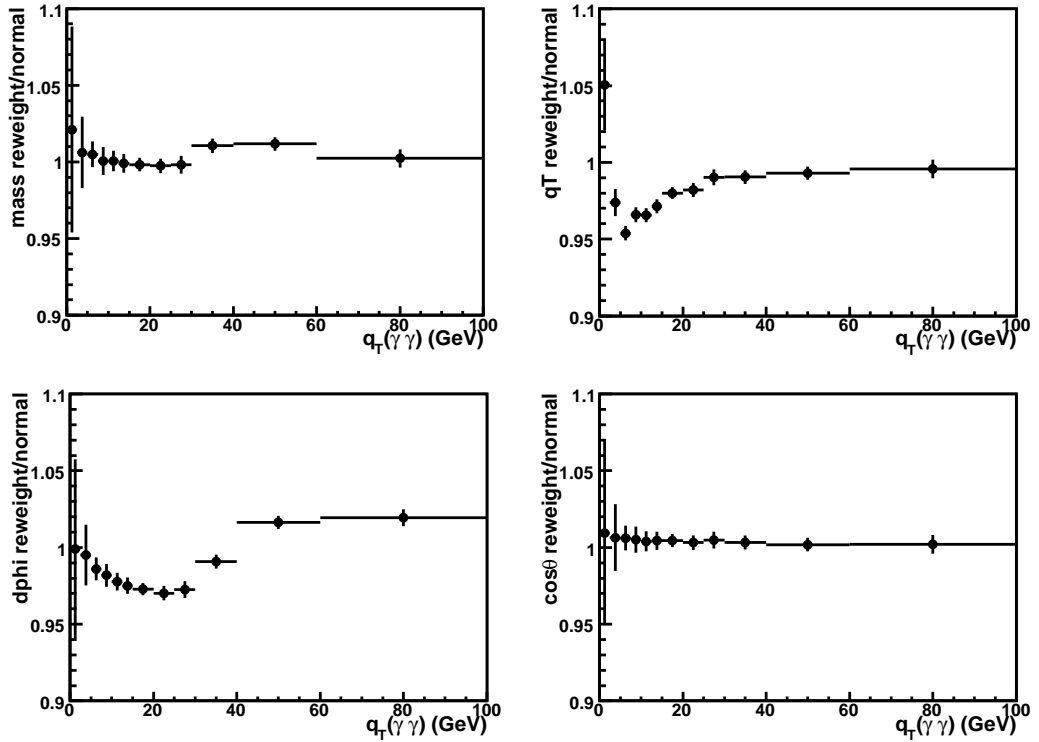


**Figure 8.26** Ratio of the acceptance calculated with the reweightings to  $M_{\gamma\gamma}$  or  $p_T^{\gamma\gamma}$  or  $\Delta\phi_{\gamma\gamma}$  or  $\cos\theta^*$  spectra to the acceptance with default RESBOS for  $p_T^{\gamma\gamma}$ .

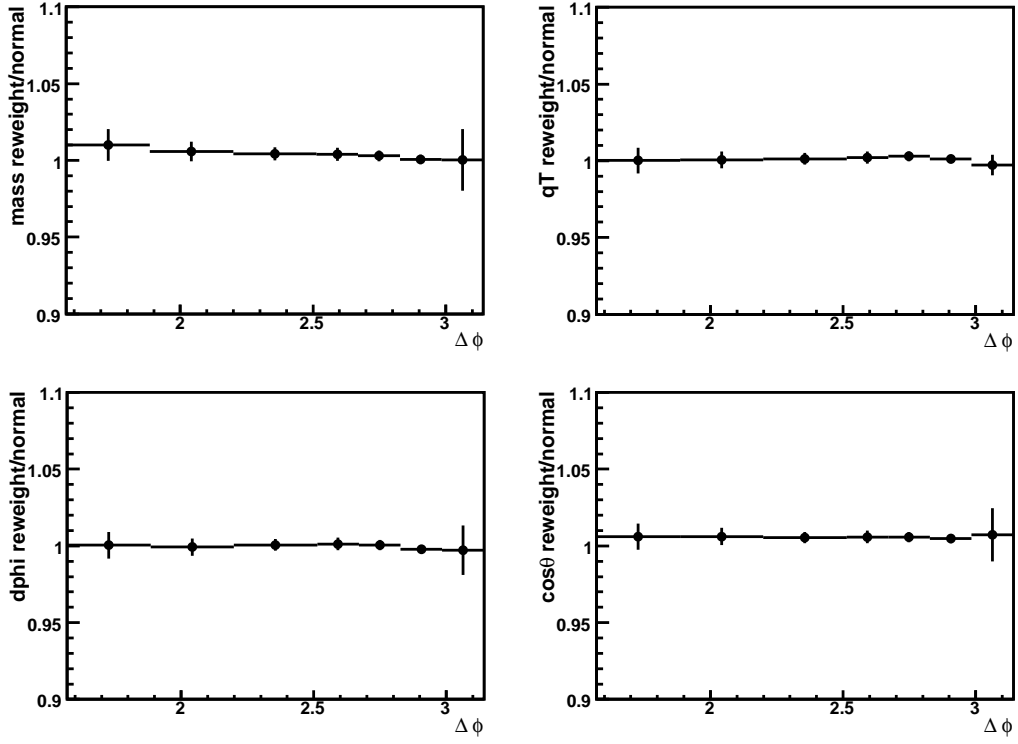


**Figure 8.27** Ratio of the acceptance calculated with the reweightings to  $M_{\gamma\gamma}$  or  $p_T^{\gamma\gamma}$  or  $\Delta\phi_{\gamma\gamma}$  or  $\cos\theta^*$  spectra to the acceptance with default RESBOS for  $\Delta\phi_{\gamma\gamma}$ .

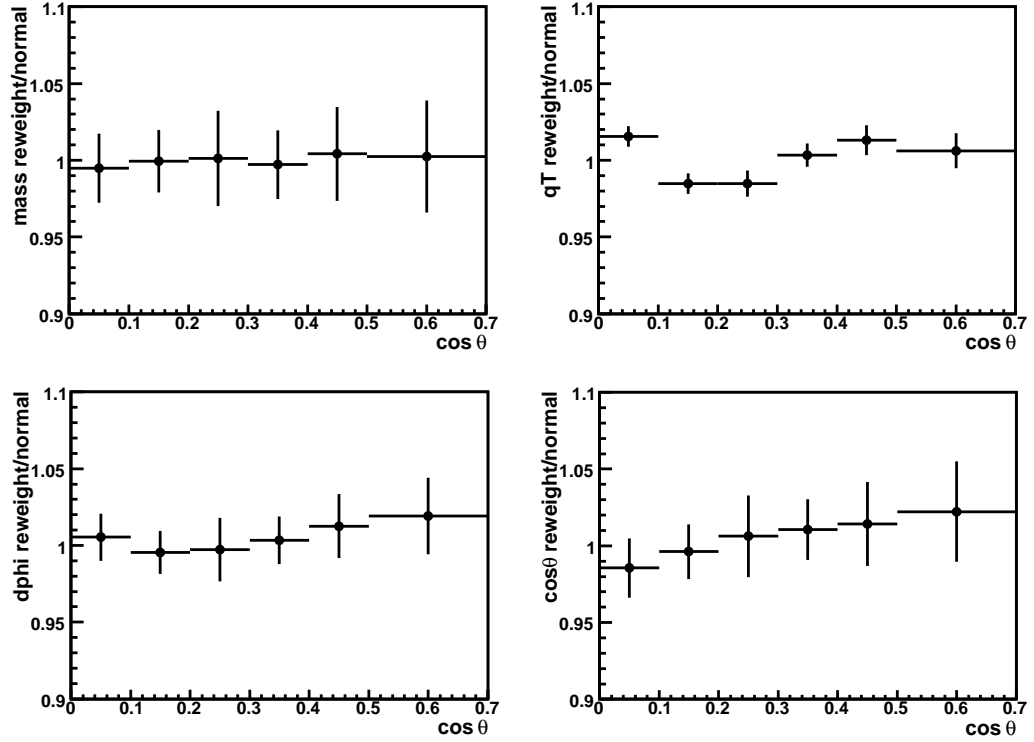


**Figure 8.28** Ratio of the acceptance calculated with the reweightings to  $M_{\gamma\gamma}$  or  $p_T^{\gamma\gamma}$  or  $\Delta\phi_{\gamma\gamma}$  or  $\cos\theta^*$  spectra to the acceptance with default RESBOS for  $\cos\theta^*$ .

statistical uncertainty ( $\sim 25\%$ ) for the data events in the first 30–40 GeV  $M_{\gamma\gamma}$  bin, for the final results, we use the larger binning 30–45 GeV instead.

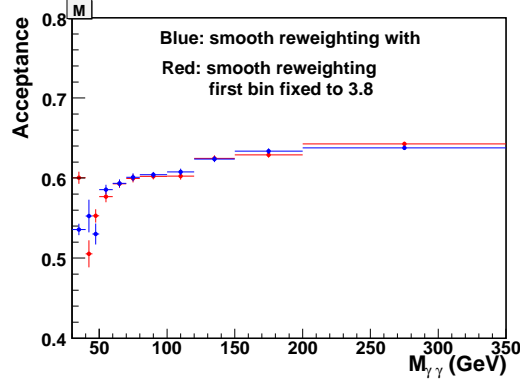


**Figure 8.29** The mass acceptance calculated either with smooth reweighting function for all the bins shown in the upper left plot of Fig. 8.21 or with the smooth reweighting for all the bin excepting the 1st one, where we used the RESBOS/data ratio directly.

We have also measured the acceptance (described in Section 5.4) using diphoton events simulated using the full PYTHIA MC. Fig. 8.30 shows comparison with the acceptance obtained using the fast RESBOS MC. One can see that the results are in good agreement with each other.

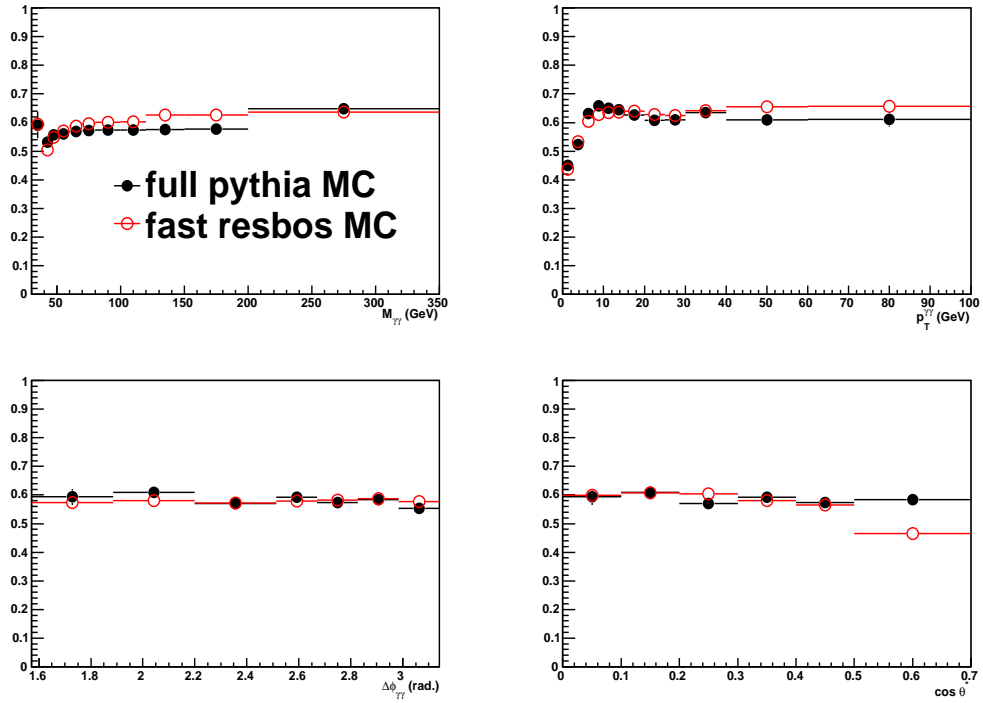


**Figure 8.30** Acceptance as a function of  $M_{\gamma\gamma}$ ,  $p_T^{\gamma\gamma}$ ,  $\Delta\phi_{\gamma\gamma}$  and  $\cos\theta^*$  from full PYTHIA (black) and fast RESBOS (red) MC simulation.

### 8.9 Cross-check of diphoton purity using 2D template fitting.

In this section we cross-check the diphoton purities found with the matrix method and presented in Section 5.5.3. For this aim, we use templates of photon ANN outputs for each of the two diphoton candidates for photons and jets in diphoton, photon+jet and dijet MC events. After application of all the photon ID cuts, including  $O_{NN} > 0.3$ , the sum of those 2D templates are fitted to data in each bin of  $M_{\gamma\gamma}$ ,  $\Delta\phi_{\gamma\gamma}$ ,  $p_T^{\gamma\gamma}$  and  $\cos\theta^*$  using TFractionFitter<sup>[59]</sup>. The results are shown in Fig. 8.31. They can be compared with the default results obtained with the matrix method shown in Fig. 5.10. The given uncertainties are statistical and caused by the template fitting. We can see that they are in good agreement with the default method within the uncertainties.

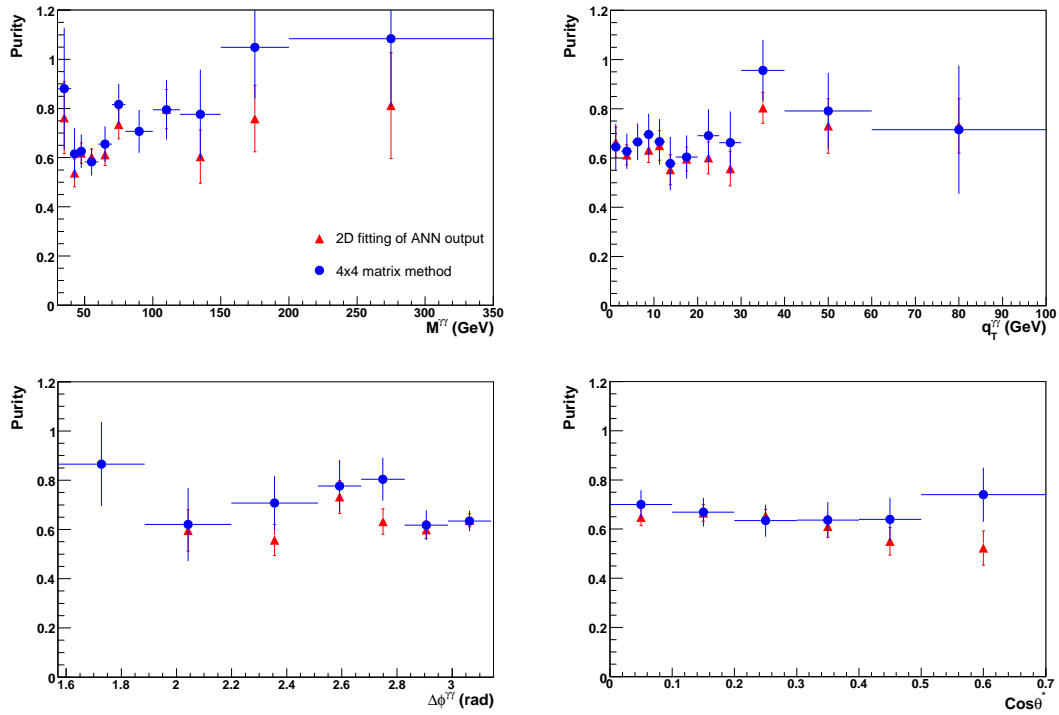


**Figure 8.31** Diphoton purities in bins of  $M_{\gamma\gamma}$ ,  $\Delta\phi_{\gamma\gamma}$ ,  $p_T^{\gamma\gamma}$  and  $\cos\theta^*$  calculated using template 2D fitting of diphoton, photon+jet and dijet ANN outputs to data. They are compared to the purities obtained from  $4\times 4$  matrix method (Fig. 5.10).

### 8.10 Systematic uncertainty for purity estimation

The uncertainty of the  $O_{NN} > 0.6$  efficiencies for the photon and photon-like jets is the source of the purity uncertainty, which is the dominant uncertainty for this analysis. We adopt the difference in the number of  $N_{\gamma\gamma}$  events from the mean efficiencies and the plus(minus) uncertainties as the systematic uncertainty.

For the photon  $O_{NN} > 0.6$  efficiency ( $\epsilon_\gamma$ ), we verify it by  $\pm 1.5\%$ , thus we got  $N_{\gamma\gamma}^{\epsilon_\gamma+1.5\%}$  and  $N_{\gamma\gamma}^{\epsilon_\gamma-1.5\%}$  di-photon events after solving the Eqs. 4.3 and 4.4. The corresponding systematic uncertainties are estimated as  $\frac{N_{\gamma\gamma}^{\epsilon_\gamma+1.5\%} - N_{\gamma\gamma}}{N_{\gamma\gamma}}$  and  $\frac{N_{\gamma\gamma}^{\epsilon_\gamma-1.5\%} - N_{\gamma\gamma}}{N_{\gamma\gamma}}$  for each bins of kinematic variables.

For the photon-like jet  $O_{NN} > 0.6$  efficiency ( $\epsilon_j$ ), we verify it by  $\pm 10\%$ . To do a robust and reasonable estimation, we fit the original purity distribution (see Fig. 8.32), then get the  $(N_{\gamma\gamma}, N_{\gamma j}, N_{j\gamma}, N_{jj})$  vector. After solving the Eq. 4.3, we get the fail-pass four vector of each bin for the four kinematic variables we considered. Later, we randomize the fail-pass four vector by the Gaussian distributions, and solve the Eq. 4.3 for each experiment with using three different  $\epsilon_j$ . Thus, after  $N_{rand}$  experiments, the systematic uncertainties from varying the  $\epsilon_j$  are

$$\text{estimated as } \frac{\sum_{i=1}^{N_{rand}} \left( \frac{N_{\gamma\gamma}^{\epsilon_j+10\%} - N_{\gamma\gamma}^{\epsilon_j}}{N_{\gamma\gamma}^{\epsilon_j}} \right)}{N_{rand}} \text{ and } \frac{\sum_{i=1}^{N_{rand}} \left( \frac{N_{\gamma\gamma}^{\epsilon_j-10\%} - N_{\gamma\gamma}^{\epsilon_j}}{N_{\gamma\gamma}^{\epsilon_j}} \right)}{N_{rand}} .$$



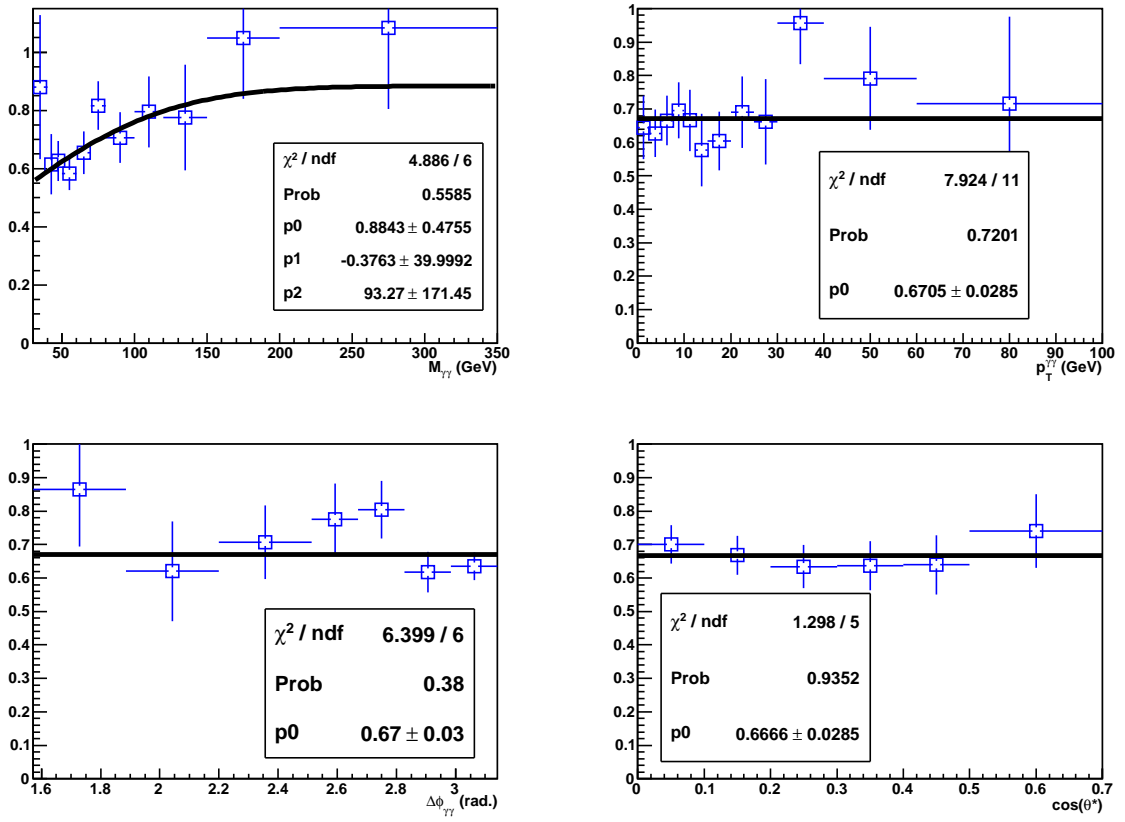


**Figure 8.32**  $\gamma\gamma$  purity as a function of  $M_{\gamma\gamma}$ ,  $p_T^{\gamma\gamma}$ ,  $\Delta\phi_{\gamma\gamma}$  and  $\cos\theta^*$ .

## 8.11 Systematic uncertainties for the 2D acceptance

**Table 8.5** Acceptance with statistical and systematic uncertainties (in %) in  $p_T^{\gamma\gamma}$  bins for  $30 < M_{\gamma\gamma} < 50$  GeV. The two numbers in each box correspond to  $+1\sigma$  and  $-1\sigma$  variations.

$p_T(\gamma\gamma)$ bin	Acc	Stat (%)	Vtx Reso (%)	Vtx MisMatching (%)	E Scale (%)	E Reso (%)	PhiMod (%)	Overall syst.(%)
0	0.49	1.55	-2.40	4.90	0.75	-0.09	1.96	5.85
			2.30	-3.59	-0.90	0.01	-2.12	-4.85
1	0.55	0.44	-1.51	3.38	1.25	-0.02	1.83	4.31
			1.71	-2.77	-0.92	0.03	-2.15	-4.01
2	0.55	0.44	-1.92	2.30	1.15	-0.07	1.79	3.68
			1.52	-2.99	-1.24	0.02	-2.23	-4.21
3	0.58	0.34	-1.67	1.86	1.48	-0.04	1.78	3.40
			1.51	-2.88	-1.58	0.03	-2.10	-4.18

**Table 8.6** Acceptance with statistical and systematic uncertainties (in %) in  $p_T^{\gamma\gamma}$  bins for  $50 < M_{\gamma\gamma} < 80$  GeV. The two numbers in each box correspond to  $+1\sigma$  and  $-1\sigma$  variations.

$p_T(\gamma\gamma)$ bin	Acc	Stat (%)	Vtx Reso (%)	Vtx MisMatching (%)	E Scale (%)	E Reso (%)	PhiMod (%)	Overall syst.(%)
0	0.51	0.71	-2.97	1.98	-0.06	-0.92	0.88	3.79
			1.11	-5.90	-1.85	-0.75	-2.91	-6.96
1	0.60	0.30	-1.25	0.77	1.50	0.25	2.09	2.97
			1.85	-0.09	-1.07	0.26	-1.80	-2.81
2	0.61	0.24	-1.02	0.17	1.98	0.64	2.45	3.38
			1.96	1.18	-0.78	0.58	-1.51	-2.91
3	0.61	0.29	-0.74	-0.20	2.23	0.63	2.38	3.41
			1.81	1.04	-1.00	0.60	-1.50	-2.83
4	0.61	0.28	-0.33	0.47	2.68	1.02	2.79	4.04
			2.33	1.33	-0.63	0.96	-1.14	-3.13
5	0.63	0.28	-1.36	-0.13	1.70	0.03	1.87	2.87
			1.34	0.25	-1.68	0.01	-2.00	-2.94

**Table 8.7** Acceptance with statistical and systematic uncertainties (in %) in  $p_T^{\gamma\gamma}$  bins for  $80 < M_{\gamma\gamma} < 350$  GeV. The two numbers in each box correspond to  $+1\sigma$  and  $-1\sigma$  variations.

$p_T(\gamma\gamma)$ bin	Acc	Stat (%)	Vtx Reso (%)	Vtx MisMatching (%)	E Scale (%)	E Reso (%)	PhiMod (%)	Overall syst.(%)
0	0.44	0.63	-8.06	3.35	-5.10	-6.20	-4.46	12.67
			-3.38	-15.35	-6.59	-5.40	-7.46	-19.37
1	0.63	0.17	-3.32	0.02	-0.18	-1.27	0.49	3.59
			0.65	-2.56	-2.43	-1.38	-3.41	-5.14
2	0.67	0.14	2.43	-0.44	5.06	3.59	5.36	8.56
			4.48	7.10	1.94	3.42	1.40	-9.38
3	0.65	0.21	-0.17	-0.89	2.77	0.96	2.73	4.11
			1.94	2.73	-0.90	0.89	-1.16	-3.77

**Table 8.8** Acceptance with statistical and systematic uncertainties (in %) in  $\Delta\phi_{\gamma\gamma}$  bins for  $30 < M_{\gamma\gamma} < 50$  GeV. The two numbers in each box correspond to  $+1\sigma$  and  $-1\sigma$  variations.

$\Delta\phi$ bin	Acc	Stat (%)	Vtx Reso (%)	Vtx MisMatching (%)	E Scale (%)	E Reso (%)	PhiMod (%)	Overall syst.(%)
0	0.56	0.35	-1.71	1.81	1.48	-0.04	1.79	3.40
			1.47	-3.10	-1.58	0.03	-2.12	-4.33
1	0.54	0.35	-1.81	3.20	1.27	-0.07	1.73	4.26
			1.62	-2.87	-1.32	0.04	-2.12	-4.14
2	0.53	0.43	-1.83	4.37	1.21	-0.07	1.70	5.18
			1.69	-3.07	-1.29	0.07	-1.89	-4.19
3	0.49	3.75	-2.60	3.85	0.43	-0.07	2.18	5.15
			2.80	-3.24	-0.96	-0.03	-2.29	-4.95

**Table 8.9** Acceptance with statistical and systematic uncertainties (in %) in  $\Delta\phi_{\gamma\gamma}$  bins for  $50 < M_{\gamma\gamma} < 80$  GeV. The two numbers in each box correspond to  $+1\sigma$  and  $-1\sigma$  variations.

$\Delta\phi$ bin	Acc	Stat (%)	Vtx Reso (%)	Vtx MisMatching (%)	E Scale (%)	E Reso (%)	PhiMod (%)	Overall syst.(%)
0	0.58	0.28	-1.51	0.56	1.96	0.21	1.97	3.22
			1.75	-0.15	-1.50	0.19	-1.79	-2.92
1	0.57	0.26	-1.36	0.83	2.07	0.29	2.22	3.44
			1.87	-0.25	-1.42	0.30	-1.91	-3.05
2	0.58	0.26	-1.23	0.73	2.06	0.37	2.11	3.30
			1.96	-0.40	-1.28	0.38	-1.70	-2.95
3	0.58	0.22	-1.19	1.10	1.97	0.37	2.08	3.32
			1.91	-0.54	-1.20	0.38	-1.66	-2.88
4	0.59	0.19	-0.95	1.49	2.10	0.64	2.34	3.66
			2.23	-0.14	-0.85	0.64	-1.25	-2.77
5	0.58	0.99	-1.21	-0.29	1.55	0.49	2.26	3.05
			1.94	-1.54	-0.87	0.52	-1.65	-3.15

**Table 8.10** Acceptance with statistical and systematic uncertainties (in %) in  $\Delta\phi_{\gamma\gamma}$  bins for  $80 < M_{\gamma\gamma} < 350$  GeV. The two numbers in each box correspond to  $+1\sigma$  and  $-1\sigma$  variations.

$\Delta\phi$ bin	Acc	Stat (%)	Vtx Reso (%)	Vtx MisMatching (%)	E Scale (%)	E Reso (%)	PhiMod (%)	Overall syst.(%)
0	0.61	0.17	2.05	3.61	5.79	3.71	5.60	9.79
			5.31	3.94	1.62	3.70	1.53	-7.90
1	0.62	0.13	-0.43	1.05	2.76	1.12	2.81	4.25
			2.62	1.17	-0.51	1.11	-0.81	-3.22
2	0.61	0.54	-0.66	0.87	2.14	0.93	2.62	3.67
			2.41	0.36	-0.30	0.92	-1.13	-2.85

**Table 8.11** Acceptance with statistical and systematic uncertainties (in %) in  $\cos\theta^*$  bins for  $30 < M_{\gamma\gamma} < 50$  GeV. The two numbers in each box correspond to  $+1\sigma$  and  $-1\sigma$  variations.

$\cos\theta$ bin	Acc	Stat (%)	Vtx Reso (%)	Vtx MisMatching (%)	E Scale (%)	E Reso (%)	PhiMod (%)	Overall syst.(%)
0	0.50	4.17	-2.22	6.95	0.75	-0.05	1.99	7.60
			1.64	1.12	-0.97	0.07	-2.22	-3.13
1	0.54	3.59	-2.21	0.70	1.05	0.01	2.01	3.24
			1.42	-4.63	-0.78	-0.00	-2.31	-5.43
2	0.52	2.79	-1.69	1.46	0.52	-0.04	1.90	2.98
			3.07	-6.70	-1.29	-0.09	-1.99	-7.75
3	0.49	6.19	-4.55	9.59	1.85	-0.63	1.95	10.97
			3.93	-0.94	-3.07	0.30	-1.65	-5.35

**Table 8.12** Acceptance with statistical and systematic uncertainties (in %) in  $\cos\theta^*$  bins for  $50 < M_{\gamma\gamma} < 80$  GeV. The two numbers in each box correspond to  $+1\sigma$  and  $-1\sigma$  variations.

$\cos\theta$ bin	Acc	Stat (%)	Vtx Reso (%)	Vtx MisMatching (%)	E Scale (%)	E Reso (%)	PhiMod (%)	Overall syst.(%)
0	0.60	0.89	-0.51	1.96	2.21	0.81	2.66	4.09
			2.00	-2.72	-0.60	0.83	-1.17	-3.72
1	0.61	1.36	-0.91	2.28	2.04	0.69	2.43	4.07
			2.35	0.95	-0.74	0.75	-1.41	-3.08
2	0.60	1.29	-0.24	1.51	2.22	1.18	3.01	4.21
			2.33	1.40	-0.38	1.19	-0.97	-3.15
3	0.60	1.27	-0.69	-0.67	1.68	0.48	2.17	2.95
			1.54	-1.67	-1.06	0.51	-1.57	-3.00
4	0.56	1.63	-1.03	1.05	2.42	1.00	2.72	4.05
			3.05	-0.12	-0.33	0.96	-1.03	-3.38
5	0.49	2.39	-3.17	-6.58	1.10	-0.15	1.40	7.52
			2.07	-2.57	-1.51	-0.13	-2.25	-4.28

**Table 8.13** Acceptance with statistical and systematic uncertainties (in %) in  $\cos\theta^*$  bins for  $80 < M_{\gamma\gamma} < 350$  GeV. The two numbers in each box correspond to  $+1\sigma$  and  $-1\sigma$  variations.

$\cos\theta$ bin	Acc	Stat (%)	Vtx Reso (%)	Vtx MisMatching (%)	E Scale (%)	E Reso (%)	PhiMod (%)	Overall syst.(%)
0	0.65	0.51	1.24	3.83	3.90	2.47	4.18	7.42
			3.56	1.52	1.06	2.45	0.43	-4.72
1	0.65	0.57	-0.89	-0.17	1.45	0.21	1.83	2.51
			1.40	-0.05	-1.19	0.20	-1.76	-2.55
2	0.55	0.77	-1.60	-1.09	2.40	0.92	2.73	4.22
			3.09	1.29	-0.43	0.93	-1.17	-3.69

## 8.12 Cross-check of background-subtracted data vs. fast MC simulation

Figs. 8.33 – 8.35 show a comparison between the background-subtracted data distributions and the smeared distributions from the generator-level-reweighted RESBOS fast MC simulation for  $p_T^{\gamma\gamma}$ ,  $\Delta\phi_{\gamma\gamma}$  and  $\cos\theta^*$  in the three mass bins,  $30 < M_{\gamma\gamma} < 50$ ,  $50 < M_{\gamma\gamma} < 80$  and  $80 < M_{\gamma\gamma} < 350$  GeV. Just statistical uncertainties are shown (i.e. one needs to keep in mind, for example, additional 12–17% caused by the diphoton events purity used in the background subtraction). One can see that the RESBOS predictions describe the data very well within uncertainties.

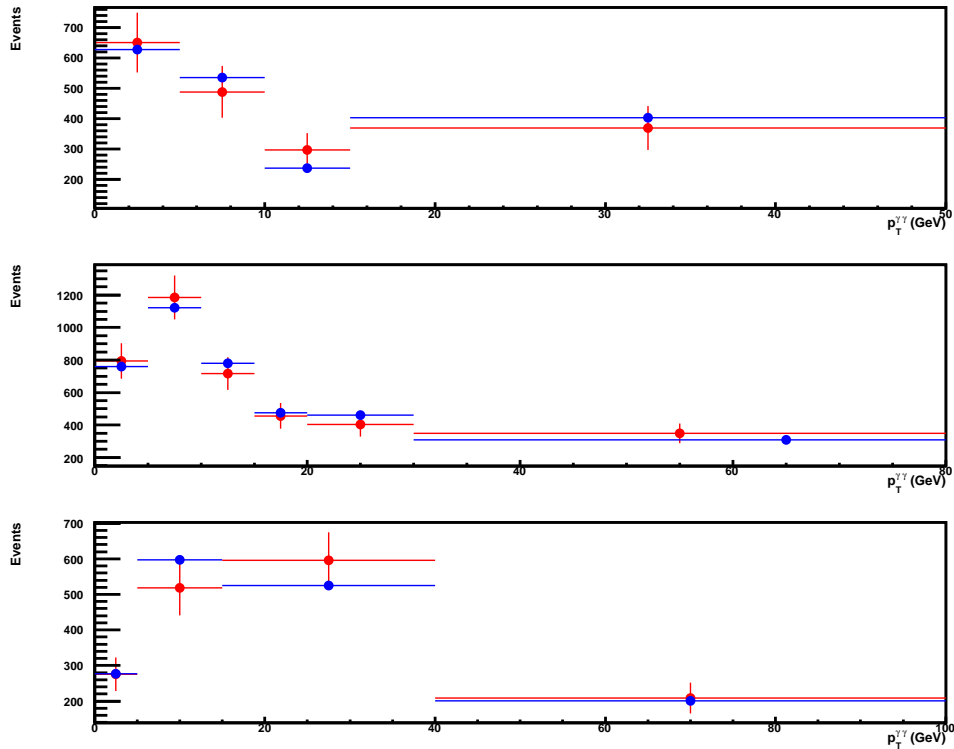


**Figure 8.33** Comparisons between the background-subtracted data distributions (red points) and the smeared distributions (blue points) from the generator-level-reweighted RESBOS fast MC simulation for  $p_T^{\gamma\gamma}$  in the three mass bins. Just statistical uncertainties are shown.

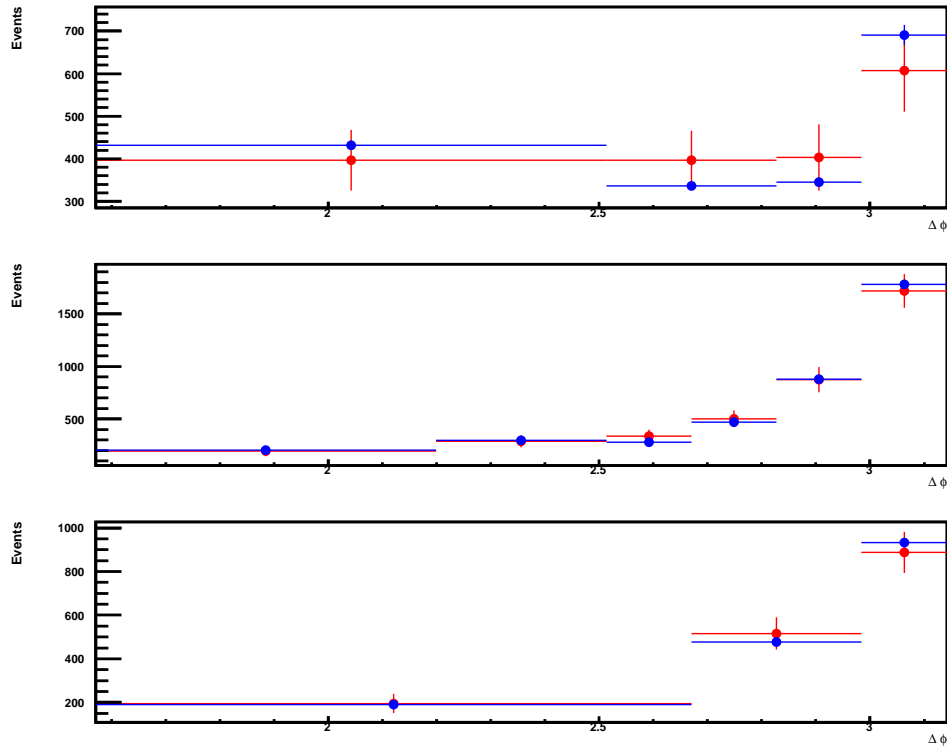


**Figure 8.34** Comparisons between the background-subtracted data distributions (red points) and the smeared distributions (blue points) from the generator-level-reweighted `RESBOS` fast MC simulation for  $\Delta\phi_{\gamma\gamma}$  (upper right) in the three mass bins. Just statistical uncertainties are shown.

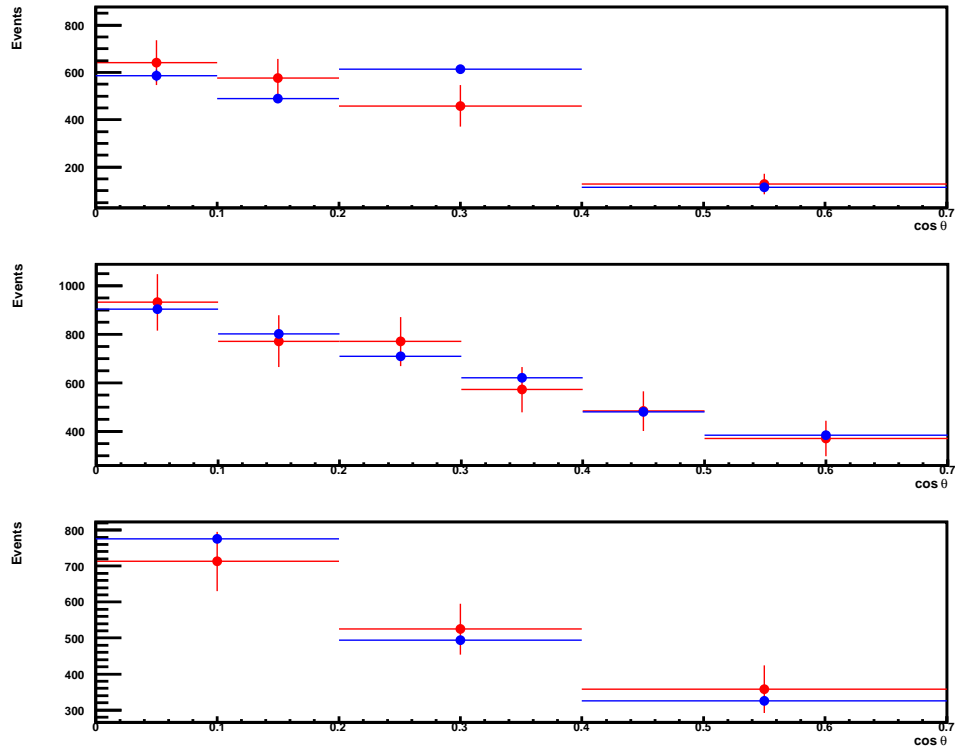


**Figure 8.35** Comparisons between the background-subtracted data distributions (red points) and the smeared distributions (blue points) from the generator-level-reweighted RESBOS fast MC simulation for  $\cos \theta^*$  in the three mass bins. Just statistical uncertainties are shown.